**Universidade de Aveiro** Departamento de Física
**Ano 2014**

**Ricardo Gonçalves Carvalho**

# LASER ASSISTED DIRECTIONAL SOLIDIFICATION OF ZIRCONIA-BASED EUTECTICS

# EUTÉTICOS À BASE DE ZIRCÓNIA SOLIDIFICADOS DIRECIONALMENTE POR LASER

**Universidade de Aveiro** Departamento de Física
**Ano 2014**

**Ricardo Gonçalves Carvalho**

# LASER ASSISTED DIRECTIONAL SOLIDIFICATION OF ZIRCONIA-BASED EUTECTICS

# EUTÉTICOS À BASE DE ZIRCÓNIA SOLIDIFICADOS DIRECIONALMENTE POR LASER

Tese apresentada à Universidade de Aveiro para cumprimento dos requisitos necessários à obtenção do grau de Doutor em Engenharia Física, realizada sob a orientação científica da Doutora Florinda Mendes da Costa, Professora Associada do Departamento de Física da Universidade de Aveiro e coorientação do Doutor Rui Ramos Ferreira e Silva, Professor Associado do Departamento de Engenharia de Materiais e Cerâmica da Universidade de Aveiro.

Apoio financeiro da FCT e do FSE no âmbito do III Quadro Comunitário de Apoio.

Dedico este trabalho aos meus pais e aos meus irmãos.

**o júri**

presidente

Prof. Doutor Mário Guerreiro da Silva Ferreira
professor catedrático do Departamento de Engenharia de Materiais e Cerâmica, Universidade de Aveiro

Prof. Doutor Andrés E. Sotelo Mieg
professor titular do Departamento Ciência de Materiais Universidade de Saragoça

Prof. Doutor João Carlos de Castro Abrantes
professor adjunto da Escola Superior de Tecnologia e Gestão do Instituto Politécnico de Viana do Castelo

Prof. Doutor Vasco Manuel Pinto Teixeira
professor associado do Departamento de Física, Escola de Ciências, Universidade do Minho

Prof. Doutor Manuel Almeida Valente
professor associado do Departamento de Física, Universidade de Aveiro

Prof. Doutora Florinda Mendes da Costa
professora associada do Departamento de Física, Universidade de Aveiro

**agradecimentos**

A realização do trabalho apresentado nesta tese não teria sido possível sem a colaboração de algumas pessoas e instituições, a quem eu desejo exprimir o meu agradecimento.

À minha orientadora Prof. Doutora Florinda Costa do Departamento de Física e ao meu coorientador Prof. Doutor Rui Silva do Departamento de Engenharia de Materiais e Cerâmica da Universidade de Aveiro pela orientação, dedicação, confiança e partilha de conhecimentos ao longo deste período.

Ao Doutor Filipe Figueiredo e ao Doutor Filipe Oliveira do Departamento de Engenharia de Materiais e Cerâmica da Universidade de Aveiro pela orientação, exigência e rigor transmitidos ao longo de todo o trabalho.

Ao Doutor Michael Lufaso do Departamento de Química Universidade North Florida, Doutor Andrei Kovalevsky, Departamento de Engenharia de Materiais e Cerâmica e ao Doutor Filipe Teixeira-Dias do Departamento de Engenharia Mecânica da Universidade de Aveiro, pela disponibilidade e ajuda que demonstraram no estudo e caracterização dos materiais.

Aos técnicos do Departamento de Física da Universidade de Aveiro, em especial ao Dr. António Fernandes pelo apoio, conselhos e partilha de conhecimentos.

À Doutora Maria do Rosário Soares, responsável técnica da equipa de DRX no Laboratório Central de Análises e ao Mestre Bruno Almeida técnico do serviço de microscopia eletrónica pela disponibilidade e conhecimentos transmitidos.

Aos meus colegas e amigos do grupo de Espectroscopia do Departamento de Física da Universidade de Aveiro pelo apoio e excelentes momentos de convívio.

À minha família e amigos pelo apoio incondicional, enorme compreensão e carinho.

**palavras-chave**

Solidificação direcional, fusão de zona com laser, fibras, eutéticos, zircónia.

**resumo**

Fibras eutéticas à base de zircónia foram crescidas por solidificação direcional pelo método de fusão de zona com laser. Investigaram-se dois sistemas: zircónia-zirconato de bário e zircónia-mulite. O objetivo foi tirar vantagem das propriedades da zircónia, particularmente como condutor iónico e como fase de reforço mecânico. A influência das condições de processamento nas características estruturais e microestruturais e as suas consequências no comportamento elétrico e mecânico das fibras compósitas foram o foco desta tese.

Os novos materiais eutéticos de zirconia-zirconato de bário foram desenvolvidos de forma a combinar a condutividade por iões oxigénio ao longo da zircónia, com a condução protónica através do zirconato de bário, promovendo um comportamento de condução iónica mista. A microestrutura das fibras é caracterizada por duas regiões alternadas: bandas com uma morfologia homogénea grosseira rica em zircónia; e zonas inter-bandas variando entre uma microestrutura eutéctica homogénea, a baixas velocidades de crescimento, e uma microestrutura colunar, para as fibras crescidas a uma velocidade maior. A distância inter-bandas aumenta com a velocidade de crescimento e a 300 mm/h desenvolvem-se dendrites de zircónia numa rede fina interpenetrada com 50 %vol. $ZrO_2$-50 %vol. $BaZrO_3$. As duas fases revelam contiguidade sem fronteiras de grão, de acordo com os resultados de espectroscopia de impedância. Composições ricas em ítria foram consideradas para promover a incorporação do ítrio nas duas fases, como revelado por espectroscopia de Raman e corroborado por análise química elementar por espectroscopia de raios-X por dispersão em energia. A incorporação simultânea do ítrio nas duas fases é condição obrigatória para se obter condutividade iónica mista. Tais resultados são suportados por medidas de espectroscopia de impedância que revelam claramente um aumento da condução iónica total para baixas temperaturas em atmosferas húmidas/redutoras (energia de ativação de 35 kJ/mol em $N_2$+$H_2$ e 48 kJ/mol em ar, no intervalo 320-500 ºC) comparado com as obtidas em condições de atmosferas secas/oxidantes (chegando a valores próximos de 90 kJ/mol, acima de 500 ºC). A temperaturas elevadas, a incorporação do protão no zirconato de bário não é favorável e a condução por iões oxigénio através da zircónia domina em ambientes secos e oxidantes, chegando ao máximo de $1{,}3 \times 10^{-2}$ S/cm em ar seco, a ~1000 ºC).

Em alternativa, a condução iónica da zircónia foi combinada com a da mullite, outro condutor de iões de oxigénio a alta temperatura, de forma a obter um domínio eletrolítico mais alargado. A velocidade de crescimento tem uma influência grande na quantidade de cada fase e na microestrutura das fibras de zircónia-mulite solidificadas direccionalmente. A sua microestrutura varia de uma morfologia eutética homogénea para eutéctica dendrítica, quando a velocidade de crescimento aumenta de 1 para 500 mm/h. Esta evolução é acompanhada de um aumento da quantidade de zircónia tetragonal. Além disso, velocidades de crescimento superiores levam ao desenvolvimento de uma fase vítrea de Al-Si-Y e a menor quantidade de mullite, o que conduz a um decréscimo considerável da condutividade iónica total das fibras. A redução da quantidade da fase amorfa depois de um tratamento térmico (10h; 1400 ºC) promove um aumento da condução iónica total (≥0.01 S/cm a 1370 °C), aumenta as frações das fases de mullite e zircónia tetragonal e conduz a diferenças microestruturais quer na distribuição quer no tamanho da zircónia. Estas modificações tiveram importantes consequências na condutividade elétrica devido ao incremento da percolação. Foi igualmente observado um aumento significativo da dureza, desde 11.3 GPa para fibras crescidas a 10 mm/h, até 21.2 GPa para as fibras crescidas a 500 mm/h. A morfologia eutética ultra-fina das fibras de 500 mm/h resulta num valor máximo de resistência à flexão de 534 MPa à temperatura ambiente, tendo diminuído para cerca de um quarto para temperaturas elevadas (1400 ºC) devido à presença da matriz vítrea.

**keywords**

Directional solidification, laser floating zone, fibres, eutectics, zirconia.

**abstract**

Directionally solidified zirconia-based eutectic (DSE) fibres were obtained using the laser floating zone (LFZ) method. Two systems were investigated: zirconia-barium zirconate and zirconia-mullite. The purpose was to take advantage of zirconia properties, particularly as an ionic conductor and a mechanical reinforcement phase. The influence of processing conditions in the structural and microstructural characteristics and their consequences on the electrical and mechanical behaviour were the focus of this thesis.

The novel zirconia-barium zirconate eutectic materials were developed in order to combine oxygen ionic conduction through zirconia with protonic conduction from barium zirconate, promoting mixed ionic conduction behaviour. The microstructure of the fibres comprises two alternated regions: bands having coarser zirconia-rich microstructure; and inter-band regions changing from a homogeneous coupled eutectic, at the lowest pulling rate, to columnar colony microstructure, for the faster grown fibres. The bands inter-distance increases with the growth rate and, at 300 mm/h, zirconia dendrites develop enclosed in a fine-interpenetrated network of 50 vol.% $ZrO_2$-50 vol.% $BaZrO_3$. Both phases display contiguity without interphase boundaries, according to impedance spectroscopy data. Yttria-rich compositions were considered in order to promote the yttrium incorporation in both phases, as revealed by Raman spectroscopy and corroborated by the elemental chemical analysis in energy dispersive spectroscopy. This is a mandatory condition to attain simultaneous contribution to the mixed ionic conduction. Such results are supported by impedance spectroscopy measurements, which clearly disclose an increase of total ionic conduction for lower temperatures in wet/reduction atmospheres (activation energies of 35 kJ/mol in $N_2$+$H_2$ and 48 kJ/mol in air, in the range of 320-500 ºC) compared to the dry/oxidizing conditions (attaining values close to 90 kJ/mol, above 500 ºC). At high temperatures, the proton incorporation into the barium zirconate is unfavourable, so oxygen ion conduction through zirconia prevails, in dry and oxidizing environments, reaching a maximum of $1.3x10^{-2}$ S/cm in dry air, at ~1000 ºC.

The ionic conduction of zirconia was alternatively combined with another high temperature oxygen ion conductor, as mullite, in order to obtain a broad electrolytic domain. The growth rate has a huge influence in the amount of phases and microstructure of the directionally solidified zirconia-mullite fibres. Their microstructure changes from planar coupled eutectic to dendritic eutectic morphology, when the growth rate rises from 1 to 500 mm/h, along with an increment of tetragonal zirconia content. Furthermore, high growth rates lead to the development of Al-Si-Y glassy phase, and thus less mullite amount, which is found to considerably reduce the total ionic conduction of as-grown fibres. The reduction of the glassy phase content after annealing (10h; 1400 ºC) promotes an increase of the total ionic conduction (≥0.01 S/cm at 1370 °C), raising the mullite and tetragonal zirconia contents and leading to microstructural differences, namely the distribution and size of the zirconia constituent. This has important consequences in conductivity by improving the percolation pathways. A notable increase in hardness is observed from 11.3 GPa for the 10 mm/h pulled fibre to 21.2 GPa for the fibre grown at 500 mm/h. The ultra-fine eutectic morphology of the 500 mm/h fibres results in a maximum value of 534 MPa for room temperature bending strength, which decreases to about one-fourth of this value at high temperature testing (1400 ºC) due to the soft nature of the glassy-matrix.

## Index

**List of abbreviations**

Directional solidified eutectic (DSE)

Electromotive force (EMF)

$Er_3Al_5O_{12}$ (EAG)

$GdAlO_3$ (GAP)

Laser floating zone (LFZ)

Laser heated pedestal growth (LHPG)

Mixed ionic conductors (MIC)

Mixed ionic-electronic conductors (MIEC)

Monoclinic zirconia (m-$ZrO_2$)

Tetragonal zirconia (t-$ZrO_2$)

Cubic zirconia (c-$ZrO_2$)

Room temperature (RT)

Scanning electron microscopy (SEM),

Slow cooling float zone (SCFZ)

Solid oxide fuel cells (SOFC)

Template grain growth (TGG)

Tetragonal zirconia polycrystal (TZP)

Variable temperature X-ray diffraction patterns (HTXRD)

X-ray diffraction (XRD)

X-ray spectroscopy (EDS)

$Y_3Al_5O_{12}$ (YAG)

Yttria-stabilized zirconia (YSZ, $(Zr,Y)O_2$)

Yttria-rich metastable tetragonal zirconia (t'-$ZrO_2$)

8 mol.% yttria-stabilized $ZrO_2$ (TZ-8Y)

## Motivation, objectives and thesis organization

Directional solidified oxide eutectics are a paradigm of composite materials with singular microstructural features, which have been presented in a first published report by Galasso and co-authors, working at the United Aircraft Research Laboratories, in 1967. Since then, the developments of the melt-grown technology along with a better knowledge of eutectic ceramics brought extra potentialities to these composites. In this way, the production of a recent generation of directional solidified eutectic (DSE) materials has been prospected to offer modern potential applications, improving the thermal efficiency of gas turbines, allowing the development of planar optical waveguides of wide gap and high melting point, being also incorporated in thermal power generation systems and solid oxide fuel cells technology. Eutectic growth is characterized by the cooperative growth of two or more solids phases from melt. If grown under controlled solidification conditions, directionally solidified ceramic eutectics have useful intrinsic features: low porosity, microstructural stability up to temperatures close to the melting point and strong bonded phases. Interestingly, the phase morphology is governed by the solidification conditions that promote an effective anisotropic effect. Additionally, their chemical and thermomechanical stabilities improve the performance of the eutectic structures, with great interest for high temperature structural and functional applications.

The goal of this work is to explore the employment of the optimized directional solidification method to novel ceramic systems: zirconia-barium zirconate and zirconia-mullite. Their potential technological applications can benefit from the microstructural design control and from the perfect match between the eutectic constituents.

The thesis is organized in four chapters. Chapter I starts with a brief review of the floating zone technology, the selected method to grow the DSE ceramic fibres, followed by the fundamental concepts of eutectic materials solidification and a concise revision of the directionally solidified materials with emphasis to the zirconia-based materials.

The experimental part of this thesis is divided in two chapters, corresponding to the two selected DSE materials. The reasons for these two approaches are related with the intention to take advantage of the zirconia outstanding potential as ionic conductor and mechanical reinforcement. Chapter II is thus devoted to the new zirconia-barium zirconate DSE material developed for electrochemical and functional devices. This chapter includes two published papers, where the synthesis of the fibres of zirconia-barium zirconate eutectics ceramics by directional solidification technique and the mixed conduction proper-

ties are respectively explored. Chapter III is dedicated to the zirconia-mullite DSE materials and encloses one published, one accepted and one submitted paper. This set of works describes two solid electrolyte materials, combining in this instance two oxide-ion conductor phases. Furthermore, the mechanical performance is scrutinized. The goal was to join the mullite strength retention at very high temperatures with the fracture toughening mechanisms of stabilized-zirconia and the eutectic microstructural stability at very high temperatures.

Finally, the thesis' epilogue in chapter IV covers the main conclusions and mentions some prospects as future research lines.

# Chapter I

## Directional solidification of eutectics

*This chapter is devoted to the fundamentals of the directional solidification method as a suitable materials processing technique to obtain zirconia-based eutectic composites. The historical background of the floating zone technique is firstly revised up to the emergence of the laser floating zone (LFZ) system and its subsequent technological upgrades (I.1.).*

*The basic concepts of fibre growth are then reported based on the solidification principles focused on the microstructural development of eutectic materials (I.2.).*

*Finally, a concise revision of the directional solidification of different eutectic systems is presented (I.3.) with special emphasis in the zirconia-based materials (I.4.).*

## I.1. History of laser floating zone

In 1951, William Pfann working at the Bell labs invented the zone refining process, a predecessor of the laser floating zone method, for the purification of germanium (Fig. 1). In this system, the impure germanium ingot is placed on a horizontal quartz or graphite crucible. Afterwards a narrow zone is molten by induction or radiation heating sources that travel from one extreme to the other [1-3]. In this way, the impurities are retained in the molten zone and loaded to the final ingot. Highly-pure materials can be achieved after multiple crossing through the zone refining system [2,4,5]. Unfortunately, this technology is improperly for silicon, due to high reactivity and contamination by the crucible material and the higher melting point (1415 ºC) [2].

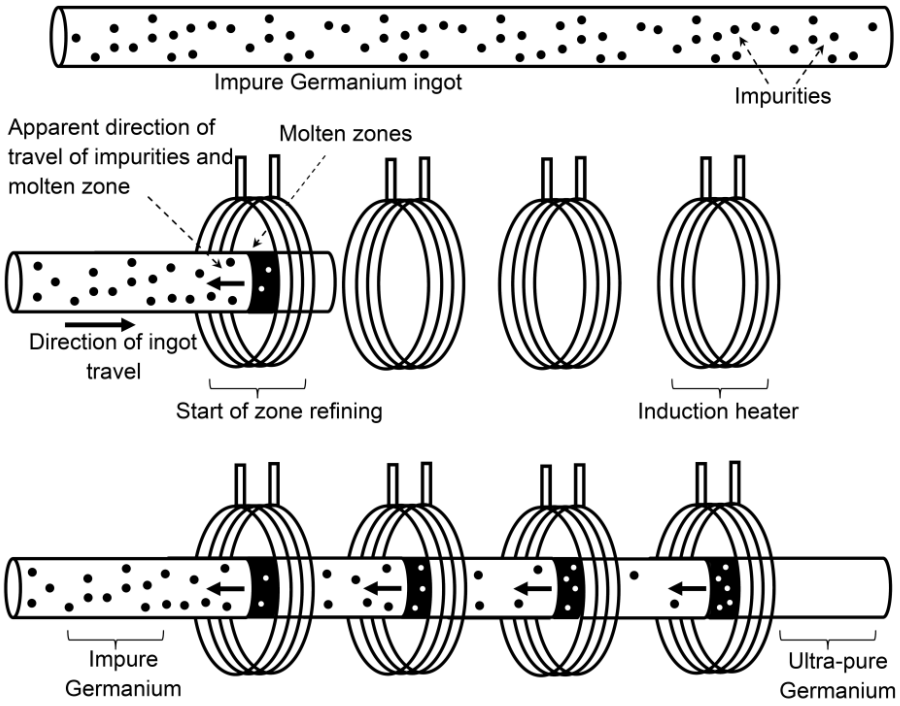


***Figure 1:*** *Illustration of a germanium zone refining technique process, adapted from [1].*

Since then, other variants of zone refining appear like the floating zone technology. In the beginning of 1952, Henry Theuerer made the first approach on the zone melting techniques (Fig. 2) in order to grow single crystals and to increase their purity. The purification process takes advantage of the concentration changes by the segregation of most impurities into the liquid. The floating zone is suspended between the melting and solidification interfaces, as depicted in Figure 3 [2,6].

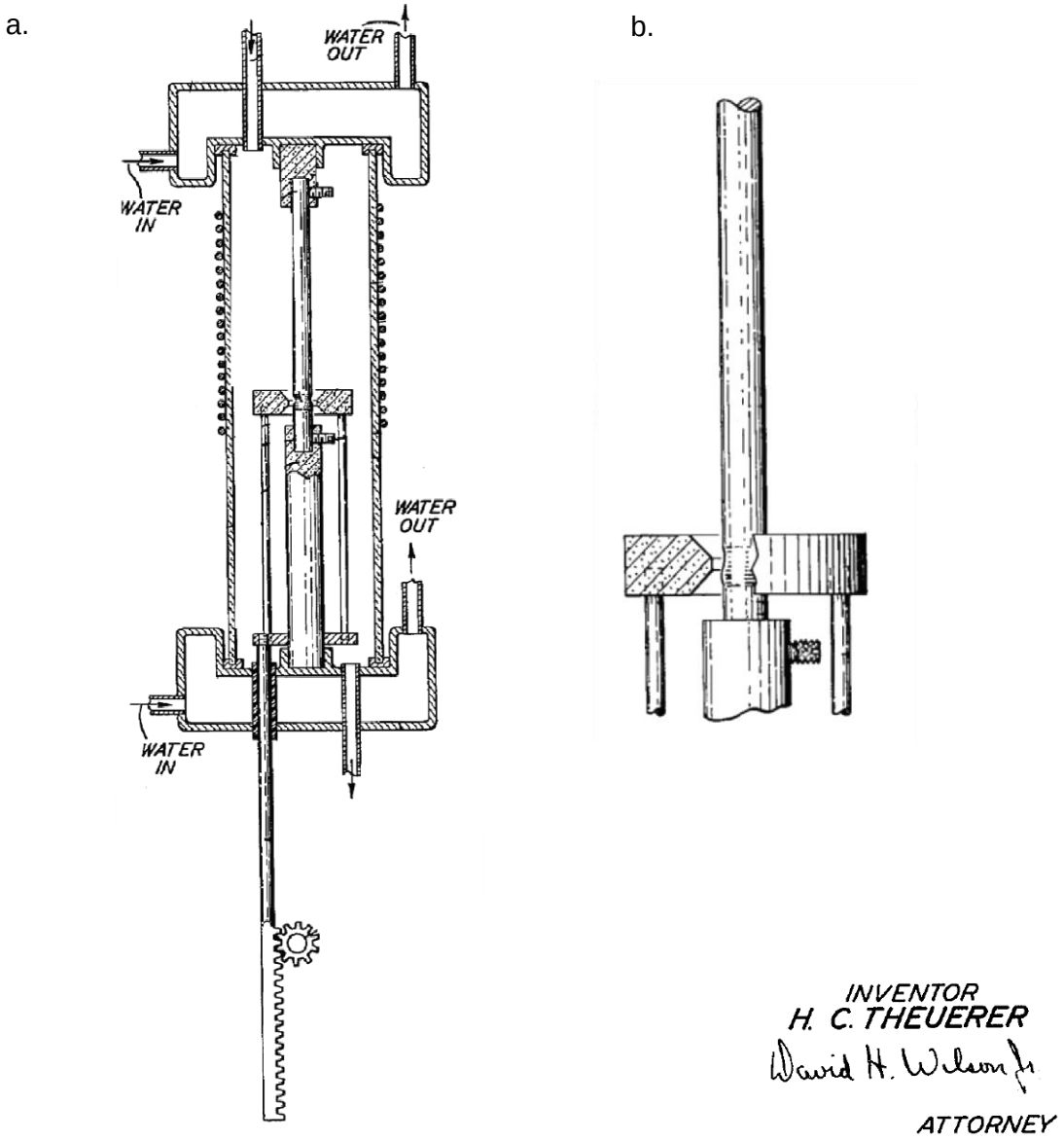


***Figure 2: (a)*** *Schematic view of the apparatus developed by Henry Theuerer for performing refining and single-crystal growing operations,* ***(b)*** *closer view of molten region during the process [6].*

For crystal growth, a feed rod is fixed in the upper side as shown in Figure 3, while a seed rod is hold at the bottom one. The heating source is focused at the bottom of the feed rod, where melting is produced and the seed rod is slowly dipped into it. During the crystal growth, the seed and feed rods are driven downwards at constant feed/seed rate ratio. Keck et al. used this method to grow the first silicon crystal, without rotating [2]. Such process was introduced by R. Emeis working at the Siemens labs [2]. Müller et al. then used high frequency induction heating, whereas their predecessors had used radiation heating sources [2].

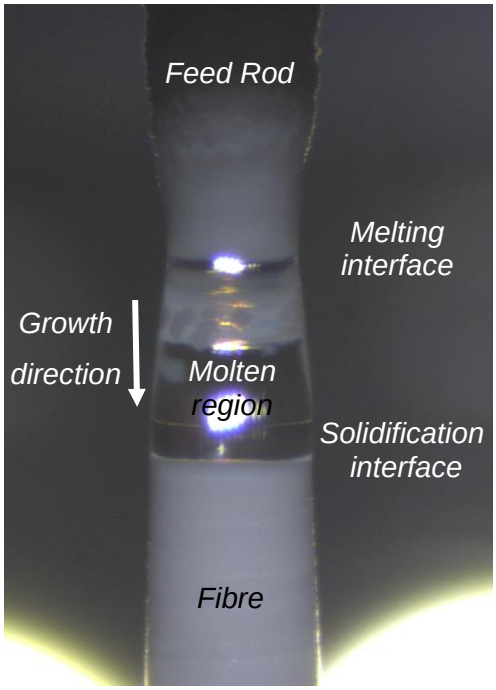


***Figure 3:*** *Photograph capture during the growth zirconia-mullite material. The main regions are labelled. The fibre is downwards pulled, as pointed by the arrow.*

Industrially, the floating zone technology is used for the manufacturing of silicon and germanium high-quality crystals, for applications in electronic and optoelectronic devices [2]. The increasing demands of crystal quality and diameter (up to 200 mm) have been the main manufacturing challenges, as illustrated in Figure 4. Floating zone technology was expanded through the development of several apparatus based on different heat sources to produce the molten zone: resistance, induction, electron beam, focus lamp and laser heating [7].

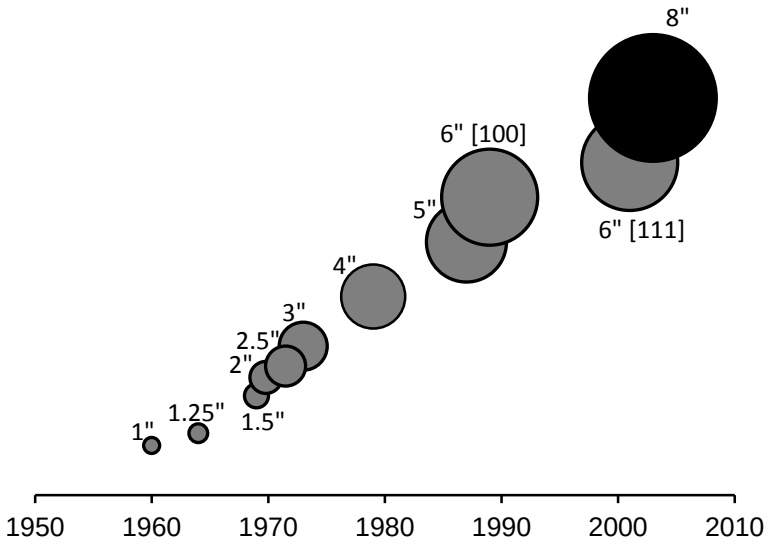


***Figure 4:*** *Evolution of crystal diameters over the last 50 years, adapted from [2].*

Eickhoff and Görs (in 1969), and then Gasson and Cockayne (in 1970), made the earliest approach to the employment of a laser beam for machining of high refractory materials [8, 9]. In the floating zone method, the laser has many advantages over the other heating sources:

(i) The beam wavelength can be chosen according to the material, while other radiation sources radiate in a large wavelength range for which the molten region is transparent.

(ii) The laser can be focussed onto the molten region, while an incandescent system heat a large region of the crystal.

(iii) No restrictions on the kind of atmosphere.

In 1972, Haggerty introduced the first laser floating zone (LFZ) apparatus, where four focused laser beams were used as heating source [3,10,11]. This allows to grow materials with very high melting points and so a number of single and polycrystalline fibres of TiC, $TiB_2$, $Al_2O_3$ and $Y_2O_3$ have been manufactured and their mechanical behaviour explored. In the following years, multiple (two or four) laser beams systems were used, but these ones led to hot spot incidence and so to large radial thermal gradients in the molten zone, making the crystal growth unstable [3]. Fejer et al. developed an optical module known as reflaxicon, promoting a much uniform energy distribution over the molten zone, as illustrated in Figure 5 [12,13].

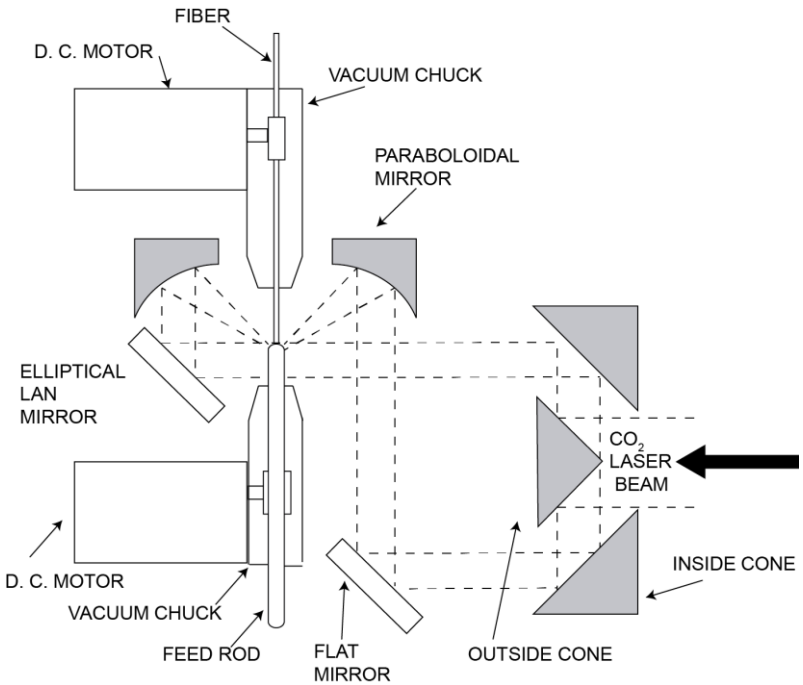


***Figure 5:*** *A cross-sectional diagram of focusing optics and translators systems of the LFZ technique [13].*

The reflaxicon has an inner cone surrounded by a larger coaxial cone section, both with reflective surfaces. The intent of this optical module is to convert the laser spot into a ring providing a much uniform incidence in the molten region [12,13]. Since then, several modifications have been proposed to improve the LFZ system. Fejer et al. developed a high-speed diameter control of the fibre during the growth process [14]. This proved to be fundamental to decrease the beam scattering at the surface of the fibre and to obtain high-quality single-crystal fibres [14]. In this way, the floating zone method became a versatile crystal melt growth technique, as revealed by the increasing number of published and cited articles, since 1983 (Fig. 6).

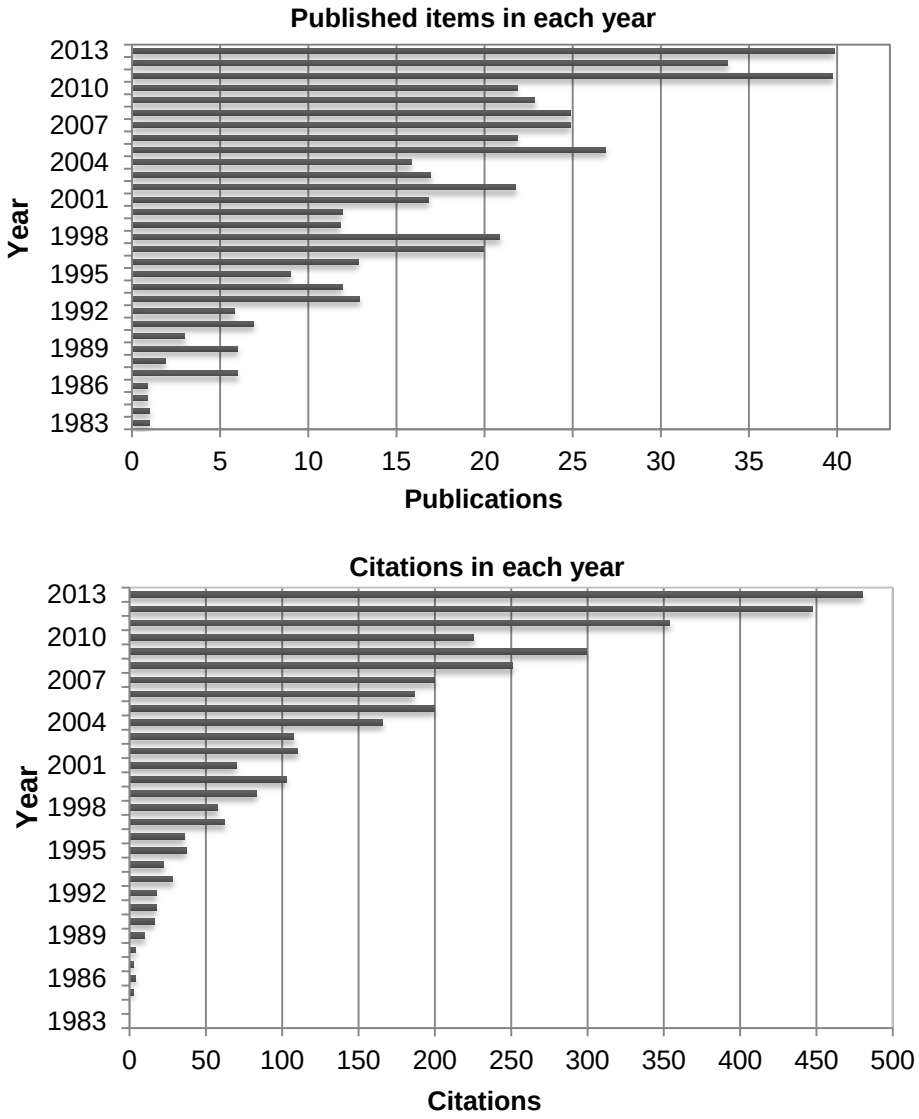


***Figure 6:*** *Publication and citation records in the LFZ topic over the last 30 years (database ISI Web of Knowledge).*

Crucibles or furnace components are not required, which could lead to contamination and confinement stress problems. Moreover, it is possible to prepared congruent and incongruent melting crystals, by controlling the composition of the starting rods. Faster growth rates can be used due to the small crystal size and the focused heating source, resulting in steep thermal gradients [7].

## I.2. Fundamentals of fibres growth

### I.2.1. Solidification of eutectic materials

The LFZ growth requires conservation of mass and energy, and shape stability. The conservation of mass is related with dimensional stability of the molten zone (constant volume and length) and of the meniscus shape. The steady-state growth of a crystalline fibre with constant cross-section is given by:

$$r = r_0\sqrt{(R/R_0)} \tag{1.1}$$

where $r$, $r_0$, are respectively the radius of the fibre and the feed rod, and $R$ and $R_0$ the fibre and feed rod growth rates. The growth rate instabilities may disrupt the mass conservation condition and lead to variations in the fibres diameter. The shape of the molten zone depends on the growth direction as it is depicted in Figures 7a and b, for downwards and upward growth, respectively. The meniscus angle (ϕ) is of extremely importance since it should be held constant in order to retain an uniform fibre diameter [15].

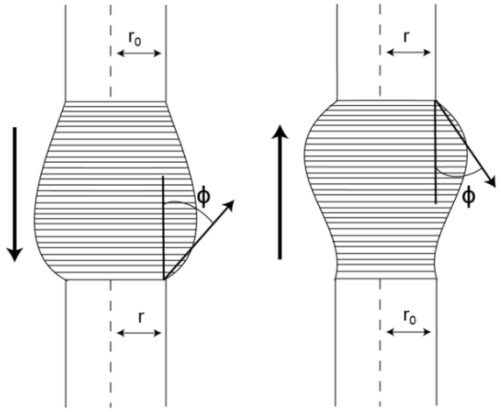


a. b.

***Figure 7:*** *Equilibrium shape of the molten zone* ***(a)*** *downward growth and* ***(b)*** *upward growth [15].*

The solidification interface shape analysis is determined by the growth rate (R), the thermal gradient (G) and the composition, as shown in Figure 8. So, for a fixed composition ($C_0$), by varying the thermal gradient or the solidification rate, the interface morphology changes between planar, cellular, dendritic and equiaxed [16].

In the case of the self-organized microstructure of eutectic materials a precise control of the growth rate is needed as well as of the thermal gradient at the solidification interface. Therefore, these are two parameters which can be adjusted to tune the system and yield the desired microstructure. The typical thermal gradients at the solidification interface ($10^3$-$10^4$ ºC/cm) of LFZ methods are significantly higher than in other melt grown tech-

niques, resulting in a wide number of advantages including: higher growth rates and better grain alignment and the possibility to obtain high temperature metastable phases [3].

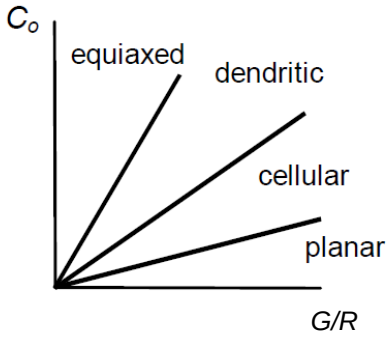


***Figure 8:*** *Influence of composition ($C_0$), thermal gradient (G) and growth rate (R) on the solidified morphology [16].*

Another important effect of the high thermal gradient is the possibility to reduce the constitutional undercooling. The planar-front growth under steady-state conditions lead to solute redistribution/diffusion, resulting in a variation of the solute concentration and changing in the equilibrium solidification temperature. So, if *G/R* at the solidification interface is lower than a critical value, the liquid just ahead of the solidification front exists below its equilibrium solidification temperature, i.e. it is undercooled. Since this modification arises from compositional or constitutional effects, the phenomenon is known as constitutional undercooling [17]. The increase of constitutional undercooling promotes the disruption of the planar-front condition due to solute segregation into the melt, ahead of the solidification interface. In this sense, directional solidified eutectics (DSE) having fully aligned microstructures can be only achieved when the solidification occurs under planar-front conditions. Mollard and Flemings provided an equation that defines the criterion for eutectic planar-front growth (avoiding of constitutional undercooling) [18]:

$$G/R \geq -m\,(C_E - C_0)/D \qquad (1.2)$$

where $C_E$ is the eutectic composition, $C_0$ the starting composition, *m* the slope of the *liquidus* line at the phase diagram, R the growth rate and D the diffusion coefficient of the solute in the melt. So, the planar-front growth is chiefly controlled by three parameters: growth rate, thermal gradient and compositional variation ($\Delta C = C_E - C_0$) [19]. The critical *G/R* ratio established for the planar-front growth, corresponds to *G/R*=0 (for $C_E = C_0$), for which the eutectic alignment can be attained by a narrow thermal gradient and high growth rate. This corresponds to a planar solidification interface, which determines that the eutectic constituents must grow at the same rate. In addition, no primary or non-eutectic constituents can grow or be projected into the melt ahead of plane-front [18]. If a

small increase of constitutional undercooling is considered owing to higher R or lower G, instabilities will develop along the growth direction, and a cellular interface will result. This corresponds to planar to cellular transition and occurs at a gradient $G_{p/c}$, as shown schematically in (Fig. 9).

Another increasing of the undercooling condition leads to dendritic morphology. The lower thermal gradient increases the space between the cells and constitutional undercooling may also occur perpendicularly to the growth direction. So, instabilities will advance on the sides of the cells, resulting in the formation of dendrites. This takes place at a thermal gradient $G_{c/d}$ (Fig. 9).

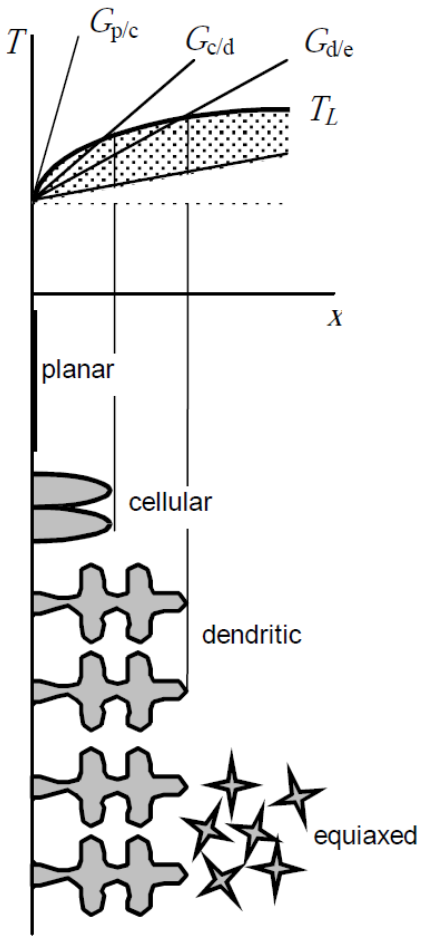


Constitutional undercooling is pronounced at very low G/R. The grains of the solid can nucleate in the melt ahead of the solid-liquid interface, resulting in equiaxed randomly oriented dendritic microstructures. The dendritic to equiaxed transition occurs at $G_{d/e}$ (Fig. 9). The growth conditions in the liquid became isotropic and new crystals having spherical shape start to develop ahead of the solidification interface. Spherical nuclei appear in the liquid, but their local surface instabilities will also grow at their interfaces and the final shape of the equiaxed crystals will not be spherical but dendritic [16].

***Figure 9:*** *Correlation between the thermal gradient at the solidification interface and the solidification morphology. The planar to cellular transition occurs at a gradient label by $G_{p/c}$, the cellular to dendritic transition happens at the $G_{c/d}$ and the dendritic to equiaxed takes place at the $G_{d/e}$ condition [16].*

In resume, the effect of the temperature gradients and growth rate on the microstructure of the eutectic materials is illustrated in Figure 10.

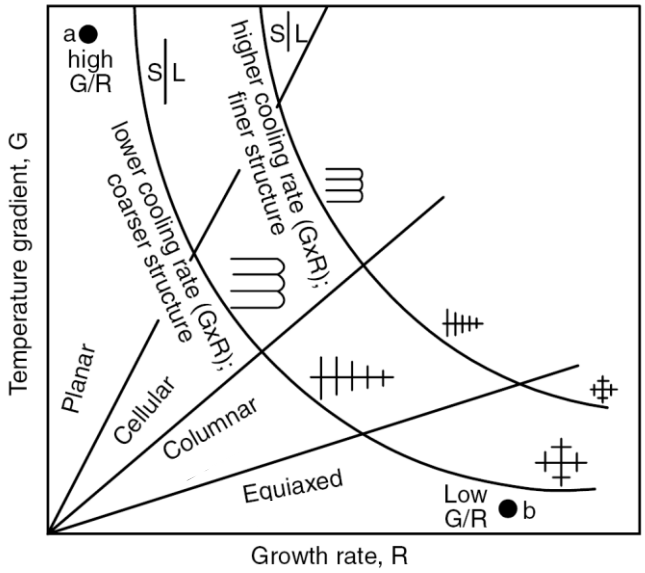


***Figure 10:*** *Effect of the temperature gradient and growth rate on the morphology and size of solidification microstructure, adapted from [20].*

The *G/R* governs the mode of solidification, while the product *GR* determines the size of the solidified microstructures. If the same solidification field is assumed, the product *GR* determines that for high growth rates finer microstructures were developed, while low cooling rates promotes coarser microstructures.

### I.2.2. Eutectic growth

In 1954, Scheil introduced the concept of coupled growth for the production of normal eutectics, where both phases grow simultaneously ahead a planar solidification interface, as cited in reference [21]. In fact, the eutectic solidifies cooperatively when the A-rich α phase rejects the B atoms by laterally diffusion in a short path, where they will be incorporated in the B-rich β phase, as illustrated in Figure 11 [17]. The same will happen with the A atoms rejected by β phase, diffusing until the tip of an adjacent α-lamella. A solute redistribution takes place as a consequence of extensive lateral diffusion, leading to concentration gradients at the solid phases interface. The eutectic growth is strongly ruled by the diffusion rate and that determines the interlamellar spacing (λ). The eutectic crystal growth rate depends on the undercooling below the equilibrium eutectic temperature and is limited by the chemical diffusion in the liquid ahead of the solidification interface. The eutectic undercooling melt combines four contributions: constitutional, thermal, interface curvature and kinetics.

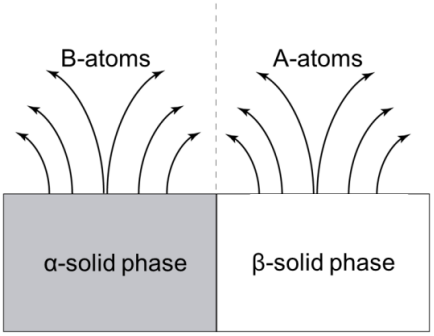


***Figure 11:*** *Interdiffusion in the liquid ahead of the planar-front interface, adapted from [17].*

For the case of lamellar eutectic growth, the thermal and kinetic components are negligible. The compositional variations along the solidification interface are the reason for undercooling that has its maximum at the centre of each lamella. The curve lamellar tip profile leads to thermal variations, with the maximum at the triple junction between the solid lamellae. However, the total undercooling at the interface must be constant since the solidification interface must be nearly isothermal in order to fulfil the planar-front condition and attain a fully aligned structure [22].

In the phase diagram of Figure 12 the coupled zone corresponds to composition/temperatures in which cooperative growth takes place. The coupled zone can be classified in two modes: symmetric (lamellar or fibrous eutectics) and asymmetric (irregular eutectic). The shape and position of the coupled zone are governed by the shape of the *liquidus* lines at the phase diagrams and the relative crystallization rates of the pure constituents [21]. The symmetrical coupled zone at phase diagram is shown in the top left plot of Figure 12 and it is associated with a normal structure, where the phases crystallize together by the advance of a common interface into the melt. For small undercoolings, the coupled zone is the region where the eutectic grows faster than α or β primary dendrites [23]. At higher undercoolings, the primary dendrites will have higher growth rate, and the final microstructure may combine dendrites with eutectic structure. At even higher undercooling, the eutectic growth rate will become again the highest, but the stronger undercooling avoids the planar structure development and equiaxed coupled growth will be created [16,23]. Notice that for high growth rates, dendrites can be found in eutectic microstructures [16,23]. This phenomenon is of great interest for the production of *in situ* composite materials, once it was not restricted to the eutectic compositions.

Anomalous eutectic microstructures will result from an asymmetric coupled zone, as depicted in Figure 12(bottom). A competitive growth takes place, without solute exchange and the two phases grow separately [21]. If one phase is heavily undercooled, this lead to

primary dendrites of such phase growing faster than the eutectic [16,23]. According with this, three kinds of microstructures will be possible: only free-dendrite eutectic, or α or β primary dendrites plus the eutectic [23]. The eutectic structure is not only obtained when the composition is exactly eutectic. In fact, depending on the growth conditions, eutectic microstructures can result from off-eutectic compositions (hypoeutectic and hypereutectic). Off-eutectic compositions tend to develop primary dendrites, where solute is rejected ahead of the dendrite tip into the remained liquid, such happens until the eutectic composition is reached and so the eutectic solidifies around the dendritic structure. Nevertheless, under controlled solidification conditions, it is possible to solidify off-eutectic materials without the formation of such primary dendrites. If the undercooling is accentuated, the eutectic grows faster than the dendrites, since diffusion-coupled growth is much faster than isolated dendritic growth the coupled zone is attained, Figure 12(bottom).

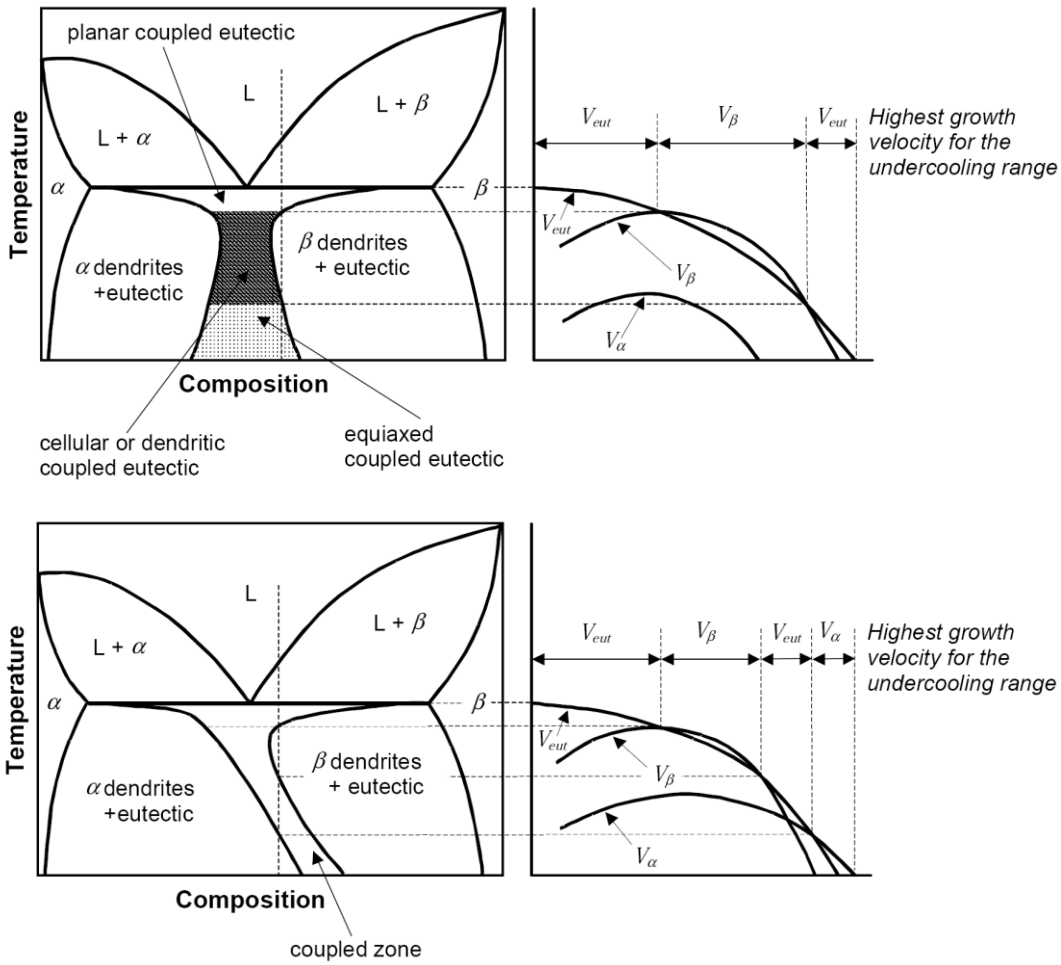


***Figure 12:*** *The symmetric (top) and asymmetric (bottom) eutectic coupled zones projected over the phase diagram for regular and anomalous systems [16].*

### I.2.3. Eutectic microstructure

Brady in 1922 and then Portevin in 1923 distinguished three eutectic categories, namely: lamellar, rod-like and irregular [24]. However, the presence of impurities in their alloys caused the development of uncertain structures in which the phase arrangement differs from pure alloys. In 1954, Scheil defined two types of eutectic microstructures based on the observation of several metallic systems: normal and anomalous as mentioned in the previous section [21]. According with this description, the normal eutectics have crystallographic alignment between both phases. The structure comprises a lamellar microstructure having an aligned plate-like arrangement of both phases and a fibrous microstructure, in which an orientated rod-like phase is enclosed in a matrix of a second phase. In the anomalous eutectic, the platelets of one phase are immersed in the second one without any apparent crystallographic relationship between them.

The theory provided by Hunt and Jackson explained the eutectic final microstructure based on the interface-roughness parameter [25]. Indeed, such parameter is chiefly dependent on the individual entropy of fusion ($\Delta S_f$) of the eutectic constituents [25]. So, the interface-roughness parameter (α) given by equation (1.3) predicts the faceted or nonfaceted growth of each phase.

$$\alpha = \xi \, \Delta S_f / \bar{R} \tag{1.3}$$

where ξ is a crystallographic parameter (~1) and $\bar{R}$ is the gas constant. Typically, most metals have low entropies of melting (α<2) growing isotropically with no facets, while the ceramic have higher ones (α>2) and grow with crystalline facets. According with this model, the eutectic microstructure will be split in three groups: nonfaceted/nonfaceted, faceted/faceted and nonfaceted/faceted [25]:

(i) If both phases have low entropies of melting (α<2) the nonfaceted/nonfaceted phases lead to lamellar or fibrous eutectic microstructure (Fig. 13a).
(ii) If only one phase have high and the other phase has a low entropy of melting (α>2) the phases appear faceted/nonfaceted leading to irregular microstructure (Fig. 13b).
(iii) If both have high entropies of melting (α>2) the eutectic is faceted/faceted with independent crystals of each phase (Fig. 13c).

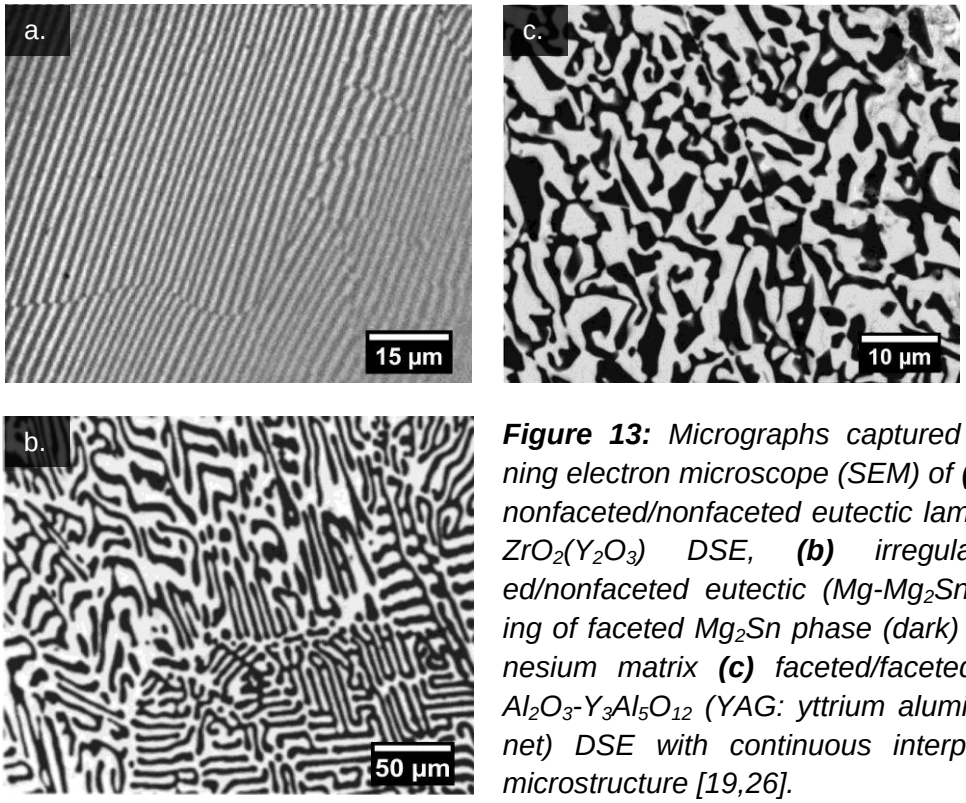


***Figure 13:*** *Micrographs captured by scanning electron microscope (SEM) of* ***(a)*** *regular nonfaceted/nonfaceted eutectic lamellar NiO-$ZrO_2$($Y_2O_3$) DSE,* ***(b)*** *irregular faceted/nonfaceted eutectic (Mg-$Mg_2Sn$) consisting of faceted $Mg_2Sn$ phase (dark) in a magnesium matrix* ***(c)*** *faceted/faceted eutectic $Al_2O_3$-$Y_3Al_5O_{12}$ (YAG: yttrium aluminium garnet) DSE with continuous interpenetrating microstructure [19,26].*

Croker et al. (1973) proposed, rather than consider the entropy of fusion of each phase, to use the entropy of solution of a single constituent in the liquid added to the volume fraction of each phase and to the growth rate [24]. According with this analysis, the eutectic are mainly divided into normal and anomalous categories. If one of the eutectic constituents has high entropy of solution ($\Delta S^{\alpha L}$), it is hoped that this one rules the eutectic microstructure. Normal eutectic microstructures (lamellar, fibrous) were defined up to $\Delta S^{\alpha L}$=23 J/mol K, while anomalous eutectics having quasi-regular, broken lamellar, irregular and other complex microstructures were obtained at higher values of entropy of solution, as shown in Figure 14.

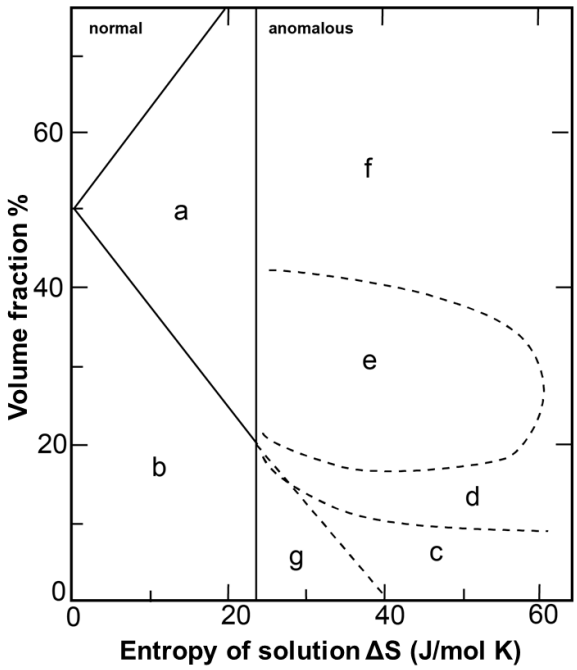


***Figure 14:*** *Correlation between the eutectic microstructures with entropy of solution and volume fraction showing the structural regions: (a) regular lamellar; (b) regular rods; (c) broken lamellar; (d) irregular; (e) complex regular; (f) quasi-regular and (g) irregular fibrous [24].*

The relationship between the volume fraction of each eutectic phase and the interface-roughness parameter is illustrated in Figure 15. According with this, if the volume fraction of both nonfaceted phases is equal ($f_\alpha/f_\beta \sim 0.5$), it solidifies as regular lamellar eutectic microstructure. If the volume fraction of one phase is significantly higher than that of the other ($f_\alpha/f_\beta < 0.28$), a fibrous microstructure will be established to minimize the interfacial energy. However, when the phase in minor amount is faceted, this lead to faceted-rods or an irregular lamellar microstructure (for higher contents) [23].

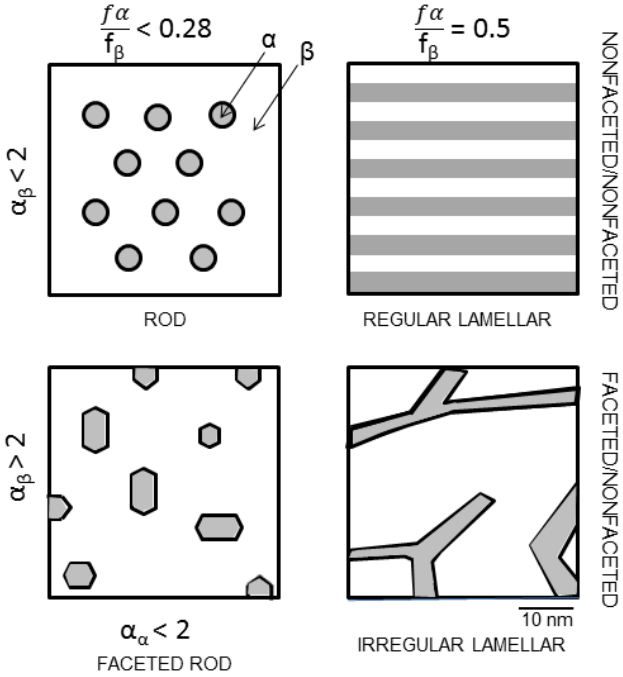


***Figure 15:*** *Types of binary eutectic morphology, adapted from [23].*

The microstructures produced during eutectic solidification are often more complex than the ones described by this model. So, features in three different size scales should be considered: phase structure (0.1-10 μm), colony structure (10-100 μm) and grain structure (100-500 μm) [21,27]. The phase dimensionality in regular eutectics is ascribed as interlamellar or interfibre spacing (λ) and the growth rate is given by the equation: $\lambda^2 R = constant$ [18]. According with this, the size of the eutectic constituents in the microstructure can be controlled by the growth rate. Higher growth rates lead to smaller sizes and distances between the phases. For example, in Figure 16, the interfibre spacing changes from 2.1 to 5.4 μm, when the growth rate increases from 0.15 to 1 mm/min [28].

The next larger feature was introduced by Weart et al. [27]. The eutectic colony (cellular) structure is developed under nonlinear growth regime. Constitutional undercooling ascribes to the probable occurrence of impurities and the segregation of these ones into

the melt. The undercooled melt leads to a cellular interface [21,29]. Eutectic colonies occur when *G/R* falls bellow critical value with the impurities presence effectively increasing the critical value of *G/R* [21,30].

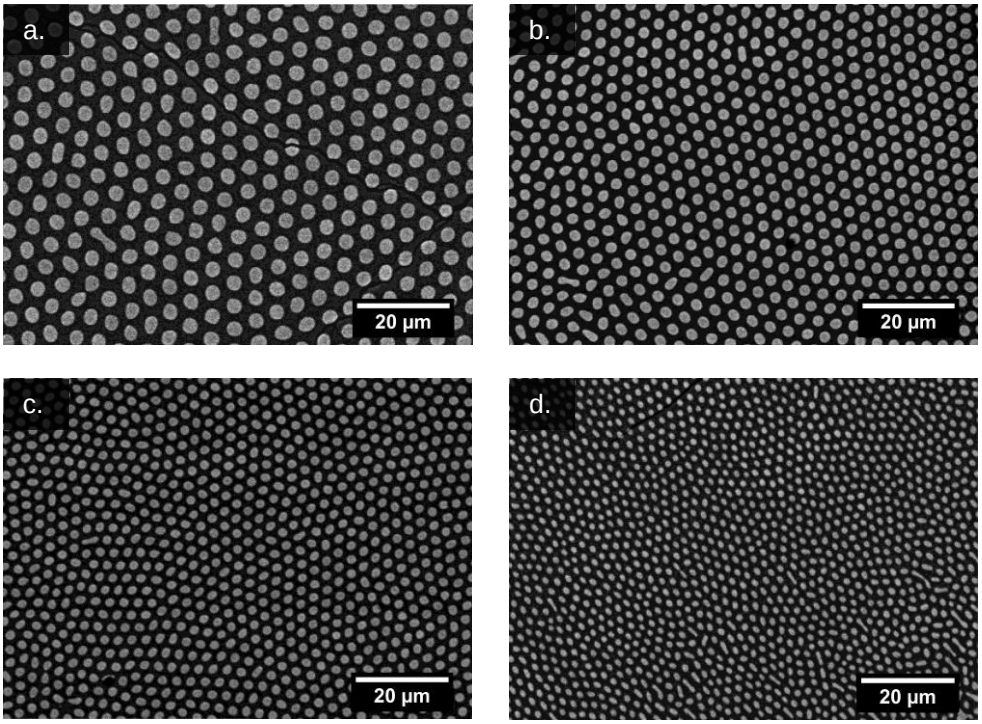


***Figure 16:*** *Self-organized eutectic microstructure of $TbScO_3$ microfibers immersed in $Tb_3Sc_2Al_3O_{12}$ matrix. The effect of growth rate (a) 0.15, (b) 0.3, (c) 0.45, and (d) 1 mm/min in the interfibre spacing 5.5, 3.7, 3.1 and 2.1 µm, respectively [28].*

The colonies' boundaries are thick coarser microstructures, oriented along the growth direction (Fig. 17a). The inter-phase spacing is significantly reduced at colony nucleus (Fig. 17), where an internal lamellar or fibrous structure can be developed due to local slower growth rate [19,21]. The columnar transversal cross-section shows a honeycomb pattern, where regular lamellar growth is observed (Fig. 17b).

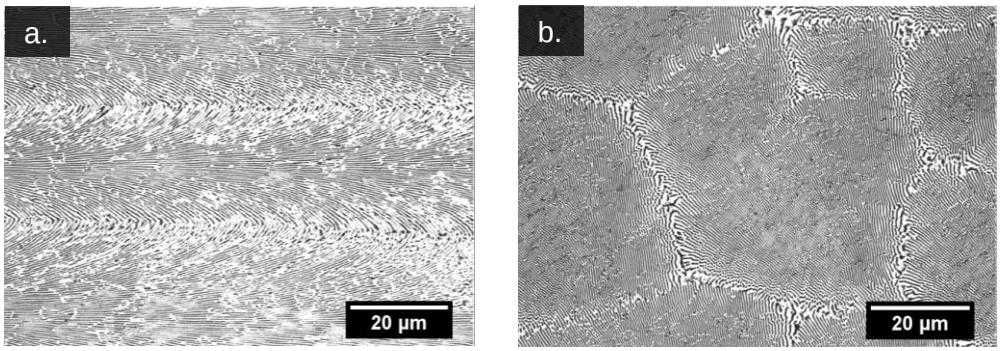


***Figure 17:*** *Eutectic metal alloy where eutectic colonies are arrays of crystal aggregates* ***(a)*** *longitudinal cross-section,* ***(b)*** *transversal cross-section, adapted from [31].*

The concept of eutectic grain is also proposed in some works [19,21], being specific of regular eutectics [19]. The eutectic grains result from adjustments of the eutectic structure promoted by small instabilities at solidification interface. So, the grain size is mainly determined by the growth conditions and eutectic ability to adapt at growth fluctuations [19]. Likewise colonies, they are elongated along the growth direction and rather smaller at the transversal section. Despite their large size, it is difficult to identify them. In Figure 18, two eutectic grains are visible being revealed by different lamellar orientations (having an angle of ~40º between them). Moreover, notice that the grains merge to a single one, at the micrograph left side [29]. Even that, it is difficult to define eutectic grains and distinguishing them from eutectic colonies, one definition of eutectic grain in such specimen is "an eutectic grain is a region of the solid of size generally much larger than the lamellar spacing, inside which all the lamellae of the same phase have the same crystal orientation, or nearly so" [32].

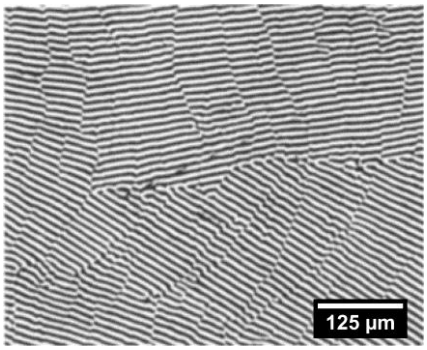


***Figure 18:*** *Regular eutectic microstructures Al-$Al_2Cu$, adapted from [26].*

## I.3. A brief review on the directional solidification of eutectics

The earliest studies on DSE materials were mainly performed in low-melting temperature metallic systems [18]. Kraft disclosed various eutectic metallic systems which may directionally solidify producing aligned microstructures and characteristic properties [31, 33]. Specially, the monovariant eutectic compositions solidify into anisotropic structures wherein one well-aligned phase of whisker or lamellar morphology is enclosed in a matrix phase. So, the metallic eutectic or eutectic-type alloys taking advantage of such microstructural benefits were foreseen to several useful applications, as cobalt-chromium-carbon, nickel or cobalt-base alloys that are used in gas turbines engines as blades or vanes [34-36]. However, metallic systems are limited by the operating temperature, so the increasing demanding for high-temperature applications naturally lead to an increasing attention to ceramic materials. This was supported by enhancements in the melt-grown technology that is applied in ceramic eutectics. In the beginning, simultaneous active research was performed in salt eutectics-type materials, as NaF-NaCl and (LiF, NaF)-$MgF_2$ [37-39].

In 1967, Galasso et al. reported the first research on directional solidification of a pure oxide eutectic system, namely the $BaFe_{12}O_{19}$-$BaFe_2O_4$ eutectic system [40]. The intention was to improve the magnetic response of the composite, aligning the c-axis of $BaFe_{12}O_{19}$ phase along the growth direction. The powders mixture was preheated in a platinum boat at 1000 ºC for 18 hours and then melted at 1500 ºC in air. Later, the boat travelled through an induction coil (at 1400 ºC) at rate of 32 mm/h along the horizontal direction. During the process oxygen flow was maintained over the sample to avoid reduction of the oxides. The eutectic comprises blades of $BaFe_{12}O_{19}$ phase (32.5 vol.%) nearly orientated along the longitudinal cross-section and enclosed in $BaFe_2O_4$ phase matrix (67.5 vol.%). The desired enhancement was not attained since the c-axis of $BaFe_{12}O_{19}$ was preferentially orientated perpendicularly to both: (i) the growth direction and (ii) blade extension, and these ones were also randomly rotated along the growth axis [40].

In the following years, Viechnicki et al. disclosed other three approaches $Al_2O_3$-$Y_3Al_5O_{12}$ (YAG), $Al_2O_3$-$ZrO_2$ and $Al_2O_3$-$ZrO_2$-$Y_2O_3$ in DSE systems [41-43]. These DSE ingots were grown by the Bridgman-type method and all revealed a colony-type microstructure [41-43]. The $Al_2O_3$-$ZrO_2$ DSEs consisted of 34 vol.% of monoclinic zirconia fine rods in an alumina matrix [42]. Yttria was added to the binary eutectic system in order to stabilize zirconia and led to significant enhancement of room temperature bending strength from 69 to 172 MPa, and 172 to 275 MPa at the transversal and longitudinal directions, respectively [43]. Moreover, the control of $Al_2O_3$-YAG DSE microstructure sug-

gested the possibility of improve the mechanical properties [41]. Later, Waku et al. fabricated $Al_2O_3$-YAG DSE by using the Bridgman method. The bending strength of $Al_2O_3$-YAG was in the range 350-400 MPa, and it was retained up to 1800 ºC [44,45]. This was attributed to a colony-free microstructure with irregular distribution of finer $Al_2O_3$ and YAG single-crystals [45]. After that, it was introduced the $Al_2O_3$-$GdAlO_3$ (GAP: gadolinium aluminum perovskite) DSE with three-dimensional (3D) microstructure. This DSE had a homogenous 3D-network of finer-interpenetrated microstructure (Fig. 19), combining $Al_2O_3$ and $GdAlO_3$ single-crystals [46]. $Al_2O_3$-GAP DSE demonstrated an incredible bending strength (~700 MPa) at high temperatures (1600 ºC) [46,47]. Rather than brittle fracture, the $Al_2O_3$-GAP DSE exhibited plastic deformation at high temperatures, owing to the dislocation motion like in metals [46,47]. These works had synergistic effect over the research of a series of new high temperature DSE systems using the same melt-grown method, including MgO-$MgAl_2O_4$, $MgTi_2O_5$-$TiO_2$, MgO-CaO, $ZrO_2$-$Al_2O_3$, $ZrO_2$-$CaZrO_3$ and $ZrO_2$-$SrZrO_3$ [48,49].

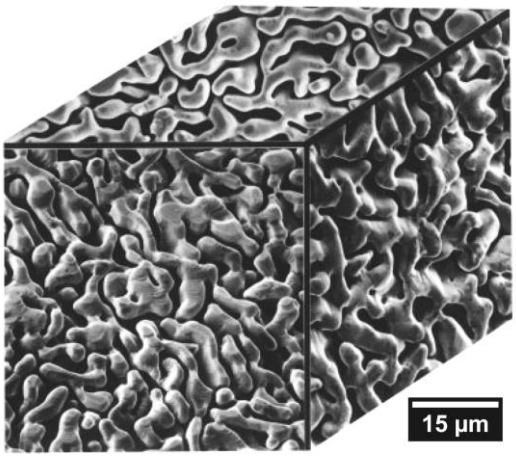


***Figure 19:*** *3D-SEM micrographs configuration of $Al_2O_3$-GAP DSE system [46].*

Rowcliffe et al. did the earliest approach to a binary oxide system grown by floating zone melting, using the electron beam as heating source [50]. A systematic study was realized over the eutectic compositions at the alumina-titania phase diagram. In this sense, it was considered the alumina-aluminium titanate eutectic (61.5 wt.% $Al_2O_3$) and the titania-aluminium titanate (18 wt.% $Al_2O_3$) eutectic compositions. The 18 wt.% $Al_2O_3$ DSE had very fine lamellae of aluminium titanate in a titania matrix, whereas the off-eutectic composites with (19 wt.% $Al_2O_3$) developed minor primary plate-like dendrites of aluminium titanate in a continuous lamellar eutectic. In both cases, the interlamellar spacing (λ) of aluminium titanate-titania eutectic system changes inversely with the square root of the growth rate. For a off-eutectic composition with 20 wt.% $Al_2O_3$ larger primary plate-

like dendrites of aluminium titanate are immersed in a quite discontinuous lamellar eutectic matrix. The richer-$Al_2O_3$ eutectic composition (61.5 wt.% $Al_2O_3$) comprises primary dendrites of alumina in a matrix of non-uniform eutectic of aluminium titanate-alumina eutectic [50].

Hulse and Batt reported a series of oxide-oxide eutectic systems, as $Al_2O_3$-$ZrO_2$ ($Y_2O_3$), $ZrO_2$-$Y_2O_3$, MgO-CaO and $ZrO_2$-$CaZrO_3$ [51]. After that, Hulse et al. described the high bending strength (424 MPa) up to 1574 ºC of $Al_2O_3$-$ZrO_2$ ($Y_2O_3$) DSE prepared by floating molten zone technique. The finely ordered lamellar phase, either fibrous or cellular in DSE preclude/deflect the crack propagation along the phases interfaces, rather than propagating in the usual ceramic brittle mode [52]. Such mechanical behaviour suggests that it has an abrasive material suitable for grinding operations [53].

Over the next decades, the development of the processing systems and the upgrade in the knowledge of DSE ceramic oxides features had a synergistic effect in their study. Moreover, the research in DSE manufacturing by floating zone methods accompanied the newest developments carried on the investigation being mainly focused in the $Al_2O_3$-based DSE material [19]. In this way, it is important to highlight the binary-eutectic systems like $Al_2O_3$-YAG, $Al_2O_3$-GAP and $Al_2O_3$-$Er_3Al_5O_{12}$ (EAG) grown by LFZ method [54-58] The $Al_2O_3$-YAG DSE fibres reveal a 3D-microstructure (observed along the longitudinal and transversal fibres cross-section), where two single-crystal phases are finely interpenetrated in a continuous microstructure, without pores, grain-boundaries or colonies [56]. The microstructure is only slightly tailored by the growth rate up to 30 mm/h, when it starts to be ruled by cellular growth. Thus happens as well for the other eutectic systems, but at 10 mm/h. The DSEs consists of continuous networks of binary single-crystal phases of $Al_2O_3$ and a perovskite (GAP) or a garnet (YAG or EAG). The $Al_2O_3$-YAG and $Al_2O_3$-EAG DSE fibres were grown from 25 to 750 mm/h. The hardness of both systems are very close (Fig. 20) and increases slightly with growth rate, while fracture toughness does not change [56,58]. The increase of hardness is ascribed to the strengthening effect at the interface between the eutectic constituents, which limits the microplastic deformation around the indentation [58].

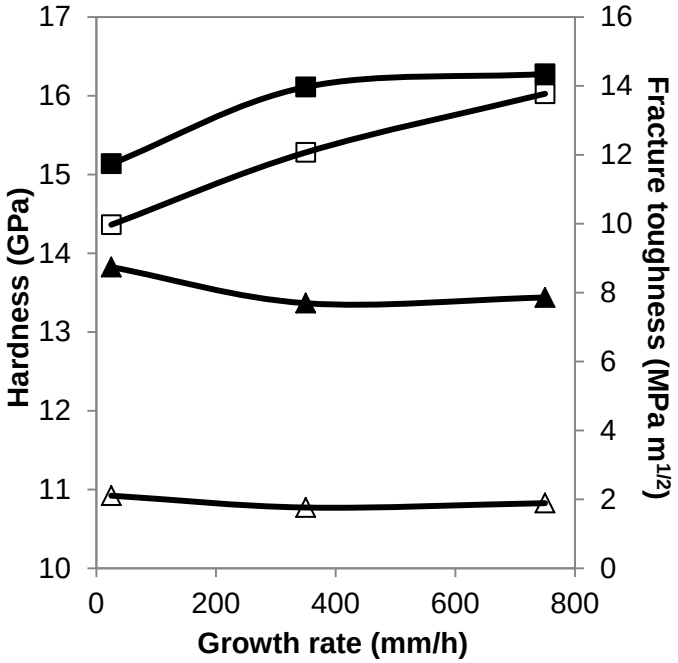


***Figure 20:*** *Microhardness (square) and fracture toughness (triangles) as a function of the growth rate, of $Al_2O_3$-YAG (open symbols) and $Al_2O_3$-EAG (closed symbols) DSEs, adapted from [56,58].*

The bending strength of the DSEs is sharply increased with the growth rate, owing to the reduction of the eutectic domain size. For $Al_2O_3$-GAP DSE fibres, it enhances from 900 MPa to 1780 MPa with growth rate increasing from 96 up to 240 mm/h. Notice that it is significantly higher than ~850 MPa obtained for the $Al_2O_3$-GAP DSE ingots prepared by the Bridgman technique [47,57]. However, the $Al_2O_3$-YAG and $Al_2O_3$-EAG DSE showed considerable higher bending strength for the different growth rates (Fig. 21a). The higher bending strength of $Al_2O_3$-EAG DSE was retained up to 1300 K, but the smallest eutectic domains lead to an abrupt reduction (Fig. 21b). Even that at room temperature the strength of $Al_2O_3$-YAG is lower than the previous one, it shows better strength retention for higher temperatures (Fig. 21b) [58].

The molten-zone methods have been presented as the most successful methods for the synthesis of higly-pure oxide-metal composites materials [59]. In this sense, several oxide-metal systems have been considered such as: $UO_2$-(W, Nb or Ta), stabilized $ZrO_2$-W, stabilized $HfO_2$-W, $CeO_2$-(Mo, W), MgO-W and $Cr_2O_3$-(Mo, Re or W) [59-63]. Such materials were the basis for other contemporary approaches, which begin with the reports of Revcolevschi et al. about NiO-oxide DSE, using a floating-zone device associated with a double ellipsoid image furnace (6.5 kW xenon lamp) [64]. Several NiO-oxide DSE sys-

tems (the oxide must have cubic symmetry as CaO, $Y_2O_3$, $NiAl_2O_4$, $Gd_2O_3$, and CaO-stabilized $ZrO_2$) were prepared and after reduction lead to metal-oxide structures [65-68].

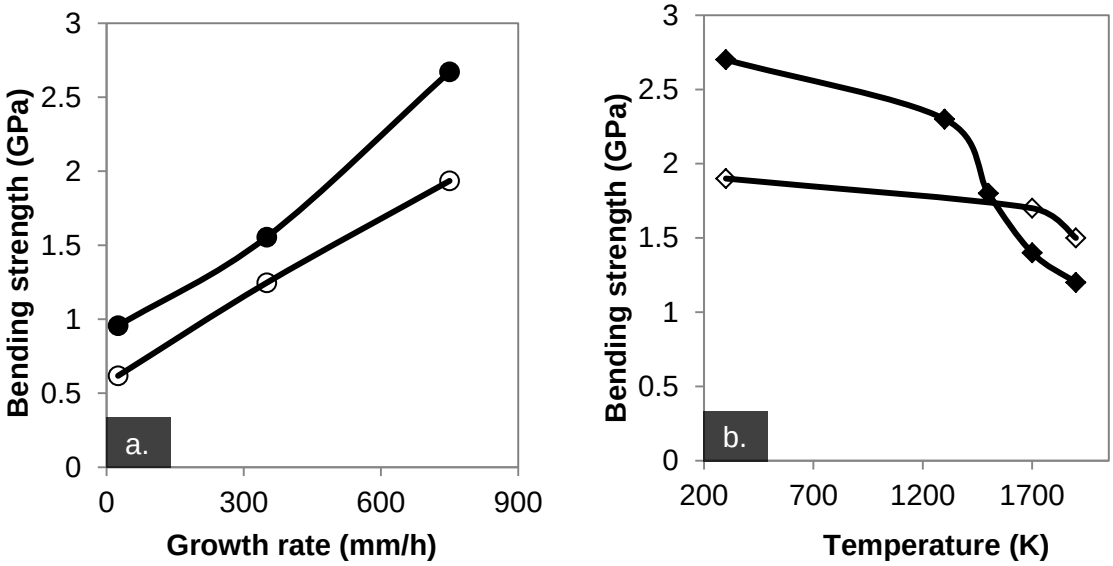


***Figure 21: (a)*** *Bending strength as function of growth rate (at room temperature) of $Al_2O_3$-YAG DSE (open symbol) and $Al_2O_3$-EAG DSE (closed symbol).* ***(b)*** *Bending strength as function of temperature for $Al_2O_3$-YAG DSE (open symbol) and $Al_2O_3$-EAG DSE (closed symbol) grown at 750 mm/h, adapted from [56, 58].*

## I.4. Zirconia based directionally solidified eutectic

Zirconia has technological significance because of its extraordinary refractoriness, mechanical and high ionic conductivity behaviour. Nowadays, $ZrO_2$-based DSEs constitute an extensive group of eutectic oxide materials, which is of great interest in many technological fields, mainly in high temperature structural applications, photonics, electrochemistry and bio-medicine [19,69]. The investigation done in mechanical and electrochemical fields will be referred in this section as it constitutes the scope of the present thesis.

$ZrO_2$-based DSE materials have been investigated since their pioneer works in oxide-oxide systems ($Al_2O_3$-$ZrO_2$ and $ZrO_2$-$CaZrO_3$) [51]. Notice that the studied of $Al_2O_3$-$ZrO_2$ materials typically contain $Y_2O_3$ to metastably retain the high temperature cubic and tetragonal polymorphs of zirconia at room temperature. $Al_2O_3$-$ZrO_2$ ($Y_2O_3$) DSEs were grown by floating zone method at 200 mm/h, showing colony-type microstructure with $ZrO_2$ whiskers (parallel to solidification interface) enclosed in the $Al_2O_3$ matrix. The bending strength only decreases from ~690 to 510 MPa from room temperature to 1575 ºC [51]. Nevertheless, less effort were made after that, due to extremely difficult processing conditions (high temperature) of $ZrO_2$-based composite materials. In opposition, the metallic systems (low melting point) were much attractive and explored [19]. However, ceramics were not forgotten, neither the potential microstructural stability, exceptional strength and significant increases in fracture toughness at elevated temperatures, of particular interest for the demanding high temperature technological applications [19,51]. The $ZrO_2$-$CaZrO_3$ DSEs grown at 100 mm/h showed lamellar microstructure. But, the bending strength (~330 MPa) was independent of the temperature up to 1600 ºC and growth rate over the range from 30 to 400 mm/h [51].

Over the last decades, the advances in the floating zone methods renewed the interest in high-temperature DSE ceramic oxides, as $ZrO_2$-($Al_2O_3$, $CaZrO_3$, $SrZrO_3$ and MgO) [49]. Sayir et al. carried out an extensive work in the $Al_2O_3$-$ZrO_2$ DSE system at the Nasa Lewis Research Center [70-73]. $Al_2O_3$-$ZrO_2$ DSE fibres were prepared by the laser heated pedestal growth (LHPG) from binary eutectic composition (62 mol.% $Al_2O_3$, 38 mol.% $ZrO_2$). Fibres have fully lamellar microstructure and solidifies without colony formation [72]. The colony microstructure appears for $Al_2O_3$-$ZrO_2$ (9.5 mol.% $Y_2O_3$) DSE fibres grown between 150 to 1500 mm/h. Below this range, fibres have heterogeneous microstructure with a finer colony structure at the periphery, increasing in size and inter-colony boundary width towards the middle. Coarse $ZrO_2$ particles and an $Y_2O_3$-rich phase in a matrix of $Al_2O_3$ result from strong radial thermal gradients, so the fibre centre is the last region to solidify

[70]. Banding phenomena, a sensitive function of the growth conditions, were identified on the fibres surface, but apparently had no influence in the mechanical strength [70].

Orera et al. have been investigating the structural/microstructural and mechanical behaviour of $Al_2O_3$-$ZrO_2(Y_2O_3)$ DSE fibres using the LFZ method [74-79]. Fibres grown at 10 mm/h reveal a homogenous coupled microstructure of irregular $ZrO_2$ lamellae (1-2 µm) enclosed in a $Al_2O_3$ matrix [77]. For higher growth rates (50-1500 mm/h), fibres were formed by colonies with ellipsoidal shape, which were oriented with the growth direction (Fig. 22a) [77,79] The tilt between their major axis and the growth direction usually increases for colonies at the periphery, due to concave profile at the solidification interface [80]. Banding was observed at the longitudinal cross-sections combining alternated finer and coarser regions (Fig. 22b) [78,79].

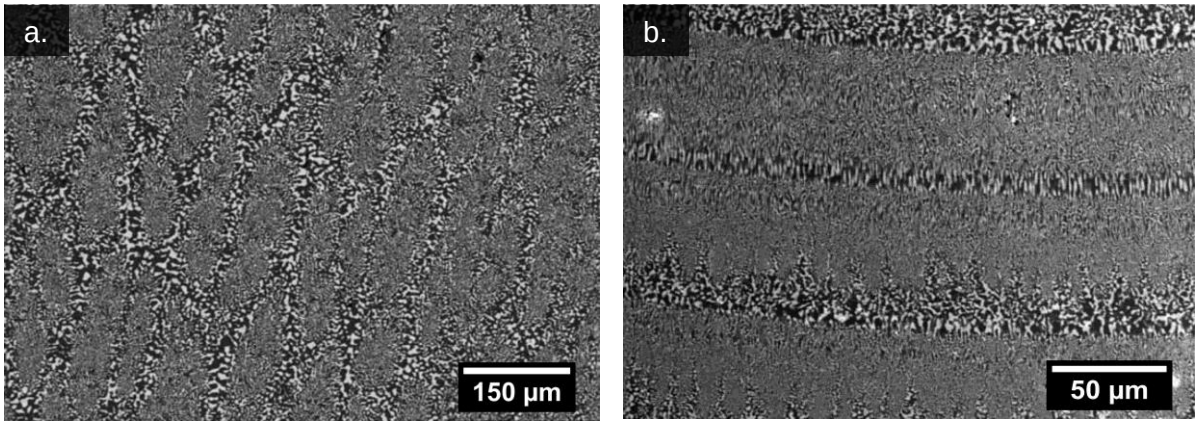


***Figure 22:*** *Micrographs of longitudinal cross-section of $Al_2O_3$-$ZrO_2(Y_2O_3)$ DSE showing the **(a)** colonies (back-scattered electrons mode) and **(b)** periodic banding oriented perpendicularly to the solidification front, adapted from [80].*

The transversal cross-section of a colony comprises an irregular dispersion of a fine-interpenetrating network of $ZrO_2$ and $Al_2O_3$ (Fig. 23a) or organized zirconia fibrils above 300 mm/h (Fig. 23b) [29,75,80]. In Figure 23b, alumina has a leading behaviour (high entropy of fusion) during solidification, and it grows along certain planes for which zirconia fibres tend grow perpendicularly, leading to distribution by three sets following trigonal symmetry [80]. The influence of the $Y_2O_3$ content in the mechanical behaviour were evaluated in the colony-free DSEs [78]. In fact, the microstructure did not change considerably with the amount of $Y_2O_3$ dissolved into $ZrO_2$ [78]. However, the density of defects increases for lower $Y_2O_3$ contents, so the bending strength varies from 1.34 GPa (3 mol.% $Y_2O_3$) to 0.6 GPa (0.5 mol.% $Y_2O_3$) at room temperature [78]. Moreover, the material with 3

mol.% $Y_2O_3$ retains 80% of bending strength up to 1427 ºC, while for 0.5 mol.% $Y_2O_3$ it sharply decreases down to 0.2 GPa at 700 ºC [78].

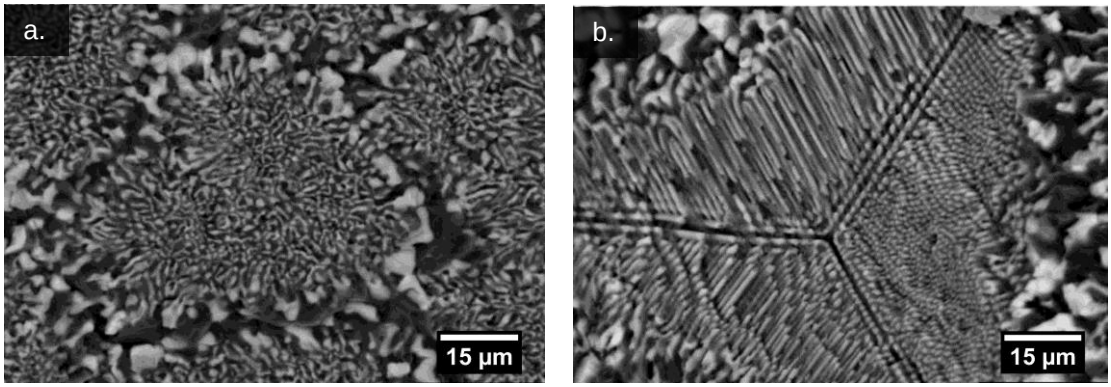


***Figure 23:*** *Back-scattered electrons micrographs of transverse sections of $Al_2O_3$-$ZrO_2(Y_2O_3)$ DSE* ***(a)*** *colony formed by a disordered dispersion of zirconia lamellae (white) embedded in alumina matrix (dark grey) and surrounded by thick coarse region with bigger zirconia particles having random shape,* ***(b)*** *colony centre with self-organized distribution of zirconia fibrous (~0.3 µm in length), adapted from [80].*

The most recent efforts in $Al_2O_3$-$ZrO_2(Y_2O_3)$ deals with the reduction of the eutectic domain size by increasing the growth rate [81]. Hence, this leads to the development of colonies, where finer zirconia particles are enclosed in the alumina matrix, surrounded by coarse dispersion of larger zirconia particles [81]. Higher growth rates yield smaller colonies, promoting thicker inter-colony regions. This $Al_2O_3$-$ZrO_2(Y_2O_3)$ DSE limits the strength to 1.0 to 1.5 GPa with fracture toughness of ~5.3 MPa $m^{1/2}$ [81]. The desired refinement could be attained by the increase of the number of eutectic constituents, which extend the coupled zone for high growth rates, and so finer microstructures could be developed [81, 82]. This is nowadays the idea for the new ternary DSE, as $Al_2O_3$-YAG-YSZ and $Al_2O_3$-EAG-$ZrO_2$ having nanometric domains [81,83]. In this way, $Al_2O_3$-YAG-YSZ DSE were grown at 1200 mm/h under nitrogen atmosphere, leading to a homogenous nanofribrillar microstructure, whose bending strength reached 4.6 GPa [81].

Textured Ni-YSZ and Co-YSZ cermets were produced from micro/nano self-organized eutectic structures. These are promising materials as anodes in solid oxide fuel cells (SOFC) or electrolyzers, owing to 30-40% porosity and the mixed ionic-electronic conduction behaviour [84,85]. The fundamentals of this idea were disclosed previously by Revcolevschi et al. with NiO-CaSZ (calcia stabilized-$ZrO_2$) DSE system. Such cermets (Fig. 24) are prepared after reduction treatment in a 4% $H_2$-$N_2$ mixture atmosphere of NiO-YSZ or CoO-YSZ directionally solidified [67,86,87]. Both DSE oxide systems have homogenous and finer lamellar microstructures, which are aligned along the growth direc-

tion. The channeled microstructure provide an appropriate thermal expansion coefficient, easy gas flow and good electrical conductivity [88].

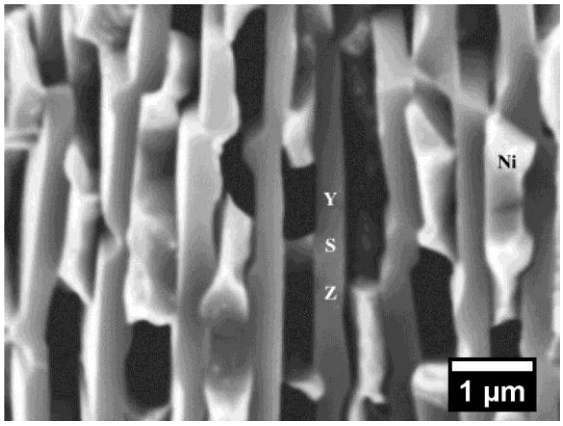


***Figure 24:*** *SEM micrograph of fractured Ni-YSZ porous cermet produced from DSE, adapted from [88].*

**References**

[1] W.G. Pfann, Zone melting, Science, 135 (1962) 1101-1109.
[2] A. Mühlbauer, History of induction heating and melting, Vulkan-Verlag GmbH, 2008.
[3] G. Dhanaraj, K. Byrappa, V. Prasad, M. Dudley, Springer handbook of crystal growth, Springer, New York, 2010.
[4] W.G. Pfann, Process for controlling solute segregation by zone melting, Bell Telephone Laboratories Incorporated, United States, 1956.
[5] W.G. Pfann, Zone melting, Bell Telephone Laboratories Incorporated, United States, 1969.
[6] H.C. Theuerer, Method of processing semiconductive materials, Bell Telephone Laboratories Incorporated, United States, 1962.
[7] R.S. Feigelson, Pulling optical fibers, Journal of Crystal Growth, 79 (1986) 669-680.
[8] K. Eickhoff, K. Gürs, Tiegelfreies zonenschmelzen von rubinkristallen durch aufheizen der schmelzzone mittels laser, Journal of Crystal Growth, 6 (1969) 21-25.
[9] B. Cockayne, D.B. Gasson, N. Forbes, Further developments in oxide crystal growth using gas lasers, Journal of Materials Science, 5 (1970) 837-838.
[10] J.S. Haggerty, W.P. Menashi, J.F. Wenckus, Method for forming refractory fibres by laser energy, Arthur D. Little, Inc., Cambridge, United States, 1976.
[11] J.S. Haggerty, W.P. Menashi, J.F. Wenckus, Apparatus for forming refractory fibres, United States, 1977.

[12] M.M. Fejer, J.L. Nightingale, G.A. Magel, R.L. Byer, Laser-heated miniature pedestal growth apparatus for single-crystal optical fibers, Review of Scientific Instruments, 55 (1984) 1791-1796.
[13] R.L. Byer, M.M. Fejer, Apparatus for growing crystal fibers, The Board of Trustees of the Leland Stanford Junior University, United States, 1983.
[14] M.M. Fejer, G.A. Magel, R.L. Byer, High-speed high-resolution fiber diameter variation measurement system, Applied Optics, 24 (1985) 2362-2368.
[15] H. Fredriksson, U. Akerlind, Solidification and crystallization processing in metals and alloys, John Wiley & Sons Ltd., West Sussex, 2012.
[16] D.M. Stefanescu, Science and engineering of casting solidification, Second edition, Springer, New York, 2009.
[17] D.A. Porter, K.E. Easterling, Phase transformation in metals and alloys, Chapman & Hall, London, 1992.
[18] R.L. Ashbrook, Directionally solidified ceramic eutectic, Journal of the American Ceramic Society, 60 (1977) 428-435.
[19] J. Llorca, V.M. Orera, Directionally solidified eutectic ceramic oxides, Progress in Materials Science, 51 (2006) 711-809.
[20] S. Kou, Welding metallurgy, Second edition, John Wiley & Sons, Inc., New Jersey, 2003.
[21] V.S. Stubican, R.C. Bradt, Eutectic Solidification in Ceramic Systems, Annual Review of Materials Science, 11 (1981) 267-297.
[22] D.M. Herlach, P. Galenko, D. Holland-Moritz, Metastable solids from undercooled melts, Elsevier B.V., Oxford, 2007.
[23] W. Kurz, D.J. Fisher, Fundamentals of solidification, Trans. Tech. Publications Ltd, Switzerland, 1992.
[24] M.N. Croker, R.S. Fidler, R.W. Smith, Characterization of eutectic structures, Proceedings of the Royal Society of London Series A-Mathematical Physical and Engineering Sciences, 335 (1973) 15-37.
[25] J.D. Hunt, K.A. Jackson, Binary eutectic solidification, Transactions of the Metallurgical Society of AIME, 236 (1966) 843-852.
[26] D.M. Stefanescu, R. Ruxanda, Metallography and microstructures, ASM International, 2004.
[27] H.W. Weart, D.J. Mack, Eutectic solidification structures, Transactions of the American Institute of Mining and Metallurgical Engineers, 212 (1958) 664-670.

[28] D.A. Pawlak, K. Kolodziejak, S. Turczynski, J. Kisielewski, K. Rożniatowski, R. Diduszko, M. Kaczkan, M. Malinowski, Self-organized, rodlike, micrometer-scale microstructure of $Tb_3Sc_2Al_3O_{12}$−$TbScO_3$:Pr eutectic, Chemistry of Materials, 18 (2006) 2450-2457.

[29] F.D. Lemkey, R.W. Kraft, Solidification structures of eutectic alloys, Metallography And Microstructures, ASM International, 1985.

[30] M. Plapp, A. Karma, Eutectic colony formation: A phase-field study, Physical Review E, 66 (2002).

[31] R.W. Kraft, Controlled eutectics, Scientific American, 216 (1967) 86-92.

[32] G. Faivre, Morphological instabilities of lamellar eutectic growth fronts: a survey of recent experimental and numerical results, Journal of Crystal Growth, 166 (1996) 29-39.

[33] R.W. Kraft, Unideractional solidification of lamellar eutectic alloys, United Aircraft Corporation, United States, 1964.

[34] E.R. Thompson, Cast nickel-columbium-aluminum alloy, United Aircraft Corporation, United States, 1971.

[35] E.R. Thompson, F.D. Lemkey, Anisotropic polyphase structure of monovariant eutectic composition, United Aircraft Corporation, United States, 1971.

[36] F.D. Lemkey, E.R. Thompson, Cobalt-chromium base alloy and articles produced therefrom, United Aircraft Corporation, United States, 1971.

[37] J.A. Batt, F.C. Douglas, F.S. Galasso, Optical properties of unidirectionally solidified naf-nacl eutectic, American Ceramic Society Bulletin, 48 (1969) 622-626.

[38] F.S. Galasso, F.C. Douglas, J.A. Batt, Recent studies of eutectics for nonstructural applications, Journal of Metals, 22 (1970) 40-44.

[39] M.W.A. Bright, M.H. Lewis, Eutectic solidification in NaF-$MgF_2$ system, Journal of Materials Science, 6 (1971) 1246-1253.

[40] F.S. Galasso, W.L. Darby, F.C. Douglas, J.A. Batt, Unidirectional solidification of $BaFe_{12}O_{19}$-$BaFe_2O_4$ eutectic, Journal of the American Ceramic Society, 50 (1967) 333-334.

[41] D. Viechnicki, F. Schmid, Eutectic solidification in system $Al_2O_3$/$Y_3Al_5O_{12}$, Journal of Materials Science, 4 (1969) 84-88.

[42] F. Schmid, D. Viechnicki, Oriented eutectic microstructures in system $Al_2O_3$/$ZrO_2$, Journal of Materials Science, 5 (1970) 470-473.

[43] F. Schmid, D. Viechnicki, Mechanical properties of eutectics in $Al_2O_3$-$ZrO_2$-$Y_2O_3$ system, American Ceramic Society Bulletin, 51 (1972) 322.

[44] Y. Waku, S. Sakata, A. Mitani, K. Shimizu, Mechanical properties and thermal stability of oxide eutectic composites at high temperatures, Materials and Manufacturing Processes, 13 (1998) 841-858.
[45] Y. Waku, N. Nakagawa, T. Wakamoto, H. Ohtsubo, K. Shimizu, Y. Kohtoku, High-temperature strength and thermal stability of a unidirectionally solidified $Al_2O_3$/YAG eutectic composite, Journal of Materials Science, 33 (1998) 1217-1225.
[46] Y. Waku, N. Nakagawa, T. Wakamoto, H. Ohtsubo, K. Shimizu, Y. Kohtoku, A ductile ceramic eutectic composite with high strength at 1,873 K, Nature, 389 (1997) 49-52.
[47] Y. Waku, A new ceramic eutectic composite with high strength at 1873 K, Advanced Materials, 10 (1998) 615-617.
[48] F.L. Kennard, R.C. Bradt, V.S. Stubican, Eutectic solidification of MgO-$MgAl_2O_4$, Journal of the American Ceramic Society, 56 (1973) 566-569.
[49] W.J. Minford, R.C. Bradt, V.S. Stubican, Crystallography and microstructure of directionally solidified oxide eutectics, Journal of the American Ceramic Society, 62 (1979) 154-157.
[50] D. Rowcliffe, W.J. Warren, A.G. Elliot, W.S. Rothwell, Growth of oriented ceramic eutectics, Journal of Materials Science, 4 (1969) 902-907.
[51] C.O. Hulse, J.A. Batt, The effect of eutectic microstructures on the mechanical properties of ceramic oxides, United Aircraft Research Labs East Hartford CT, United States, 1974.
[52] C.O. Hulse, J.A. Batt, Directionally solidified refractory oxide eutectic, United Aircraft Corporation, United States, 1973.
[53] D.W. Marshall, S.J. Roschuk, Fused alumina-zirconia abrasives, Norton Company, United States, 1965.
[54] E.R.M. Andreeta, M.R.B. Andreeta, A.C. Hernandes, Laser heated pedestal growth of $Al_2O_3$/$GdAlO_3$ eutectic fibers, Journal of Crystal Growth, 234 (2002) 782-785.
[55] J.M. Fernandez, A. Sayir, S.C. Farmer, High temperature creep deformation of directionally solidified $Al_2O_3$/$Er_3Al_5O_{12}$, Acta Materialia, 51 (2003) 1705-1720.
[56] J.Y. Pastor, J. Llorca, A. Salazar, P.B. Oliete, I. de Francisco, J.I. Pena, Mechanical properties of melt-grown alumina-yttrium aluminum garnet eutectics up to 1900 K, Journal of the American Ceramic Society, 88 (2005) 1488-1495.
[57] I.S. Medeiros, E.R.M. Andreeta, A.C. Hernandes, $Al_2O_3$/$GdAlO_3$ eutectic fibers of high modulus of rupture produced by the laser heated pedestal growth technique, Journal of Materials Science, 42 (2007) 3874-3877.

[58] M.C. Mesa, P.B. Oliete, V.M. Orera, J.Y. Pastor, A. Martín, J. Llorca, Microstructure and mechanical properties of $Al_2O_3/Er_3Al_5O_{12}$ eutectic rods grown by the laser-heated floating zone method, Journal of the European Ceramic Society, 31 (2011) 1241-1250.
[59] J.W. Stendera, J.F. Benzel, Rare-earth-oxide-metal eutectic composites, Journal of the American Ceramic Society, 58 (1975) 116-119.
[60] A.T. Chapman, G.W. Clark, D.E. Hendrix, $UO_2$-W cermets produced by unidirectional solidification, Journal of the American Ceramic Society, 53 (1970) 60-61.
[61] R.P. Nelson, J.J. Rasmusse, Composite solidification in systems $Cr_2O_3$-Mo, $Cr_2O_3$-Re, $Cr_2O_3$-W, and MgO-W, Journal of the American Ceramic Society, 53 (1970) 527.
[62] T.A. Johnson, J.F. Benzel, Unidirectional solidification of stabilized $HfO_2$-W, Journal of the American Ceramic Society, 56 (1973) 234-234.
[63] C.C. Jen, J.F. Benzel, Unidirectional solidification of $UO_2$-Mo, $UO_2$-Nb, and $UO_2$-Ta systems, Journal of the American Ceramic Society, 57 (1974) 232-233.
[64] L. Trouilleux, G. Dhalenne, A. Revcolevschi, P. Monod, Growth and anisotropic magnetic-behavior of aligned eutectic-type structures in the system $La_{2-x}Sr_xCuO_4$-Copper oxide, Journal of Crystal Growth, 91 (1988) 268-273.
[65] M. Fragneau, A. Revcolevschi, D. Michel, Crystallography of directionally solidified NiO-$Y_2O_3$ eutectic, Journal of the American Ceramic Society, 65 (1982) C102-C104.
[66] M. Fragneau, A. Revcolevschi, Crystallography of the directionally solidified NiO-CaO eutectic, Journal of the American Ceramic Society, 66 (1983) C162-C163.
[67] A. Revcolevschi, G. Dhalenne, Crystallographically aligned metal-oxide composite made by reduction of a directionally solidified oxide-oxide eutectic, Nature, 316 (1985) 335-336.
[68] B. Dubois, G. Dhalenne, F. D' Yvoire, A. Revcolevschi, Crystallography of the directionally solidified NiO-$Gd_2O_3$ Eutectic, Journal of the American Ceramic Society, 69 (1986) C6-C8.
[69] Y. Hakamatsuka, Composite structure useful as artificial bones, Olympus Optical Co. Ltd., 1990.
[70] A. Sayir, S.C. Farmer, P.O. Dickerson, H.M. Yun, High temperature mechanical properties of $Al_2O_3/ZrO_2(Y_2O_3)$ Fibers, Materials Research Society Symposium Proceedings, 365 (1995) 21-27.
[71] A. Sayir, S.C. Farmer, The effect of the microstructure on mechanical properties of directionally solidified $Al_2O_3/ZrO_2(Y_2O_3)$ eutectic, Acta Materialia, 48 (2000) 4691-4697.
[72] S.C. Farmer, A. Sayir, Tensile strength and microstructure of $Al_2O_3$-$ZrO_2$ hypoeutectic fibers, Engineering Fracture Mechanics, 69 (2002) 1015-1024.

[73] J. Yi, A.S. Argon, A. Sayir, Creep resistance of the directionally solidified ceramic eutectic of $Al_2O_3$/c-$ZrO_2$($Y_2O_3$): experiments and models, Journal of the European Ceramic Society, 25 (2005) 1201-1214.
[74] V.M. Orera, R.I. Merino, J.A. Pardo, A. Larrea, J.I. Peña, C. González, P. Poza, J.Y. Pastor, J. Llorca, Microstructure and physical properties of some oxide eutectic composites processed by directional solidification, Acta Materialia, 48 (2000) 4683-4689.
[75] J.Y. Pastor, P. Poza, J. Llorca, J.I. Peña, R.I. Merino, V.M. Orera, Mechanical properties of directionally solidified $Al_2O_3$-$ZrO_2$($Y_2O_3$) eutectics, Materials Science and Engineering A, 308 (2001) 241-249.
[76] N.R. Harlan, R.I. Merino, J.I. Peña, A. Larrea, V.M. Orera, Phase distribution and residual stresses in melt-grown $Al_2O_3$-$ZrO_2$($Y_2O_3$) Eutectics, Journal of the American Ceramic Society, 85 (2002) 2025-2032.
[77] J.I. Peña, R.I. Merino, N.R. Harlan, A. Larrea, G.F. de la Fuente, V.M. Orera, Microstructure of $Y_2O_3$ doped $Al_2O_3$-$ZrO_2$ eutectics grown by the laser floating zone method, Journal of the European Ceramic Society, 22 (2002) 2595-2602.
[78] J. Llorca, J.Y. Pastor, P. Poza, J.I. Pena, I. de Francisco, A. Larrea, V.M. Orera, Influence of the $Y_2O_3$ content and temperature on the mechanical properties of melt-grown $Al_2O_3$-$ZrO_2$ eutectics, Journal of the American Ceramic Society, 87 (2004) 633-639.
[79] I. de Francisco, R.I. Merino, V.M. Orera, A. Larrea, J.I. Peña, Growth of $Al_2O_3$/$ZrO_2$($Y_2O_3$) eutectic rods by the laser floating zone technique: effect of the rotation, Journal of the European Ceramic Society, 25 (2005) 1341-1350.
[80] J.Y. Pastor, J. Llorca, P. Poza, I. de Francisco, R.I. Merino, J.I. Peña, Mechanical properties of melt-grown $Al_2O_3$-$ZrO_2$($Y_2O_3$) eutectics with different microstructure, Journal of the European Ceramic Society, 25 (2005) 1215-1223.
[81] P.B. Oliete, J.I. Peña, A. Larrea, V.M. Orera, J. LLorca, J.Y. Pastor, A. Martín, J. Segurado, Ultra-high-strength nanofibrillar $Al_2O_3$-YAG-YSZ eutectics advanced materials, 19 (2007) 2313-2318.
[82] J.I. Peña, M. Larsson, R.I. Merino, I.d. Francisco, V.M. Orera, J. Llorca, J.Y. Pastor, A. Martín, J. Segurado, Processing, microstructure and mechanical properties of directionally-solidified $Al_2O_3$-$Y_3Al_5O_{12}$-$ZrO_2$ ternary eutectics, Journal of the European Ceramic Society, 26 (2006) 3113-3121.
[83] F.A. Huamán-Mamani, M. Jiménez-Melendo, M.C. Mesa, P.B. Oliete, Microstructure and high-temperature mechanical behavior of melt-growth $Al_2O_3$/$Er_3Al_5O_{12}$/$ZrO_2$ ternary eutectic composites, Journal of Alloys and Compounds, 536, Supplement 1 (2012) S527-S531.

[84] M.A. Laguna-Bercero, A. Larrea, J.I. Peña, R.I. Merino, V.M. Orera, Structured porous Ni- and Co-YSZ cermets fabricated from directionally solidified eutectic composites, Journal of the European Ceramic Society, 25 (2005) 1455-1462.
[85] A. Larrea, M.A. Laguna-Bercero, J.I. Pena, R.I. Merino, V.M. Orera, Orientation relationship and interfaces in Ni and Co-YSZ cermets prepared from directionally solidified eutectics, Central European Journal of Physics, 7 (2009) 242-250.
[86] B. Bonvalot-dubois, G. Dhaleene, J. Berthon, A. Revcolevschi, R.A. Rapp, reduction of NiO platelets in a NiO/$ZrO_2$(CaO) directional composite, Journal of the American Ceramic Society, 71 (1988) 296-301.
[87] A. Revcolevschi, G. Dhalenne, Engineering oxide-oxide and metal-oxide microstructures in directionally solidified eutectics, Advanced Materials, 5 (1993) 657-662.
[88] M.A. Laguna-Bercero, A. Larrea, R.I. Merino, J.I. Pena, V.M. Orera, Stability of channeled Ni-YSZ cermets produced from self-assembled NiO-YSZ directionally solidified eutectics, Journal of the American Ceramic Society 88 (2005) 3215-3217.

# Chapter II

## A novel zirconia-barium zirconate directionally solidified eutectic

*This chapter begins with a brief review (II.1.) of the ionic conductor materials, defect chemistry mechanisms and relevant thermodynamic conditions for ion conduction, foreseeing specific applications. Particular attention is given to the mixed protonic-oxide ionic conduction behaviour of some materials and structures. Finally, the ionic conductivity in directionally solidified eutectic (DSE) materials is described.*

*The investigation done in the zirconia-barium zirconate DSE materials was the subject of a patent application (PPP 106.488, untitled: "Mixed ionic-ionic conductors, synthesis of such conductors by directional solidification and their use"). The results were then reported in two SCI papers presented here in three main sections.*

*The first paper (II.2.) deals with the influence of the LFZ growth conditions on the structural and microstructural characteristics and their consequences on the electrical properties.*

*A succinct description of the banding phenomena observed in the zirconia-barium zirconate DSE fibres is reported as supplementary information to the previous subsection.*

*The second paper is mainly focused on the mixed ionic conduction behaviour of these DSE materials (II.3.).*

## II.1. Overview of the solid electrolyte materials

### II.1.1. Oxygen ion conductor and proton conductor materials

A solid electrolyte is a material characterized by high ionic conductivity (of anions or cations) and negligible electronic conduction [1,2]. In 1899, Walther Nernest reported the earliest observation of ionic conductivity in a solid oxide electrolyte, using platinium-wire electrodes. Nernst proposed the substitution of carbon filaments in electric lamps by a solid (named Nernst mass) with the composition $ZrO_2$ (15 wt.% $Y_2O_3$) [3]. In 1935, Shottky suggested the employment of Nernst mass as a solid electrolyte in fuel cells, and two years later Baur and Preis demonstrated the operation of the first ceramic fuel cell, using $ZrO_2$-based materials as oxygen ionic conductors ($ZrO_2$ with 10 wt.% MgO or 15 wt.% $Y_2O_3$ addition) in the form of a tubular crucible as electrolyte, with carbon or iron as the anode and $Fe_3O_4$ as a cathode [3]. Nowadays, oxygen ion conductors represent the most extensively investigated types of electrolytes. Other electrolytes appeared, and these ones can be classified by their structure type: fluorite (zirconia, ceria, thoria and bismuth oxide), perovskites as $LaGaO_3$, derivates of $Bi_4V_2O_{11}$ (BIMEVOX) and $La_2Mo_2O_9$ (LAMOX), perovskites/brownmillerites like as $Bi_4In_2O_{11}$, apatites ($RE_{10-x}Si_6O_{26\pm\delta}$, where RE is rare-earth element, phosphor or germanium element) and pyrochlores ($(Ga,Ca)_2Ti_2O_{7-\delta}$) [2,4]. Electrolyte materials have been used in a widely variety of electrochemical devices, namely as an electrolyte in solid oxide fuel cells (SOFC), oxygen pumps, high temperature oxygen sensors and membranes [5]. More than high ionic conduction, other general requirements are necessary [2,6]:

(i) high thermodynamic and microstructural stability over a wide range of temperature and oxygen partial pressure,
(ii) negligible interaction with electrodes under operation conditions,
(iii) thermal expansion match with the electrodes and other constituent materials of a device,
(iv) no evaporation under operation conditions,
(v) appropriate thermomechanical behaviour,
(vi) easy to produce into different profiles (shape and sizes),
(vii) easy to create as hermetic seals.

Although the requirements for each application changes, fluorite-type electrolytes have attracted a greater interest than the other oxygen ion conductors, since they obey to several of those mandatory conditions [6]. In this way, the zirconia-based electrolyte has been

the most commonly used electrolyte material, once it exhibits the extraordinary combination of high termomechanical behaviour with high ionic conduction over a wide range of partial pressures at elevated temperatures [7].

Although pure ceria and thoria have fluorite-type structure stabilized from ambient temperature up to their melting points, bismuth oxide and zirconia show a number of polymorphs at different temperature ranges [8]. Pure zirconia melts at ~2680 ºC, but until there, it can exhibit three polymorphic structures: monoclinic (m-$ZrO_2$), tetragonal (t-$ZrO_2$) and cubic (c-$ZrO_2$) (Fig. 1). The c-$ZrO_2$ phase corresponds to a non-distorted structure of the fluorite type (space group $Fm\bar{3}m$). The coordination number of oxygen is four, while the zirconium in relation to oxygen is eight. The Zr-O bond length is equal for all the eight pairs in the structure [6,9,10]. The cubic to tetragonal transformation takes place at 2370 ºC and occurs when the cubic structure on cooling becomes unstable, leading to small displacement of the oxygen atoms from their ideal position (1/4, 1/4, 1/4). Indeed, t-$ZrO_2$ has a crystal structure of slightly distorted fluorite, but this does not lead to any modification of the coordination number. The length of the four Zr-O bonds is shorter than that of the other four bonds. The second transition happens at 1170 ºC, when the tetragonal structure transforms into monoclinic one. Monoclinic crystals are very common in the Earth's crust, and are known as baddeleyite. In fact, this transformation results of further distortion c-$ZrO_2$, leading to an extensive rearrangement and new structure (Fig. 1) [6,9, 10]. Notice that, this transformation shows significant hysteresis, since on cooling occurs at a slightly lower temperature ~200 ºC [6].

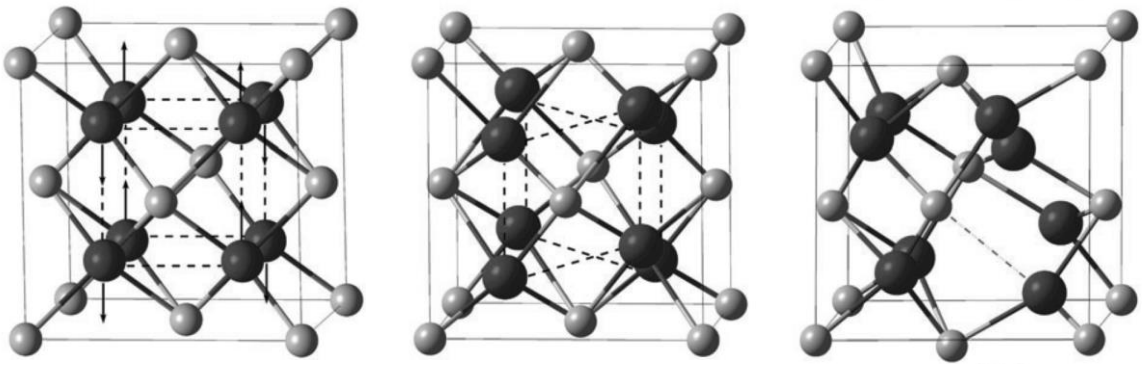

| c-$ZrO_2$ phase | t-$ZrO_2$ phase | m-$ZrO_2$ phase |
|---|---|---|
| $Fm\bar{3}m$ | $P4_2/nmc$ | $P2_1/c$ |
| c=b=a, $\beta$=90º | c>b=a, $\beta$=90º | c>b>a, $\beta$>99º |

***Figure 1:*** *Schematic representation of crystalline structures of monoclinic, tetragonal and cubic $ZrO_2$ phases. The arrows correspond to the oxygen displacement directions, taking as reference the cubic cell. Large dark spheres and small light grey spheres represent O and Zr atoms, respectively [11].*

The high temperature cubic and tetragonal structures can be stabilized at room temperatures by doping with metal oxides (CaO, MgO, $Y_2O_3$ etc.) forming solid solutions with zirconia. The composition range over which tetragonal and cubic structures occurs is narrow and depends on temperature that is function of the type of dopant. If the dopant concentration is in low amount to fully stabilize the high temperature structure, it results in a mixture of different phases. Besides the c-$ZrO_2$, t-$ZrO_2$ and m-$ZrO_2$ phases shown in Figure 2, another metastable phase (t'-$ZrO_2$) has been reported in the $ZrO_2$-$Y_2O_3$ system, for a dopant content of 7-13 mol.% $YO_{1.5}$, while a minimum of 16-18 mol.% $YO_{1.5}$ is needed to stabilize the cubic phase [6,12-14]. The t'-$ZrO_2$ is promoted by diffusionless phase transformation during fast cooling rates [6,15]. Notice that, pure zirconia is a poor ion conductor due to low number of vacancies available for conduction (Fig. 2). The low value of conductivity results mainly from electronic conduction [6].

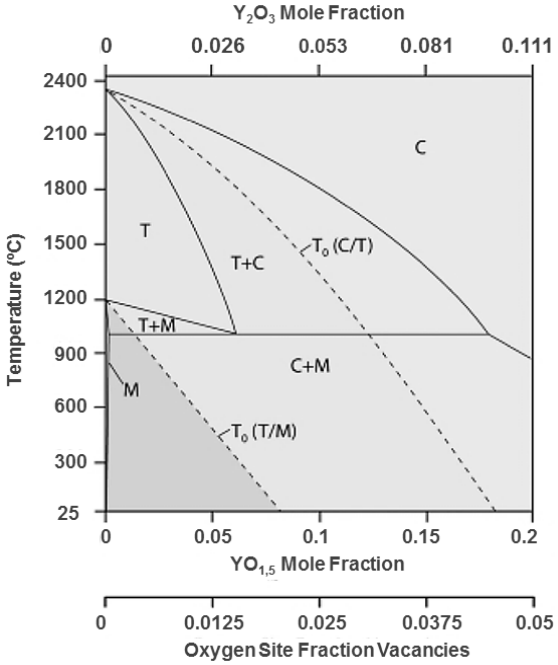


***Figure 2:*** *Metastable zirconia-yttria phase diagram, adapted from [12].*

So, simultaneously to the stabilization role at atmospheric pressure and room temperature of the high temperature metastable phases, the dopants incorporation gives rise to the ionic conductivity. This is promoted by the substitution of zirconium ion ($Zr^{4+}$) in the lattice sites by divalent ($Ca^{2+}$, $Mg^{2+}$) or trivalent ($Y^{3+}$, $Sc^{3+}$, $Nd^{3+}$, etc.) cations inducing the generation of oxygen vacancies ($V_O^{\cdot\cdot}$) for charge compensation, as described by the defect formation reaction according with Kroger-Vink notation (appendix 1) [16]:

$$Y_2O_3 \xrightarrow{ZrO_2} 2Y'_{Zr} + 3O_O^x + V_O^{\cdot\cdot} \quad (2.1)$$

However, due to Coulombic interaction between $Y'_{Zr}$ and $V_O^{\cdot\cdot}$, these two defects can be associate (clustering) giving rise to complex defects [7]:

$$Y'_{Zr} + V_O^{\cdot\cdot} = (Y_{Zr}V_O)^{\cdot} \quad (2.2)$$

and

$$2Y'_{Zr} + V_O^{\cdot\cdot} = (2Y_{Zr}V_O)^{\times} \quad (2.3)$$

At low temperatures, the association is almost complete, affecting the population of free vacancies [16]:

$$[(Y_{Zr}V_O)^{\cdot}] \gg [V_O^{\cdot\cdot}] \quad (2.4)$$

and

$$[V_O^{\cdot\cdot}] = A/Texp(-E_{association}/\bar{R}T) \quad (2.5)$$

where $E_{association}$ corresponds to the association binding enthalpy, $A$ is a constant, $T$ the absolute temperature and $\bar{R}$ the gas constant. In this way, the ionic conductivity is given by:

$$\sigma = z\mu[V_O^{\cdot\cdot}] \quad (2.6)$$

where $z$ is a charge number of ion and $\mu$ is the specie mobility expressed as:

$$\mu = B/Texp(-E_{motion}/\bar{R}T) \quad (2.7)$$

here $E_{motion}$ is the enthalpy for motion and $B$ is a constant. The activation energy for conduction ($E_a$) is given by $E_a = E_{association} + E_{motion}$. In this sense, the ionic conductivity is function of the concentration of charge carriers, temperature, number of vacancies sites and ion facility to move to another site.

The curvature at the Arrhenius plots of the electrical conductivity (Fig. 3) results from dissociation of complex defects comprising oxygen vacancy joined with dopant ion.

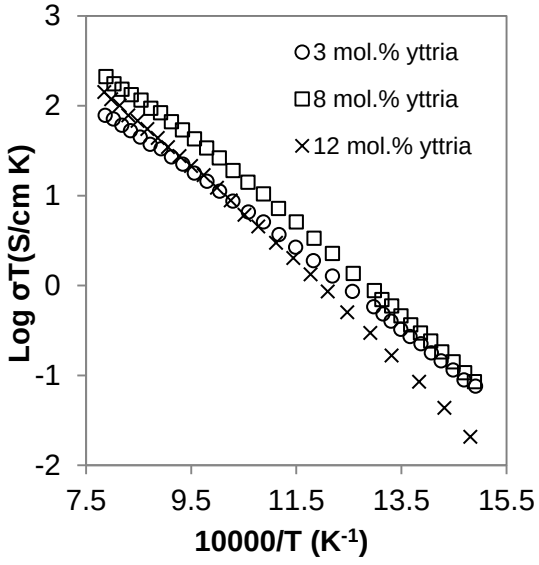


***Figure 3:*** *Arrhenius plots for three $ZrO_2$-$Y_2O_3$ compositions showing different curvature with increasing temperature, adapted from [6].*

At high temperatures the complex defects dissociate completely. The oxygen vacancy concentration (in high temperature field) is ruled by the total concentration of dopant. So, $E_a = E_{motion}$ the migration enthalpy can be inferred from the slope of the temperature dependence for conduction in the high temperature regime. The association enthalpy can be determined from the slopes difference between the higher and lower temperature ranges (Fig. 3). The curvature in the Arrhenius plots decreases for lower dopant amount, reaching almost straight line behaviour (Fig. 3) [6]. The high activation enthalpies for ion transport is the main disadvantage of $(Zr,Y)O_2$ [17]. In fact, this also makes difficult the combination with other materials at low temperatures and the employment on the different electrochemical devices [17]. The relationship between the ionic conductivity and the migration and association enthalpies of different $(Zr,M)O_2$ systems were resolved as function of the dopant ionic radius, as shown in Figure 4 [2]. The tendency for clusters formation increases with increasing the variation between the ion radius of the zirconium and the dopant cation [2,18]. Therefore, the activation energy for association ($\Delta H_a$) decreases for ionic radii differences (Fig. 4).

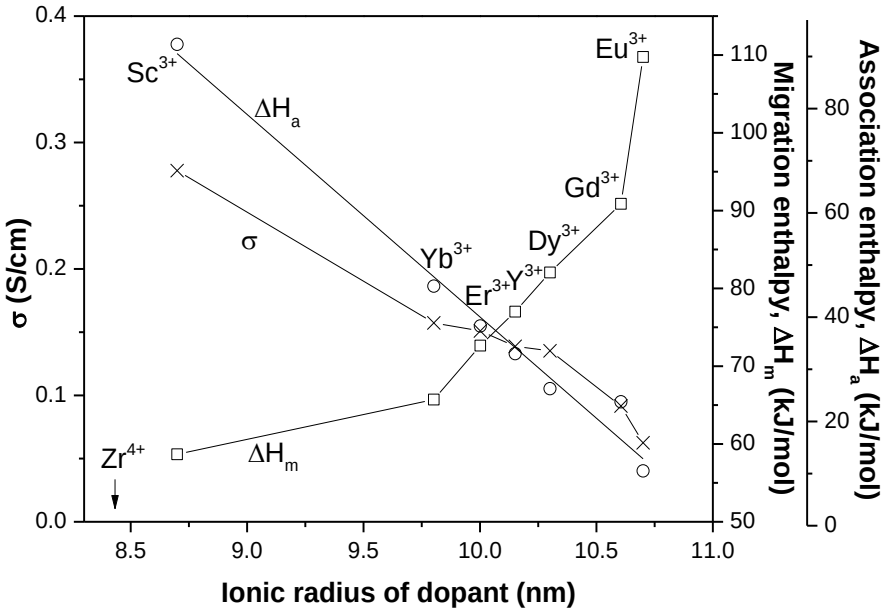


***Figure 4:*** *Maximum conductivity in the binary $ZrO_2$-$M_2O_3$ system at 1000 ºC, and the oxide ion conductivity migration and association enthalpies in function of the dopant (M - $Sc^{3+}$, $Yb^{3+}$, $Er^{3+}$, $Y^{3+}$, $Dy^{3+}$, $Gd^{3+}$,$Eu^{3+}$) ionic radius, adapted from [2].*

On the other hand, the mobility of the oxide ions does not only depend on clusters but also on lattice distortions. The later effect occurs essentially if the ion radius of the dopant cation is greater than the ion radius of the host lattice. In this sense, if the dopant cation radius is well-adapted to the ion radius of $Zr^{4+}$ ($r_{ion}$=8.4 nm), the transport pathways will be less disrupted and the oxide ion mobility is higher [2,18]. Figure 4 depicts as well the max-

imum conductivity (at 1000 ºC) of doped zirconia with respect to cation radius. The Sc-doped ($r_{ion}$=8.7 nm) zirconia shows a higher conductivity than Y-doped ($r_{ion}$=10.2 nm) zirconia and Gd-doped ($r_{ion}$=10.6 nm) zirconia. Considering a small deviation between the ion radii of the dopant cation and $Zr^{4+}$, the migration enthalpy ($\Delta H_m$) is low and therefore the mobility high. Otherwise, for a larger deviation in the radii, the activation energy for migration is increased and so the mobility and the conductivity decreased [2,18].

The clustering involves only the nearest neighbour, which is responsible for the observed low conductivity and increase of activation energy in highly doped $ZrO_2$ [8]. The maximum ionic conductivity in $ZrO_2$-based systems is observed for the minimum dopant concentration necessary to fully stabilize fluorite-type phase, as shown in Figure 5 [8].

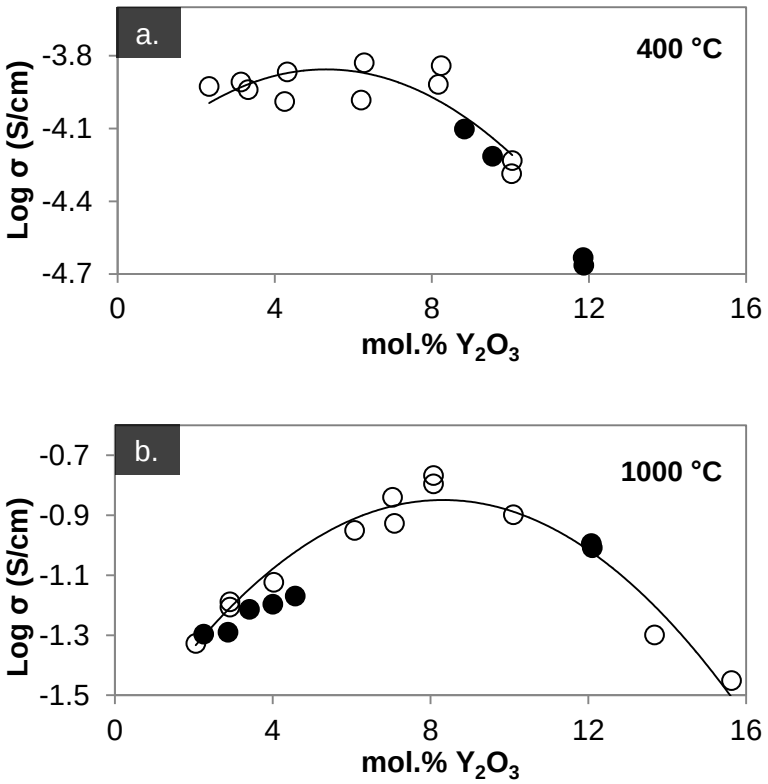


***Figure 5:*** *Conductivity of $(Zr,Y)O_2$ as a function of mol.% $Y_2O_3$ content of single-crystal (open symbol) and polycrystalline samples (closed symbols).* ***(a)*** *The data at 400 °C are either for single-crystal or the grain-boundary conductivity of polycrystalline materials.* ***(b)*** *The data at 1000 °C for polycrystalline specimens are taken only for those materials which showed a very small grain-boundary resistivity at lower temperatures (about 400 °C), adapted from [6].*

The conductivity clearly increases up to 8 mol.% $Y_2O_3$ at 1000 °C, above it, decreases significantly. Even not so clear, the conductivity at 400 °C shows the same trend. Further additions of $Y_2O_3$ above the minimum necessary to obtain fluorite phase increases the association of the oxygen vacancies and dopant cations into complex defects with lower

mobility [2,6,19]. Since the relative contribution of the grain-boundary resistivity decreases rapidly with increasing temperature, the data at 1000 °C for polycrystalline materials can be considered to represent the bulk conductivity [6]. Notice that, similar changes were observed in other fluorite, perovskite and pyrochlore systems [2].

The transport properties of polycrystalline electrolytes do not only depend on the dopant but also on the sample microstructure. The symmetry of the crystal lattice is disrupted at the grain boundaries, which impedes the migration of oxide ions along the sample [18]. Therefore, the grain boundaries of doped-$ZrO_2$ present a blocking effect to the ionic transport across them, i.e. specific grain-boundary conductivity [20]. In 1969, Bauerle et al. reported the blocking effect at $ZrO_2$ grain boundaries based on impedance spectroscopy measurements [21]. AC impedance measurements followed by complex plane analysis of the data provide an accurate separation of the grain bulk and grain boundary conductivity. The frequency decreases with the real component of impedance. The bulk resistance is calculated from the interception of the higher frequency on the real axis. The intermediate arc corresponds to the grain boundary resistance, which diminishes with the increasing of the temperature, while the arc at the lowest frequency is related to the electrode resistance. The blocking effect of the grain boundaries is often ascribed to siliceous impurities, but even in highly pure $(Zr,Y)O_2$ grain boundary conductivity is at least two orders of magnitude lower than that of the bulk one, depending on the temperature and dopant level [20,22].

In 1982, van Dijk et al. proposed that this effect happens on the charge layers adjacent to the grain boundaries, i.e. in the area that is depleted by mobile oxygen vacancies [23]. In Figure 6, the core of the grain boundary corresponds to positive charge and it is balanced by a depletion of $V_O^{\cdot\cdot}$ and an increase of $Y_{Zr}'$ concentration in the space charge layer [22].

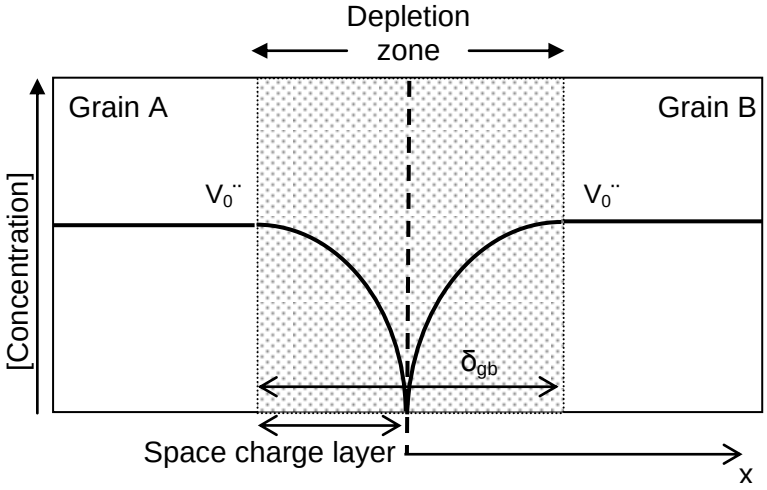


***Figure 6:*** *Schematic representation of a grain boundary, consisting of one grain-boundary core (dash line) and two adjacent space-charge layers. Illustration of oxygen vacancy concentration profile in grain, space charge layers and grain boundary core, adapted from [24].*

The $V_O^{\cdot\cdot}$ depletion zone results in a much lower conductivity than the bulk zone with uniform distribution (Fig. 6). In detail, from a crystallographic point of view a grain-boundary is an crystallographic mismatch zone, where the space-charge layer is part of the bulk. However, electrically the grain-boundary consists of a core added to the adjacent space-charge layers (Fig. 6) [20]. The ionic conduction of polycrystalline material can be modelled by the brick layer model (Fig. 7), where grains with a cubic profile of the same size and homogenous grain boundary were assumed.

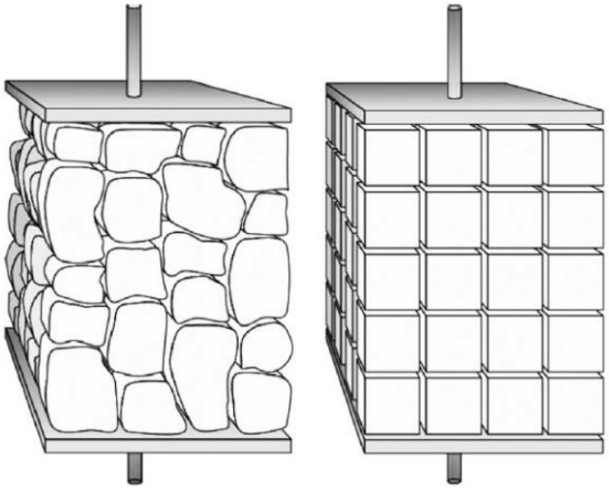

***Figure 7:*** *Illustration of real ceramic microstructure (left) and brick layer model (right) [24].*

The bulk capacitance ($C_{bulk}$) and grain boundary capacitance ($C_{gb}$) are given by [24]:

$$C_{bulk} = \varepsilon_0 \varepsilon_{bulk} \frac{A}{nG} \tag{2.8}$$

$$C_{gb} = \varepsilon_0 \varepsilon_{gb} \frac{A}{n\delta_{gb}} \tag{2.9}$$

where $A$ is the sample cross-section area, $\varepsilon_0$ is the vacuum permittivity, $G$ the average grain size and $n$ the number of grains that crossed through the current direction. If the dielectric constant of the space charge layer ($\varepsilon_{gb}$) is approximated to that of the bulk ($\varepsilon_{bulk}$), the grain boundary thickness ($\delta_{gb}$) is given by,

$$\delta_{gb} = \frac{C_{bulk}}{C_{gb}} G \tag{2.10}$$

In this way, from the boundary thickness is known, the specific grain boundary conductivity ($\sigma_{gb}^{sp}$) is expressed by [24]:

$$\sigma_{gb}^{sp} = \frac{L\delta_{gb}}{R_{gb}AG} \approx \frac{LC_{bulk}}{R_{gb}AC_{gb}} \tag{2.11}$$

here $R_{gb}$ corresponds to the grain boundary resistance and $L$ to the sample thickness. The specific grain-boundary conductivity is about two orders of magnitude lower than the

bulk conductivity [24]. The specific grain-boundary conductivity values for 8 mol.% $Y_2O_3$-doped $ZrO_2$ ceramic of high purity are plotted in Figure 8 as a function of temperature. The bulk conductivities are also plotted for comparison [24]. The activation energy for the bulk conductivity of 8 mol.% $Y_2O_3$-doped $ZrO_2$ is ~1.05 eV, while for the grain boundary conductivity is slightly higher ~1.16 eV (Fig. 8). The decrease of bulk conductivity for lower dopant content increases the difference between the two activation energies [24].

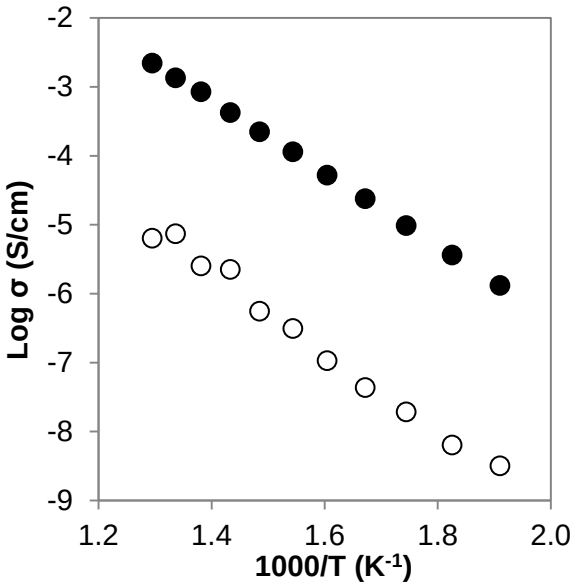


***Figure 8:*** *Bulk (closed symbols) and grain-boundary (open symbols) conductivities of 8 mol.% $Y_2O_3$-doped $ZrO_2$ of high purity as a function of temperature, adapted from [24].*

The intrinsic defects lead to an electron or hole conduction described by the follow equations, respectively [18]:

$$O_O^x \rightarrow 1/2O_2(g) + 2e' + V_O^{\cdot\cdot} \quad (2.12)$$

$$1/2O_2(g) + V_O^{\cdot\cdot} \rightarrow O_O^x + 2h^{\cdot} \quad (2.13)$$

The ionic ($\sigma_i$) and electronic conductivity ($\sigma_e$ or $\sigma_h$) reported for $ZrO_2$-based materials are function of temperature and oxygen partial pressure ($P_{O_2}$), as depicted in Figure 9. The following equations describe the conductivity of each specie [25]:

$$\sigma_i = 1.63 \times 10^2 e^{(-0.79 k_B T^{-1})} \quad (2.14)$$

$$\sigma_e = 1.31 \times 10^7 e^{(-3.88 k_B T^{-1})} \left(P_{O_2}\right)^{-1/4} \quad (2.15)$$

$$\sigma_h = 2.35 \times 10^2 e^{(-1.67 k_B T^{-1})} \left(P_{O_2}\right)^{1/4} \quad (2.16)$$

where is the $k_B$ is the Boltzmann constant. The ionic and electronic (p-type or n-type) conduction domains were now depicted in Figure 9a, as function of the $P_{O_2}$ and temperature. The electronic conductivity (p or n-type) dominate at high temperature and for very high or very low $P_{O_2}$ (Fig. 9a) [18,28]. For the stabilized-zirconia based electrolytes, the interesting $P_{O_2}$ range (Fig. 9b) correspond to the region where the ionic conductivity is

independent of $P_{O_2}$ (1<$P_{O_2}$<$10^{-20}$ atm), since the oxide ion conductivity is predominantly done through the oxygen vacancies [8,18,25].

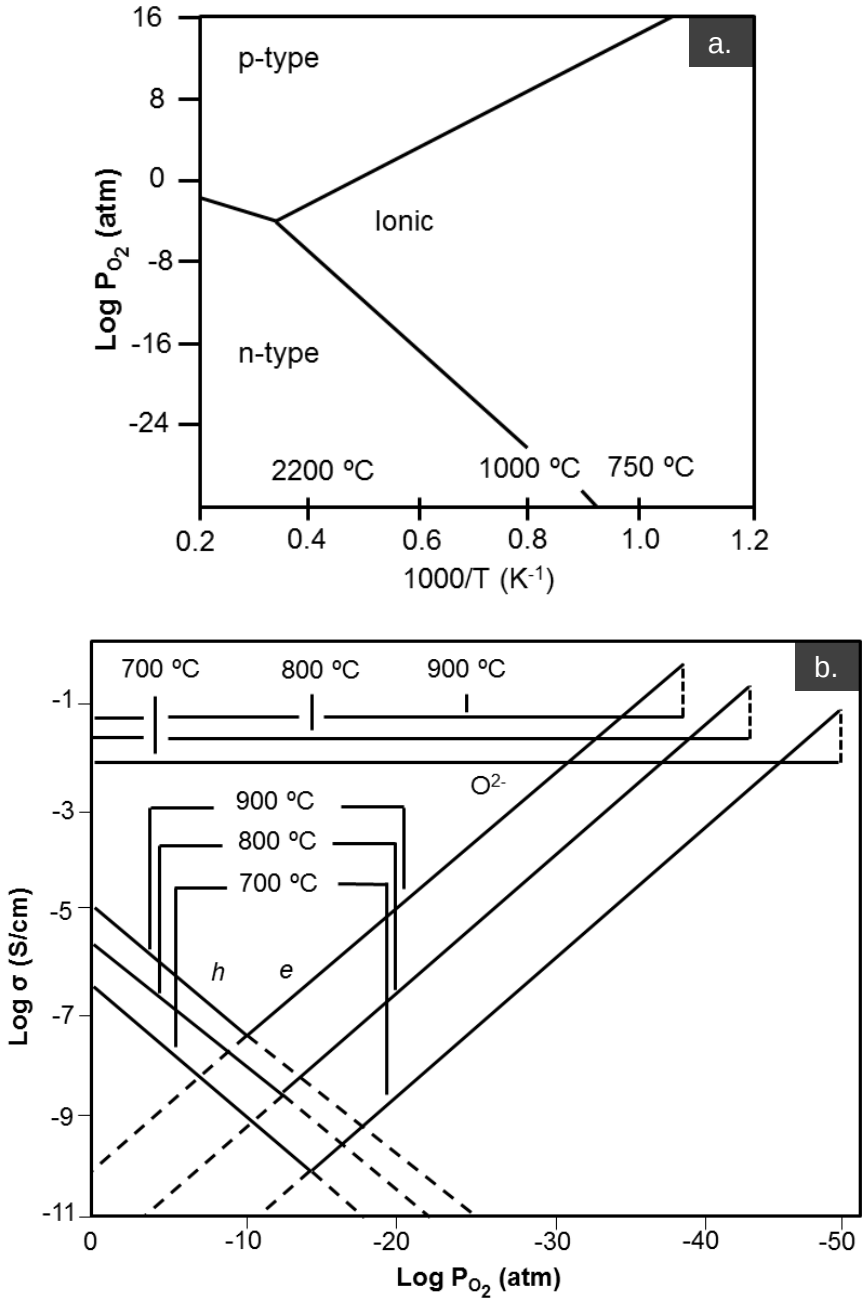


***Figure 9: (a)*** *Ionic, n-type and p-type conduction domains of yttrium-stabilized zirconia as a function of temperature and* $P_{O_2}$, ***(b)*** *electrical conductivity of yttrium-stabilized zirconia as a function of* $P_{O_2}$ *[26,27].*

Considering the difficult conditions to process zirconia materials, requesting high temperatures, high grain boundary resistivity and dissociation enthalpy, other materials based on oxide ion conduction were investigated as an alternative. Materials like $LaYO_3$ and $SrZrO_3$ exhibit low oxide ion conductivity, but they evidence even better protonic conduc-

tion due to superior specie mobility [17]. In 1980, Iwahara et al. discovered the protonic conduction in $ABO_3$ perovskites structure, namely they tried doped $SrCeO_3$-based materials as the solid electrolyte in fuel cells [29-35]. Later, higher protonic conductivity was found in doped-$BaCeO_3$. Such behaviour was attributed to the larger lattice parameter which raises the proton mobility [36-39]. The conductivity of $Ba(Ce,Yb)O_3$ in wet air reached $10^{-2}$ S/cm at 800 ºC, which is about one order of magnitude higher than that of $Sr(Ce,Yb)O_3$ [40].

The protonic conductivity is compromised by the composition, temperature (favourable hydration kinetics), proton mobility and chemical robustness [5]. In 1993, Iwahara began the study in distinct zirconates, as calcium, strontium and barium systems [41]. The barium zirconate ($BaZrO_3$) is an ideal perovskite (Table 1), according with the Goldschmidt tolerance factor given by:

$$t_G = (r_A + r_O)/\left(\sqrt{2}(r_B + r_O)\right) \tag{2.17}$$

where $r_O$ is the radius of the anion, $r_A$ and $r_B$ is the radius of the A and B cations, respectively. From the crystallographic point of view, the perovskite structure $ABO_3$, occurs only within the range $0.75<t_G<1.00$. $BaZrO_3$ has $t_G$=0.92, which means that the A-O and B-O bond length are equal to the sums of the corresponding ionic radii. Additionally, the relative stabilities of various barium perovskite oxides were inferred by $t_G$ and the molar enthalpy of formation ($\Delta H_f$) from the constituent binary oxides. The decrease of $\Delta H_f$ follows the trend of $t_G$and increases with the ionic radius of the tetravalent cation ($Zr^{4+}$) [42]. However, the high $t_G$= 0.92 of $BaZrO_3$ have been received special interest, due to a good chemical stability and high protonic conductivity at intermediate temperatures [41-43].

***Table 1:*** *Illustration of crystalline structures and summary of some properties of $BaZrO_3$ [44-47].*

| | **$BaZrO_3$** | |
|---|---|---|
| 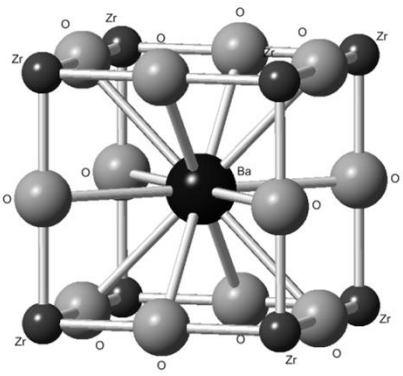 | Structure name | Perovskite |
| | Structure type | $ABX_3$ |
| | Coordination number of A:B:X | 12:6:6 |
| | Anion packing | Cubic (FCC) |
| | Space group | $Pm\bar{3}m$ |
| | Lattice parameters (nm) | 0.4192 |
| | Density ($g/cm^3$) | 6.24 |
| | Melting temperature (ºC) | 2978 |
| | Young's modulus (GPa) | 243 |
| | Vickers hardness (GPa) | 4.95 |
| | Linear thermal expansion ($K^{-1}$) | $7.13\times10^{-6}$ |

From literature, an extensive list of synthesis method of barium zirconate is available: solid state reaction, sol-gel, co-precipitation, thermal-decomposition and hydrothermal techniques. Typically the procedures are extensive, particularly the solid state reaction which is commonly used, needing long time thermal treatments at elevate temperatures (~1700 ºC), which is prone to the impurities incorporation [40,43,48,49].

Shevchenko et al. reported a $ZrO_2$-BaO phase diagram (Fig. 10a) based on DTA (between 1800°-2800°C) and room temperature X-ray diffraction analysis of samples prepared from $ZrO_2$ and $BaCO_3$ (both analytically pure), after calcining the powders at 1200°C, and two steps annealing (1st-1300 °C, 2nd-1700 ºC). Annealing was carried out isothermally in a furnace with a tungsten heating element in riveted molybdenum crucibles at 1700°C for 2 h. The formation of a compound of equimolar composition ($BaZrO_3$) which melts congruently was confirmed with a melting point of 2540 °C. The *liquidus* has a eutectic point at 25 mol.% BaO at 2240 °C. Moreover, BaO addition does not lower the temperature of the polymorphic transitions of $ZrO_2$ significantly [50]. Paschoal et al. disclosed another $ZrO_2$-BaO phase diagram (Fig. 10b), where the samples were prepared from $BaZrO_3$ and $BaCO_3$ as raw materials, after calcinated at 1300°C (for 16 h) and then annealed at 1700°C (for 100 h). This has a particular interest, concerning the new information reported for the melting of $BaZrO_3$ at 2620 ºC and compositional differences for the ($BaZrO_3$-$ZrO_2$) eutectic point defined now at 15 mol.% BaO with a decrease of about 200 ºC for the eutectic reaction (2050 ºC) [51].

Protonic conduction results from creation of $V_O^{\cdot\cdot}$ intrinsically, due to variations of the ratio of the main constituents, or may be formed extrinsically to compensate the dopant incorporation [17]. The introduction of accepting substitutional defects as yttrium (extrinsic defects) into $BaZrO_3$ and formation of $V_O^{\cdot\cdot}$, in the structure is expressed by the equation 2.1, as a consequence [52,53]:

$$[V_O^{\cdot\cdot}] = {}^1/_2\,[Y'_{Zr}] \tag{2.18}$$

In the presence of water vapour and intermediate temperatures (300-600 ºC), protons are introduced into the $BaZrO_3$ lattice. The water dissociates into a hydroxide ion and a proton (hydration reaction). The hydroxide will be placed at the $V_O^{\cdot\cdot}$, while the proton establishes a covalent bond with a lattice oxygen, according with the reaction given by [48,52,53]:

$$H_2O + V_O^{\cdot\cdot} + O_O^x \rightarrow 2(OH)_O^{\cdot} \tag{2.19}$$

and consequently generates protonic conductivity. The principal features of the transport mechanism are rotational diffusion of the proton defect and proton transfer towards a neighboring oxide ion [17,52]. The proton concentration in the oxide is,

$$[(OH)_O^{\cdot}] = K_h^{1/2}[V_O^{\cdot\cdot}]^{1/2}\left(P_{H_2O}\right)^{1/2} \tag{2.20}$$

here $K_h$ is the equilibrium constant for the hydration reaction. Protonic conductivity increases for higher humidity levels and lower temperature, following the raise of water vapour solubility and the raise of proton concentration. The high temperatures lead to low water vapour solubility, so it was found that the protonic conductivity should be proportional to $\left(P_{H_2O}\right)^{1/2}$ [52,54].

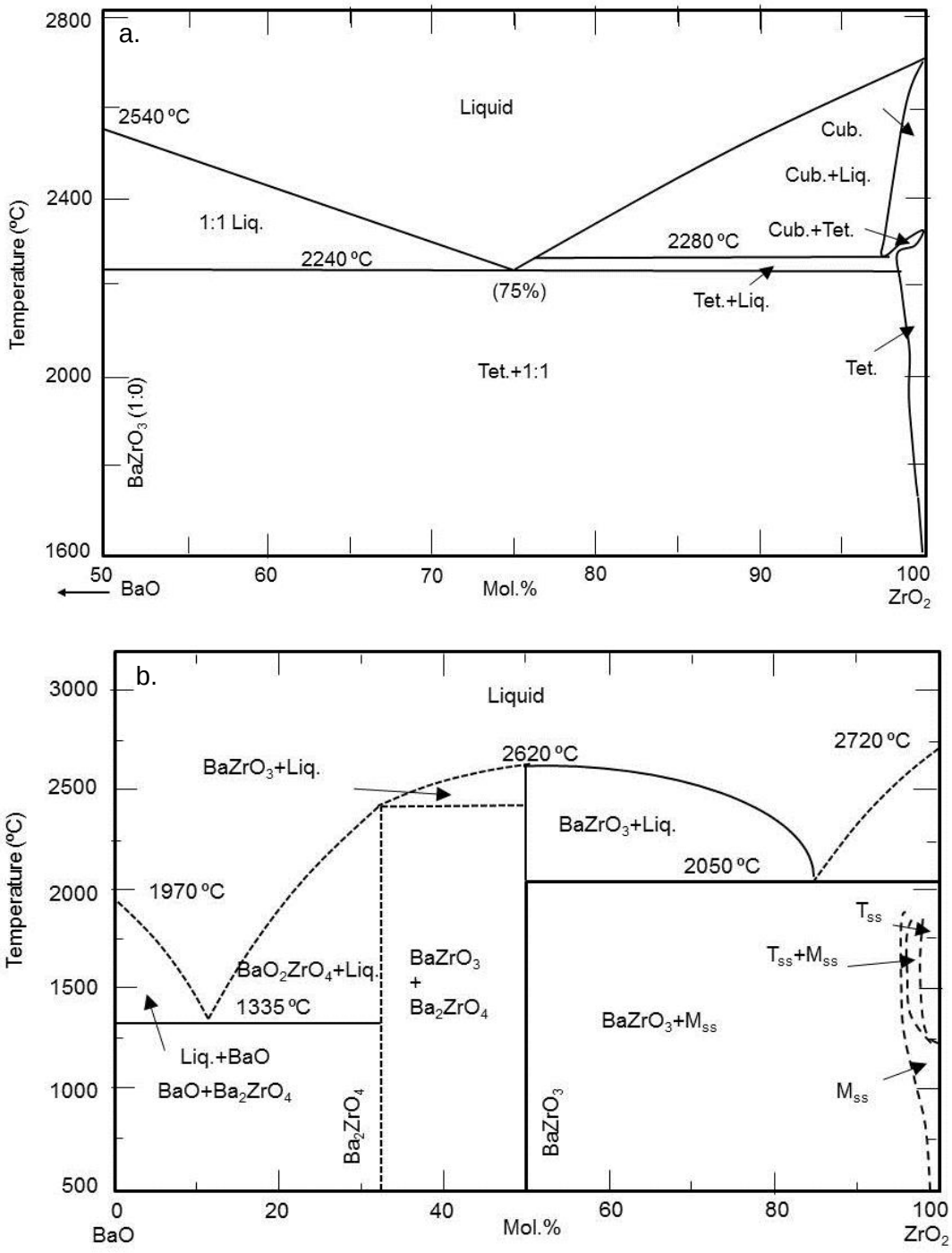


***Figure 10:*** *Phase diagrams of BaO-$ZrO_2$ system reported by* ***(a)*** *Shevchenko et al. and* ***(b)*** *Paschoal et al. [50,51].*

In hydrogen atmospheres, protonic conduction is based on the molecular hydrogen dissociation and then proton attachment at the oxygen ion site forming hydroxide ions ($\frac{1}{2}H_2 + O_O^x \rightarrow (OH)_O^{\cdot} + e^{\cdot}$) [49].

The thermodynamic data for the formation and mobility of proton defects are found to be very sensitive towards the type/concentration of acceptor dopant. For barium zirconate, yttrium is found to perfectly match as an acceptor dopant on the Zr-site, i.e. the enthalpy of the formation (hydration enthalpy) and mobility of proton defects (activation energy) are almost unchangeable by doping (Fig. 11) [48]. Yttrium doping zirconate showed favourable proton mobility as evidenced by the lower enthalpy for proton mobility $E_a$=41.5 kJ/mol (Fig. 11), which slightly increases to 46.3 kJ/mol for higher yttrium concentration (from 2 up to 20 mol.%) [48].

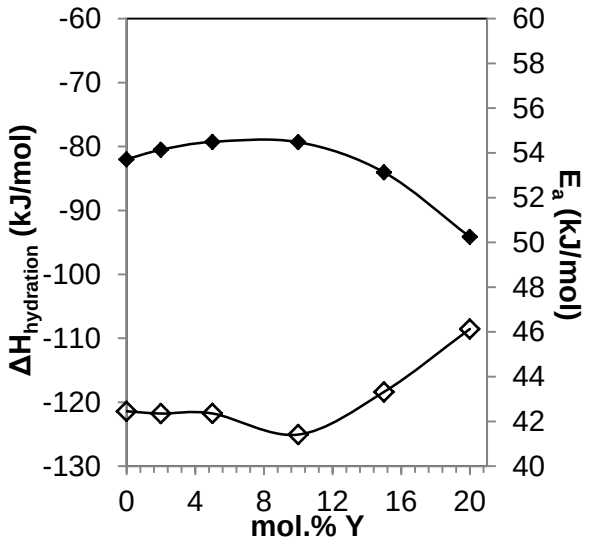


***Figure 11:*** *Hydration enthalpy and activation energy of the mobility of proton defects in barium zirconate as function of the yttrium concentration, adapted from [48].*

So, considering the same composition Ba(Zr,M)$O_3$ and distinct dopants (M= Sc, Y, Ho, Dy, Gd, In), the highest ionic conductivity was obtained for the yttrium case, $\sigma = 3.6 \times 10^{-3}$ S/cm at 800 ºC (Fig. 12) [43]. However, proton mobility is function of dopant size, as demonstrated by the variation of activation energy for proton migration in distinct structural distortions [48,55]. Highly textured Ba(Zr,Y)$O_3$ films obtained by pulsed laser deposition (PLD) on (100)-oriented MgO substrates, show the largest protonic conductivity (0.11 S/cm, at 500 ºC) ever reported for such material [56].

Likewise zirconia, the protonic conductivity of Ba(Zr,Y)$O_3$ is mainly controlled by the high resistivity of grain boundary, for lower temperatures. The structural distortions in the grain boundary lead to a decrease of proton mobility and possibly to a depletion of proton

defects, which result in raise of proton resistance [17,57]. This depends on the dopant type and concentration, once the enrichment of the dopant decreases the depletion zone size and is much effective to improve proton transport properties across the grain boundary. It was observed an enhancement of grain boundary and total conductivities for higher yttrium content (5 to 15 mol.%) [57,58].

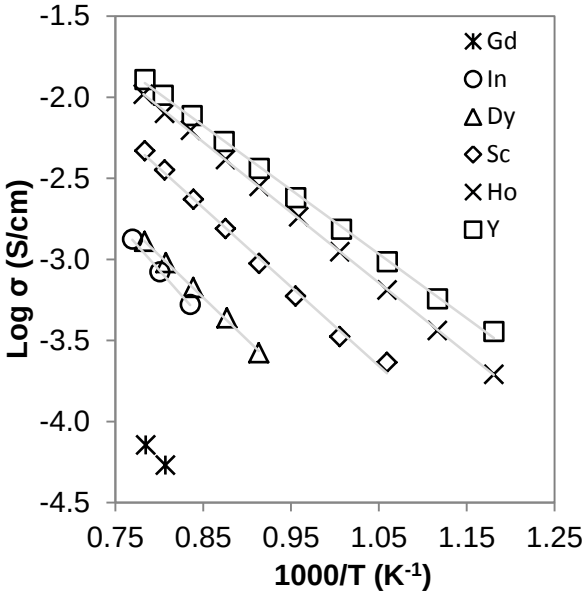


***Figure 12:*** *Arrhenius plots of total conductivity for Ba(Zr,M)$O_3$ (M - Gd, In, Dy, Sc, Ho and Y) in air with water vapour (at 23.5 ºC), adapted from [43].*

### II.1.2. Mixed conductivity

Recently, much attention has been given to mixed conductors materials. Taking advantage of their inherent versatility, numerous electrochemical devices have been developed [59-62]. Mixed conductors materials are capable to transport multiple species. They are defined as mixed ionic conductors (MIC) if transport oxide ions and protons, or mixed ionic-electronic conductors (MIEC) if ions and electron/holes are conducted [59-61]. Mixed conductivity in ceramics has been obtained by two distinct ways: single-phase materials under multiple atmospheric conditions or combining individual conductive phases into a composite structure which in the same conditions have propensity to transport different species [63].

When mixed conduction outcomes from different charge carriers such as anions, cations, electrons and electron holes, it is the transference number (*t*) that expresses the contribution to the conductivity of each one. The individual transference number depends of the oxide, doping and atmosphere [64].

$$t_{ion} + t_{electronic} = 1 \qquad (2.21)$$

where $t_{ion}$ and $t_{electronic}$ corresponds to the transference numbers of ionic [combining proton ($t_p$) and/or oxide ions ($t_O$)] and electronic (electron and/or holes) species. The protonic ($\sigma_{H^+}$), oxygen ion ($\sigma_{O^{2-}}$) and electronic ($\sigma_e$ ) conductivities can be separately measured and are typically function of composition, atmosphere and temperature. The electronic fraction combines the hole conduction through zirconia (conditions in Fig. 9) and barium zirconate (it prevails for $P_{O_2}$> 1 Pa, between 500-700 ºC) [49,64]. An equivalent circuit describing steady state can be planned for the electrolyte fraction. The ionic conductivity of binary system is given by;

$$I_i = V_{applied}\left(\frac{R_{i,Z}+R_{i,BZ}}{R_{i,Z}R_{i,BZ}}\right) \tag{2.22}$$

and the hole currents is,

$$I_h = V_{applied}\left(\frac{R_{h,Z}+R_{h,BZ}}{R_{h,Z}R_{h,BZ}}\right) \tag{2.23}$$

where $V_{applied}$, $R_{h,Z}$, $R_{i,Z}$, $R_{h,BZ}$ and $R_{i,BZ}$ are respectively the applied voltage, electronic-type and ionic resistances of zirconia and barium zirconate. Then the measured total current is given by;

$$I = I_i + I_h = V_{applied}\left(\frac{R_{i,Z}+R_{i,BZ}}{R_{i,Z}R_{i,BZ}} + \frac{R_{h,Z}+R_{h,BZ}}{R_{h,Z}R_{h,BZ}}\right) \tag{2.24}$$

or

$$\frac{V_{applied}}{I} = \frac{R_{i,Z}R_{i,BZ}R_{h,Z}R_{h,BZ}}{(R_{i,Z}+R_{i,BZ})R_{h,Z}R_{h,BZ}+(R_{h,Z}+R_{h,BZ})R_{i,Z}R_{i,BZ}} \tag{2.25}$$

For a predominant ionic (protonic, oxide ionic) conduction hole transport must be considered as negligible [59,65].

Iwahara et al. disclosed the earliest single-phase materials having significant mixed protonic-oxide ionic conductivity based on $BaCeO_3$-based electrolytes. The contribution of both species varies with the temperature, so distinct domains were defined. Protonic conductivity prevails at 700 ºC and oxide ion conduction dominates at 1000 ºC [66-70]. Additionally, the $t_p$ and $t_O$ changes with the dopant type in $BaCeO_3$, since they affect lattice spacing and distortion, which influence the mobility of ions (Fig. 13) [66-70]. The highest ionic conductivity (0.011 S/cm, at 600 ºC) was obtained for $Ba(Ce,Gd)O_3$ (with 10 at.% of Gd) [71].

Later, Lybye *et al.* reported $(La,Sr)(Sc,Mg)O_3$ (with 10% of strontium and magnesium), a single-phase material prepared by two different methods glycine-nitrate process and solid state reaction showing MIC behaviour [72]. Likewise for $BaCeO_3$-based electrolytes, the mixed conductor domains were defined by the temperature and also by $P_{O_2}$. Electronic conductivity (~$2.02\times10^{-2}$ S/cm at 800 ºC) was found at high oxygen partial pressure ($P_{O_2}$=1

atm). However, for low $P_{O_2}$ a combined protonic and oxide ionic conductivity were observed below and above 800 ºC, respectively. Notice that below 700 ºC, the total conductivity (~1.9×10$^{-4}$ S/cm at 600 ºC) is considerable lower than the obtained for Ba(Ce,Gd)$O_3$, since protonic conduction prevails in this domain. On the other hand, above 800 ºC, oxide ion conductivity is dominant and reached 1.6×10$^{-2}$ S/cm at 800 ºC [71].

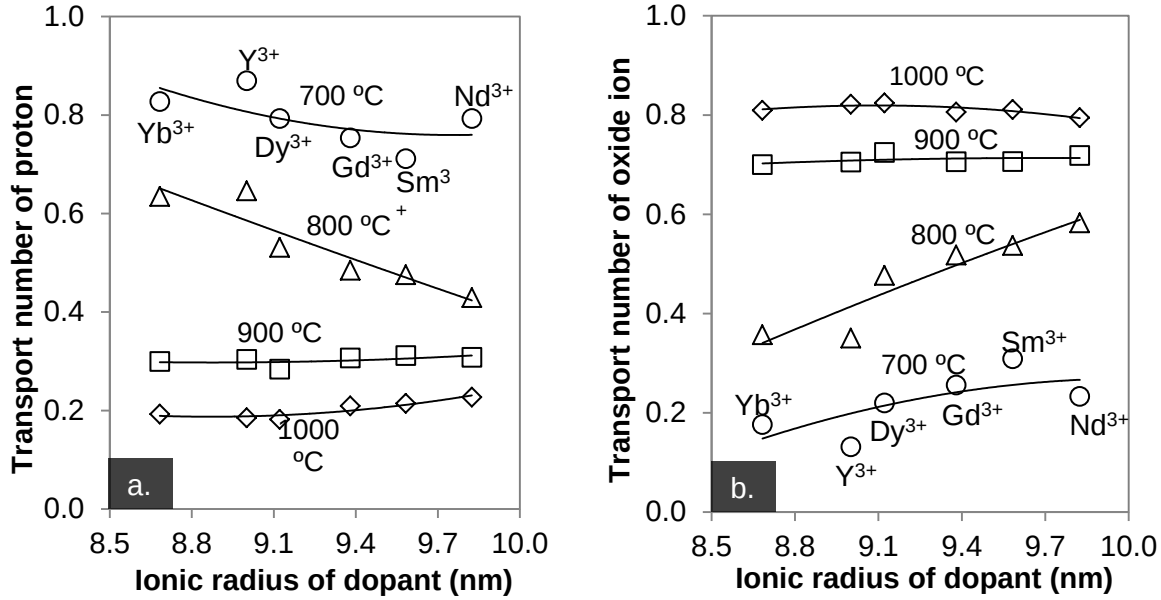


***Figure 13:*** *Plots of transport numbers of* ***(a)*** *protonic and* ***(b)*** *oxide ionic conduction in Ba(Ce,M)$O_3$ (M - $Yb^{3+}$, $Y^{3+}$,$Dy^{3+}$, $Gd^{3+}$,$Sm^{3+}$, $Nd^{3+}$) as function of the dopant ionic radius, adapted from [67].*

The multiple charge carrier transportation was also observed in Ba(Zr,Y)$O_3$ samples for proton, oxide ion and hole, under restricted conditions [49,52,54,64,73,74]. Notice that, the prevailing transported specie can be defined based on measurements with variable temperature, water vapour partial pressures ($P_{H_2O}$), hydrogen partial pressures ($P_{H_2}$) and oxygen partial pressure ($P_{O_2}$) [52,64]. In general, for a single-phase material, the protonic conductivity is dominant under reducing atmosphere and lower temperatures, while oxide ion and hole conductivities are evident in oxidizing conditions and/or high temperatures [52,64,74]. In oxidizing conditions, hole conduction was promoted by the dissociation and reaction of oxygen molecules with oxygen vacancies, according with ($V_O^{\cdot\cdot} + \frac{1}{2}O_2 \rightarrow 2h^{\cdot} + O_O^x$) [54]. The total conductivity can be estimated from $\sigma = \sigma_i + \sigma_h^0 P_{O_2}^{1/n}$, where $\sigma_i$ is the ionic conductivity (oxide ion and/or proton) and $\sigma_h^0 P_{O_2}^{1/n}$ is ascribed to hole conductivity ($\sigma_h^0$ the pre-exponential factor with dimensions of conductivity and $n$ is typically 4 or 6 depending on $P_{O_2}$ and temperature) [73]. The ionic transference number ($t_{ion}$) can be given by:

$$t_{ion} = \sigma_i / \left( \sigma_i + \sigma_h^0 P_{O_2}^{1/4} \right) \quad (2.26)$$

where $\sigma_h^0$ is the hole conductivity at $P(O_2)$= 1 atm.

In dry conditions, the hole conductivity can be distinguish from ionic conductivity based on measurements performed at different $P_{O_2}$ (Fig. 14) [49,52,64]. Indeed, the improvement of total conductivity observed for $P_{O_2}$> 1 Pa is ascribed to predominant hole conduction [49,64]. For $P_{O_2}$< 1 Pa (Fig. 14), the conductivity is independent of $P_{O_2}$, suggesting that the ionic conduction is predominant [49,64]. In the same way, Nomura et al. found for $Ba(Zr_{0.8}Y_{0.2})O_{3-\delta}$ oxide ion conductivity domain for $P_{O_2}$<$10^{-5}$ Pa. For $P_{O_2} \leq 2 \times 10^{-11}$ Pa reach $t_{O^{2-}} \geq 0.99$, leading to oxide ion conductivity of $4.1 \times 10^{-3}$ S/cm at 1000 ºC, with $E_a$ = 72.4 kJ/mol [64]. This suggests mixed oxide ion and hole conduction under low $P_{H_2O}$ once it decreases with humidity [64]. In the wet state (Fig. 14), protonic conduction surpasses the hole conduction even for higher $P_{O_2}$. The proton defect reduces the hole concentration and hindered their mobility [49,52].

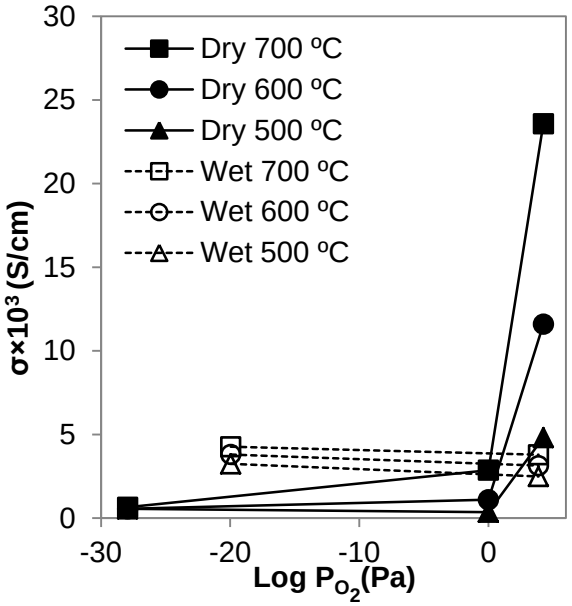


***Figure 14:*** *Dependence of the bulk conductivity of Ba(Zr,Y)$O_3$ on $P_{O_2}$ for 500, 600, and 700 °C in wet and dry environment, adapted from [49].*

Conductivity is independent of $P_{O_2}$ in wet conditions, so protonic conduction must prevail [64]. Kuz'min et al. confirms this result, in dry air ($P_{H_2O}$= 0.04 kPa, Fig. 15a) the $Ba(Zr,Y)O_3$ is nearly purely hole-type, the temperature dependence of conductivity shows convex curves at the Arrhenius plots, with linear segments at the low and high temperature regions (Fig. 15a) [52]. The convexity of curves decreases with the increase in the dopant content. The increase of humidity ($P_{H_2O}$ = 0.61 kPa, Fig. 15b) shows weak inflec-

tion, which became more pronounced for higher humidity ($P_{H_2O}$ = 3.17kPa, Fig. 15c). The inflections in temperature (~750 ºC) was attributed to the overlap of ionic conductivity that arouse in humid air on the hole conductivity [52]. In dry air, the activation energy of hole conduction domain (high temperature), slowly decrease with yttrium content (0.05-0.20 at.%) from 67.5 to 62.7 kJ/mol. Notice, for the smallest yttrium amount (0.02 at.%) the activation energy was much higher, 83.9 kJ/mol. Activation energies for lower temperatures were higher and decreased more sharply with the increase of yttrium content. As the humidity increase, protonic conduction lead to an increment of the activation energies in the high and low temperature ranges and for all compositions [52].

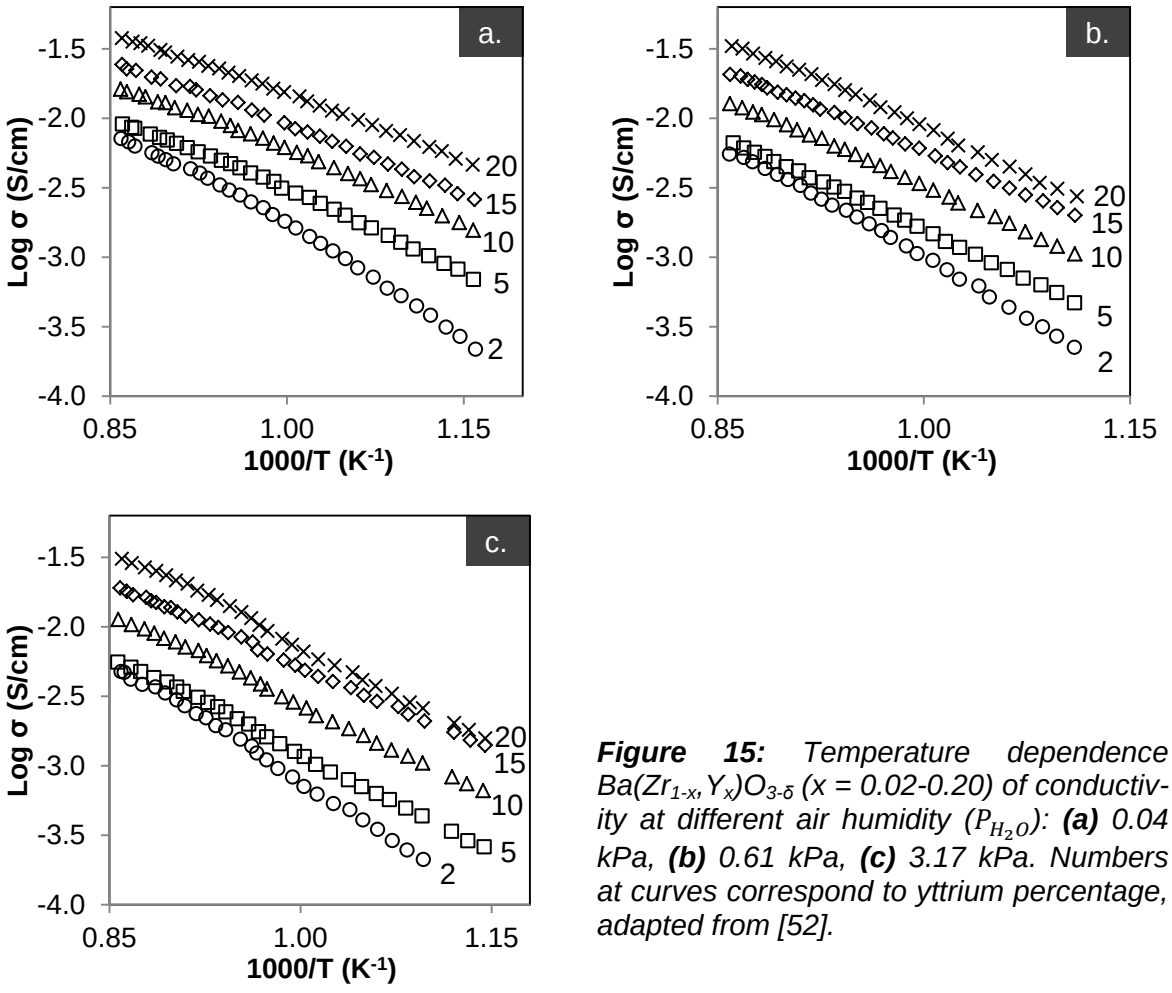


***Figure 15:*** *Temperature dependence $Ba(Zr_{1-x},Y_x)O_{3-\delta}$ (x = 0.02-0.20) of conductivity at different air humidity ($P_{H_2O}$): **(a)** 0.04 kPa, **(b)** 0.61 kPa, **(c)** 3.17 kPa. Numbers at curves correspond to yttrium percentage, adapted from [52].*

At high temperature, the protonic conductivity is weakly dependent on yttrium amount, but it is strongly enhanced for lower temperature and/or high humidity levels [54].

Oxide ionic conductivity of $Ba(Zr,Y)O_3$ occurs via a vacancy mechanism, so it should be proportional to the concentration of oxygen vacancies. According to the hydration reaction (Eq. 2.19), the concentration of vacancies decreases with increasing air humidity, and so oxygen conductivity should also decrease [54]. The activation energy for oxide ion

conduction was 72.4 kJ/mol in $Ba(Zr,Y)O_3$ ceramics, which showing a conductivity of $4.1\times10^{-3}$ S/cm at 1000 ºC [64].

In summary, the hole conduction in $Ba(Zr,Y)O_3$ materials is dominant in dry and high $P_{O_2}$, while the oxide ion conduction prevails in dry and low $P_{O_2}$. Protonic conduction governs below 600 ºC in the presence of water vapour and/or hydrogen [64]. Although, Gorelov et al. reported a mixed ionic conductivity in a humid atmosphere involving both ionic species protons and oxide ions (Fig. 16) [54]. The ionic and electronic conductivity are weakly dependent of the yttrium content, but ionic fraction increase for lower temperature and higher humidity levels (Fig. 16) [54].

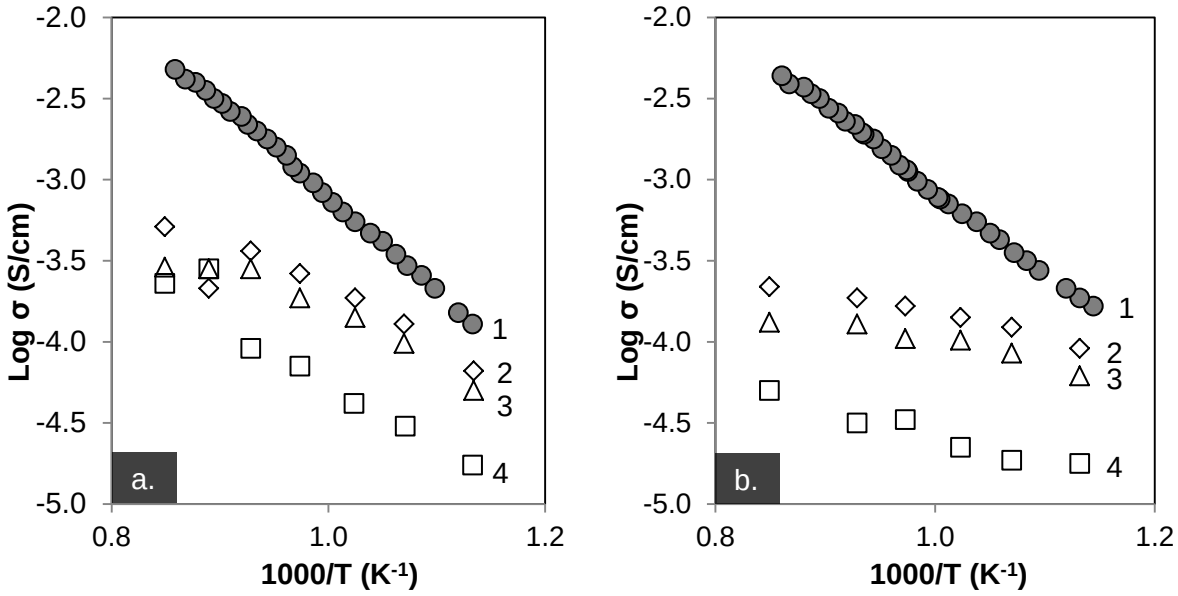


**Figure 16:** Temperature dependence of $Ba(Zr,Y)O_3$ at $P_{H_2O}$=3.57 kPa of (1) total conductivity, (2) ionic conduction fraction, (3) protonic conductivity and (4) oxide ion conductivity for **(a)** 2 at.% Y, **(b)** 15 at.% Y, adapted from [54].

Several composites materials comprising doped-$CeO_2$ and other inorganic compounds (salt, hydrates or oxides) have been studied [75-80]. Here, relevance must be given to binary-oxide systems combining typically a perovskite and fluorite structures, namely $(Ce,Sm)O_2$-$Ba(Ce,Sm)O_3$ [77,78], $(Ce,Gd)O_2$-$Ba(Ce,Gd)O_3$ [79] and $(Ce,Sm)O_2$-$Ba(Ce,Y)O_3$ [80]. The mixed ionic conductor $(Ce,Sm)O_2$-$Ba(Ce,Sm)O_3$ was synthesized by sol-gel combustion method [78]. Protonic conductivity prevails below 550 ºC, once the highest total conductivity is $8.82\times10^{-6}$ S/cm at 300 ºC under wet air (3% $H_2O$). The improvement of total conductivity under dry air over argon atmosphere evidence a hole conduction behaviour [78]. Later, it was studied the purely ionic (in wet air and from 700 to 900 ºC) and mixed ionic-hole conduction (dry air) as function of $(Ce,Sm)O_2$/$Ba(Ce,Sm)O_3$

phase volume ratio [77]. In fact, ionic conductivity prevails for higher ratio, while the higher $Ba(Ce,Sm)O_3$ content lead to MIEC behaviour. The $E_a$ did not change significantly, since oxide ion and hole conductivity were almost equivalent, while in wet atmosphere (from 500 to 700 ºC) the protonic conductivity has lower $E_a$ [77]. The highest ionic conductivity ($2.2\times10^{-2}$ S/cm at 750 ºC) was acquired for equal proportion $0.5(Ce,Sm)O_2$-$0.5Ba(Ce,Sm)O_3$. The ionic conductivity was controlled by $(Ce,Sm)O_2$ at higher temperature (900 ºC), while below 750 ºC the $Ba(Ce,Sm)O_3$ prevails [77].

Likewise, the total conductivity ($3.4\times10^{-2}$ S/cm at 800 ºC) of $0.8(Ce,Gd)O_2$-$0.2Ba(Ce,Gd)O_3$ prepared by citrate route at 1450 ºC was mainly controlled by $(Ce,Gd)O_2$. Although grain conductivity increases for higher $Ba(Ce,Gd)O_3$ amounts, the reduction of total conductivity composite was ascribed to the decrease of the sum charge concentration. Additionally, it was observed that the reduction of $Ba(Ce,Gd)O_3$ grain sizes, lead to percolation improvement [79]. Another binary-system, $(Ce,Sm)O_2$-$Ba(Ce,Y)O_3$, synthesized by sol-gel and co-precipitation methods showed mixed conductivity [80]. In this case, it was reported a significant interfacial conduction between $(Ce,Sm)O_2$ and $Ba(Ce,Y)O_3$ phases, but the responsible mechanism was not revealed [80]. However, the main problem of these cerates-type materials are their poor chemical stability, which become critical at lower temperatures, due to strong tendency of the alkali-earth hydroxides formation in addition to the carbonate formation [81]. On the other hand, the $ZrO_2$-$BaZrO_3$ dual-phase fields defined for molar fractions of $X_{ZrO_2}$≥0.5, $X_{BaO}$≤0.5 and for $X_{YO_{1.5}}$ up to 0.68 on the solidus surface of the BaO-$ZrO_2$-$Y_2O_3$ phase diagram (Fig. 17) are really promising, since it combines a high individual chemical stability and the highest conductivity at intermediate temperatures [81,82].

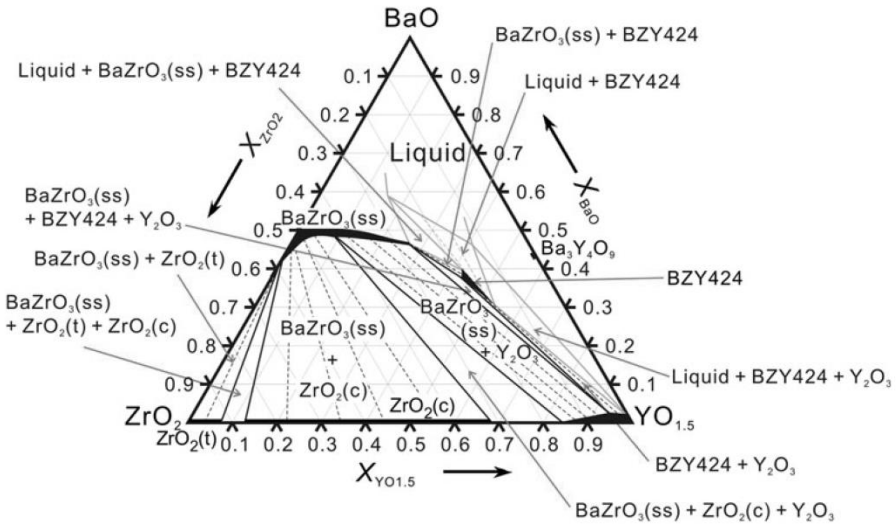


***Figure 17:*** *The BaO-$ZrO_2$-$YO_{1.5}$ ternary phase diagram system at 1600 ºC [82].*

### II.1.3. Ionic conductivity in DSE materials

The DSE materials have microstructural features often explored in order to obtain a substantial enhancement on their properties, namely electrical conductivity [83-85]. Typically, the maximum conductivity of directionally solidified materials is observed for compositions near the eutectic one, owing to the much finer and homogenous microstructure, along with better matching between phases and absence of intermediate segregations or voids between them, which commonly occurs in ceramic samples [85-87]. Notice that, most of the investigation done in the electric properties of DSE oxides was performed in $ZrO_2$-based materials, where it have been combined an ionic conductor phase ($ZrO_2$) with an insulating phase. In this way, a single phase is responsible for the conduction.

The first studies in DSE oxide systems were realized with $(Zr,Ca)O_2$-$CaZrO_3$ and $(Zr,Mg)O_2$-MgO [84]. The eutectic domain size did not change considerably the conductivity, but the anisotropic effect is clearly revealed. Both systems comprise oxide ion conducting phase 29 mol.% CaO stabilized-$ZrO_2$ and 20 mol.% MgO stabilized-$ZrO_2$ and other mainly insulating phases $CaZrO_3$ ($1.7\times10^{-9}$ S/cm at 1000 K) and MgO ($10^{-10}$ S/cm at 1000 K), respectively [85]. However, these DSE have significantly different microstructures. $(Zr,Ca)O_2$-$CaZrO_3$ shows lamellar arrangement well-aligned with growth axis, while a fibrous microstructure prevails for $(Zr,Mg)O_2$-MgO DSE, consisting of MgO fibres immersed into $(Zr,Mg)O_2$ matrix. The anisotropic effect in the conductivity of both systems is depicted in Figure 18.

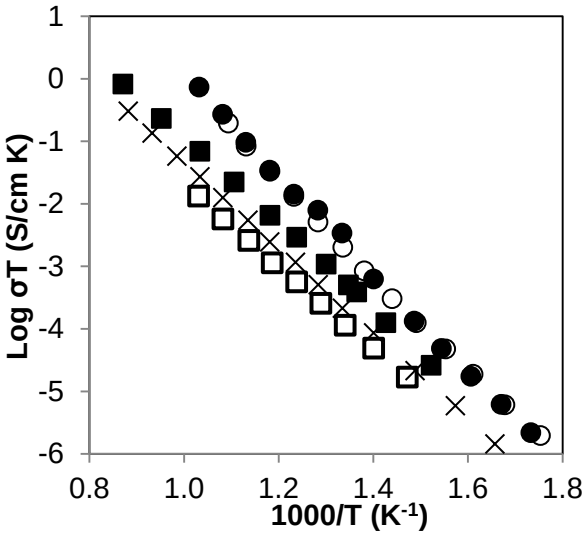


***Figure 18:*** *Arrhenius plot of the conductivity for the $(Zr,Ca)O_2$-$CaZrO_3$ DSE: (open square) perpendicular to the growth axis, (closed square) parallel to the growth axis and (×) were values obtained on a granular sample (with eutectic composition). For $(Zr,Mg)O_2$-MgO DSE (open circles) perpendicular to the growth axis, (closed circles) parallel to the growth axis, adapted from [85].*

The conductivity of $(Zr,Mg)O_2$-MgO DSE is the highest, not showing the anisotropic effect. In this system, the matrix corresponds to the conducting phase, and so there are always conduction paths available in this arrangement.

$(Zr,Ca)O_2$-$CaZrO_3$ composites were also prepared by conventional sintering according with the eutectic composition, revealing random granular microstructure. The ionic conductivity of $(Zr,Ca)O_2$-$CaZrO_3$ along the growth direction (parallel to lamellae plane) is higher than that in perpendicular direction, while random granular sample lying between them [85]. The conductivity of the $(Zr,Ca)O_2$-$CaZrO_3$ composites can be predicted based on the general mixing equation defined for multiphase materials. For a random granular ceramic sample assuming spherical particle shape [85],

$$(1-f)\frac{\sigma-\sigma_2}{2\sigma+\sigma_2}+f\frac{\sigma-\sigma_1}{2\sigma+\sigma_1}=0 \quad (2.27)$$

where $f$ is the filling factor and corresponds to the volume fraction of the conducting phase, while $\sigma_1$ and $\sigma_2$ are the conductivity of each single phase. The DSE conductivity having well-aligned lamellar arrangement parallel to the growth axis is given by [85]:

$$\sigma_{\parallel DSE}=f\sigma_1+(1-f)\sigma_2 \quad (2.28)$$

While, for the perpendicular direction:

$$\sigma_{\perp DSE}=[(f/\sigma_1)+(1-f/\sigma_2)]^{-1} \quad (2.29)$$

The estimated values are in agreement with those obtained experimentally, as depicted in Table 2. The differences in the $\sigma_{\perp DSE}$ was ascribed to the lamellar miss alignment [85].

***Table 2:*** *DC conductivity (S/cm) data at 600 ºC for the eutectic $(Zr,Ca)O_2$-$CaZrO_3$ system [85,88].*

| | Experimental | Theoretical |
|---|---|---|
| $\sigma_{\parallel DSE}$ | $1.4\times10^{-5}$ | $1.8\times10^{-5}$ |
| $\sigma_{\perp DSE}$ | $2\times10^{-6}$ | 0 |
| $\sigma_{granular}$ | $5.7\times10^{-6}$ | $5.2\times10^{-6}$ |

The DSE conductivity was not drastically lower than in $(Zr,Ca)O_2$ single-crystal grown by LFZ [84,89]. However, a substantial reduction of volume fraction (41 vol.% $(Zr,Ca)O_2$) of the conducting phase in DSE materials is necessarily imposed by the eutectic composition [84]. Even through that, the mixed ionic conductor behaviour was not explored, the distinct conductive nature of $(Zr,Ca)O_2$ and $CaZrO_3$ was mentioned [89].

The eutectic composition is effectively a limitation imposed to the DSE ionic conductivity, as illustrated Figure 19a by the higher total ionic conductivity of tetragonal zirconia polycrystalline (TZP) ceramic with respect to $Al_2O_3$-$ZrO_2$(3 mol.% $Y_2O_3$) DSE. Considering this result, the growth rate and composition of directionally solidified $Al_2O_3$-$ZrO_2$(3 mol.% $Y_2O_3$) systems were explored in order to improve the ionic conductivity.

So, the eutectic (33.5 vol.% stabilized-$ZrO_2$) composition were tested along with two off-eutectic $ZrO_2$-rich composition (40,45 vol.% stabilized-$ZrO_2$).

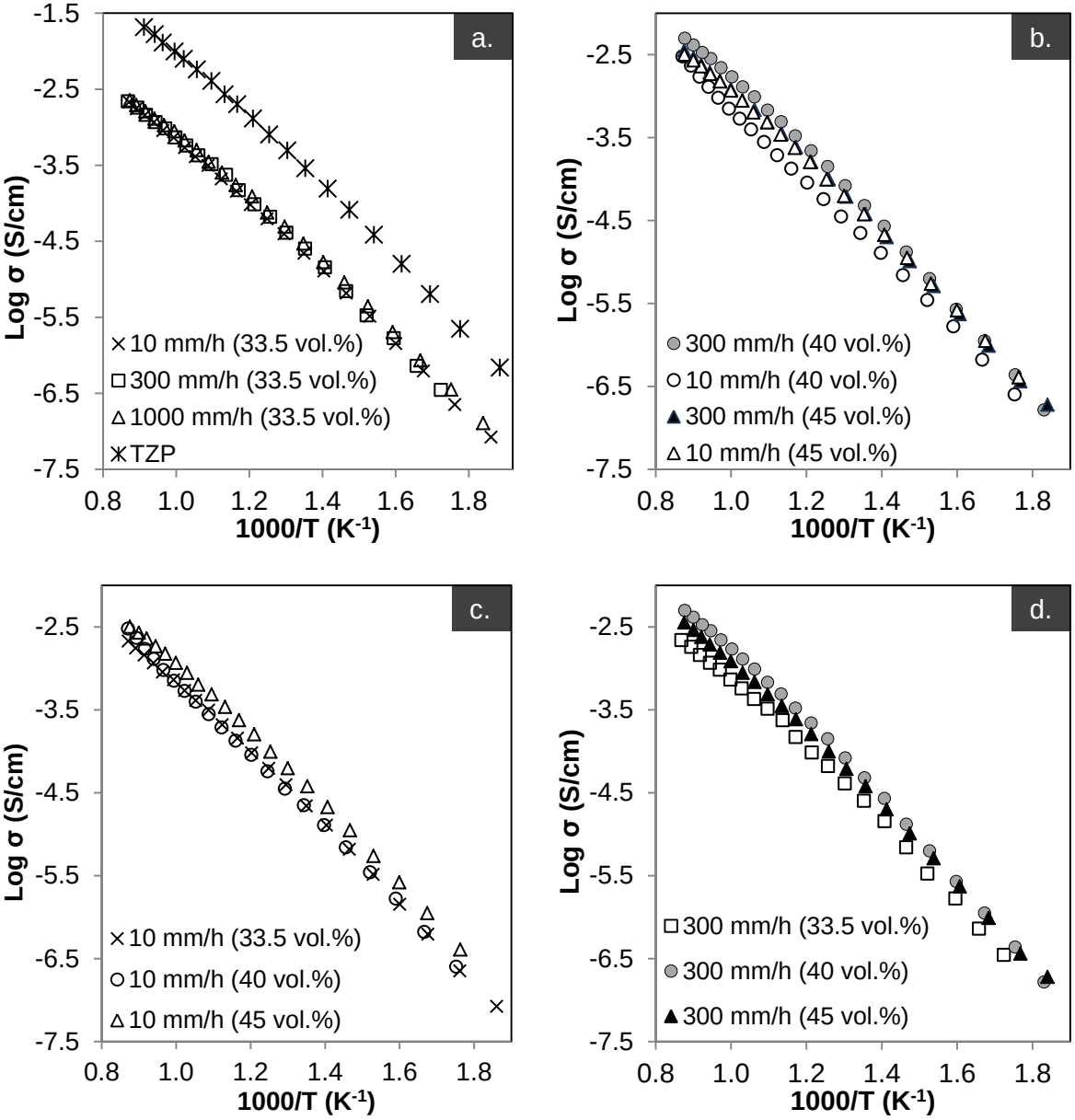


***Figure 19:*** *Arrhenius plots of the conductivity of the LFZ grown samples* ***(a)*** *eutectic composition and total (diamonds) conductivity of TZP ($ZrO_2$-3 mol.% $Y_2O_3$) ceramic,* ***(b)*** *off-eutectic compositions. The influence of grown rate* ***(c)*** *10 mm/h and* ***(d)*** *300 mm/h, adapted from [88].*

Indeed, the conductivity slightly increases with the growth rate, which was ascribed to the anisotropic effect revealed by the elongated profile of zirconia particles along the growth axis. For the fibres grown at the slowest rates (10 mm/h), the ionic conductivity increases sharply (2.8 times, Figs. 19b,c) with the rise of zirconia content (up to 12 vol.%). However, the mandatory $Y_2O_3$ addition to make zirconia an ionic conductor, can contribute as well to

the constitutional undercooling. So, the maximum conductivity was precluded for $ZrO_2$-richest off-eutectic compositions (Figs. 19b,d), due to the reduction of the effective volume contributing to conduction by the development of primary $ZrO_2$-dendrites which are poorly conductive.

The YSZ-$Al_2O_3$ DSEs was assayed as a Nernst glower element, due to the outstanding mechanical strength and the appropriate ionic conductivity [90]. The DSE was preheated to 815 ºC and reached 1600 ºC upon dissipating 14 W, showing suitable thermal shock resistance. After 160 h working, no mechanical damage or conductivity decline was identified. However, the DSE microstructure greatly changed from colony-type to coarsening microstructure. These attempts are very attractive and support the research for other DSE materials, looking for a better conducting electrolyte with thermally and mechanically stable microstructure.

**References**


[1] V.V. Kharton, E.N. Naumovich, A.A. Vecher, Research on the electrochemistry of oxygen ion conductors in the former Soviet Union. I: $ZrO_2$-based ceramic materials, Journal of Solid State Electrochemistry, 3 (1999) 61-81.

[2] V.V. Kharton, F.M.B. Marques, A. Atkinson, Transport properties of solid oxide electrolyte ceramics: a brief review, Solid State Ionics, 174 (2004) 135-149.

[3] N.Q. Minh, T. Takahashi, Science and technology of ceramic fuel cells, Elsevier, New York, 1995.

[4] A.J. Jacobson, Materials for solid oxide fuel cells, Chemistry of Materials, 22 (2010) 660-674.

[5] T. Ishihara, Perovskite oxide for solid oxide fuel cells, Springer, London, 2009.

[6] S.P.S. Badwal, Zirconia-based solid electrolytes: microstructure, stability and ionic conductivity, Solid State Ionics, 52 (1992) 23-32.

[7] V.V. Kharton, Solid state electrochemistry I: fundamentals, materials and their applications, WILEY-VCH Verlag GmbH & Co. KGaA, Weinheim, 2009.

[8] E.C. Subbarao, H.S. Maiti, Solid electrolytes with oxygen ion conduction, Solid State Ionics, 11 (1984) 317-338.

[9] Y.S. Kuzminov, E.E. Lomonova, V.V. Osiko, Cubic zirconia and skull melting, Cambridge International Science Publishing, Cambridge, GBR, 2008.

[10] T. Tojo, H. Kawaji, T. Atake, T. Mori, H. Yamamura, Proceedings of the 1st International discussion meeting on superionic conductor physics, World Scientific Publishing Co. Pte. Ltd., Japan, 2003, 129-134.

[11] F. Gallino, C. Di Valentin, G. Pacchioni, Band gap engineering of bulk $ZrO_2$ by Ti doping, Physical Chemistry Chemical Physics, 13 (2011) 17667-17675.
[12] J. Chevalier, L. Gremillard, A.V. Virkar, D.R. Clarke, The Tetragonal-monoclinic transformation in zirconia: lessons learned and future trends, Journal of the American Ceramic Society, 92 (2009) 1901-1920.
[13] C. Viazzi, J.-P. Bonino, F. Ansart, A. Barnabe, Structural study of metastable tetragonal YSZ powders produced via a sol-gel route, Journal of Alloys and Compounds, 452 (2008) 377-383.
[14] K.H. Stern, Metallurgical and ceramic protective coatings, Chapman & Hall, Glasgow, 1996.
[15] G. Dhanaraj, K. Byrappa, V. Prasad, M. Dudley, Springer handbook of crystal growth, Springer, New York, 2010.
[16] Y. Arachi, H. Sakai, O. Yamamoto, Y. Takeda, N. Imanishai, Electrical conductivity of the $ZrO_2$–$Ln_2O_3$ (Ln=lanthanides) system, Solid State Ionics, 121 (1999) 133-139.
[17] K.D. Kreuer, Proton-conducting oxides, Annual Review of Materials Research, 33 (2003) 333-359.
[18] C. Peters, Grain-size effects in nanoscaled electrolyte and cathode thin films for solid oxide fuel cells (SOFC), KIT Scientific Publishing, Karlsruhe, 2008.
[19] J.B. Goodenough, Oxide-ion electrolytes, Annual Review of Materials Research, 33 (2003) 91-128.
[20] G. Cao, C.J. Brinker, Annual review of nano research, World Scientific Publishing Co. Pte. Ltd., Singapore, 2008.
[21] J.E. Bauerle, Study of solid electrolyte polarization by a complex admittance method, J. Phys. Chem. Solids, 30 (1969) 2657-2670.
[22] X. Guo, J. Maier, Grain boundary blocking effect in zirconia: A Schottky barrier analysis, Journal of the Electrochemical Society, 148 (2001) E121-E126.
[23] T.v. Dijk, A.J. Burggraaf, Grain-boundary effects on ionic-conductivity in ceramic $Gd_xZr_{1-x}O_{2-(x/2)}$ solid-solutions, Physica Status Solidi a-Applied Research, 63 (1981) 229-240.
[24] X. Guo, R. Waser, Electrical properties of the grain boundaries of oxygen ion conductors: acceptor-doped zirconia and ceria, Progress in Materials Science, 51 (2006) 151-210.
[25] S.P. Jiang, Y. Yan, Materials for high-temperature fuel cells, Wiley-VCH Verlag GmbH & Co. KGaA, Weinheim, 2013.

[26] S.C. Singhal, K. Kendall, High temperature solid oxide fuel cells: fundamentals, design and applications, Elsevier, New York, 2003.
[27] C.K. Dyer, P.T. Moseley, Z. Ogumi, D.A.J. Rand, B. Scrosati, Encyclopedia of electrochemical power sources, Elsevier Science, 2010.
[28] D.S. Ginley, H. Hosono, D.C. Paine, Handbook of transparent conductors, Springer, New York, 2010.
[29] H. Iwahara, T. Esaka, H. Uchida, N. Maeda, Proton conduction in sintered oxides and its application to steam electrolysis for hydrogen-production, Solid State Ionics, 3-4 (1981) 359-363.
[30] H. Iwahara, H. Uchida, N. Maeda, High-temperature fuel and steam electrolysis cells using proton conductive solid electrolytes, Journal of Power Sources, 7 (1982) 293-301.
[31] H. Uchida, N. Maeda, H. Iwahara, Steam concentration cell using a high-temperature type proton conductive solid electrolyte, Journal of Applied Electrochemistry, 12 (1982) 645-651.
[32] H. Uchida, N. Maeda, H. Iwahara, Relation between proton and hole conduction in srceo3-based solid electrolytes under water-containing atmospheres at high-temperatures, Solid State Ionics, 11 (1983) 117-124.
[33] H. Iwahara, H. Uchida, S. Tanaka, high-temperature type proton conductor based on $SrCeO_3$ and its application to solid electrolyte fuel-cells, Solid State Ionics, 9-10 (1983) 1021-1025.
[34] H. Iwahara, T. Esaka, H. Uchida, T. Yamauchi, K. Ogaki, High-temperature type protonic conductor based on $SrCeO_3$ and its application to the extraction of hydrogen gas, Solid State Ionics, 18-9 (1986) 1003-1007.
[35] T. Ishigaki, S. Yamauchi, K. Kishio, K. Fueki, H. Iwahara, Dissolution of deuterium into proton conductor $SrCe_{0.95}Yb_{0.05}O_{3-\delta}$, Solid State Ionics, 21 (1986) 239-241.
[36] A.N. Virkar, H.S. Maiti, Oxygen ion conduction in pure and yttria-doped barium cerate, Journal of Power Sources, 14 (1985) 295-303.
[37] H. Uchida, K. Ogaki, H. Iwahara, high-temperature hydrogen sensor and steam sensor using $BaCeO_3$-based proton conducting ceramics, Journal of the Electrochemical Society, 134 (1987) C522-C522.
[38] H. Iwahara, H. Uchida, K. Ono, K. Ogaki, Proton conduction in sintered oxides based on $BaCeO_3$, Journal of the Electrochemical Society, 135 (1988) 529-533.
[39] T. Hibino, K. Mizutani, T. Yajima, H. Iwahara, Evaluation of proton conductivity in $SrCeO_3$, $BaCeO_3$, $CaZrO_3$ and $SrZrO_3$ by temperature programmed desorption method, Solid State Ionics, 57 (1992) 303-306.

[40] A. Mitsui, M. Miyayama, H. Yanagida, Evaluation of the activation-energy for proton conduction in perovskite-type oxides, Solid State Ionics, 22 (1987) 213-217.
[41] H. Iwahara, T. Yajima, T. Hibino, K. Ozaki, H. Suzuki, Protonic conduction in calcium, strontium and barium zirconates, Solid State Ionics, 61 (1993) 65-69.
[42] T. Matsui, Thermodynamic properties of ternary barium oxides, Thermochimica Acta, 253 (1995) 155-165.
[43] V.P. Gorelov, V.B. Balakireva, Y.N. Kleshchev, V.P. Brusentsov, Preparation and electrical conductivity of $BaZr_{1-x}R_xO_{3-\alpha}$ (R = Sc, Y, Ho, Dy, Gd, In), Inorganic Materials, 37 (2001) 535-538.
[44] M.W. Barsoum, Fundamentals of ceramics, Institute of Physics Publishing, Philadelphia, 2003.
[45] S. Yamanaka, M. Fujikane, T. Hamaguchi, H. Muta, T. Oyama, T. Matsuda, S.-i. Kobayashi, K. Kurosaki, Thermophysical properties of $BaZrO_3$ and $BaCeO_3$, Journal of Alloys and Compounds, 359 (2003) 109-113.
[46] W. Martienssen, H. Warlimont, Springer handbook of condensed matter and materials data, Springer, New York, 2005.
[47] J.B. Wachtman, W.R. Cannon, M.J. Matthewson, Mechanical properties of ceramics, John Wiley & Sons, Inc., New Jersey, 2009.
[48] K.D. Kreuer, S. Adams, W. Münch, A. Fuchs, U. Klock, J. Maier, Proton conducting alkaline earth zirconates and titanates for high drain electrochemical applications, Solid State Ionics, 145 (2001) 295-306.
[49] H.G. Bohn, T. Schober, Electrical Conductivity of the high-temperature proton conductor $BaZr_{0.9}Y_{0.1}O_{2.95}$, Journal of the American Ceramic Society, 83 (2000) 768-772.
[50] A.V. Shevchenko, L.M. Lopato, G.I. Gerasimyuk, Z.A. Zaitseva, Reactions in the system $HfO_2$-SrO, $HfO_2$-BaO, and $ZrO_2$-BaO in high $HfO_2$ or $ZrO_2$ regions, Inorganic Materials, 23 (1987) 1322-1325.
[51] J.O.A. Paschoal, H. Kleykamp, F. Thümmler, Phase equilibria in the pseudoquaternary BaO-$UO_2$-$ZrO_2$-$MoO_2$ system, Journal of Nuclear Materials, 151 (1987) 10-21.
[52] A. Kuz'min, V. Balakireva, S. Plaksin, V. Gorelov, Total and hole conductivity in the $BaZr_{1-x}Y_xO_{3-\alpha}$ system (x=0.02−0.20) in oxidizing atmosphere, Russian Journal of Electrochemistry, 45 (2009) 1351-1357.
[53] E. Fabbri, D. Pergolesi, S. Licoccia, E. Traversa, Does the increase in Y-dopant concentration improve the proton conductivity of $BaZr_{1-x}Y_xO_{3-\delta}$ fuel cell electrolytes, Solid State Ionics, 181 (2010) 1043-1051.

[54] V. Gorelov, V. Balakireva, A. Kuz'min, Ionic, proton, and oxygen conductivities in the $BaZr_{1-x}Y_xO_{3-\alpha}$ system (x =0.02−0.15) in humid air, Russian Journal of Electrochemistry, 46 (2010) 890-895.

[55] M.E. Bjorketun, P.G. Sundell, G. Wahnstrom, Effect of acceptor dopants on the proton mobility in $BaZrO_3$: A density functional investigation, Physical Review B, 76 (2007).

[56] D. Pergolesi, E. Fabbri, A. D'Epifanio, E. Di Bartolomeo, A. Tebano, S. Sanna, S. Licoccia, G. Balestrino, E. Traversa, High proton conduction in grain-boundary-free yttrium-doped barium zirconate films grown by pulsed laser deposition, Nature Materials, 9 (2010) 846-852.

[57] F. Iguchi, N. Sata, H. Yugami, Proton transport properties at the grain boundary of barium zirconate based proton conductors for intermediate temperature operating SOFC, Journal of Materials Chemistry, 20 (2010) 6265-6270.

[58] F. Iguchi, N. Sata, T. Tsurui, H. Yugami, Microstructures and grain boundary conductivity of $BaZr_{1-x}Y_xO_3$ (x=0.05, 0.10, 0.15) ceramics, Solid State Ionics, 178 (2007) 691-695.

[59] A.V. Virkar, Transport through mixed proton, oxygen ion and electron (hole) conductors: Goldman-Hodgkin-Katz type equation, Journal of Power Sources, 194 (2009) 753-762.

[60] N.O. Taniguchi, JP), Niikura, Junji (Hirakata, JP), Hatoh, Kazuhito (Daitou, JP), Gamo, Takaharu (Fujiidera, JP), Mixed ionic conductors, Matsushita Electric Industrial Co., Ltd. (Osaka, JP), United States, 1995.

[61] N.O. Taniguchi, JP), Mixed ion conductor, Matsushita Electric Industrial Co., Ltd. (Osaka, JP), United States, 2008.

[62] M.S. Islam, P.R. Slater, J.R. Tolchard, T. Dinges, Doping and defect association in $AZrO_3$ (A=Ca, Ba) and $LaMO_3$ (M=Sc, Ga) perovskite-type ionic conductors, Dalton Transactions, 0 (2004) 3061-3066.

[63] A.V. Virkar, Transport of $H_2$, $O_2$ and $H_2O$ through single-phase, two-phase and multiphase mixed proton, oxygen ion, and electron hole conductors, Solid State Ionics, 140 (2001) 275-283.

[64] K. Nomura, H. Kageyama, Transport properties of $Ba(Zr_{0.8}Y_{0.2})O_{3-\delta}$ perovskite, Solid State Ionics, 178 (2007) 661-665.

[65] T. A. Ramanarayanan, Wayne L. Worrell, Harry L. Tuller, Proceedings of the 2nd International Symposium on Ionic and mixed conducting ceramics, The Electrochemical Society Inc., 1994.

[66] N. Taniguchi, K. Hatoh, J. Niikura, T. Gamo, H. Iwahara, Proton conductive properties of gadolinium-doped barium cerates at high temperatures, Solid State Ionics, 53 (1992) 998-1003.
[67] H. Iwahara, T. Yajima, H. Ushida, Effect of ionic radii of dopants on mixed ionic conduction ($H^+$+$O^{2-}$) in $BaCeO_3$-based electrolytes, Solid State Ionics, 70-71, Part 1 (1994) 267-271.
[68] T. Yajima, H. Iwahara, H. Uchida, Protonic and oxide ionic conduction in $BaCeO_3$-based ceramics - effect of partial substitution for Ba in $BaCe_{0.9}O_{3-\alpha}$ with Ca, Solid State Ionics, 47 (1991) 117-124.
[69] H. Iwahara, Oxide-ionic and protonic conductors based on perovskite-type oxides and their possible applications, Solid State Ionics, 52 (1992) 99-104.
[70] H. Iwahara, T. Yajima, T. Hibino, H. Ushida, Performance of solid oxide fuel-cell using proton and oxide-ion mixed conductors based on $BaCe_{1-X}Sm_XO_{3-\alpha}$, Journal of the Electrochemical Society, 140 (1993) 1687-1691.
[71] N. Bonanos, B. Ellis, K.S. Knight, M.N. Mahmood, Ionic conductivity of gadolinium-doped barium cerate perovskites, Solid State Ionics, 35 (1989) 179-188.
[72] D. Lybye, N. Bonanos, Proton and oxide ion conductivity of doped $LaScO_3$, Solid State Ionics, 125 (1999) 339-344.
[73] W. Wang, A.V. Virkar, Ionic and electron-hole conduction in $BaZr_{0.93}Y_{0.07}O_{3-\delta}$ by 4-probe dc measurements, Journal of Power Sources, 142 (2005) 1-9.
[74] V. Gorelov, V. Balakireva, Synthesis and properties of high-density protonic solid electrolyte $BaZr_{0.9}Y_{0.1}O_{3-\alpha}$, Russian Journal of Electrochemistry, 45 (2009) 476-482.
[75] T. Schober, H. Ringel, Proton conducting ceramics: Recent advances, Ionics, 10 (2004) 391-395.
[76] B. Zhu, M.D. Mat, Studies on dual phase ceria-based composites in electrochemistry, International Journal of Electrochemical Science, 1 (2006) 383-402.
[77] D. Medvedev, V. Maragou, E. Pikalova, A. Demin, P. Tsiakaras, Novel composite solid state electrolytes on the base of $BaCeO_3$ and $CeO_2$ for intermediate temperature electrochemical devices, Journal of Power Sources, 221 (2013) 217-227.
[78] W. Sun, Y. Jiang, Y. Wang, S. Fang, Z. Zhu, W. Liu, A novel electronic current-blocked stable mixed ionic conductor for solid oxide fuel cells, Journal of Power Sources, 196 (2011) 62-68.
[79] M. Khandelwal, A. Venkatasubramanian, T.R.S. Prasanna, P. Gopalan, Correlation between microstructure and electrical conductivity in composite electrolytes containing

Gd-doped ceria and Gd-doped barium cerate, Journal of the European Ceramic Society, 31 (2011) 559-568.
[80] B. Zhu, X. Liu, T. Schober, Novel hybrid conductors based on doped ceria and BCY20 for ITSOFC applications, Electrochemistry Communications, 6 (2004) 378-383.
[81] Y. Oyama, A. Kojima, X. Li, R.B. Cervera, K. Tanaka, S. Yamaguchi, Phase relation in the $BaO$-$ZrO_2$-$YO_{1.5}$ system: Presence of separate $BaZrO_3$ phases and complexity in phase formation, Solid State Ionics, 197 (2011) 1-12.
[82] S. Imashuku, T. Uda, Y. Nose, Y. Awakura, To journal of phase equilibria and diffusion phase relationship of the $BaO$-$ZrO_2$-$YO_{1.5}$ system at 1500 and 1600 ºC, Journal of Phase Equilibria and Diffusion, 31 (2010) 348-356.
[83] V.M. Orera, R.I. Merino, J.A. Pardo, A. Larrea, J.I. Peña, C. González, P. Poza, J.Y. Pastor, J. Llorca, Microstructure and physical properties of some oxide eutectic composites processed by directional solidification, Acta Materialia, 48 (2000) 4683-4689.
[84] J. Llorca, V.M. Orera, Directionally solidified eutectic ceramic oxides, Progress in Materials Science, 51 (2006) 711-809.
[85] R.I. Merino, J.I. Peña, V.M. Orera, G.F. de la Fuente, Conductivity anisotropy in directionally solidified $CaZrO_3$-CaSZ and MgO-MgSZ eutectics, Solid State Ionics, 100 (1997) 313-318.
[86] V. Trnovcová, M. Starostin, V. Labas, R. Cicka, Microstructure and physical properties of directionally solidified alumina-zirconia eutectic composites, Ionics, 4 (1998) 275-284.
[87] V. Trnovcová, P.P. Fedorov, Č. Bárta, V. Labaš, V.A. Meleshina, B.P. Sobolev, Microstructure and physical properties of superionic eutectic composites of the $LiF$–$RF_3$ (R=rare earth element) system, Solid State Ionics, 119 (1999) 173-180.
[88] R.I. Merino, I. de Francisco, J.I. Peña, Ionic conductivity in directionally solidified $Al_2O_3$-$ZrO_2$(3% mol $Y_2O_3$) near eutectic composites, Solid State Ionics, 178 (2007) 239-247.
[89] J.I. Peña, R.I. Merino, G.F.d.l. Fuente, V.M. Orera, Aligned $ZrO_2$(c)-$CaZrO_3$ eutectics grown by the laser floating zone method: electrical and optical properties, Advanced Materials, 8 (1996) 909-912.
[90] R.I. Merino, J.I. Peña, Á. Larrea, G.F.d.l. Fuente, V.M. Orera, Melt grown composite ceramics obtained by directional solidification: structural and functional applications, Recent Research Developments in Materials Science, 4 (2003) 1-24.

## II.2.Laser melting processing of $ZrO_2$-$BaZrO_3$ ceramic eutectics

R.G. Carvalho[1], F.M. Figueiredo[2], A.J.S. Fernandes[1], R.F. Silva[2], F.M. Costa[1]

[1]I3N, Department of Physics, University of Aveiro, 3810-193 Aveiro, Portugal
[2]CICECO, Department of Ceramic and Materials Engineering, University of Aveiro 3810-193 Aveiro, Portugal

Science of Advanced Materials, 5 (2013) 1847-1856
**DOI:** http://dx.doi.org/10.1166/sam.2013.1650

### Abstract

Ceramic composites based on zirconia and barium zirconate are expected to possess good thermomechanical properties and mixed ionic (protons and oxide ions) transport properties. However, their processing by conventional sintering is difficult due to their refractoriness. This work reports on the processing of a directionally solidified yttrium-doped $ZrO_2$-$BaZrO_3$ eutectic by the laser floating zone (LFZ) method, with a focus on the effect of growth rates between 20 mm/h and 100 mm/h. X-ray diffraction and Raman spectroscopy data confirmed the presence of tetragonal $ZrO_2$ and cubic $BaZrO_3$ phases. Scanning electron microscopy reveals a fine eutectic microstructure, changing from coupled to colony-type morphology with increasing growth rate. Periodically spaced bands with a coarse eutectic microstructure are also observed. X-ray energy dispersive spectroscopy shows that the yttrium tends to occupy the $ZrO_2$ lattice. Both $ZrO_2$ and $BaZrO_3$ phases display contiguity without interphase boundaries, according to impedance spectroscopy data. It is further shown that the ionic conductivity of the fibres is not influenced by the water vapour partial pressure, and it is slightly lower ($9.7 \times 10^{-3}$ S/cm at 824 ºC) than for pure YSZ $(ZrO_2)_{0.97}(Y_2O_3)_{0.03}$ ($1.6 \times 10^{-2}$ S/cm at 800 ºC). These results suggest that oxide ion transport through zirconia dominates the conduction mechanism, in agreement with the observed preferential location of yttrium in the zirconia phase.

***Keywords:*** $BaZrO_3$, $ZrO_2$, eutectic, directional solidification, electrical properties.

## II.2.1. Introduction

Zirconia-based ceramics, particularly yttrium-doped zirconia, $(Zr,Y)O_2$, are well established engineering materials due to an unusual combination of high ionic conductivity, mechanical strength, fracture toughness, thermal insulation and refractoriness. The application of these materials as the functional core of gas sensors, fuel cells and thermal barrier coatings are established markets [1]. However, they still suffer from important drawbacks. For example, the limited resistance to thermal cycling (due to phase transformations) and corrosion problems (due to excessive oxide ion conduction) of yttrium-doped zirconia when applied as a thermal barrier [2]. Several alternatives to $(Zr,Y)O_2$ for application as thermal barrier have indeed been suggested [2], including the zirconates $SrZrO_3$, $La_2Zr_2O_7$, and $BaZrO_3$ [3]. These authors reported that the $BaZrO_3$ coatings are not very resistant to thermal cycling due to BaO loss, but it has been later defended that the thermal shock resistance of yttrium-doped zirconia thermal barriers can be enhanced by a $(Zr,Y)O_2$-$BaZrO_3$ composite protective coating deposited by plasma spray [4].

From a fuel cell and related applications perspective, current efforts are made towards reduction of the operating temperature of the device by exploiting new material combinations or designs [5-7]. The high oxide ion conductivity of $(Zr,Y)O_2$ (0.1 S/cm) is available only at temperatures close to 1000 °C, being considered an important limitation to the use of zirconia solid electrolytes in devices operating below 800 °C [5,8]. Ceramic proton conductors with a perovskite-type structure ($ABO_3$), such as barium zirconate ($BaZrO_3$), having high protonic conductivity at moderate temperatures (450 - 650 ºC) and possessing good chemical stability and high mechanical strength, are considered very promising candidates [9-12]. The combination of such proton conducting ceramic with an oxide ion conductor such as $(Zr,Y)O_2$ is a potentially interesting approach for the development of composite mixed ionic solid electrolytes for electrochemical applications such as fuel cells, electrolyzers or sensors able to operate in a broad range of conditions, namely temperature [13-15].

However, both the zirconia and the barium zirconate demand for high sintering temperatures, with $BaZrO_3$ being particularly difficult to produce as a dense ceramics, requiring sintering temperatures as high as 1700 °C [12]. The $ZrO_2$-$BaZrO_3$ phase diagram presents a eutectic transformation that can be advantageously used for the synthesis of this composite by solidification from the melt. The literature is contradicting on the exact eutectic composition, reported to occur at 2240 °C for 50 mol.% $BaZrO_3$:50 mol.% $ZrO_2$ [16] or, very distinctly, at 2050 °C for 29 mol.% $BaZrO_3$:71 mol.% $ZrO_2$ [17]. Regardless of the actual composition, this type of eutectics belongs to an important class of multiphase ma-

terials with unique morphology outcoming from their single solidification procedure, where a cooperative growth of two solid phases from a liquid takes place.

These oxides, however, are extremely refractory ($ZrO_2$ melts at 2720 ºC, and $BaZrO_3$ at ~2620 ºC) precluding conventional melting in a crucible. The laser floating zone (LFZ) method is often used to obtain directional solidification eutectic (DSE) oxide materials, yielding multiphase microstructures with preferential grain alignment [18-20]. The large thermal gradient employed at the solidification interface yields typical microstructures consisting of interpenetrating columnar grains of both eutectic phases. This is favourable for electrical percolation, and has the added benefit of minimizing the formation of grain boundaries in the conducting phase [18,19]. The latter may be an important advantage over conventional polycrystalline ceramics, where electrically resistive grain boundaries contribute in large measure to the overall high resistance at low temperatures (300-700 °C) measured for $(Zr,Y)O_2$ (with 3 mol.% $Y_2O_3$) [7,21], and particularly for $Ba(Zr,Y)O_3$ [12]. The investigation of DSE produced by LFZ has already been reported for several zirconia-based materials, including $Al_2O_3$-$ZrO_2$, NiO-$ZrO_2$, MgO-$ZrO_2$ and CaO-$ZrO_2$ [18,19,22,23], but not for $ZrO_2$-$BaZrO_3$, at least to the best of our knowledge.

In this study we describe the development of $(Zr,Y)O_2$-$BaZrO_3$ composite fibres processed by LFZ. A detailed structural and morphological characterization is presented in order to understand the influence of the growth conditions on the microstructural features of the composites. These are, on a second part of the paper, correlated with the electrical properties measured by impedance spectroscopy under variable temperature and in dry and wet atmospheres.

### II.2.2. Experimental

The LFZ apparatus (previously described in [24]) comprises a continuous excited double tube 200 W $CO_2$ laser working in the $TEM_{00}$ mode (Spectron-GSI group) and a reflexicon mirror to convert the original cylindrical laser beam to a circular crown shape. The fibres were grown from rods of $BaCO_3$ (Flucka 99%) and $(ZrO_2)_{0.97}(Y_2O_3)_{0.03}$ (Tosho Co.) in molar fractions of 0.25 and 0.75, respectively (nominal molar composition 24.9% $BaCO_3$ - 71.7% $ZrO_2$ - 4.4% $YO_{1.5}$). This composition corresponds to the eutectic $BaZrO_3$-$ZrO_2$ reported by Shevchenko et al. [16] (50 mol.% $BaZrO_3$:50 mol.% $ZrO_2$), which has an excess of BaO with respect to that suggested by Paschoal et al. [17] (29 mol.% $BaZrO_3$:71 mol.% $ZrO_2$). However, stoichiometric deviations resulting from BaO volatilization due to the proximity between the melting and boiling temperatures of this oxide were predictable.

This was, as shown ahead, a correct assumption since our results confirm the phase diagram by Paschoal and co-authors. The rods with ~1.4 mm in diameter were obtained by cold extrusion of mixtures of the precursor powders (dry milled for 1h30m) and polyvinyl alcohol (PVA) as binder (Sigma-Aldrich 99%, hydrolyzed).

Figure 1 shows snapshots obtained with a CCD camera of the early stages of the LFZ process. The seed and the feed rods are aligned (Fig. 1a) before melting (Figs. 1b,c). Both tips contract at this point due to decomposition of the binder (Fig. 1d), which is when the laser power is increased (Fig. 1e) until both molten zones are joined (Fig. 1f). After stabilizing the molten zone, the fibre is pulled downwards at variable rate (20, 50 and 100 mm/h), always in air. The feed/seed pulling rates were independently controlled in the range 2/1 to 3/1 to maintain a constant fibre diameter, with both rods rotating at 5 rpm in opposite directions.

The structural characterization was performed by X-ray diffraction (XRD) with a Rigaku Geigerflex diffractometer, Cu-$K_\alpha$ radiation, step width 0.02°, from 4 to 80° and with a scan rate of 3° $min^{-1}$), and by Raman spectroscopy using a Horiba Jobin Yvon HR800 system (with a laser wavelength of 532 nm). The microstructures of transverse and longitudinal fibre sections were observed on polished surfaces by scanning electron microscopy (SEM) and energy dispersive X-ray spectroscopy (EDS) on a Hitachi S4100 microscope. SEM images were analyzed with the Image J 1.45s software [25] to measure the fractional area occupied by each phase.

Impedance spectroscopy was used to evaluate the electrical conductivity in dry and wet atmospheres of air and of a 95%$N_2$+5%$H_2$ gas mixture, always under variable temperature from 350 to 1000 °C. The nominal dry atmospheric conditions were obtained by flowing 50 mL/min of the gas through a column with a desiccating agent. Alternatively, the same flow was humidified through another column containing distilled water at a room temperature, with a corresponding water vapour pressure of ~3.5 kPa. The oxygen partial pressure inside the chamber was monitored by means of an (Zr,Y)$O_2$ potentiometric sensor, whereas the water vapour partial pressure was monitored at the exit of the chamber by means of a resistive humidity sensor. The measured fibre pieces were cut to around 5 mm in length from the central part of the grown fibres. Afterwards, electrodes were applied to the tips with a platinum paste followed by a thermal treatment at 1000 ºC for one hour (to ensure the necessary mechanical stability of the electrodes). The spectra were collected with a Hewlett Packard 4984a LCR meter in the frequency range from 20 Hz to 1 MHz and with test signal amplitudes of 0.1, 0.5 and 1.0 V.

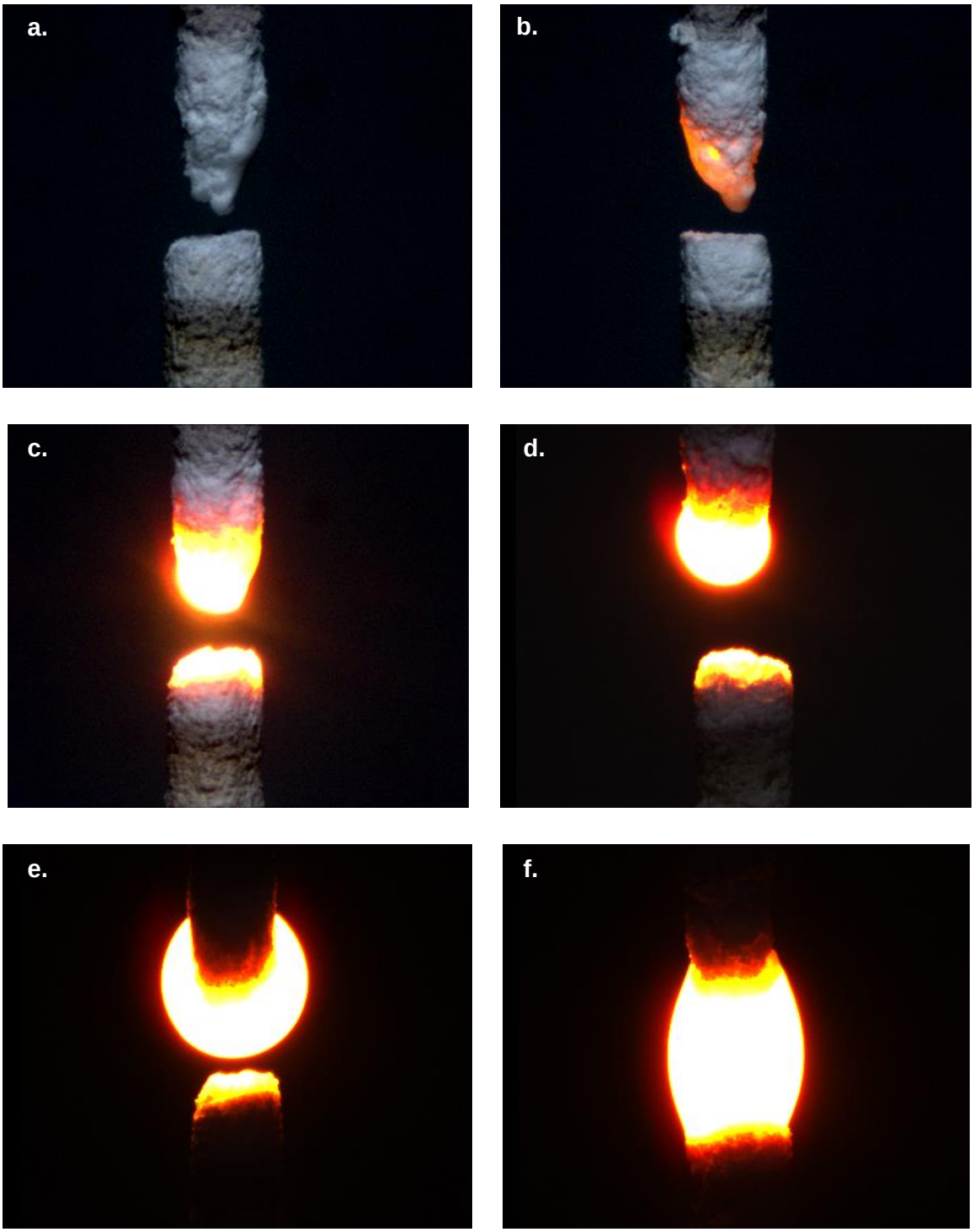


***Figure 1:*** *Snapshots obtained with a CCD camera of the initial growth stages of the $ZrO_2$-$BaZrO_3$ fibres by the LFZ method:* ***(a)*** *alignment of seed (bottom) and feed (top) rods;* ***(b)*** *feed melting;* ***(c)*** *seed and feed melting;* ***(d)*** *contraction of the tops due to PVA decomposition;* ***(e)*** *increasing of laser power and rods approximation;* ***(f)*** *joining of molten zones.*

### II.2.3. Results and discussion

#### II.2.3.1. Fibre appearance and structural characterization

Figure 2 shows the typical appearance of the $ZrO_2$-$BaZrO_3$ ceramic fibres obtained by the LFZ process with lengths up to 25 mm and diameters in the range 1.1-1.4 mm. Surface striations perpendicular to the fibre axis are visible in the macrograph, as observed in other directionally solidified ceramic systems [24]. Such growth striations are due to the thermal asymmetry of the molten zone resulting from the displacement of the rotation axis from the thermal centre.

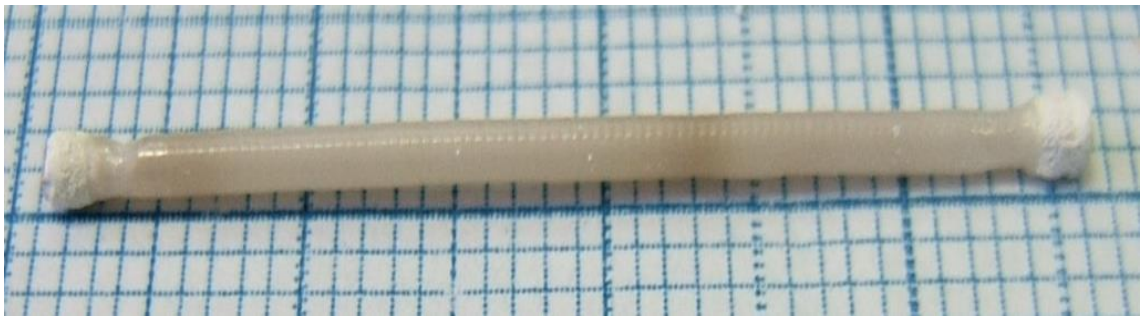

***Figure 2:*** *$ZrO_2$-$BaZrO_3$ fibre grown at 100 mm/h by the LFZ method.*

The XRD analysis of powdered fibres confirms the presence of the expected mixture of cubic $BaZrO_3$ ($Fm\bar{3}m$ space group, JCPDS card file 01-072-7548) and tetragonal $ZrO_2$ ($P4_2/nmc$ space group, JCPDS card file 01-088-1007) phases, as shown by the patterns in Figure 3. It is interesting to note that the tetragonal structure of the $(ZrO_2)_{0.97}(Y_2O_3)_{0.03}$ precursor is retained after melting, with no obvious precipitation of the monoclinic polymorph in the fibres. This series of XRD patterns also suggests that the growth rate does not have a significant influence on the phase nature of the fibres. However, it is apparent that the ratio between the XRD intensity of the $BaZrO_3$ (211) and $ZrO_2$ (112) reflections increases with increasing pulling rate, suggesting an increase of the $BaZrO_3$ fraction due to the reduction of the time for barium evaporation.

Figure 4a shows the Raman spectra obtained for fibres grown at different pulling rates. The improved signal-to-noise ratio and the narrower, better defined peaks observed in the spectra obtained for the fibres grown at slow rate suggest a higher crystallinity for these samples. The spectra were acquired at the polished longitudinal and transversal cross-sections, in order to evaluate the fibres anisotropy. However, no clear evidence of anisotropy was observed, since the $ZrO_2$ Raman signal dominates and this phase is randomly distributed. Therefore, only the data from the transversal configuration were systematically

considered, along which the good homogeneity was verified. The main bands correspond to six theoretically Raman-active modes for the tetragonal phase of zirconia ($A_{1g}$ at 602 $cm^{-1}$, $2B_{1g}$ at 319 and 648 $cm^{-1}$, and $3E_g$ at 149, 269 and 461 $cm^{-1}$) [26], as depicted in the inset of Figure 4b for a fibre grown at 100 mm/h. The weak Raman contributions at 208 and 751 $cm^{-1}$ were assigned to $BaZrO_3$ [27,28]. According to the literature, no first-order Raman scattering is expected for cubic perovskite structures (space group $Pm\bar{3}m$) [27-29].

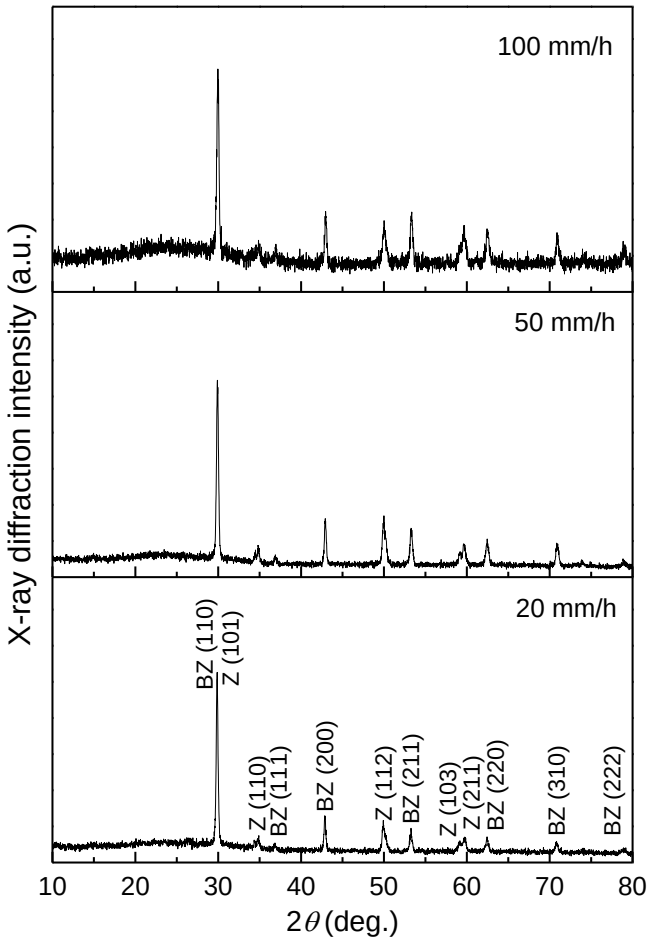


***Figure 3:*** *X-ray diffraction patterns of $ZrO_2$-$BaZrO_3$ eutectic fibres grown at 20, 50 and 100 mm/h. BZ and Z are acronyms of $BaZrO_3$ and tetragonal $ZrO_2$, respectively.*

However, local structural distortions (dopant incorporation, existence of oxygen vacancies, etc.) break the selection rules thus allowing the observation of several Raman bands [28]. In this case, two main distinct regions can be observed in the $BaZrO_3$ spectrum: i) up to 250 $cm^{-1}$, involving the cationic network and the lattice vibration modes; ii) up to 800 $cm^{-1}$, featuring bending (300-500 $cm^{-1}$) and stretching (above 600 $cm^{-1}$) modes of the $ZrO_6$ octahedron [29]. Although the remaining band at 691$cm^{-1}$ cannot be definitely assigned, it may correspond to the weak right "shoulder" ($B_{1g}$ at 638 $cm^{-1}$) observed in tetragonal $ZrO_2$ [30,31].

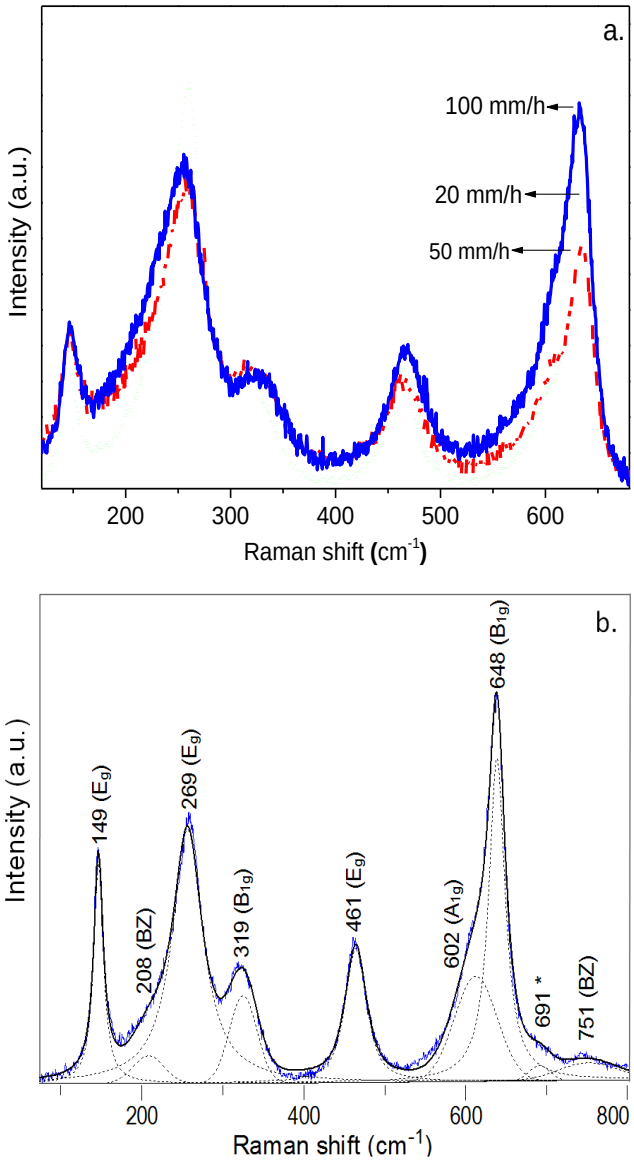


***Figure 4:*** ***(a)*** *Raman spectra (normalized to the 149 cm$^{-1}$ band) obtained at the transversal cross-sections of $ZrO_2$-$BaZrO_3$ eutectic fibres grown at 20, 50 and 100 mm/h.* ***(b)*** *Typical fitting of a 100 mm/h fibre spectrum, based on Gauss-Lorentzian functions after linear background removal (LabSpec 5.25 software). BZ - $BaZrO_3$ phase, * - non identified band and the remaining bands ascribe to the tetragonal $ZrO_2$ phase.*

### II.2.3.2. Solidification bands

The directional growth process of fibres with $ZrO_2$-$BaZrO_3$ eutectic composition leads to the occurrence of solidification bands appearing as dark lines in the low magnification SEM views of longitudinal sections shown in Figure 5a to c. These quasi-periodic microstructural features extend from the periphery of the fibre to the centre in a convex shape similar to the solidification front. In longitudinal sections, the distance between consecutive bands is a function of the pulling rate. The band inter-distance in fibres grown at 20, 50 and 100 mm/h, is ~85, ~155 and ~325 $\mu$m, respectively, closely matching the solidified length per one turn of the eutectic rod [32]. These solidification bands are also observed in transversal sections, in the form of spirals (Fig. 5d).

Banding phenomenon has been extensively studied mainly for metallic systems [33,34], where they are identified by quasi-periodic structures that develop parallel to the moving solidification front, consisting of alternating regions with different microstructure or composition, or both features simultaneously [33]. Banding was observed both at low (e.g. welding) and rapid (e.g. melt spinning) solidification processing. Externally driven (due to the solidification technique) or internally driven (from the solidifying system) causes are beneath the phenomenon. Under the relatively low solidification rates of the present system, external causes prevail and the progression velocity of the solid-liquid interface is smaller than the velocity of the unstable flow [33]. These instabilities may arise from periodic perturbations in the melt driven by buoyancy convection or by the surface energy Marangoni flow [33]. In LFZ processing, laser power fluctuations and axis misalignments may also contribute to the phenomenon [35].

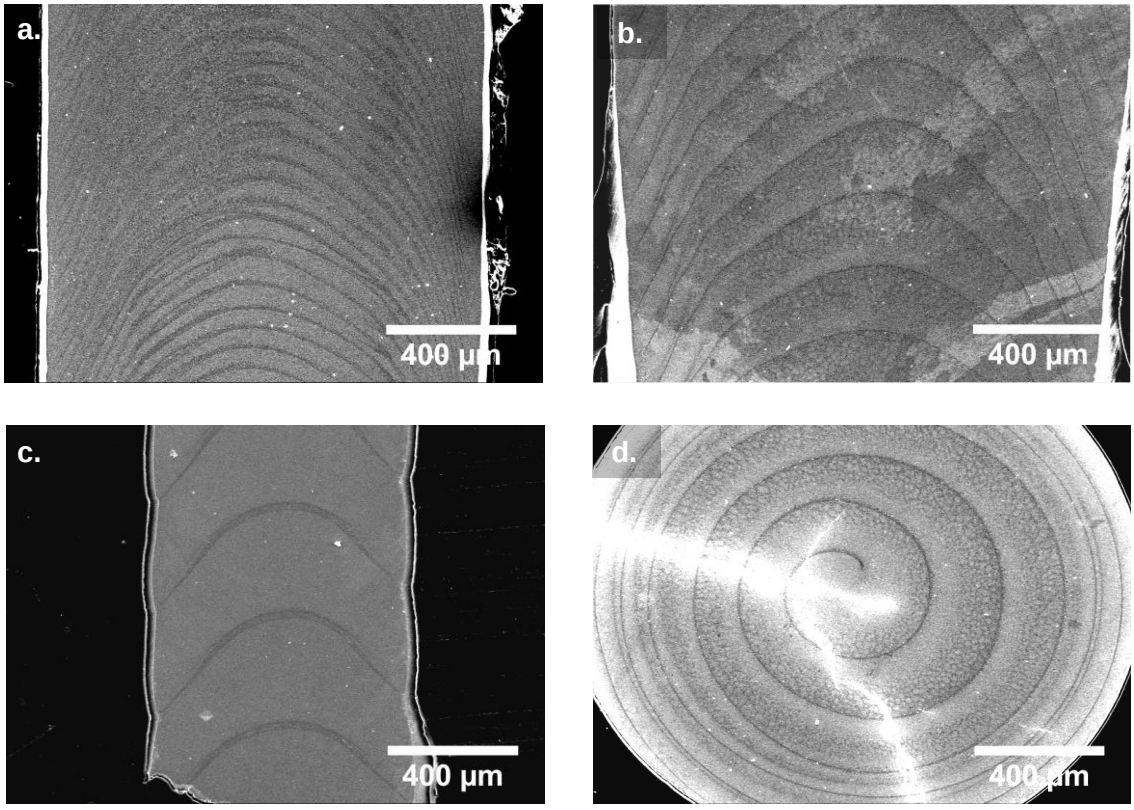


***Figure 5:*** *SEM micrographs illustrating the banding phenomenon observed at the longitudinal cross-sections of $ZrO_2$-$BaZrO_3$ fibres grown at 20 mm/h* ***(a)****, 50 mm/h* ***(b),*** *100 mm/h* ***(c)****, and of the transversal cross-section of fibres grown at 50 mm/h* ***(d)****.*

The final eutectic microstructure is controlled by the shape of the solidification interface, which, unfortunately, cannot be directly monitored during growth. However, the aspect of the bands is that of frozen-in interfaces, thus providing a good indication of the evolution of the solid-liquid interface during growth [32]. In this way, the local growth rate

oscillates around the pulling rate, leading to quasi-periodic, alternating fine and coarse regions resulting from the rupture of the solidification front [35]. The growth rate fluctuation during LFZ is promoted by convective instabilities and related temperature oscillations at the solidification interface [36].

### II.2.3.3. Coupled and colony eutectic microstructures

Banding inhomogeneities were also reported for directionally solidified ceramic eutectics based in oxide systems such as $Al_2O_3/ZrO_2(Y_2O_3)$ eutectic rods processed by LFZ [32,35]. In this system, bands presenting a coarse eutectic microstructure intercalate between finer eutectic regions. Very similar solidification bands are observed in the present system, particularly at the lowest pulling rate (20mm/h), where the band frequency is the highest (Fig. 5a). The two alternating regions have a similar morphology, but with a different length scales, also comprising coarse (Fig. 6b) and fine (Fig. 6c) eutectic-like patterns. The former correspond to the solidification bands whereas the latter appear in the inter-band regions.

The bands show the coupled (interpenetrating) microstructure of $ZrO_2$ (dark) and $BaZrO_3$ (light). In this eutectic constituent, the dark phase has a globular morphology aligned perpendicularly to the banding curvature, as shown by Figure 6a. At the slowest pulling rate (20mm/h), where bands predominate (Fig. 6a), the distance between bands is short and the finer eutectic at the inter-band regions is irregular, without any preferential orientation (Fig. 6c). The corresponding transversal cross-sectional micrographs confirm the irregularity of the eutectic morphology (Figs. 7a and b).

A significant decrease of the band periodicity is observed when the pulling rate increases to 50mm/h (Fig. 5b). Again, the band morphology is somewhat globular (Fig. 6e), but the inter-banding eutectic displays a regular lamellar $ZrO_2$-$BaZrO_3$ microstructure that is preferentially aligned with the fibre axis (Fig. 6f). The development of ill-defined colonies immediately after the banding are observed for this pulling rate, both in the longitudinal (Fig. 6d) and the transversal (Figs. 7c and d) sections of the fibre.

The maximum pulling rate (100mm/h) further increases the band inter-distance (Fig. 5c), and a columnar colony microstructure clearly develops in the inter-band region (Fig. 6g), consisting of the $ZrO_2$-$BaZrO_3$ lamellar eutectic micro-constituent (Figs. 6h and i). A thick zirconia-rich boundary region exhibiting a coarser microstructure is apparent between the colonies (Fig. 6h). In the longitudinal sections of the fibre, the colonies present an ellipsoidal shape with the longer axis perpendicular to the bands (Fig. 6g).

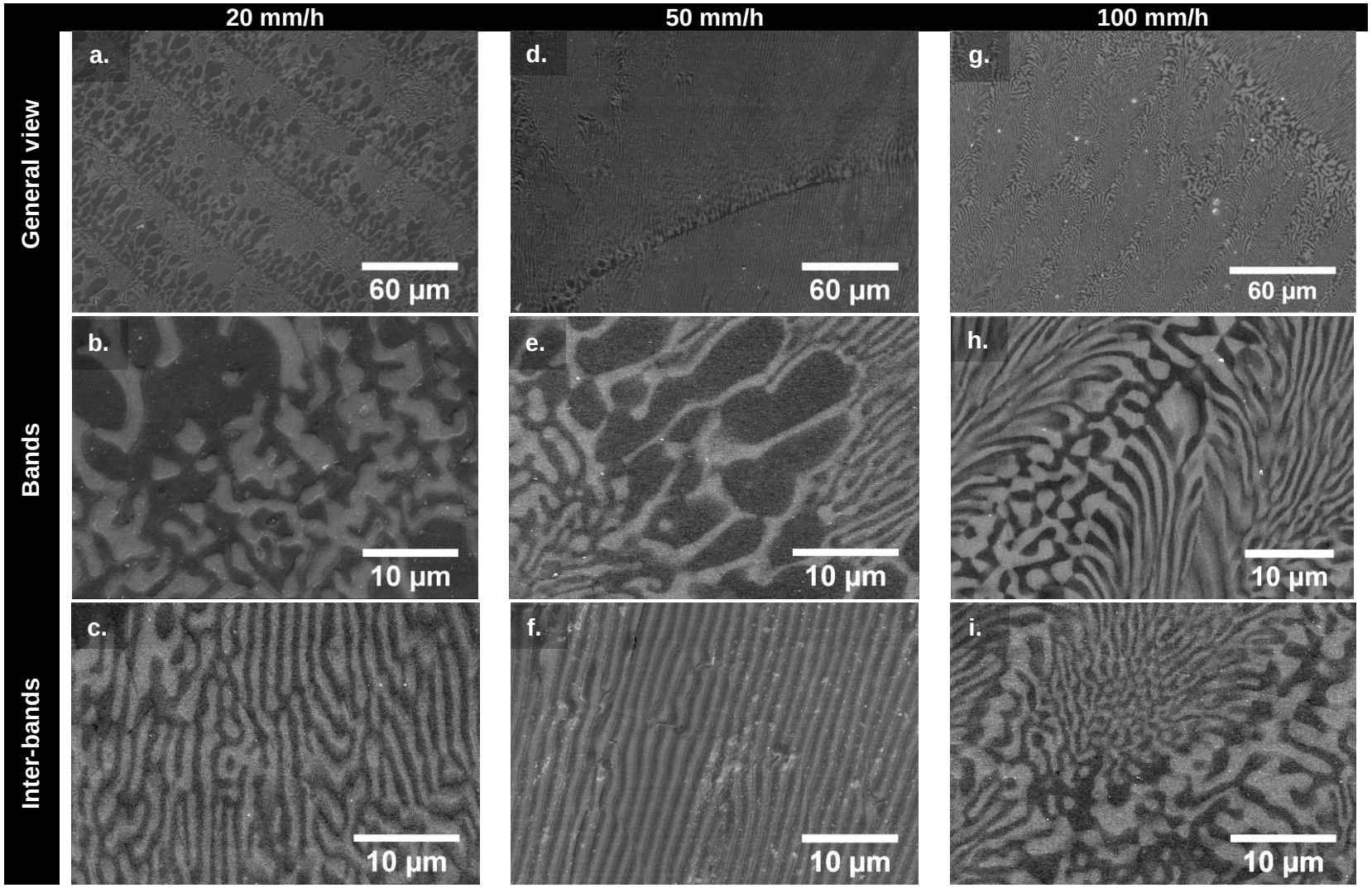


***Figure 6:*** *SEM micrographs of longitudinal cross-sections of $ZrO_2$-$BaZrO_3$ fibres grown at 20 mm/h* ***(a, b, c)****, 50 mm/h* ***(d, e, f)*** *and 100 mm/h* ***(g, h, i)****. The coarse regions are depicted at* ***(b, e, h)****, while finer ones are shown at* ***(c, f, i).***

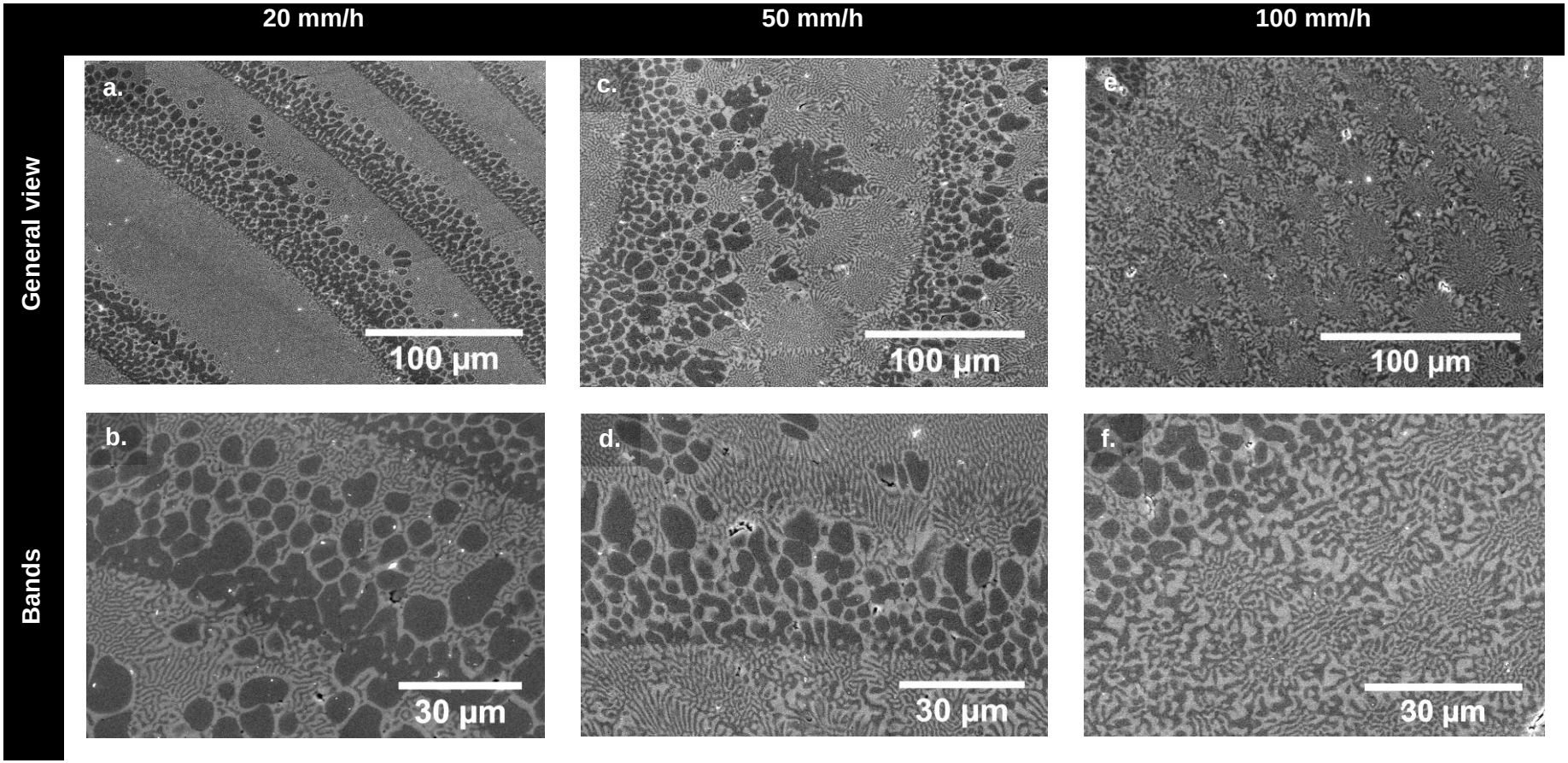


***Figure 7:*** *SEM micrographs of the transversal cross-sections of $ZrO_2$-$BaZrO_3$ fibres grown at 20 mm/h* ***(a, b)****, 50 mm/h* ***(c, d)*** *and 100 mm/h* ***(e, f)****.*

This pulling rate magnitude is enough to install columnar growth conditions that disrupt the coupled eutectic growth, according to the well-known constitutional undercooling criterion originally derived by Chalmers [37]. Lastly, note the apparent contiguity of both phases in all the captured images, denoting the absence of any type of interphase boundaries, in particular grain boundaries, as expected for ceramic components processed by the LFZ method.

### II.2.3.4. Compositional effects

The simple observation of band and inter-band regions suggests compositional differences in terms of the fraction of each phase. The semi-quantification of the fractional surface areas (equivalent to volume percentages) of SEM micrographs is illustrated in Figure 8. The inter-band regions of all samples (Figs. 8d to f), regardless of the pulling rate, exhibit a composition of ~50 vol.% $BaZrO_3$:50 vol.% $ZrO_2$ that fits to the $ZrO_2$-$BaZrO_3$ eutectic (29 mol.% $BaZrO_3$:71 mol.% $ZrO_2$) [17,38]. This value deviates from the nominal composition (25 mol.% BaO:75 mol.% $ZrO_2$ or 29 vol.% $BaZrO_3$:71 vol.% $ZrO_2$) showing that some barium loss under the laser beam took place. This is somehow expected given the extremely high temperatures attained during the LFZ process (at least higher than the melting point of $ZrO_2$, ~2720 °C), which are clearly higher than the boiling point of BaO (~2000 °C). It is perhaps interesting to reinforce that our results support the eutectic composition of the phase diagram proposed by Paschoal et al., instead of the one (50 mol.% $BaZrO_3$:50 mol.% $ZrO_2$) reported by Shevchenko et al. [16], currently available in the Factsage data base [39].

The vaporization of barium can also disturb the solidification front, further contributing to the microstructural banding discontinuity. The band front starts by nucleation of the zirconia phase with a finer structure that coarsens towards the band periphery (Figs. 6a, 7a and 7c). The band composition obtained at 20 mm/h (~25 vol.% $BaZrO_3$:75 vol.% $ZrO_2$) is even richer in $ZrO_2$ than the eutectic composition of the inter-band region, revealing an additional loss of barium. At such slow pulling rates the exposure time of the material to high temperatures is relatively high and bands perform as self-adjusting compositional discontinuities. At the highest pulling rate (100 mm/h), the vaporization time is shorter than for 20 mm/h, and thus the inter-band and band compositions are similar (Figs. 8c and 8f). An intermediate situation is observed for fibres pulled at 50 mm/h with ~45 vol.% $BaZrO_3$:55 vol.% $ZrO_2$ in the band region (Fig. 8b).

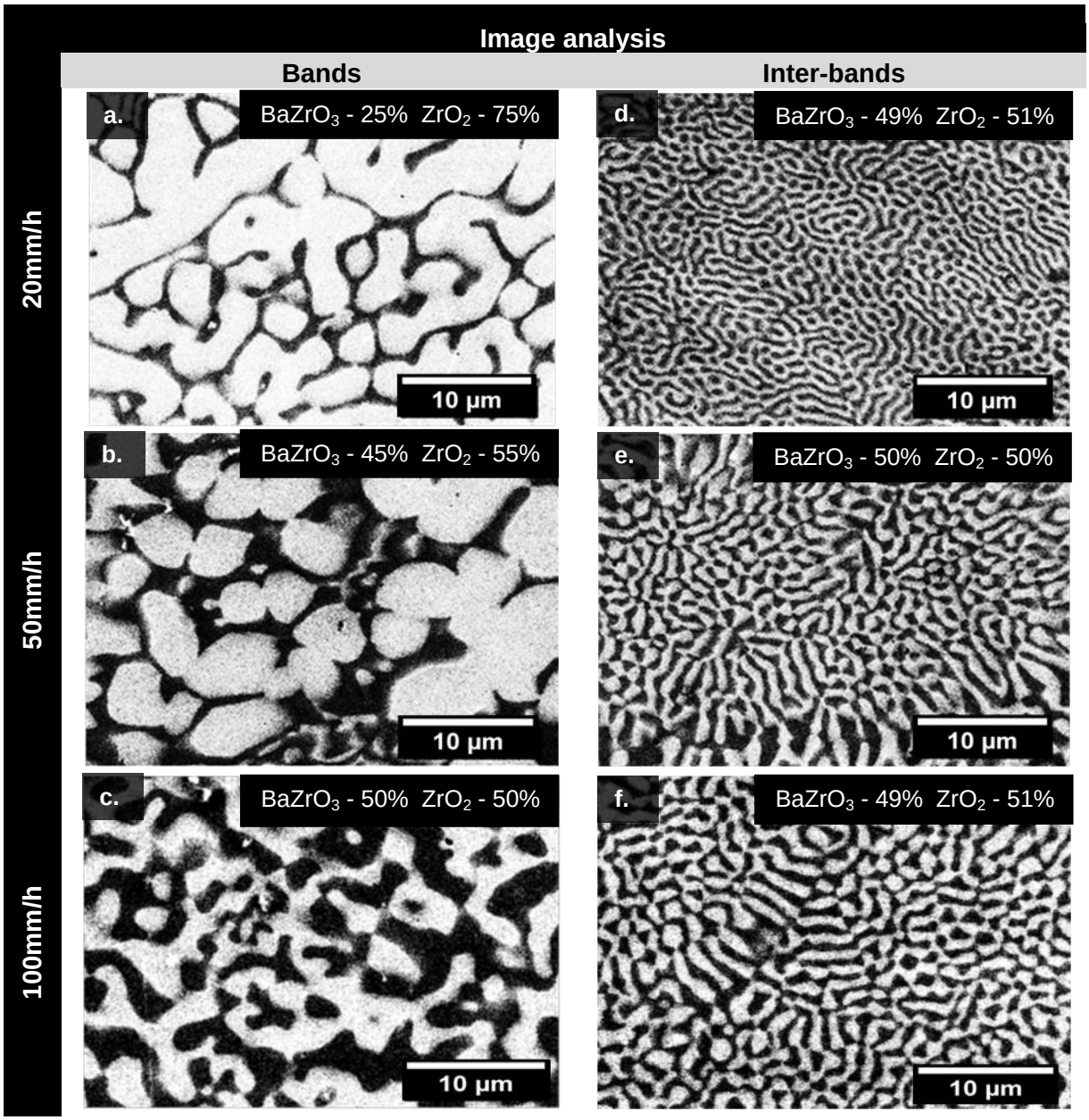


***Figure 8:*** *Binary images showing the distribution and the corresponding fractional areas of $ZrO_2$ (white) and $BaZrO_3$ (black) phases at the band* ***(a, b, c)*** *and inter-band regions* ***(d, e, f)*** *observed along the longitudinal cross-sections of fibres grown at different pulling rates. Note that these images are negatives of the original micrographs, where $ZrO_2$ appears in darker grey and $BaZrO_3$ in a lighter tonality.*

The EDS analysis performed in a fibre grown at 100mm/h clearly shows that the yttrium tends to prefer the $ZrO_2$ fluorite structural environment (Fig. 9a). This is also apparent across a fine eutectic lamellar region, where the yttrium follows the inverse trend of the barium concentration profile (Fig. 9b).

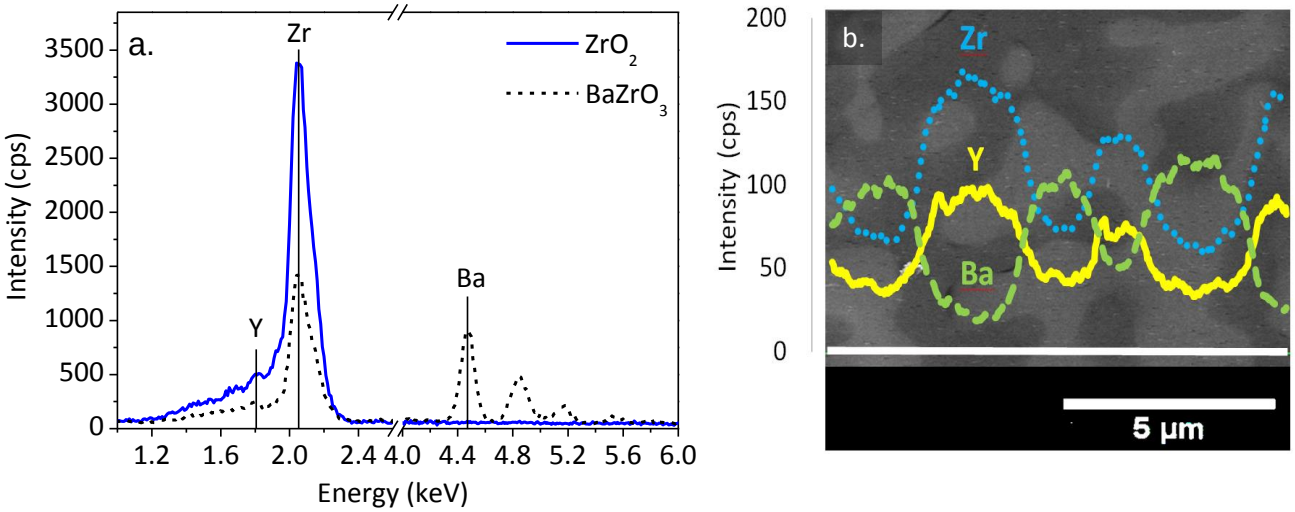


***Figure 9: (a)*** *EDS spectra of $BaZrO_3$ (black dash line) and $ZrO_2$ (blue continuous line) from 100 mm/h grown fibres.* ***(b)*** *Elemental EDS concentration profiles for yttrium, zirconium and barium superimposed to a 100 mm/h fibre micrograph along the white line across $ZrO_2$ (light grey)) and $BaZrO_3$ (dark grey) regions.*

The relevance of the yttrium dopant for the properties of these materials (*e.g.* crystal structure, ionic conductivity, mechanical properties) and the potential impact of this component on the processing conditions (e.g. type of dopant, precursors composition, laser power, pulling rate) and resulting microstructure, are issues currently being addressed.

### II.2.3.5. Phase contiguity by impedance spectroscopy

In polycrystalline oxide ion conductors such as Y-doped zirconia, the space-charge potential existing at grain boundaries depletes the oxide vacancy concentration along these regions, hence locally reducing the conductivity with respect to the bulk. The high density of resistive grain boundaries existing on conventional ceramics with a grain size of the order of few micron (or less) will have a significant impact on the total resistance of the sample. Due to differences in the ionic relaxation frequencies (lower in the grain boundary), impedance spectroscopy is a suitable method to separate the resistive contributions of the bulk and the grain boundaries to the total resistance of the sample, thus providing a very solid correlation between the conductivity and the microstructure [40-42]. Contrarily to conventional polycrystalline yttrium-doped zirconia or barium zirconate displaying two semicircles ascribed to the ionic relaxations in the bulk and grain boundaries [40,41], the Nyquist plots obtained for the fibres prepared in this work show only one semicircle with a capacitance in the range of 10 to 20 pF (Figs. 10a to c). These values are of the order of magnitude expected for the bulk capacitance ($C_b$) measured for pelletized samples of a good ionic conductor (such as $(Zr,Y)O_2$) with typical dimensions (1-2 mm thick and elec-

trode areas of 0.25-0.5 $cm^2$), but are much higher than those expected for a similar material with the geometrical factor of the fibres (length <5 mm combined with extremely small electrode area < 0.01 $cm^2$). In this case, the $C_b = \varepsilon_r\varepsilon_0 SL^{-1}$ should be close to 0.05 pF ($\varepsilon_r$ is the bulk relative permittivity (taken as 30), $\varepsilon_0$ is the permittivity of the vacuum ($8.854\times10^{-14}$ F/cm), S is the surface area of the electrodes (0.01 $cm^2$) and L is the length of the fibre (0.5 cm). This means that the semicircle observed in Figure 10 cannot be due to ionic transport in the bulk of the grains.

Grain boundaries represent resistive contributions to ionic transport due to the formation of a space charge layer [42]. The resulting capacitances ($C_{gb}$) are typically 2 orders of magnitude higher than $C_b$. According to the brick layer model of ionic transport in a polycrystalline ionic conductor such as stabilized zirconia, the grain boundary capacitance can be estimated by $C_{gb}=C_bG\delta^{-1}$, where G is the average grain size and δ is the grain boundary thickness [40]. Considering $C_b$=0.05 pF (as estimated above) and assuming δ≈2 nm [42], the $C_{gb}$ is of the order of 27, 270 and 2700 pF for G=1, 10 and 100 μm, respectively. The estimates for the two large grain cases cannot explain the Nyquist plots, where the capacitances (10-20 pF) are much lower. The 1 $\mu$m sized grains may indeed yield $C_{gb}$ values similar to the capacitances measured experimentally. However, such hypothetic fine-grained microstructure is far from that observed by SEM, as depicted in Figures 5 to 8. Moreover, neither the shape of the spectra nor the capacitances change with the pulling rate (Fig. 10c), which means that they are independent of the fibre microstructure. The only reasonable explanation for the observed capacitive effects contribution is thus the stray capacitance of the experimental set-up (mainly the cables), which is typically of few pF. This capacitance is in parallel with the (much lower) sample capacitance and the (much higher) sample ohmic resistance.

The onset of a low frequency tail with increasing temperature observed in Fig. 10a indicates the growing importance of the electrode impedance, which dominates the spectra at the high temperatures. However, the high frequency capacitive stray contribution persists up to high temperatures, disappearing only above 900 °C, when the fibre resistance is sufficiently low and the corresponding relaxation frequency increases to levels well above the 1 MHz upper limit of the LCR meter. In spite of the dominating stray capacitance, the fibre resistance can be easily estimated as corresponding to the amplitude of the semicircle for temperatures up to 900 °C, and then on to the high frequency intercept with the real axis of the electrode contribution.

As expected for an ionic conductor, the total resistivity of $ZrO_2$-$BaZrO_3$ eutectic fibres decreases with increasing temperature (Fig. 10a). The spectra remain essentially unal-

tered by changing the surrounding atmosphere from air (oxygen partial pressure, $P_{O_2}$=21 kPa) to the hydrogen atmosphere ($P_{O_2}$ lower than $1\times10^{-16}$ Pa at all temperatures), thus suggesting pure ionic conduction (and residual n-type electronic transport). No evidence for proton conductivity could be found either, in agreement with the insensitivity of the resistivity to changes in the water vapour pressure in the surrounding atmosphere, both the air and the hydrogen containing mixture (Fig. 10b).

All these observations strongly suggest that the transport properties of the fibres are dominated by the oxide ion conductivity along the yttrium-doped zirconia phase. In fact, the zirconia is essentially a pure solid oxide electrolyte with negligible electronic and protonic conductivities. Therefore, any proton transport in the composite fibres would necessarily occur through the barium zirconate, but not in pure $BaZrO_3$ since the yttrium doping of $BaZrO_3$ is fundamental to promote the proton conductivity [43]. The electrical behaviour of the fibres is thus in excellent agreement with the EDS and Raman data suggesting that the yttrium cations are preferentially solubilized in the zirconia lattice, since yttrium doping of the $BaZrO_3$ phase is required in order to achieve proton conduction in this phase.

Indeed, the conductivity values measured for the composite fibres (*e.g.* $6.5\times10^{-3}$ S/cm at 775 ºC) are relatively close to the values measured for a pure $(ZrO_2)_{0.97}(Y_2O_3)_{0.03}$ ceramic sample ($1.1\times10^{-2}$ S/cm at 750 ºC) [44], with the lower values measured for the composites being explained by the obviously higher volume fraction of zirconia in the single phase ceramics. On the other hand, the relatively modest difference between the two sets of values confirms the electrical percolation through the zirconia, in agreement with the SEM observations.

Figure 10c shows that the resistivity of the fibres decreases with decreasing pulling rate. This behaviour can again be explained by the increasing content of conducting zirconia in the fibres with higher band density (obtained with decreasing growth rates). Similar microstructural evolution, from a coupled to colony morphology when the growth rate was increased, was observed in directionally solidified $Al_2O_3$-$ZrO_2$ (3 mol.% $Y_2O_3$) eutectics processed by the LFZ method [32]. The highest conductivity value for these $Al_2O_3$-$ZrO_2$ composites was $3.4\times10^{-3}$ S/cm at 800 ºC, obtained for an off-eutectic composition with 45 vol.% $ZrO_2$ grown at low pulling rates (10 mm/h) [21]. This conductivity is considerably lower than for pure $(ZrO_2)_{0.97}(Y_2O_3)_{0.03}$, and also lower than our $ZrO_2$-$BaZrO_3$ eutectic fibres with about 50 vol.% $ZrO_2$ ($7.9\times10^{-3}$ S/cm at 815 ºC). It is reported in reference [21] that the maximum conductivity is limited by the formation of primary zirconia poor in yttrium at the solidification stage of the $Al_2O_3$-$ZrO_2$ composites.

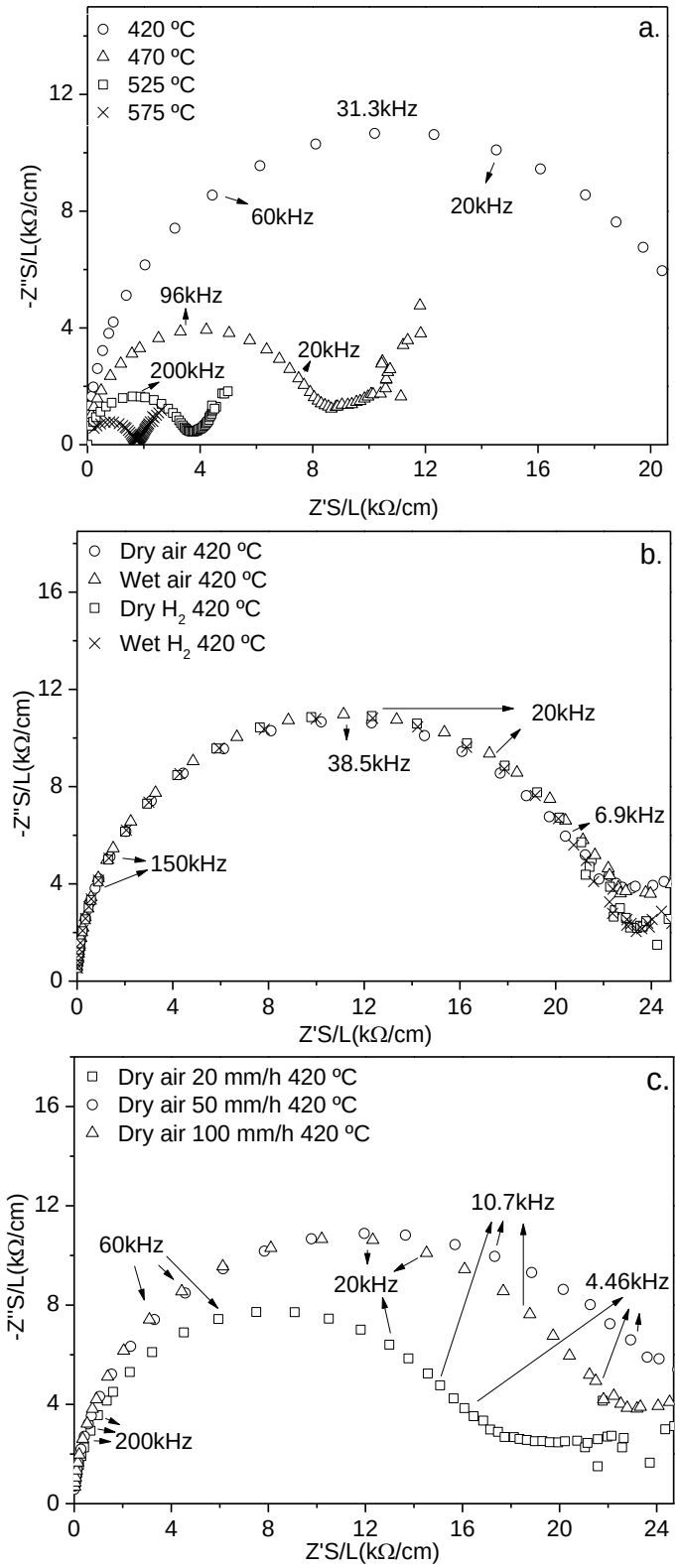


***Figure 10:*** *Nyquist plots for* ***(a)*** *different temperatures (100mm/h, dry air),* ***(b)*** *dry and humidified air or 95% $N_2$+5% $H_2$ (100mm/h, 420 °C) and* ***(c)*** *different pulling rates (420 °C, dry air).*

## II.2.4. Conclusions

Novel directional solidified eutectic (DSE) fibres from the $ZrO_2$-$BaZrO_3$ system were grown by the laser floating zone (LFZ) method, using growth rates from 20 to 100 mm/h. XRD and Raman spectroscopy results confirmed the occurrence of the expected $ZrO_2$ and $BaZrO_3$ phases with tetragonal and cubic crystal structures, respectively.

A detailed microstructural characterization gives a clear presence of solidification bands with a convex shape, due to periodic perturbations on the solidification interface. The band inter-distance increases with the growth rate. Band and inter-band regions present coarse and fine eutectic-like patterns, respectively. However, the average chemical composition in both regions is somewhat similar, except for low pulling rates where the exposure time under the high energy density of the LFZ process causes significant barium losses. In the inter-band region the microstructure changes from a homogeneous coupled eutectic, at the lowest pulling rate, to columnar colony microstructure, for the faster grown fibres. In general, the yttrium dopant tends to solubilize in the zirconia fluorite lattice.

The ionic conductivity (*e.g.* $9.7\times10^{-3}$ S/cm at 824 ºC) of $ZrO_2$-$BaZrO_3$ eutectic fibres was mainly controlled by the oxide ion conductivity of $ZrO_2$, which increases for lower growth rates. Moreover, no evidence of protonic conductivity was identified, since no influence by water vapour partial pressure was identified. As the latter would necessarily occur in the Y-doped $BaZrO_3$, the electrical conductivity results confirm the microstructural observations that the yttrium cations are preferentially located in the zirconia lattice. Further work is needed in order to exploit the full range of processing conditions and compositions (*e.g.* the yttrium content) allowing solubilizing yttrium also in the perovskite structure, hence introducing proton conduction functionality in the composite.

The difference observed for the conductivity of fibres grown at different rates was attributed to the band density and the $ZrO_2$ content in the bands. Impedance spectroscopy did not show any evidence for the resistive contribution of grain boundaries to the electrical behaviour within the zirconia phase, in agreement with the SEM observation of phase contiguity within the eutectic constituent.

## References

[1] N. Claussen, M. Ruhle, A.H. Heuer, Science and technology of zirconia II, American Ceramic Society Ohio, 1984.

[2] X.Q. Cao, R. Vassen, D. Stoever, Ceramic materials for thermal barrier coatings, Journal of the European Ceramic Society, 24 (2004) 1-10.

[3] R. Vassen, X. Cao, F. Tietz, D. Basu, D. Stöver, Zirconates as new materials for thermal barrier coatings, Journal of the American Ceramic Society, 83 (2000) 2023-2028.
[4] H. Pachschwoell, J. Klose, C. Rothe, S. Jonas, T. Stolte, Insulating material capable of withstanding cyclically varying high temperatures, FNE Forschungsinstitut fuer Nichteisen-Metalle Freiberg GmbH (Freiberg, DE), United States, 2008.
[5] L. Malavasi, C.A.J. Fisher, M.S. Islam, Oxide-ion and proton conducting electrolyte materials for clean energy applications: structural and mechanistic features, Chemical Society Reviews, 39 (2010) 4370-4387.
[6] A. Evans, A. Bieberle-Hütter, J.L.M. Rupp, L.J. Gauckler, Review on microfabricated micro-solid oxide fuel cell membranes, Journal of Power Sources, 194 (2009) 119-129.
[7] F.M.L. Figueiredo, F.M.B. Marques, Electrolytes for solid oxide fuel cells, Wiley Interdisciplinary Reviews: Energy and Environment, 2 (2013) 52-72.
[8] B.C.H. Steele, A. Heinzel, Materials for fuel-cell technologies, Nature, 414 (2001) 345-352.
[9] H. Iwahara, T. Yajima, T. Hibino, K. Ozaki, H. Suzuki, Protonic conduction in calcium, strontium and barium zirconates, Solid State Ionics, 61 (1993) 65-69.
[10] H.G. Bohn, T. Schober, Electrical conductivity of the high-temperature proton conductor $BaZr_{0.9}Y_{0.1}O_{2.95}$, Journal of the American Ceramic Society, 83 (2000) 768-772.
[11] I. Antunes, A. Brandão, F.M. Figueiredo, J.R. Frade, J. Gracio, D.P. Fagg, Mechanosynthesis of nanopowders of the proton-conducting electrolyte material $Ba(Zr,Y)O_{3-\delta}$, Journal of Solid State Chemistry, 182 (2009) 2149-2156.
[12] P. Babilo, S.M. Haile, Enhanced sintering of yttrium-doped barium zirconate by addition of ZnO, Journal of the American Ceramic Society, 88 (2005) 2362-2368.
[13] W. Sun, Y. Jiang, Y. Wang, S. Fang, Z. Zhu, W. Liu, A novel electronic current-blocked stable mixed ionic conductor for solid oxide fuel cells, Journal of Power Sources, 196 (2011) 62-68.
[14] A.V. Virkar, Transport through mixed proton, oxygen ion and electron (hole) conductors: Goldman-Hodgkin-Katz-type equation, Journal of Power Sources, 194 (2009) 753-762.
[15] C. Xia, Y. Li, Y. Tian, Q. Liu, Y. Zhao, L. Jia, Y. Li, A high performance composite ionic conducting electrolyte for intermediate temperature fuel cell and evidence for ternary ionic conduction, Journal of Power Sources, 188 (2009) 156-162.
[16] A.V. Shevchenko, L.M. Lopato, G.I. Gerasimyuk, Z.A. Zaitseva, Reactions in the system $HfO_2$-SrO, $HfO_2$-BaO and $ZrO_2$-BaO in high $HfO_2$ or $ZrO_2$ regions, Inorganic Materials, 23 (1987) 1322-1325.

[17] J.O.A. Paschoal, H. Kleykamp, F. Thümmler, Phase equilibria in the pseudoquaternary BaO-$UO_2$-$ZrO_2$-$MoO_2$ system, Journal of Nuclear Materials, 151 (1987) 10-21.
[18] V.M. Orera, R.I. Merino, J.A. Pardo, A. Larrea, J.I. Peña, C. González, P. Poza, J.Y. Pastor, J. Llorca, Microstructure and physical properties of some oxide eutectic composites processed by directional solidification, Acta Materialia, 48 (2000) 4683-4689.
[19] J. Llorca, V.M. Orera, Directionally solidified eutectic ceramic oxides, Progress in Materials Science, 51 (2006) 711-809.
[20] R.I. Merino, J.I. Peña, V.M. Orera, G.F. de la Fuente, Conductivity anisotropy in directionally solidified $CaZrO_3$-CaSZ and MgO-MgSZ eutectics, Solid State Ionics, 100 (1997) 313-318.
[21] R.I. Merino, I. de Francisco, J.I. Peña, Ionic conductivity in directionally solidified $Al_2O_3$-$ZrO_2$(3% mol $Y_2O_3$) near eutectic composites, Solid State Ionics,178(2007) 239-247.
[22] J.I. Peña, R.I. Merino, G.F.d.l. Fuente, V.M. Orera, Aligned $ZrO_2$(c)-$CaZrO_3$ eutectics grown by the laser floating zone method: electrical and optical properties, Advanced Materials, 8 (1996) 909-912.
[23] A. Revcolevschi, G. Dhalenne, Crystallographically aligned metal-oxide composite made by reduction of a directionally solidified oxide-oxide eutectic, Nature, 316 (1985) 335-336.
[24] R.G. Carvalho, A.J.S. Fernandes, F.J. Oliveira, E. Alves, N. Franco, C. Louro, R.F. Silva, F.M. Costa, Single and polycrystalline mullite fibres grown by laser floating zone technique, Journal of the European Ceramic Society, 30 (2010) 3311-3318.
[25] W.S. Rasband, ImageJ, in, Bethesda, MD: National Institutes of Health, 1997-2012. http://imagej.nih.gov/ij/.
[26] X.P. Tan, S.Q. Liang, G.W. Zhang, Y. Zhang, L.Y. Chai, Structural evolution of $ZrO_2$-mullite nanocomposites from the Si-Al-Zr-O amorphous bulk, Phase Transitions, 84 (2011) 157-166.
[27] M. Karlsson, A. Matic, C.S. Knee, I. Ahmed, S.G. Eriksson, L. Borjesson, Short-range structure of proton-conducting perovskite $BaIn_xZr_{1-x}O_{3-x/2}$ (x=0-0.75), Chemistry of Materials, 20 (2008) 3480-3486.
[28] M. Karlsson, I. Ahmed, A. Matic, S.G. Eriksson, Short-range structure of proton-conducting $BaM_{0.10}Zr_{0.90}O_{2.95}$ (M = Y, In, Sc and Ga) investigated with vibrational spectroscopy, Solid State Ionics, 181 (2010) 126-129.
[29] A. Slodczyk, P. Colomban, D. Lamago, M. H. Limage, F. Romain, S. Willemin, B. Sala, Phase transitions in the $H^+$ conducting perovskite ceramics by the quasi-elastic neutron and high-pressure Raman scattering, Ionics, 14 (2008) 215-222.[30] G.G. Siu, M.J.

Stokes, Y.L. Liu, Variation of fundamental and higher-order Raman spectra of $ZrO_2$ nanograins with annealing temperature, Physical Review B, 59 (1999) 3173-3179.
[31] C.J. Szepesi, J.H. Adair, High Yield Hydrothermal Synthesis of Nano-Scale Zirconia and Y-TZP, Journal of the American Ceramic Society, 94 (2011) 4239-4246.
[32] I. de Francisco, R.I. Merino, V.M. Orera, A. Larrea, J.I. Peña, Growth of $Al_2O_3/ZrO_2(Y_2O_3)$ eutectic rods by the laser floating zone technique: effect of the rotation, Journal of the European Ceramic Society, 25 (2005) 1341-1350.
[33] W. Kurz, D.J. Fisher, Fundamentals of solidification, Trans. Tech. Publications Ltd, Switzerland, 1992.
[34] M. Gremaud, M. Carrard, W. Kurz, Banding phenomena in Al-Fe alloys subjected to laser surface-treatment, Acta Metallurgica et Materialia, 39 (1991) 1431-1443.
[35] J.Y. Pastor, J. Llorca, P. Poza, I. de Francisco, R.I. Merino, J.I. Peña, Mechanical properties of melt-grown $Al_2O_3$-$ZrO_2(Y_2O_3)$ eutectics with different microstructure, Journal of the European Ceramic Society, 25 (2005) 1215-1223.
[36] H.J. Scheel, Theoretical and technological solutions of the striation problem, Journal of Crystal Growth, 287 (2006) 214-223.
[37] Chalmers, Principles of Solidification, John Wiley & Sons, Inc., New York, 1964.
[38] Y. Yamazaki, C. K. Yang, S.M. Haile, Unraveling the defect chemistry and proton uptake of yttrium-doped barium zirconate, Scripta Materialia, 65 (2011) 102-107.
[39] FactSage thermochemical software and databases, GTT-Technologies, Germany.
[40] C.M. Fernandes, A. Castela, F.M. Figueiredo, J.R. Frade, Microstructure-property relations in composite yttria-substituted zirconia solid electrolytes, Solid State Ionics, 193 (2011) 52-59.
[41] S. Imashuku, T. Uda, Y. Nose, G. Taniguchi, Y. Ito, Y. Awakura, Dependence of dopant cations on Microstructure and proton conductivity of barium zirconate, Journal of the Electrochemical Society, 156 (2009) B1-B8.
[42] X. Guo, R. Waser, Electrical properties of the grain boundaries of oxygen ion conductors: Acceptor-doped zirconia and ceria, Progress in Materials Science, 51 (2006) 151-210.
[43] K.D. Kreuer, Proton-conducting oxides, Annual Review of Materials Research, 33 (2003) 333-359.
[44] M.A. Lourenco, G.G. Cunto, F.M. Figueiredo, J.R. Frade, Model of two-step sintering conditions for yttria-substituted zirconia powders, Materials Chemistry and Physics, 126 (2011) 262-271.

### II.2.5. Supplementary information to the banding phenomena in $ZrO_2$-$BaZrO_3$ directional solidified eutectics fibres

Banding phenomenon is common in solidification systems involving high-energy beams (such as lasers) that yield periodic variations in the microstructure [1-3]. The banded structure displays the pattern of the successive solidification interface positions [2,4]. Considering the nature of the mechanism responsible for the bands formation, different banding structures could be observed, as depicted in Figure 1 [1]. The first banded structure (Fig. 1a) consists of the same microstructure, but alternating fine and coarse zones. This is the case of our $ZrO_2$-$BaZrO_3$ DSE fibres grown at high growth rate (≥50 mm/h), Figure 7 in II.2.3.3. section. Banded structures developed at high rates are characterized by a periodic formation of two distinct microstructures due to nonequilibrium effects at the solidification interface. On the other hand, at low pulling rates the same microstructure is observed in band and interband regions (Fig. 8 in II.2.3.4.), but with different scale and composition. Such banding structure does not exactly matches the models proposed in Figure 1, since in our case we have an eutectic constituent instead of monophasic bands.

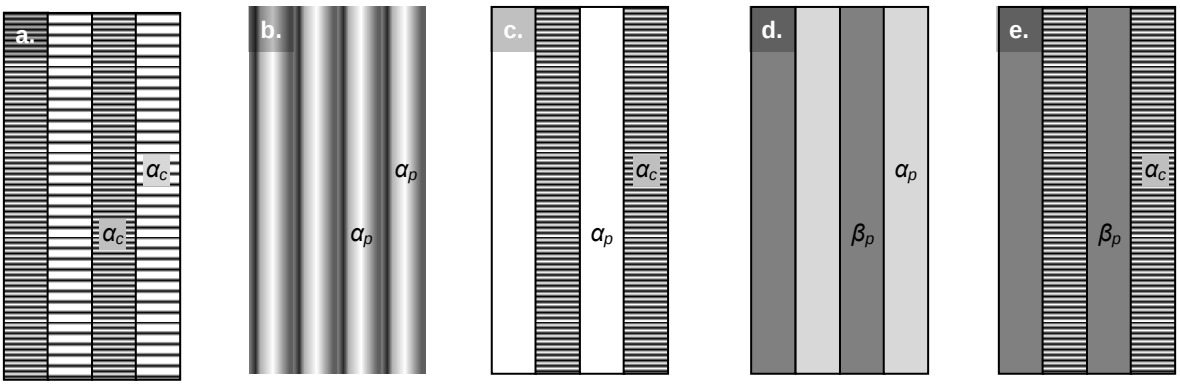


***Figure 1:*** *Illustration of the different banding structures* ***(a)*** *different scales of same microstructure and phase;* ***(b)*** *fluctuations of composition in plane front growth of same phase (generally do not form visible bands);* ***(c)*** *different microstructures of same phase;* ***(d)*** *different phases with plane front growth morphology and* ***(e)*** *different phases and microstructures (c = cells, p = plane front), adapted from [1].*

In order to model the bands geometry, longitudinal and transversal sections of the 50 mm/h directional solidified eutectic (DSE) fibre were observed by optical microscopy (OM). Samples were impregnated in araldite epoxy resin and then carefully polished in steps of ~0.1 mm. An optical microscope Olympus BH2-UMA equipped with U-series CMOS camera was used to capture the aspect of the polished surfaces at each step.

The solidification interface and the fibre transversal cross-section profile were photographed (Fig. 2). The solidification interface profile (Fig. 2a) is clearly non-planar and cor-

responds to a non-symmetric curve (dashed line). Notice that the bands tend to follow the same shape of the solidification interface, as it was previously reported in the literature for other DSE systems [4]. It was observed a completed spiral shape across the fibre transverse section (Fig. 2b), in which the central point from where the spiral emanates is closer of the fibre axis. Moreover, the bands thickness is reduced at the fibres periphery and such is accompanied by a shorter banding interspacing.

The results depicted in Figure 3 correspond to the banding profile at longitudinal cross-sections. The snapshots did not correspond to all consecutive polishing steps, but to selected observations of the in-depth profiles. However, the sequence was kept in order to show only the most significant differences observed during the process. In the first polishing steps, the banding profile is not so well-defined, as shown in Figure 3a. However, in the subsequent steps it was revealed an increase of the banding resolution (Figs. 3b,c) along with an increase of their thickness (Fig. 3d). After that, it was observed an odd banding split profile at the middle region in Figures 3d,e and also in Fig. 2a, probably due to the misalignment of the laser incidence. Lately, since the fibre centre is exceeded, the split and the banding profile became again unclear, as shown in the Figures 3g,h.

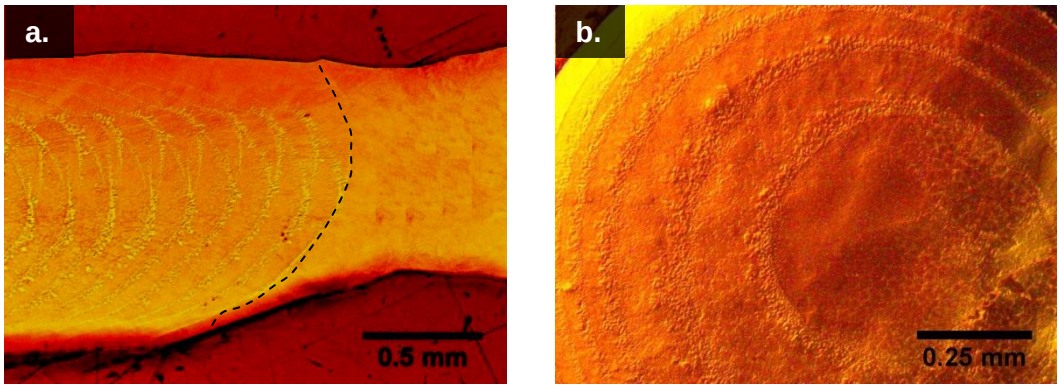


***Figure 2:*** *Photographs of 50 mm/h $ZrO_2$-$BaZrO_3$ DSE fibre capture* ***(a)*** *at the solidification interface (dashed line) in the longitudinal fibre cross-section and* ***(b)*** *transversal fibre cross-section.*

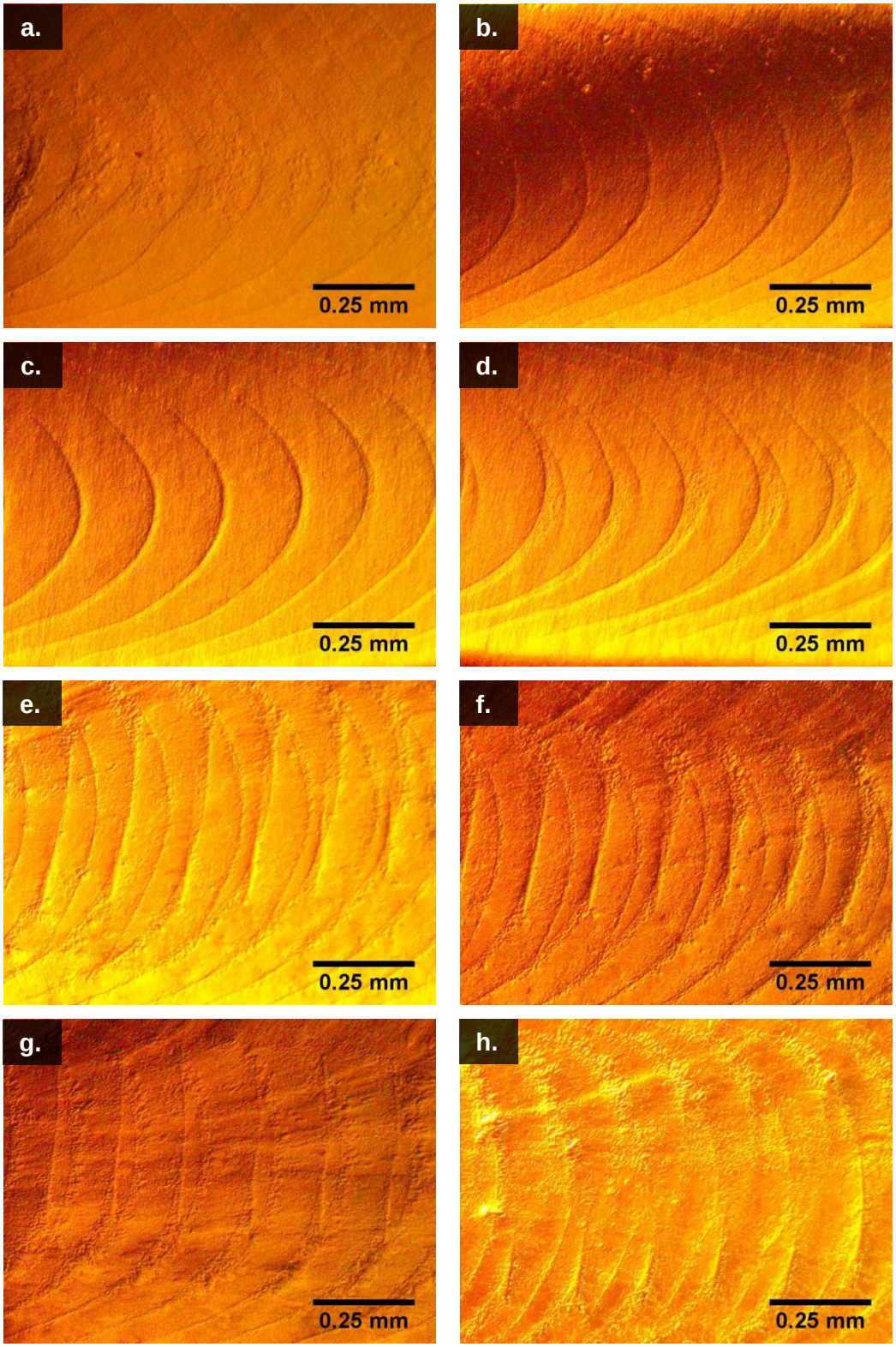


***Figure 3:*** *Photographic captures of longitudinal cross-sections of a 50 mm/h $ZrO_2$-$BaZrO_3$ DSE fibre polished step by step, keeping the original sequence.*

The band shape was simulated using the AutoCAD software. The main intent was to reproduce the experimental observation (Figs. 2 and 3). In these attempts, some of the experimental growing conditions were assumed as inputs. The model consider the typical fibre diameter, the rod rotation and translation rates. The best approach to the experimental data is depicted in the perspective in Figure 4a. Such result was obtained considering the rotation and translation of an uneven arc. The longitudinal (Fig. 4b) and transversal (Fig. 4c) cross-sections are much similar to the shapes identified in the Figure 2 and also in the Figure 5 of II.2.3.2. section. No oscillations of the arc around the fibres axis were considered, assuming that the spiral central point is always collinearly with the fibre axis.

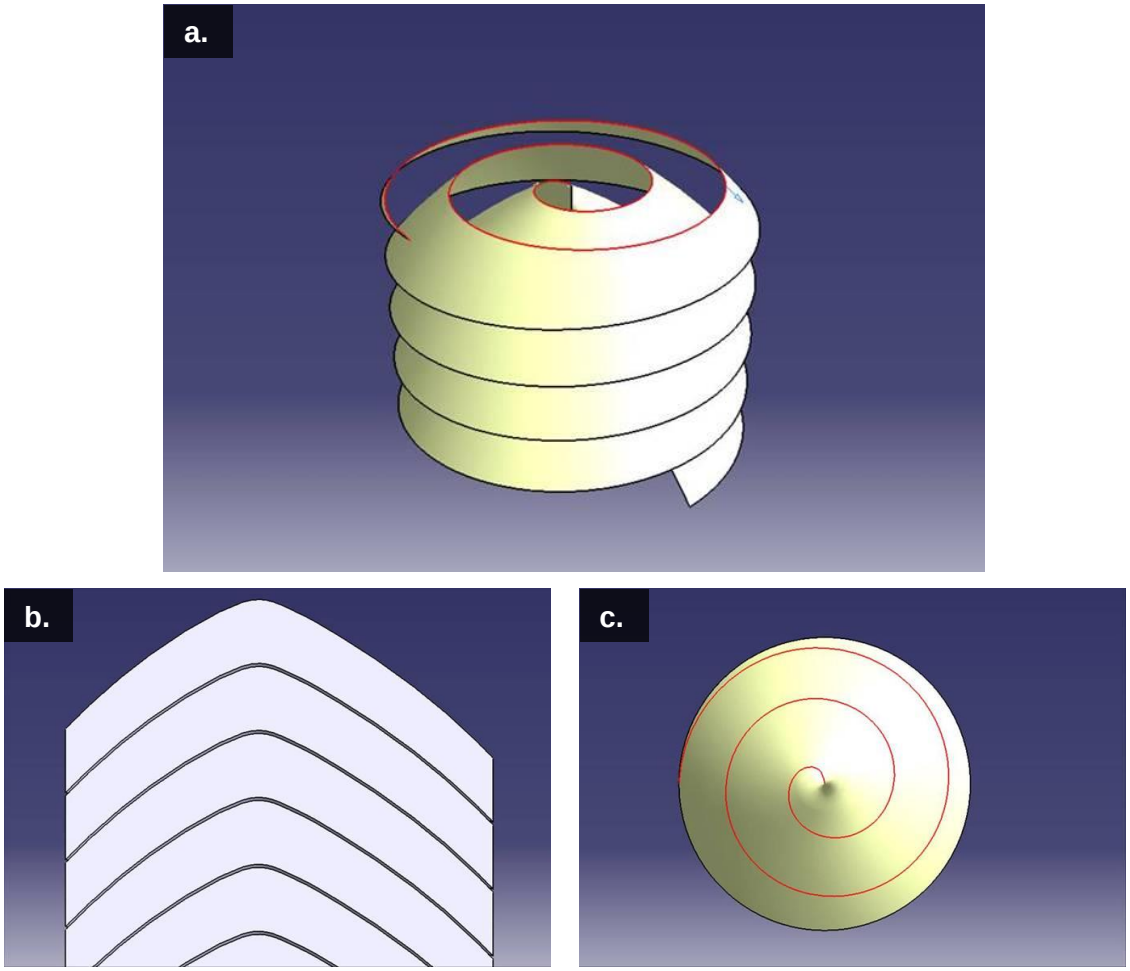


***Figure 4:*** *Illustration obtained by AutoCAD of the* ***(a)*** *the model in perspective, the banding pattern in the* ***(b)*** *longitudinal and* ***(c)*** *transversal cross-sections.*

## References

[1] W. Kurz, R. Trivedi, Banded solidification microstructures, Metallurgical and Materials Transactions A-Physical Metallurgy and Materials Science, 27 (1996) 625-634.

[2] M. Gremaud, M. Carrard, W. Kurz, Banding phenomena in Al-Fe alloys subjected to laser surface-treatment, Acta Metallurgica et Materialia, 39 (1991) 1431-1443.

[3] A. Karma, W.J. Rappel, B.C. Fuh, R. Trivedi, Model of banding in diffusive and convective regimes during directional solidification of peritectic systems, Metallurgical and Materials Transactions A-Physical Metallurgy and Materials Science, 29 (1998) 1457-1470.

[4] I. de Francisco, R.I. Merino, V.M. Orera, A. Larrea, J.I. Peña, Growth of $Al_2O_3/ZrO_2(Y_2O_3)$ eutectic rods by the laser floating zone technique: effect of the rotation, Journal of the European Ceramic Society, 25 (2005) 1341-1350.

## II.3. Directional solidification of $ZrO_2$-$BaZrO_3$ composites with mixed protonic-oxide ionic conductivity

R.G. Carvalho[1], A.J.S. Fernandes[1], R.F. Silva[2], F.M. Costa[1], F.M. Figueiredo[2]

[1]I3N, Department of Physics, University of Aveiro, 3810-193 Aveiro, Portugal

[2]CICECO, Department of Ceramic and Materials Engineering, University of Aveiro 3810-193 Aveiro, Portugal

Solid State Ionics, (2013)

**DOI:** http://dx.doi.org/10.1016/j.ssi.2013.10.051

### Abstract

The synthesis and characterization of directionally solidified yttrium-doped zirconia-barium zirconate eutectic materials by the laser floating zone technique (LFZ) is presented in the search for novel mixed ionic conductors by protons and oxide ions. Emphasis is placed on the control of the LFZ conditions that promote the solubilization of yttrium in both eutectic phases, and how the dopant influences the ionic conductivity. Fast growth under constitutional undercooling conditions leads to the development of $ZrO_2$-dendrites above the solidification interface, which are dipped into a finer-interpenetrated network of $ZrO_2$ and $BaZrO_3$. Yttrium-doping of the $ZrO_2$ fluorite-type lattice is favoured by the high thermodynamic stability of $BaZrO_3$. However, even low Y-substitution levels in $BaZrO_3$ leads to dominating protonic conduction in the composite under humidified atmospheres below 500 ºC. At higher temperatures, the proton incorporation is unfavourable, and the total conductivity of the composite is determined by the hole conduction in the $Ba(Zr,Y)O_3$, and/or oxide ion conductivity through the $(Zr,Y)O_2$.

***Keywords:*** $BaZrO_3$, $ZrO_2$, eutectic, directional solidification, mixed ionic conductivity.

## II.3.1. Introduction

Yttria-stabilized zirconia (YSZ) is the prototypical solid oxide electrolyte for a variety of high temperature electrochemical technologies such as fuel cells, electrolyzers and oxygen sensors due unmatched thermo-chemical stability and compatibility with existing electrode materials. The major drawback of YSZ is the relatively low oxide ion conductivity below 800 °C [1].

Perovskite protonic conductors with general formula $AB_{1-x}C_xO_{3-x/2}$ (A=Ca, Sr or Ba; B=Zr, Ce; C=Y, Yb) have bulk conductivities higher than $10^{-2}$ S/cm at ~500 °C and have thus been considered alternatives for low temperature applications [2,3]. While the protonic conductivity is indeed high, the poor stability of some of these compounds in contact with wet atmospheres or under carbon dioxide (in this case readily forming alkaline earth carbonates [4]) is a major drawback. Yttrium-doped barium zirconate, $Ba(Zr,Y)O_3$, is remarkably more stable than the e.g. the cerates [4], and the bulk protonic conductivity is amongst the highest reported for ceramic protonic conductors [5-7].

The combination of such proton conducting ceramics with an oxide ion conductor into a composite with mixed protonic-oxide ionic conductivity is a potentially interesting approach to develop new multifunctional electrolytes able to operate in a broad range of conditions [8-11]. The concept has been tested with ceria-based oxide conductors and barium cerate protonic conductors [8,10] but, as mentioned above, the thermo-chemical stability of these composites is predictability insufficient.

A zirconia-barium zirconate composite would be a more attractive solution, if it can be made. In fact, the refractoriness and the inherent difficult ceramic processing ability of $Ba(Zr,Y)O_3$ (sintering temperatures higher than 1700 °C are often reported) combined with a high grain boundary resistivity [11] results in an overall low conductivity than can be several orders of magnitude lower than the bulk property [6,7]. Zirconia powders, although available in high quality grades, also require relatively high sintering temperatures.

We have shown that directional solidified eutectic (DSE) fibres of $(ZrO_2)_{0.97}(Y_2O_3)_{0.03}$-$BaZrO_3$ composites with approximately 50 vol.% of each phase (corresponding to the eutectic 29 mol.% $BaZrO_3$-71 mol.% $ZrO_2$ [12]) can be obtained by the laser floating zone (LFZ) method [13]. LFZ takes advantage of the existing eutectic to synthesize this composite by solidification from the melt. These materials feature very large, oriented grains and have an extraordinary low grain boundary density that should minimize the high grain boundary resistance of $Ba(Zr,Y)O_3$. However, the yttrium cations are preferentially located in the $ZrO_2$ lattice, whereas the $BaZrO_3$ remains non-doped, thus precluding protonic transport in the composite. Here, we further explore the potential of LFZ to obtain $ZrO_2$-

$BaZrO_3$ composites with yttrium in both phases to obtain a novel mixed protonic-oxide ionic conductor.

### II.3.2. Experimental

The fibre-shaped samples were grown by melting precursor bars using a 200 W $CO_2$ laser, as previously described [13]. These precursor bars were prepared by cold extrusion of mixtures of $BaCO_3$ (Flucka 99%), $(ZrO_2)_{0.97}(Y_2O_3)_{0.03}$ (Tosho Co.) and $Y_2O_3$ (Sigma-Aldrich, 99.99%), bound with polyvinyl alcohol (PVA, Sigma-Aldrich 99%), with a composition corresponding to 20.5 mol.% BaO, 61.4 mol.% $ZrO_2$ and 18.2 mol.% $YO_{1.5}$. The barium excess in this formulation (molar $ZrO_2$:BaO≈3) with respect to the nominal eutectic composition ($ZrO_2$:BaO≈3.3, or $ZrO_2$:$BaZrO_3$=71:29 [12]) is to compensate for the losses by volatilization during the laser melting. Fibres were grown in air with a pulling rate of 300 mm/h, and the seed and feed bars rotating in opposite direction at 5 revolutions per minute.

The structure of the fibres was analyzed by powder X-ray diffraction (XRD) on a X'Pert MPD Philips diffractometer using Cu-$K_\alpha$ radiation with step width 0.01° and scan rate 0.9°/min. Raman spectra were collected on a T64000 Jobin Yvon spectrometer with a 532 nm laser beam focused on the sample surface through a microscope objective (50x) with a spot of diameter <0.8 mm. The microstructure was studied by scanning electron microscopy (SEM) on a Hitachi S4100 microscope equipped with an energy dispersive spectroscopy (EDS) detector. The fractional area occupied by each phase on SEM images was assessed using Image J 1.45s software, and is assumed to be strongly correlated to the corresponding volume fraction in the composite.

The electrical conductivity was measured by impedance spectroscopy using a Hewlett Packard 4984a LCR meter. The spectra were collected from 20 Hz to 1 MHz with test signal amplitudes of 0.1 V or 1.0 V. Pieces with ~0.5 cm in length were cut from the central part of the fibres for these measurements. Electrodes were applied on both tips of the fibres by brushing a platinum paste and subsequent thermal treatment at 1000 ºC for 1 h. The measurements were carried out under a flow of air or a 95%$N_2$+5%$H_2$ mixture (50 mL/min), either dried through a column with a desiccant, or humidified in distilled water at room temperature ($P_{H_2O}$≈3.5 kPa). The oxygen partial pressure ($P_{O_2}$) was monitored inside the chamber by an YSZ oxygen sensor, whereas the $P_{H_2O}$ in the gas outlet was measured by a resistive humidity sensor. The samples were equilibrated overnight at each atmosphere at around 1000 °C, and the electrical measurements were carried out upon cooling,

giving 30 min at each temperature to ensure stabilization. The impedance spectra were analyzed using ZView (Scribner) to obtain the fibre resistance ($R$) to be used to calculate the conductivity through $\sigma = R^{-1}LS^{-1}$, where $L$ and $S$ are, respectively, the length and the cross section area of the piece of fibre used for the measurement.

### II.3.3. Results and discussion

The yttrium-doped $ZrO_2$-$BaZrO_3$ LFZ fibres grown at 300 mm/h have a similar appearance to those obtained with smaller pulling rates (until 100 mm/h [13]). They have diameters of approximately 1.2 mm and an opaque light grey appearance (Fig. 1A). However, the pulling rate during the laser melting has a major impact on the microstructure, and consequently the properties of the $ZrO_2$-$BaZrO_3$ fibres [13]. Briefly, coarse eutectic regions (called “solidifications bands”) arise from periodic perturbations on the solidification interface, intercalated by a much finer eutectic microstructure. The band inter-distance increases with increasing pulling rate (from 20 mm/h to 100 mm/h), closely matching the solidified length per one turn of the rod. Also, columnar growth (colonies) tends to occur in the inter-band regions for the highest pulling rates, disrupting the coupled eutectic growth characteristic from the low velocities, in agreement with the constitutional undercooling criterion [14]. Another important consequence slow pulling rates is that the yttrium preferentially occupies the $ZrO_2$ lattice due to the comparatively higher thermodynamic stability of $BaZrO_3$. Therefore, since the conductivity of the undoped $BaZrO_3$ is very low, the transport properties of the composites are entirely dominated by the oxide ion conductivity along the yttrium-doped zirconia phase [13].

In the present work, the pulling rate was increased to 300 mm/h in order to almost totally eliminate the $ZrO_2$ bands and to force the solid-liquid interface instability conditions, resulting in dendritic growth within the inter-band regions. This is indeed achieved, as shown by the SEM micrograph in Figure 1B, taken at a section of the growth direction (longitudinal) of the fibre depicted. Dendrites of $ZrO_2$ (dark grey phase in Fig. 1B) with lengths varying from 20 to 300 $\mu$m tend to have their main arm inclined with respect to the fibre axis. This single-phase instability is the result of a heavy constitutional undercooling in the boundary layer built up ahead of the solid/liquid interface, where the *liquidus* temperature of off-eutectic compositions is higher than the eutectic. Consequently, the primary zirconia phase is undercooled and tends to grow faster than the eutectic. The finer interdendritic eutectic microstructure develops with a coupled morphology of both phases (light grey is $BaZrO_3$) within a scale of 1 $\mu$m or smaller (inset). Based on the areas occupied by each phase on the image, the composition in these regions roughly corresponds

to 50 vol.% $ZrO_2$ - 50 vol.% $BaZrO_3$, in agreement with the nominal eutectic composition 71 mol.% $ZrO_2$ - 29 mol.% $BaZrO_3$ [12]. As expected for DSE materials, intra-phase boundaries are not observed in any region of the fibre, suggesting phase contiguity of both phases, and also that the grain boundary density in these materials is indeed very small.

Panel C in Figure 1 shows the EDS elemental mapping for the yttrium distribution in the interdendritic regions of the fibre grown at 300 mm/h. Only regions larger than the spatial resolution of EDS (~1 $\mu$m) were selected for analysis, in order to avoid the cross signal contributions from one phase to the other. This was verified by identifying the presence of Ba only in the light grey $BaZrO_3$ phase. The yttrium map shows that the higher pulling rate used in this work can effectively promote the solubilization of yttrium also in the $BaZrO_3$. However, the intensity is clearly higher in the $ZrO_2$ than in the $BaZrO_3$, which confirms our previous finding that yttrium prefers the fluorite lattice [13]. This is also in agreement with the equilibrium diagram of the $ZrO_2$-BaO-$YO_{1.5}$ ternary system, where the strong thermodynamic stability of $BaZrO_3$ in this ternary system prevails for low $YO_{1.5}$ contents [15].

The powder XRD pattern shown in Figure 1D confirms the mixture of $BaZrO_3$ and $ZrO_2$ as the only crystalline phases present in the fibres. The $ZrO_2$ diffraction maxima can be indexed to the cubic or tetragonal crystal structures. However, in light of known phase diagrams and considering the high yttria content, the fluorite-type cubic structure is retained for indexation.

This analysis of the XRD patterns is fully confirmed by the Raman data presented in Figure 1E, where only the peaks corresponding to $Ba(Zr,Y)O_3$ and $(Zr,Y)O_2$ phases are identified. The bands at 151, 275, 561, 597 and 678 $cm^{-1}$ are due to cubic $(Zr,Y)O_2$ [16]. The $(Zr,Y)O_2$ dominant band at ~597 $cm^{-1}$ can be assigned to a triply degenerated $F_{2g}$ mode, which corresponds to the out-of-phase stretching of Zr/O bounds. The position of this band represents a significant shift with respect to undoped $ZrO_2$ (where it appears at 617 $cm^{-1}$), which correlates to doping levels in excess of 30 mol.% $YO_{1.5}$ [16]. The weak broad band at 194 $cm^{-1}$ denotes a residual amount of monoclinic $ZrO_2$ [17]. The remaining bands at 225, 383, 470 and 746 $cm^{-1}$ can be ascribed to doped-barium zirconate, since only the non-cubic symmetry has Raman-active modes [18]. These modes result from local structural distortions promoted by the presence of oxygen vacancies [18]. While the Y-doping in barium zirconate seems to be confirmed, the broadening (by 50-80 $cm^{-1}$) and shift (from 740 to 725 $cm^{-1}$) of the band appearing at the highest Raman shift (740-750

$cm^{-1}$), which has been correlated to an increase of yttrium content in $Ba(Zr_{1-x,}Y_x)O_{3-\delta}$ from 1 to 15 at.% [19], suggests that the dopant concentration is indeed small.

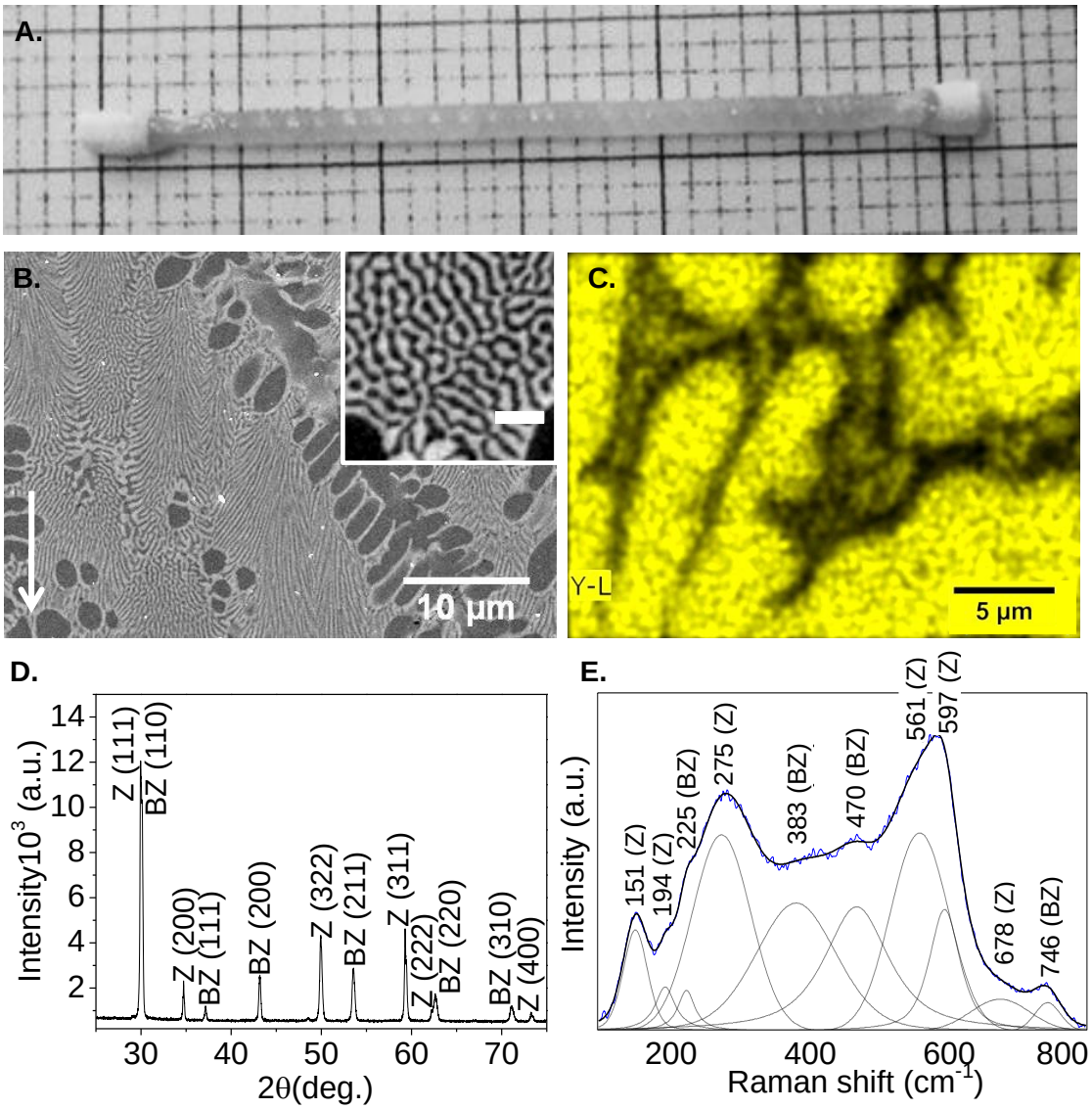


***Figure 1:*** *Structural and microstructural characterization of the yttrium-containing zirconia-barium zirconate fibre grown at 300 mm/h:* ***(A)*** *typical appearance of the fibres;* ***(B)*** *SEM micrograph of the longitudinal section showing the eutectic microstructure of zirconia (dark) and barium zirconate (light grey), with the inset showing a zoomed, contrast-enhanced view with a scale bar of 3 µm and the arrow indicating the growth direction;* ***(C)*** *EDS map showing the yttrium distribution;* ***(D)*** *powder XRD pattern indexed according to $BaZrO_3$ (BZ, JCPDS card file nº 01-074-1299) and cubic zirconia (Z, JCPDS card file nº 04-015-0405); and (E) Raman spectrum.*

In summary, both the XRD and Raman data agree with the SEM/EDS analysis to show that the yttrium incorporation in $BaZrO_3$ in the presence of $ZrO_2$ is not easy to achieve due to the highly thermodynamic stability of $BaZrO_3$, in agreement with the known ternary

phase diagram [15]. Nevertheless, even such small amount of yttrium in $BaZrO_3$ has a major impact on the ionic conductivity of the fibres, as it will be further demonstrated.

Figure 2 shows typical impedance spectra obtained at ~370 °C for the $(Zr,Y)O_2$-$Ba(Zr,Y)O_3$ eutectic fibres exposed to dry and wet atmospheres, all dominated by one single, nearly perfect semicircle. This semicircle is observed up to temperatures as high as 800 °C with a capacitance of about 10 pF, which is due to the stray capacitance of the platinum wires of the experimental set-up, in series with the sample. Note that due to the particular geometric factor of the fibres ($SL^{-1}\approx0.02$), the expected capacitance generated by the bulk ionic relaxation ($C_b=\varepsilon_r\varepsilon_0 SL^{-1}$, where $\varepsilon_r$ is the bulk relative permittivity - taken as 30 - and $\varepsilon_0$ is the permittivity of the vacuum) should be of the order of 0.05 pF, which is much smaller than the measured value. Therefore, no direct correlation can be established between the spectra and the fibre microstructural characteristics, namely the absence of intra-phase grain boundaries. However, admitting the brick layer model of ionic transport in a polycrystalline ceramic [20], it is possible to estimate a grain boundary capacitance ($C_{gb}=C_b G\delta^{-1}$) of the order of 265 pF for an average grain size ($G$) of 10 µm and a grain boundary thickness ($\delta$) of 2 nm [20]. This value is much larger than the stray capacitance (<10 pF), which combined with the expectedly high grain boundary resistance (particularly for $BaZrO_3$), should originate a second semicircle at low frequencies. The absence of such additional semicircle indirectly supports the low density of grain boundaries of these DSE composites suggested by SEM.

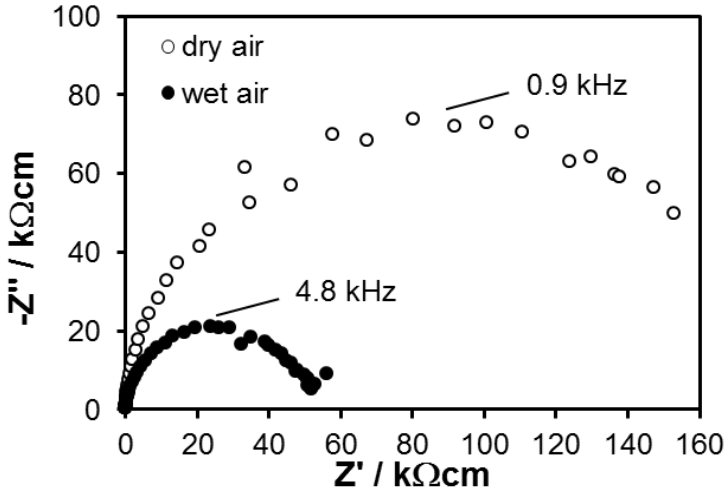


***Figure 2:*** *Nyquist plots of a $(Zr,Y)O_2$-$Ba(Zr,Y)O_3$ fibre measured at 367 °C in humidified and dry air atmospheres.*

Figure 2 also depicts a significant decrease of the total resistance under humidified air, which can be explained by the proton incorporation and transport in $Ba(Zr,Y)O_3$. In parallel

with the proton diffusion in the zirconate, oxide ion transport through $(Zr,Y)O_2$ is also expected to occur. However, the expectedly high yttrium content in the zirconia may lead to a oxide ion conductivity lower than usually observed for the reference solid electrolyte composition with 8 mol.% $Y_2O_3$ (see dotted lines in Fig. 3). Since the proton incorporation in $Ba(Zr,Y)O_3$ becomes thermodynamically unfavourable with increasing temperature, a decrease of the protonic conductivity is expected above a certain temperature (noticeably above 500 °C) [6]. Moreover, in oxidizing conditions ($P_{O_2}$>10 Pa) and in the absence of a proton source (humidity or hydrogen), the p-type electronic conductivity of $Ba(Zr,Y)O_3$ predominates, whereas under reducing conditions the hole concentration is decreased and the material is a protonic solid electrolyte [5,6].

The total conductivity of the fibre is shown in Figure 3 as a function of the temperature under dry and humidified oxidizing and reducing conditions. The global trend seems to reflect the predominance in the composite of the transport properties of the $Ba(Zr,Y)O_3$. At temperatures below 500 °C, the conductivity in the humid atmospheres ($P_{H_2O}$≈3.5 kPa) is higher than in the corresponding dry environments, indicating dominant proton transport, which is reinforced by the low apparent activation energy in the 320-500 °C temperature range (35 kJ/mol in $N_2$+$H_2$ and 48 kJ/mol in air), typical of proton migration [6]. Above 500 °C, the progressive increase of the activation energy (reaching values close to 90 kJ/mol) indicates an increasing role of another charge carrier, either the electron holes along the barium zirconate or oxide ions in the zirconia, or even mixed transport. At intermediate temperatures, the higher conductivity in air with respect to 90%$N_2$+10%$H_2$ (in dry atmospheres and to a smaller degree also in humid conditions) suggests that electron holes in the zirconate are the dominating charge carriers, whereas, at high temperature, the convergence of the 4 sets of data with literature data for the bulk conductivity of a heavily yttrium-doped zirconia (30 mol.% $YO_{1.5}$) (dotted lines) indicates an increasing role of the oxide ion conductivity through the zirconia phase. We recall that the high yttria content in the $ZrO_2$ phase suggested by the electrical measurements is in good agreement with the EDS and the Raman spectra. Likewise, the comparison of the fibre low temperature conductivity measured in humid conditions with the published bulk conductivity of $Ba(Zr_{1-x},Y_x)O_{3-\delta}$ x=0.02 [6], x=0.05, 0.10 and 0.15 [7] (red solid lines in Fig. 3) agrees well with the low yttrium content in the zirconate suggested by EDS.

A more fine analysis of the data in Figure 3 is possible by invoking a simple equivalent circuit model. In such composites, the oxide ion and proton transport pathways are parallel along the zirconia and the barium zirconate phases, respectively. Under wet atmosphere and low $P_{O_2}$ (such as the 90%$H_2$+10%$N_2$ mixture), the simplest description of the

electrical behaviour of these composites can be based on an equivalent circuit comprising two resistors in parallel, one ($R_O^Z$) accounting for oxide ions in the zirconia, and another branch ($R_H^{BZ}$) accounting for the proton transport in the zirconate, which predominates in these conditions (oxide ion transport is negligible [21]). This circuit has an equivalent resistance $R_{eq}=R_H^{BZ}R_O^Z(R_H^{BZ}+R_O^Z)^{-1}$, which can be easily demonstrated to be dominated by smallest resistance. If we now look at the properties of the phases involved, the oxide ionic conductivity of zirconia is not affected by the atmosphere (within the range covered) and, when heavily doped with yttrium, has a (high) activation energy of ~120 kJ/mol (for 30 mol.% $Y_2O_3$ [22]). The activation energy for the bulk protonic conductivity of the barium zirconate (~45 kJ/mol [6,7]) is about one third of the activation energy for the oxide ion conductivity in zirconia. This means that the resistance associated to the latter phase decreases at a rate that is almost 3 fold that for the decrease of the resistance of barium zirconate, with increasing temperature. On the other hand, the hydration of the barium zirconate becomes thermodynamically unfavourable with increasing temperature, particularly above 500 °C [6]. These two factors combine to significantly increase the resistance of the zirconate relatively to the zirconia, and somewhere close to 650 °C the conductances associated to the two processes are equalized (or $R_O^Z \approx R_H^{BZ}$). Above this temperature, it should be the higher conductance of zirconia dominating the conductivity of the composite (or in terms of resistance $R_{eq}^Z \approx R_O^Z$). This explains the trends evolving from the comparison of the conductivity data obtained in wet and dry $N_2$+$H_2$ gas mixtures shown in Figure 3, including the high activation energy at high temperatures (expected for heavily Y-substituted zirconia).

Under oxidizing conditions (e.g. air), the barium zirconate has significant p-type electronic conductivity, and the equivalent circuit must be modified to include a third parallel resistor accounting for the electronic transport ($R_p^{BZ}$). If, in addition, the humidity is low (e.g. in dry air), the hydration level and thus the protonic conductivity of the zirconate will be very small. In these conditions and over the entire temperature range (or at least until 900 °C), the p-type electronic resistance should be the smallest, and hence $R_{eq} \approx R_p^{BZ}$. The result is an Arrhenius dominated by the p-type electronic conductivity of the zirconate, in agreement with the observed single slope (activation energy 92 kJ/mol) depicted by the dry air data in Figure 3, and also with the p-type electronic conductivity data reported in the literature for lightly yttrium-doped barium zirconate [23]. In wet air, the protonic transport comes in, decreasing the activation energy and increasing the conductivity at low temperature. Increasing the temperature decreases the protonic conductivity, and at approximately 450 °C the conductivity measured in wet air equalizes the values measured

in dry air. Since, in addition, the electronic conductivity of the zirconate increases for low humidity [21], than we can also understand the highest conductivity observed in dry air at the intermediate temperature range (500-900 °C) as due to electron hole transport in the barium zirconate.

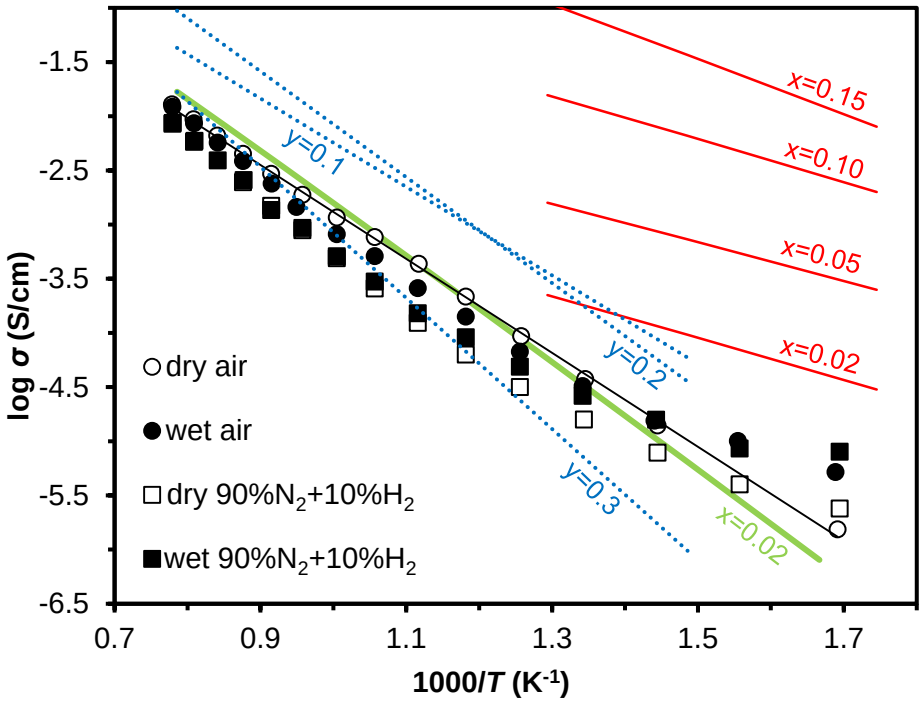


***Figure 3:*** *Arrhenius plot of the total conductivity (black symbols) of a $(Zr,Y)O_2$-$Ba(Zr,Y)O_3$ fibre measured in wet and dry atmospheres of atmospheric air and 90%$N_2$+10%$H_2$. The black line is the linear fit to the data obtained in dry air (activation energy 92 kJ/mol). Literature data for the (red solid lines) bulk protonic conductivity of $BaZr_{1-x}Y_xO_{3-\delta}$ (x=0.02 [6], x=0.05, 0.10 and 0.15 [7], all at $P_{H_2O}$≈23 kPa), the (green thicker line) p-type electronic conductivity of $BaZr_{0.98}Y_{0.02}O_{3-\delta}$ at $P_{H_2O}$≈0.04 kPa [23], and (blue dotted lines) for the $(ZrO_2)_{1-y}(YO_{1.5})_y$ [22] are given for comparison.*

### II.3.4. Conclusions

The initial difficulties in promoting the yttrium-substitution on the barium zirconate phase of directionally solidified $ZrO_2$-$BaZrO_3$ composites produced by LFZ [13] can be overcome by increasing both the yttrium content in the initial zirconia precursor, and especially by using fast pulling rates of 300 mm/h or higher. The microstructure along the growth direction of these fibres showed well-aligned $ZrO_2$ dendrites enclosed in a finer-interpenetrated eutectic matrix, with 50 vol.% $ZrO_2$ - 50 vol.% $BaZrO_3$. The yttrium dopant is predominantly in the fluorite-$ZrO_2$ lattice due to the high thermodynamic stability of $BaZrO_3$, as revealed by Raman spectroscopy and corroborated by EDS analysis. The mixed

ionic transport properties of the fibres were confirmed by impedance spectroscopy, with proton conduction along $Ba(Zr,Y)O_3$ prevailing under humidified atmospheres at temperatures lower than 500 ºC. At higher temperatures, the oxide vacancies or electron holes are the predominant charge carriers.

**Acknowledgements**

Work funded by FCT (Portugal) through projects CICECO PEst-C/CTM/LA0025/2011 and I3N PEst-C/CTM/LA0011/2011. R.G. Carvalho acknowledges FCT for a PhD grant (SFRH/BD/64891/2009).

**References**

[1] B.C.H. Steele, A. Heinzel, Materials for fuel-cell technologies, Nature, 414 (2001) 345-352.

[2] H. Iwahara, T. Yajima, T. Hibino, K. Ozaki, H. Suzuki, Protonic conduction in calcium, strontium and barium zirconates, Solid State Ionics, 61 (1993) 65-69.

[3] T. Norby, Y. Larring, Concentration and transport of protons in oxides, Current Opinion in Solid State & Materials Science, 2 (1997) 593-599.

[4] K.H. Ryu, S.M. Haile, Chemical stability and proton conductivity of doped $BaCeO_3$-$BaZrO_3$ solid solutions, Solid State Ionics, 125 (1999) 355-367.

[5] T. Schober, H.G. Bohn, Water vapor solubility and electrochemical characterization of the high temperature proton conductor $BaZr_{0.9}Y_{0.1}O_{2.95}$, Solid State Ionics, 127 (2000) 351-360.

[6] K.D. Kreuer, S. Adams, W. Münch, A. Fuchs, U. Klock, J. Maier, Proton conducting alkaline earth zirconates and titanates for high drain electrochemical applications, Solid State Ionics, 145 (2001) 295-306.

[7] F. Iguchi, T. Tsurui, N. Sata, Y. Nagao, H. Yugami, The relationship between chemical composition distributions and specific grain boundary conductivity in Y-doped $BaZrO_3$ proton conductors, Solid State Ionics, 180 (2009) 563-568.

[8] B. Zhu, X. Liu, T. Schober, Novel hybrid conductors based on doped ceria and BCY20 for ITSOFC applications, Electrochemistry Communications, 6 (2004) 378-383.

[9] A.V. Virkar, Transport through mixed proton, oxygen ion and electron (hole) conductors: Goldman-Hodgkin-Katz-type equation, Journal of Power Sources, 194 (2009) 753-762.

[10] W. Sun, Y. Jiang, Y. Wang, S. Fang, Z. Zhu, W. Liu, A novel electronic current-blocked stable mixed ionic conductor for solid oxide fuel cells, Journal of Power Sources, 196 (2011) 62-68.
[11] M. Shirpour, R. Merkle, J. Maier, Space charge depletion in grain boundaries of Ba-$ZrO_3$ proton conductors, Solid State Ionics, 225 (2012) 304-307.
[12] J.O.A. Paschoal, H. Kleykamp, F. Thümmler, Phase equilibria in the pseudoquaternary BaO-$UO_2$-$ZrO_2$-$MoO_2$ system, Journal of Nuclear Materials, 151 (1987) 10-21.
[13] R.G. Carvalho, F.M. Figueiredo, A.J.S. Fernandes, R.F. Silva, F.M. Costa, Laser Melting Processing of $ZrO_2$-$BaZrO_3$ Ceramic Eutectics, Science of Advanced Materials, 5 (2013) 1847-1856.
[14] B. Chalmers, Principles of Solidification, John Wiley & Sons, Inc., New York, 1964.
[15] Y. Oyama, A. Kojima, X. Li, R.B. Cervera, K. Tanaka, S. Yamaguchi, Phase relation in the BaO-$ZrO_2$-$YO_{1.5}$ system: Presence of separate $BaZrO_3$ phases and complexity in phase formation, Solid State Ionics, 197 (2011) 1-12.
[16] M.B. Pomfret, C. Stoltz, B. Varughese, R.A. Walker, Structural and compositional characterization of yttria-stabilized zirconia: Evidence of surface-stabilized, low-valence metal species, Analytical Chemistry, 77 (2005) 1791-1795.
[17] D. Gazzoli, G. Mattei, M. Valigi, Raman and X-ray investigations of the incorporation of $Ca^{2+}$ and $Cd^{2+}$ in the $ZrO_2$ structure, Journal of Raman Spectroscopy, 38 (2007) 824-831.
[18] M. Karlsson, I. Ahmed, A. Matic, S.G. Eriksson, Short-range structure of proton-conducting $BaM_{0.10}Zr_{0.90}O_{2.95}$ (M = Y, In, Sc and Ga) investigated with vibrational spectroscopy, Solid State Ionics, 181 (2010) 126-129.
[19] F. Giannici, M. Shirpour, A. Longo, A. Martorana, R. Merkle, J. Maier, Long-Range and Short-Range Structure of Proton-Conducting Y:$BaZrO_3$, Chemistry of Materials, 23 (2011) 2994-3002.
[20] X. Guo, R. Waser, Electrical properties of the grain boundaries of oxygen ion conductors: acceptor-doped zirconia and ceria, Progress in Materials Science, 51 (2006) 151-210.
[21] V. Gorelov, V. Balakireva, A. Kuz'min, Ionic, proton, and oxygen conductivities in the $BaZr_{1-x}Y_xO_{3-\alpha}$ system (x=0.02-0.15) in humid air Russian Journal of Electrochemistry, 46 (2010) 890-895.
[22] S. Ikeda, O. Sakurai, K. Uematsu, N. Mizutani, M. Kato, Electrical conductivity of yttria-stabilized zirconia single crystals, Journal of Materials Science, 20 (1985) 4593-4600.

[23] A. Kuz'min, V. Balakireva, S. Plaksin, V. Gorelov, Total and hole conductivity in the $BaZr_{1-x}Y_xO_{3-\alpha}$ system (x=0.02-0.20) in oxidizing atmosphere, Russian Journal of Electrochemistry, 45 (2009) 1351-1357.

# Chapter III

## Zirconia-mullite directionally solidified eutectic

*This chapter starts with an overview of mullite and zirconia-mullite composite materials, with special emphasis to the processing methods and the mechanical and electrical properties, envisaging advanced applications (III.1.).*

*The investigation done in the zirconia-mullite DSE materials was described in three SCI papers, one extended abstract and one conference proceedings work. The chapter is divided in three main sections corresponding to the contents of the more extensive publications in scientific journals.*

*The earliest results in the zirconia-mullite DSE fibres were introduced in an extended abstract published at the Microscopy and Microanalysis journal with the title: "Microstructure of mullite-zirconia fibres grown by directional solidification". A detailed paper on this subject was then published with a full description of the processing of the zirconia-mullite composite fibres according to eutectic and off-eutectic compositions and the influence of the growth parameters on the final microstructure and phase development (III.2.).*

*The electrical properties of the zirconia-mullite DSE fibres were briefly reported in the proceedings paper of IS-AF/ECAPD/PFM conference 2012 untitled: "Ionic conductivity of eutectic mullite-zirconia fibres". Thereafter, in the full-length paper the ionic conductivity of zirconia-mullite DSE fibres was explored, as a potential dual-phase solid oxide electrolyte for high temperature applications (III.3.).*

*The final section of this chapter is focused on the mechanical behaviour of the zirconia-mullite DSE fibres and corresponds to a submitted paper to a SCI journal. The microstructural design allowed by directional solidification and the intrinsic nature of the constituent phases are under scrutiny (III.4.).*

## III.1. Overview of mullite and mullite-matrix composites

### III.1.1. Processing and thermomechanical behaviour

Mullite ($M$$Al_2O_3$-$N$$SiO_2$, with $M/N$ varying from 3/2 to 2 approximately) is one of the most interesting engineering ceramics. The reason for such interest is mainly linked to the combination of high temperature fracture strength, high creep resistance, low thermal expansion coefficient, low thermal conductivity and phase stability, up to the melting point [1]. Chemical composition has an important effect on the high strength and fracture toughness ($K_{IC}$) and their retention for high temperatures, having a great potential for high-temperature structural applications (as the example in Fig. 1) [2].

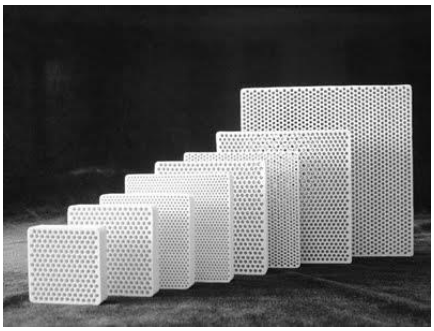

***Figure 1:*** *Ceramic honeycomb filter used in the foundry industry for the casting of molten metal. This honeycomb ceramic component can filter impurities, reduce casting porosity, and improve casting quality [2,3].*

Guse et al. obtained the earliest large single-crystals of mullite using the Czochralski technique [4]. Well-oriented crystals were grown at 1.5 mm/h in nitrogen environment, along [100] or [001] growth directions [4]. In 1990, Shindo used the slow cooling float zone (SCFZ) method with a quartz halogen lamp furnace to prepare single-crystal mullite (from 5 to 70 mm in size) from alumina and silica powders [3]. The compositional analysis performed along the transversal cross-section revealed that melt-grown methods conduct to $2Al_2O_3$-$SiO_2$ (2:1) mullite stoichiometry [5]. Sayir et al., starting from precursors with $3Al_2O_3$-$2SiO_2$ (3:2) nominal composition also grown 2:1 mullite polycrystalline fibres by the LFZ method. It was reported the “bamboo-like” surface is due to the highly incorporation of gas bubbles. However, fibres exhibited tensile strength values of 550-1450 MPa at room temperature [6]. Even though a glassy phase was present between neighbouring grains, the tensile strength kept values between 560 to 630 MPa up to 1400 ºC [6]. Recently, 2:1 single-crystal mullite fibres, having small microstructural defects were downward pulled at 10 mm/h, by the LFZ method [7]. Polycrystalline fibres grown by the same method from 40 to 100 mm/h showed faceted mullite grains, which were well-aligned with

the growth direction. Amorphous silicate enrichment was found at the grain-boundaries, which is typical of melt-techniques [6,7]. Lamellar inclusions at the single-crystal fibres (10 mm/h) lead to the reduction of room temperature fracture toughness (1.2 MPa.$m^{1/2}$) and flexural strength (431 MPa) compared to polycrystalline fibres (631 MPa and 1.6 MPa.$m^{1/2}$) [7]. The fracture toughness enhancement obtained for polycrystalline fibres was ascribed to well-oriented grain boundaries which are really effective precluding crack propagation, contrarily to the free crack development observed in the single-crystal ones [7].

The reinforcement of mullite using different energy-dissipating agents (i.e. metals, fibres, whiskers, platelets or particles) has been under investigation for long time. These reinforcement agents promote the deflection of the crack path or even preclude its own progress. In this sense, it has been evaluated the reinforcement of mullite-matrix composites with aligned non-oxide fibres or whiskers as carbon-fibres and SiC-fibres or whiskers. These systems revealed a significant improvement of the fracture toughness and bending strength (σ) with respect to the values obtained for pure-mullite [3]:

- **i.** Carbon-fibres reinforced mullite composites reveal a bending strength at room temperature of 610 MPa instead of the 380 MPa for monolithic mullite. The strength increases up to 882 MPa at 1200 ºC. Moreover, the fracture toughness increases up to 18 MPa.$m^{1/2}$ contrary to 2.6 MPa.$m^{1/2}$ for mullite and almost did not change with temperature [2].
- **ii.** SiC-fibres reinforced mullite composites showed a remarkable increase of bending strength and fracture toughness at room temperature to 840 MPa and 33.8 MPa.$m^{1/2}$ over the 260 MPa and 2 MPa.$m^{1/2}$ for monolithic mullite, respectively [2].
- **iii.** SiC-whiskers ($SiC_w$) reinforced mullite showed a high level of bending strength (>500 MPa) up to 1300 ºC, but the values drop drastically above 1300 ºC. Such might be promoted by the deterioration of the mullite matrix and by the chemical reactions between the whiskers and the matrix. It was observed that the increase of the bending strength and fracture toughness is controlled by the $SiC_w$ amount, The addition of 40 vol.% $SiC_w$ lead to an increase of bending strength from 320 to 940 MPa and fracture toughness from 2.7 to 6.9 MPa.$m^{1/2}$ [2,3].

Despite these examples, the enhancement of the mechanical behaviour is obtained only if appropriate chemical bonding between fibres and the matrix is reached. Oxidation is the biggest issue at the interface between the mullite matrix and the fibres or whiskers leading

to a sudden degradation of the mechanical properties. Furthermore, the mechanical behaviour improvement is restricted to the perpendicular direction to the fibres loading. Table 1 resumes the five major ceramic reinforcing mechanisms and reinforcement phase morphologies along with some material examples [8].

***Table 1:*** *Ceramic toughening mechanisms [8].*

| Mechanism/morphology | Highest fracture toughness ($MPa.m^{1/2}$) | Example materials |
|---|---|---|
| Transformation | ≈20 | $ZrO_2$ (MgO) |
| Microcracking | ≈10 | $Al_2O_3/ZrO_2$, $SiC/TiB_2$, $Si_3N_4/SiC$ |
| Metal dispersion | ≈25 | $Al_2O_3$/Al, $Al_2O_3$/Ni |
| Whiskers/platelets | ≈15 | $Si_3N_4/SiC$, $Si_3N_4/Si_3N_4$, $Al_2O_3/SiC$ |
| Fibres | ≥30 | $Al_2O_3/SiC$, SiC/C, $Al_2O_3/Al_2O_3$, SiC/SiC |

Transformation toughening is achieved by the incorporation of a second phase which is responsible for phase transition. Garvie et al. introduced the potential of zirconia for increasing both the strength and fracture toughness of ceramic materials, taking advantage of the phase transformation of the metastable tetragonal particles to monoclininc induced by the stress field ahead of the crack [9]. Furthermore, the addition of lower valence oxides, such as CaO, MgO and $Y_2O_3$ etc, can result in stabilization of tetragonal zirconia, which helps on such transformation toughening process. The further addition of the oxide-stabilizer results in the stabilization of cubic phase, which does not have the transformation toughening behaviour. So, the zirconia toughening requires the presence of the metastable tetragonal zirconia phase. The stability of the tetragonal structure can be ruled by three factors: the grain size, the constraint from a surrounding matrix, and the amount of dopant additions [10-12]. These factors also highly depend on the processing of such composites requiring a careful selection of compositions and advanced processing technology to achieve the desired microstructures [13]. The critical zirconia grain size for tetragonal phase retention was linked to yttria concentration according to Figure 2. For example, a composition containing 1.5 mol.% $Y_2O_3$ precludes the tetragonal retention, grain growth during sintering leading to an average grain size higher than 0.2 $\mu$m. The pure $ZrO_2$ is completely monoclinic for all grain size. The increase in the critical grain-size with increasing $Y_2O_3$ content is consistent with the theoretical prediction that the critical grain-

size would increase as the magnitude of the change in chemical free-energy decreases [14].

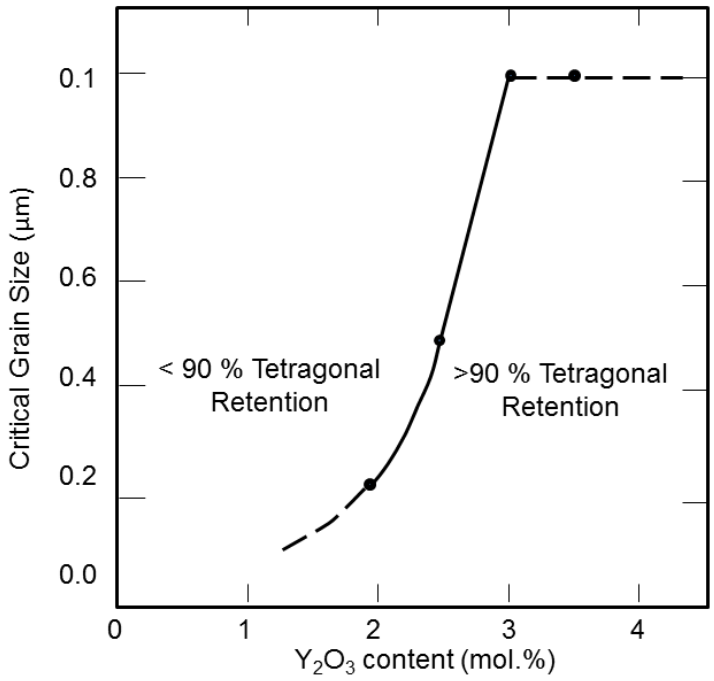


***Figure 2:*** *Retention of tetragonal phase as function of the critical grain size and yttria content in zirconia [14].*

Zirconia-mullite composites can thus benefit from the interesting thermomechanical behaviour of mullite and transformation toughening effect of zirconia. The zirconia-mullite mechanical behaviour is influenced by the composite microstructure, which was found to change considerably with the starting material composition and the processing method [2]. The $ZrO_2$ grains are preferentially dispersed intergranularly and/or intragranularly in the mullite matrix. Consequently, the toughness requirements will depend upon an extremely high density, the finest possible microstructure, highest possible purity, high bonding strength, and minimum internal stresses due to differences in thermal expansion. Becher have shown that the material design relies heavily on the control of the material properties and microstructural components influencing the toughening behaviour in order to optimize the contributions of both the reinforcing and the matrix phase [13].

Several toughening mechanisms by zirconia addition to mullite were proposed: stress-induced, microcracking, grain boundary strengthening, surface compression toughening, crack bowing and crack deflection, as depicted in Figure 3 [15].

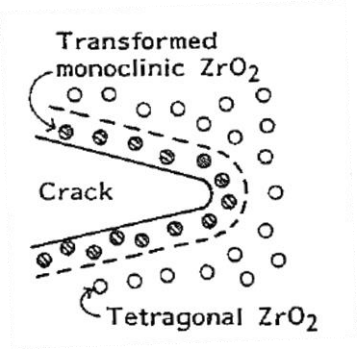


**Stress-induced toughening**, due to the tetragonal to monoclinic phase transformation of zirconia

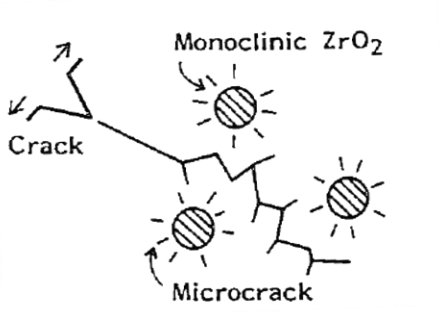


**Microcrack toughening**, due to the thermal expansion mismatch of zirconia particles and mullite matrix

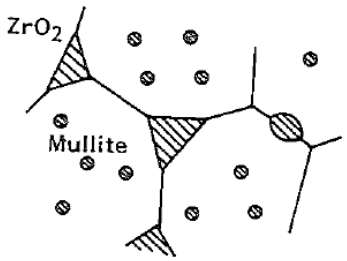


**Grain-boundary strengthening**, due to metastable zirconia incorporation into the mullite matrix.

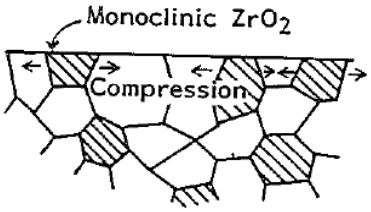


**Surface-compression toughening**, due to the presence of monoclinic zirconia at the surface of samples.

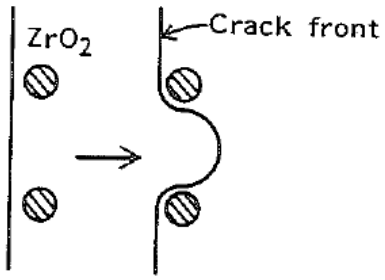


**Crack bowing** at zirconia grains.

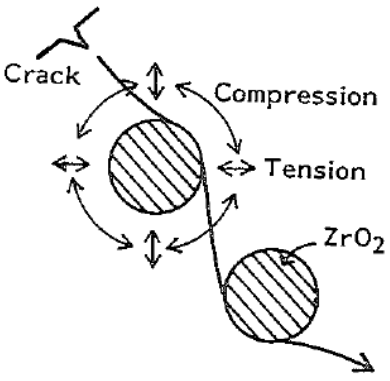


**Crack deflection** at zirconia grains, strengthened by thermal compression.

***Figure 3:*** *Illustration of proposed toughening mechanisms by zirconia addition to mullite [2].*

It is generally recognized that the toughening improvement is mainly enhanced via two mechanisms: stress-induced and microcracking [2,16].

Stress-induced zirconia toughening corresponds to phase transformation mechanism through which decreases the driving force that is responsible by the propagated crack. If the composite contains metastable tetragonal zirconia particles dispersed in the matrix, the large stresses at the tip crack can force the transformation to their thermodynamically stable monoclinic form. This is accompanied by volume expansion (4-6%) and shear strain (~14%), providing a compressive stress field which will block the further crack propagation [15,17]. In resume, the fracture toughness of brittle composite material ($K_{IC}^{C}$) is given by [16,18,19]:

$$K_{IC}^{C} = K_{IC}^{M} + \Delta K_{IC}^{T} \tag{3.1}$$

where $K_{IC}^{M}$ is the matrix toughness and $\Delta K_{IC}^{T}$ is the contribution associated with the transformation of tetragonal zirconia particles. If a suitable distribution of t-$ZrO_2$ metastable particles is obtained, the tetragonal to monoclinic transformation is stress-activated in the stress field. The volume change creates a compressive strain field around the crack tip opposing to the crack propagation, while the strain energies ascribed to the net shear component of the transformation strain in the transformation zone contributes to an effective increase in the energy of fracture [18]. The latter can be described as [19]:

$$\Delta K_{IC}^{T} = AVE^{C}e^{T}(r_T)^{1/2} \tag{3.2}$$

where $A$ is a constant which depends on the type of stress responsible for trigger the zirconia particles transformation (0.45 to 0.5 for shear stress and 0.2 to 0.25 for principal stresses), $V$ is the volume fraction of the transformable zirconia, $E^C$ is the Young's modulus of the composite, $e^T$ is the dilatant transformation strain and $r_T$ is the radius of the transformation zone along the crack path. The later parameter is a function of the maximum stress intensity that the crack tip can support, which will be dependent on the $K_{IC}^{M}$, and the stress needed to transform a tetragonal particle ($\sigma_T^T$) [19]:

$$r_T = B(K_{IC}^{M}/\sigma_T^T)^2 \tag{3.3}$$

where $B$ is a stress-related constant. Notice that the toughening in $ZrO_2$-based composites is ruled by the temperature when transformation toughening occurs.

Microcraking toughening occurs by the residual stress associated with the volume variations promoted by the zirconia transformation. So, microcracking occurs by the spontaneous transformation during cooling in the post-synthesis. The fracture toughness can be increased by the growth of the microcracks and their interaction with the tip of the main crack. This toughening mechanism requires the minimization of the microcrack size, in order to avoid their linkage. Otherwise, microcracks will deteriorate the matrix and lower

the composite fracture toughness. So, the better toughening performance would be reserved for well-dispersed microcracks. Notice that zirconia particles, even in low amounts, revealed better improvement of fracture toughness over the $SiC_w$ reinforced mullite (Fig. 4) [2].

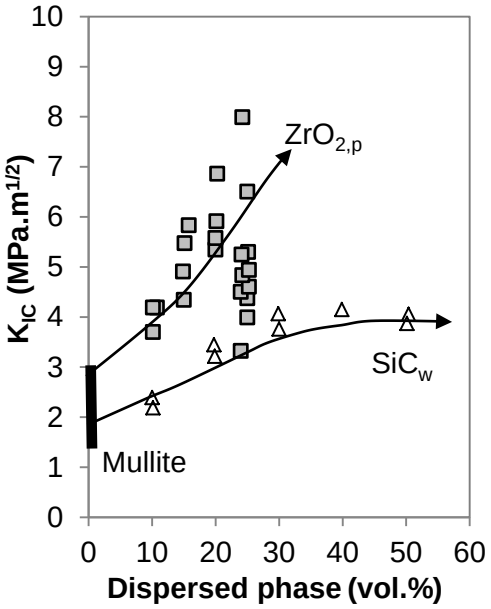


***Figure 4:*** *Relationship between fracture toughness of $ZrO_2$-particles-mullite ($ZrO_{2,p}$) and content of dispersed particles, adapted from [2].*

The optimum conditions are attained when the particles are large enough to transform but small in size to cause limited microcrack development. The composite toughness (Eq. 3.1) will be now described by the substitution of the ($\Delta K_{IC}^{T}$) for crack-tip stress-induced microcracking ($\Delta K_{IC}^{\mu c}$) [16]. Here, increasing the crack-tip fracture resistance will increase the size of the stress-induced microcrack zone. The zone radius, $r_{\mu c}$, depends on the matrix toughness [16]:

$$r_{\mu c} = \left[(K_{IC}^{M} + K'_{IC})/2\sigma_c^{\mu c}\right]^2 \tag{3.4}$$

where $K'_{IC}$ is the local stress intensity modified by the microcrack presence and $\sigma_c^{\mu c}$ is the stress required to initiate the microcracking [16]. Notice that the increasing of the matrix toughness will effectively decrease the probability of microcrack linkage and decrease the density and/or size of the microcracks [16].

According with equation 3.1, the fracture toughness of $ZrO_2$-toughened composites can be enhanced by further increasing $K_{IC}^{M}$. Therefore, it should be mentioned, that nowadays most of the attempts have been focused in the increase of matrix fracture toughness, which itself may be a composite rather than a single-phase material. Moreover, it have

been suggested that the introduction of multiple toughening mechanisms by the use of numerous toughening agents should lead to a combination of toughness increments that might be equal or greater than the sum of the individual toughness increments achieved for single toughening agent [16].

Figure 5 shows that zirconia-particle toughened mullite is much effective in the improvement of the fracture toughness than the bending strength, while $SiC_w$-mullite follows a different trend [2].

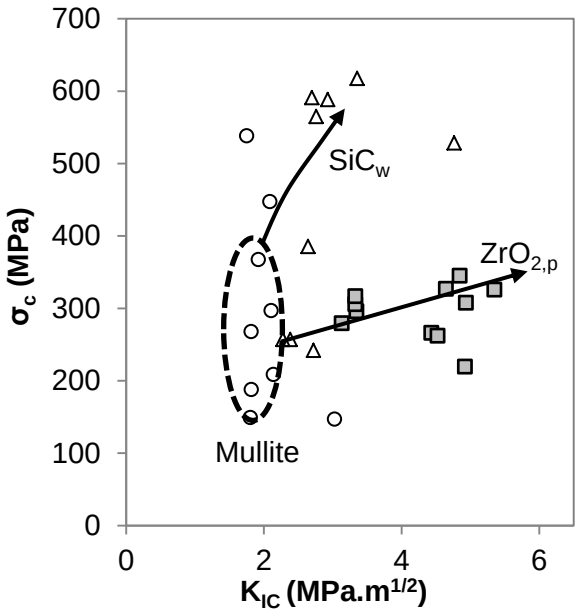


***Figure 5:*** *Bending strength ($\sigma_c$) and fracture toughness ($K_{IC}$) of mullite-based composites, adapted from [2].*

In 1980, Claussen and Janke have determined a room temperature strength of 400 MPa and fracture toughness of about 4.5 MPa.m$^{1/2}$ (data 1, Fig. 6) for mullite composite prepared according with the reaction [20]:

$$2ZrSiO_4 + 3Al_2O_3 \rightarrow 3Al_2O_3 2SiO_2 + 2ZrO_2 \quad (3.5)$$

Such result have supported many subsequent studies devoted to $ZrO_2$-toughened mullite and several processing routes appear [21,22]. According with this work, the toughening mechanism of zirconia-mullite composite is due to stress-induced transformation. An increase of tetragonal $ZrO_2$ usually conducts to an improvement of $K_{IC}$ (data 5,6 and 7, Fig. 6). However, Kubota e Takagi have observed a different trend (data 2, Figure 6) and Yuan et al. reported that it almost did not change up to ~35% (data 3, Fig.6).

Ruh et al. had studied the influence $Y_2O_3$-stabelized $ZrO_2$ in a composite with 35.4% $ZrO_2$-mullite. The fracture toughness with $Y_2O_3$ (ranging from 0 to 15%) was 4 MPa.m$^{1/2}$ and did not change with the tetragonal $ZrO_2$ content [23].

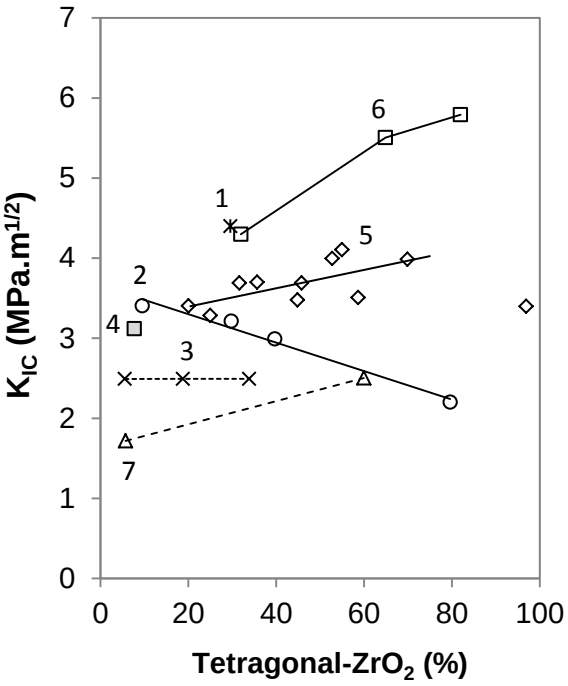


***Figure 6:*** *Relationship between mechanical properties of $ZrO_2$-mullite composites and tetragonal zirconia amount. 1 Claussen and Jahn (1980), 2 Kubota and Takagi (1986), 3 Yuan et al. (1986), 4 Leriche (1990), 5 Rundgren et al. (1990), 6 Shiga and Ismail (1990) and 7 Nishiyama et al. (1991), adapted from [2].*

In this kind of brittle materials, the incorporation of a second phase leads to great variability of defects, scattering the bending strength results and thus decreasing the Weibull modulus, whose distribution function is given by [24]:

$$P_f = 1 - exp\left[-\left(\sigma_f/\sigma_0\right)^m\right] \tag{3.6}$$

where $P_f$ is the cumulative probalility of fracture, $\sigma_0$ and $m$ are Weibull parameters: the scale parameter and Weibull modulus, respectively. The Weibull modulus has values between 5 and 20 for typical ceramics. However, the development of the processing conditions can improve the fracture toughness and minimize the strength distribution (increasing the Weibull modulus) [13].

Ismail et al. did not observed a significant improvement of the bending strength in 15 vol.% $ZrO_2$-mullite composites compared to mullite at very high temperatures. However, a high level strength (>350 MPa) is retained up to 1350 ºC (Fig. 7) [2]. Otherwise, Rundgren et al. reported two data series of near stoichiometric mullite (72.1 wt.% $Al_2O_3$ and 72.9 wt.% $Al_2O_3$) and zirconia-mullite composites, using 20 vol.% $ZrO_2$ or 20 vol.% stabilized-$ZrO_2$ (with 3 mol.% $Y_2O_3$). Samples were prepared by sol-gel method and then sintered from 1550 to 1650 ºC for different periods, which go from 2 up to 4 hours.

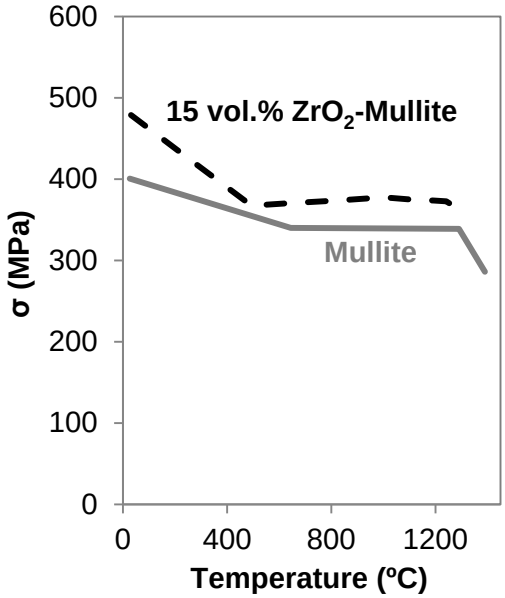


***Figure 7:*** *Bending strength of mullite and 15 vol.% $ZrO_2$-mullite as function of temperature, adapted from [2].*

Table 2 summarizes the processing conditions tested for each composition and their own average bending strength and fracture toughness. The highest bending strength (632 MPa) at RT was obtained for a composite with $Y_2O_3$ stabilized-zirconia sintered at the lowest temperature (1550 ºC) [25]. Considering the compositional differences, the high temperature data is divided in three main points:

(1) the bending strength of mullite was retained up to 1300 ºC, which was attributed to the presence of viscous glassy at the triple points of the mullite grains junctions;

(2) the strength of composites with zirconia addition decreases with the temperature, owing to the weakening of the grain-boundary behaviour;

(3) the strength of the composite with $Y_2O_3$-stabilized zirconia was kept up to 1200 ºC, above this temperature the glassy phase at the grain-boundaries promoted an abrupt drops until 1300 ºC [25];

Industrially (Elfusa, Electro Abrasives Inc.), zirconia-mullite composites have been produced by melting of high purity alumina and zircon ($ZrSiO_4$) powders in an electric arc furnace. The composites show low thermal expansion and high thermal shock resistance that have been used in slide gates, hot gas nozzles for exhaust devices of a turboprop aircraft (2D-Nextel mullite composite) and special refractory parts for glass and steel industries.

***Table 2:*** *Sintering conditions and mechanical results of mullite and mullite-zirconia materials [25].*

| | | Temperature (time) | t-$ZrO_2$ fraction | E (GPa) | $K_{IC}$ (MPa.$m^{1/2}$) | $\sigma_c$ (MPa) (RT/1200 ºC) |
|---|---|---|---|---|---|---|
| **72.1 wt.% $Al_2O_3$** | Single-mullite | 1650 ºC (4h) | - | 216 | 1.9 | 374/315 |
| | | 1650 ºC (2h) | - | 202 | 2.1 | 307/301 |
| | 20 vol.% $ZrO_2$ | 1650 ºC (2h) | 36 | 218 | 3.7 | 339/269 |
| | | 1600 ºC (4h) | 46 | 214 | 3.7 | 396/345 |
| | | 1600 ºC (2h) | 53 | 205 | 4.0 | 453/311 |
| | 20 vol.% $ZrO_2$ (3 mol.% $Y_2O_3$) | 1600 ºC (4h) | 45 | 216 | 3.5 | 368/364 |
| | | 1600 ºC (2h) | 59 | 214 | 3.5 | 367/366 |
| **72.9 wt.% $Al_2O_3$** | Single-mullite | 1650 ºC (4h) | - | 223 | 1.8 | 343/290 |
| | | 1650 ºC (2h) | - | 207 | 1.9 | 379/357 |
| | | 1630 ºC (4h) | - | 204 | 2.1 | 343/305 |
| | 20 vol.% $ZrO_2$ | 1650 ºC (2h) | 20 | 221 | 3.4 | 416/329 |
| | | 1600 ºC (4h) | 25 | 214 | 3.3 | 403/341 |
| | | 1600 ºC (2h) | 32 | 198 | 3.7 | 396/369 |
| | 20 vol.% $ZrO_2$ (3 mol.% $Y_2O_3$) | 1600 ºC (4h) | 55 | 213 | 4.1 | 400/411 |
| | | 1600 ºC (2h) | 70 | 213 | 4.0 | 452/451 |
| | | 1550 ºC (4h) | 97 | 180 | 3.4 | 560/494 |

### III.1.2. Mullite and zirconia-mullite composite electrolytes

The $ZrO_2$ addition to mullite could change other intrinsic physical and chemical properties, namely the ionic conductivity. Zirconia, as aforementioned, has been exhaustively used as solid electrolyte, namely in gas sensors due to wide range of $P_{O_2}$ for ionic conduction. Almost all of the applications of oxygen conductors have been concentrated in oxides ($CeO_2$, $ThO_2$, $ZrO_2$, $HfO_2$, $Bi_2O_3$), which crystallize with the fluorite structure or with distorted variants of it. However, it has been of great interest to explore and look for alternative materials with different structures, which might upgrade the electrochemical performance. Mullite have been investigated in this way. It has crystalline structure of orthorhombic symmetry and belongs to $P_{bam}$ space group (Fig. 8) [26].

Mullite is a non-stoichiometric compound and can be described by the chemical notation: $Al_2^{VI}(Al_{2+2x}^{IV}Si_{2-2x}^{IV})O_{10-x/2}V_{x/2}$, where $IV$ and $VI$ represent the coordination numbers of the cations, $V$ is the number of oxygen vacancies per unit cell and $x$ goes from 0.5 to 0.8 as the $Al_2O_3/SiO_2$ ratio changes from 3:2 to 2:1 [27]. Therefore, similarly with what it happens in doped-$ZrO_2$, it might exhibit oxygen ion conduction behaviour. Assuming this, the earliest evaluation of the mullite oxygen ion conductivity was performed in natural mullite samples [28]. However, these samples usually comprise a considerable amount of impurities, which might influence the conductivity value along with the transportations mechanisms [28]. The compositional mullite variation with temperature is clearly shown at the $Al_2O3$-$SiO_2$ phase diagram (for example $3Al_2O_3$-$2SiO_2$ ranging from 59 to 62 mol.% $Al_2O_3$) [29], and corresponds to the substitution of aluminium by silicon accompanied by the formation of $V_O^{\cdot\cdot}$ (Fig.8) [30].

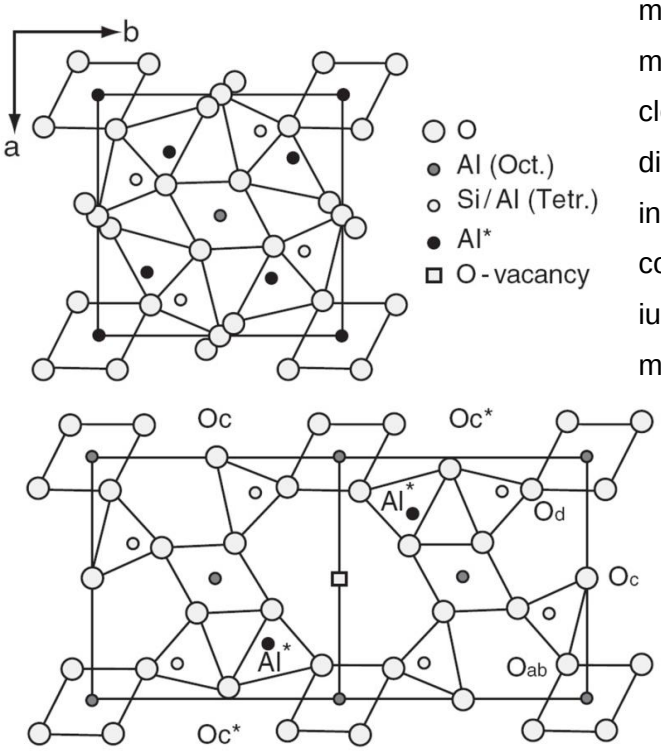


***Figure 8:*** *The structure of mullite (top) has octahedral $AlO_6$ chains parallel to the c-axis that are cross-linked by tetrahedral $(Al,Si)O_4$ chains. Atomic displacement around an oxygen vacancy (bottom) [31].*

Gas sensors are mainly based on the EMF to determine the oxygen activity in the liquid melts (Fe, Co, Ni, Cu, Ag, Sn, Pb), by means of an electrochemical cell comprising:

Liquid metal ‖ Solid $O^{2-}$ ion conductor ‖ Reference electrode

The difference of the oxygen potentials in this electrochemical cell can be measured with $O^{2-}$ conduction through the solid electrolyte. Solid metal-metal oxide wires (Mo-$MoO_2$, Cr-$Cr_2O_3$, Ni-NiO) have been used as reference electrodes, which are dipped into homogenous gaseous blends of Ar-$O_2$, $H_2O$-$H_2$ or air. The EMF will be generated by the different oxygen potential between the electrolyte interfaces [33].

The contribution of n-type electronic conduction in the solid electrolyte to the measured EMF of an electrochemical probe can be expressed by [30]:

$$EMF = \frac{\bar{R}T}{4F} \ln \left[ \frac{(\mathrm{P_{O_2}})^{1/4} + (\mathrm{P_\theta})^{1/4}}{(\mathrm{P'_{O_2}}) + (\mathrm{P_\theta})^{1/4}} \right] \quad (3.7)$$

where $F$ is the Faraday constant, $T$ is the absolute temperature, $\bar{R}$ gas constant, $\mathrm{P'_{O_2}}$ and $\mathrm{P_{O_2}}$ are the partial pressures of oxygen at two electrolyte interfaces and $\mathrm{P_\theta}$ is defined as the oxygen partial pressure at which both ionic and electronic conductivity components are equal [30]. If the $P_{O_2}$ satisfy this condition $P'_{O_2} \ll P_\theta \ll P_{O_2}$, the foregoing equation can be simplified to [30]:

$$EMF = \frac{\bar{R}T}{4F} \ln \left[ \frac{\mathrm{P_{O_2}}}{\mathrm{P_\theta}} \right] \quad (3.8)$$

The oxygen ion transport occurs from the interface with high oxygen potential to the interface with lower one, and this is triggered by external voltage. The rate of deoxidation of the metal decreases for lower oxygen content in the metal. In this sense, it was reported the EMF of the oxygen concentration of three cells combining [32]:

Air ‖ mullite ‖ $H_2O$, $H_2$

Air ‖ mullite ‖ iron melt (1600 ºC)

Air ‖ mullite ‖ Al melt saturated with $Al_2O_3$ (1000 - 1600 ºC)

It was reported that the mullite phase enriched with $SiO_2$ shows good ionic conductivity at 1600 ºC for $P_{O_2}$ value above $10^{-8}$ atm. Moreover, this indicates that mullite-type oxygen sensors for steelmaking industry show superior performance to those of zirconia-type

sensors, especially at high temperatures and for very low oxygen activity ($a_O$). Figure 9 shows an apparatus developed for measure oxygen activities in liquid iron deoxidized by aluminium at 1600 ºC [30,32]. The results obtained with mullite electrolyte probe (using a Cr-$Cr_2O_3$ reference mixture) were compared with those obtained by a commercial 8 mol.% MgO-$ZrO_2$ tube and plug to 9 mol% MgO-$ZrO_2$ probes [34]. The tubular mullite probe was manufactured from high purity materials co-precipitated by a sol-gel method [30,32]:

$$\text{Mo, Cr-}Cr_2O_3 \parallel \text{mullite} \parallel O_{\text{in Fe-Al alloy}}\text{, Mo}$$

The probes are dipped in the iron melt with different aluminium contents (0.0009-0.42 wt.%).

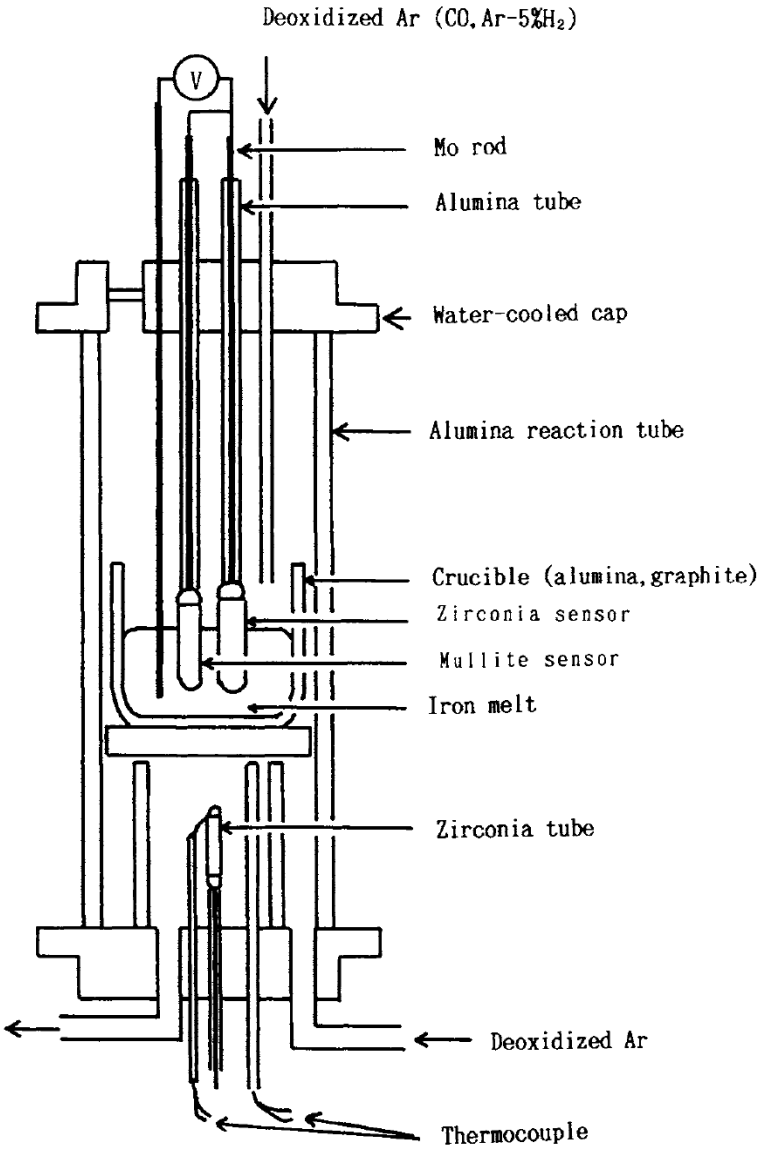


***Figure 9:*** *Schematic diagram of experimental apparatus for measuring oxygen activity in iron melt. [32].*

Moreover, it was assumed for the mullite case that the solid electrolyte has pure ionic conduction and the thermodynamic equilibrium at the electrolyte/electrode interface is reached. The oxygen activity for Al contents below 0.5 wt.% are in good agreement with Nernst equation and so to the $Al/Al_2O_3$ equilibrium [32,34]. The values obtained by the zirconia probe need to be corrected by the electronic conductivity component, in order to be in agreement with those obtained by the mullite probe (using the Nernst equation). It was found that the electrical conductivity of mullite is lower than that of zirconia (about three orders of magnitude). Although, zirconia-based are a solid electrolyte, when exposed to high temperatures and low oxygen potentials, they exhibit mixed ionic and n-type electronic conduction. The conductivity is influenced by the type and concentration of the stabilizing oxide, the phase composition, the impurities in the electrolyte and the microstructure of the electrolyte [30]. Nagatani et al. confirmed the greater accuracy of mullite-based oxygen sensor for very low oxygen activity ($a_O$) [30]. Additionally, the $P_\theta$ values were determined for mullite and $ZrO_2$-9 mol.% MgO solid electrolytes (~1400 to 1650 ºC) [30]. The EMF values obtained by using the mullite probe are in agreement with the Nernst law at very low oxygen activities (Fig. 10), while the EMF values for the zirconia-based sensors exhibit substantial deviations in the same conditions (below 5 ppm).

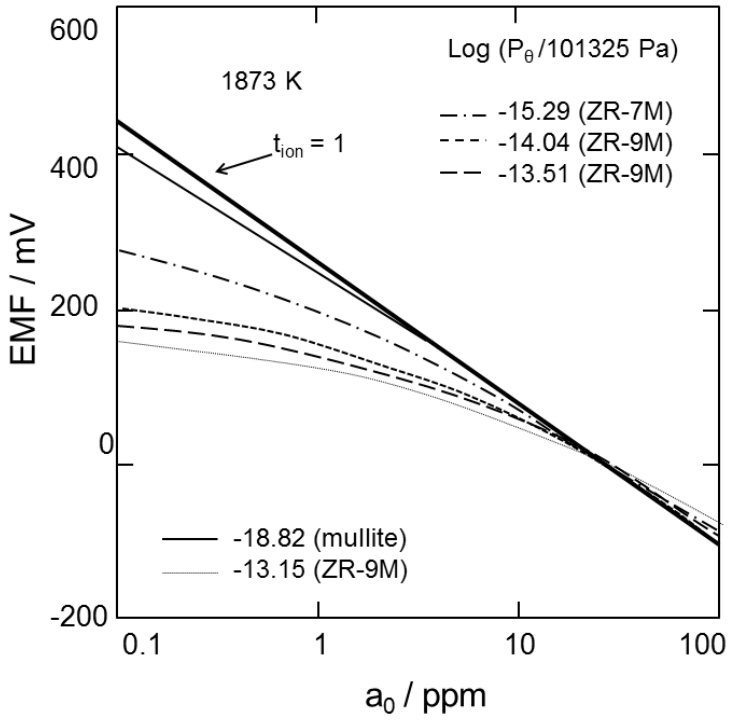


***Figure 10:*** *Relationship between EMF and oxygen activity ($a_0$) at various $P_\theta$ values for ZR-7 and 9M (7 and 9 mol.% MgO-stabilized zirconia) and mullite electrolytes, adapted from [30].*

Rommerskirchen et al. characterized the temperature dependence of the mullite ionic conduction domain by the mean of the $P_\theta$ parameter. The $P_\theta$ parameter was determined for 1400 ºC ($1.69 \times 10^{-15}$ Pa) and 1600 ºC ($1.97 \times 10^{-11}$ Pa). Therefore, the $t_{ion}$ number of 3:2 mullite as function of the $P_{O_2}$ was determined from $t_{ion} = \left[1 + \left(P_{O_2}/P_\theta\right)^{-1/4}\right]^{-1}$ and it is depicted in Figure 11 [26].

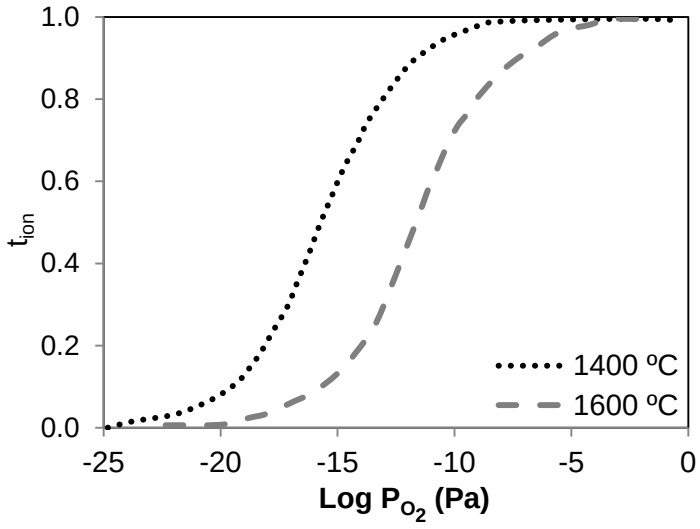


***Figure 11:*** *The $t_{ion}$ in 3:2 mullite as a function of the oxygen partial pressure, adapted from [26].*

In 1983, Meng and Huggins reported a new chemical method to synthesize pure and intentionally doped-mullite at rather low temperatures (1300 ºC) [27]. In this sense, the oxide ion conductivity of the mullite solid solution was measured in air by AC impedance spectroscopy technique in the frequency range 20 Hz-100 kHz and the temperature range 450-950°C. The results reveal that the composition and sintering temperatures significantly influence the conductivity (Fig. 12). It was observed that the conductivity increases for $SiO_2$-rich mullite (Fig. 12b), and for some compositions two regions with different slope (so different activation energy) were defined. Nevertheless, the conductivity of the 3:2 mullite is higher than those reported earlier (by a factor of about 6 at 800°C), which were ascribed to the low concentration of impurities. The increase of the processing temperature had beneficial influence over the conductivity of 3:2 mullite (Fig. 12c). However, it was verified a non-reproducibility in the conductivity values for temperatures above 700-800 ºC, which was endorsed to instabilities in the structure. To avoid such behaviour, the samples were subjected to annealing experiments (1300 ºC for 24 h). The conductivity of annealed samples had increased by about one order of magnitude (Fig 12d). Moreover, the conduc-

tivity of samples annealed at 1300 ºC showed a clear curve profile, where two regions with distinct slopes were defined, with an inflection temperature at about 700 ºC. Such behaviour consisting of three regimes have been also reported for other structures (Fig. 13), as aforementioned for the fluorite case [35].

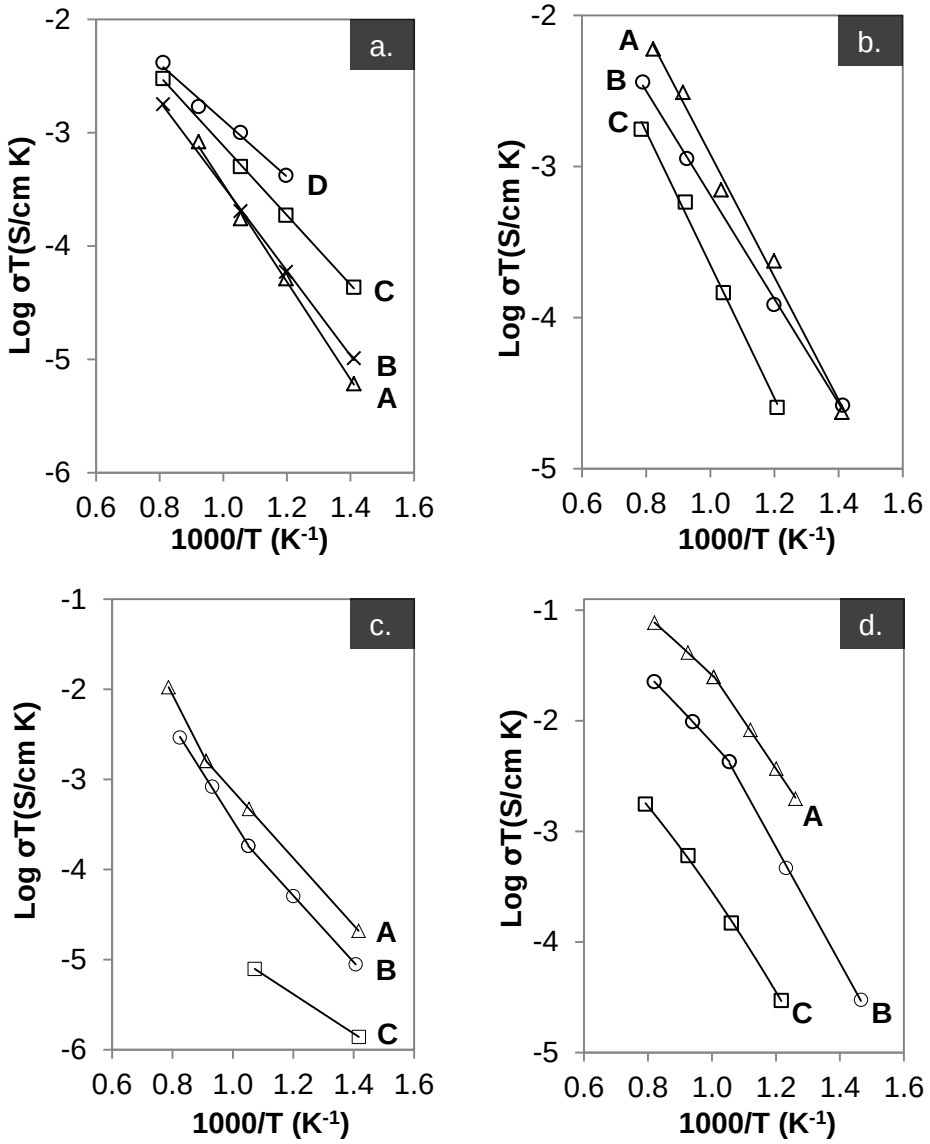


***Figure 12:*** *Arrhenius plots for the total conductivity* ***(a)*** *in specimens fired at 1300 °C with composition (A) $3Al_2O_3$:$2SiO_2$, (B) $3.25Al_2O_3$:$2SiO_2$, (C) $3.5Al_2O_3$:$2SiO_2$, (D) $3.75Al_2O_3$:$2SiO_2$,* ***(b)*** *in specimens sintered at ~1800 °C with the composition (A) 3.25 $Al_2O_3$:$2SiO_2$, (B) $3.5Al_2O_3$:$2SiO_2$, (C) $3.75Al_2O_3$:$2SiO_2$,* ***(c)*** *of 3:2 mullite heat treated at (A) 1750-1800 °C (B) 1300 ºC (C) 1031 °C,* ***(d)*** *of several mullite samples: (A) $3Al_2O_3$:$2SiO_2$, 1300 °C/10 h, 1800 °C/1 h, 1300 °C/24 h; (B) $3.75Al_2O_3$:$2SiO_2$, 1300 °C/10 h, 1800 °C/1 h, 1300 °C/24 h; (C) $3.75Al_2O_3$:$2SiO_2$, 1300 °C/10 h, 1800 °C/1 h, adapted from [28].*

The range of each regime will depend upon many aspects: the melting point of the material, the energy of formation of the intrinsic defect, the dopant concentration and the ener-

gy of association of the complex defects. This is due certainly to some differences between different crystalline structures [35]. At this point, it is important to remain that the ionic conduction of doped oxide conductor obeys to the general equation:

$$\sigma = (\sigma_0/T)exp(-E_a/k_BT) \quad (3.9)$$

where $\sigma$ is the ionic conductivity, $T$ the absolute temperature, $\sigma_0$ pre-exponential factor and $E_a$ is the activation energy. The pre-exponential factor can be expressed by [36],

$$\sigma_0 = C\gamma(Z^2e^2/k_B)x_d^2\nu_0 exp(\Delta S_m/k_B) \quad (3.10)$$

where $C$ is the concentration of charge carriers, $\gamma$ is a geometrical factor, $Ze$ is the charge of the carriers, $x_d$ the jump distance, $\nu_0$ the jump attempt frequency, $\Delta S_m$ the entropy of migration and $k_B$ is the Boltzmann constant. The concentration of carriers $C$ is determined by the number of $V_O^{\cdot\cdot}$ able to exchange site with oxygen ion. However, in most of the cases, the defects interactions lead to the formation of complex defects between the dopant cations and the $V_O^{\cdot\cdot}$. This association happens specially at low temperatures regime. In this way, the dopant concentration will change and it is necessary to include the enthalpy of the defect association [36].

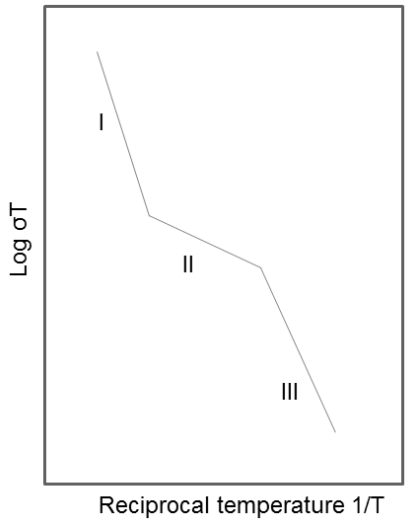


***Figure 13:*** *A schematic representation of the conductivity behaviour of an oxide or halide ionic conductor, adapted from [35].*

**I:** At high temperatures, the intrinsic defect concentration prevails and the activation energy results from the enthalpy of the defect formation plus the enthalpy for motion.

**II:** At intermediate temperatures, the charge carrier defects are ruled by the dopant concentration, since this is independent of the temperature. The activation energy corresponds only to the enthalpy of motion.

**III:** At low temperatures, the association becomes important and the concentration of charge carrier defects is modified by the thermodynamic equilibrium between free defects and complex defects, which lead to an increase of the activation energy.

In this sense, the regimes of mullite conductivity should be understood in terms of the association defects, i.e. to the transition between regions II and III in this model [28]. Non-doped mullite was considered, and so the $Al^{3+}$ ions proceed like the aliovalent ion in the doped-fluorite structures, leading to the formation of complex defects as [28]:

$$Al'_{Si} + V_{\ddot{O}} \rightarrow (Al'_{Si}V_{\ddot{O}})^{\cdot} \quad (3.11)$$

and

$$Al'_{Si} + V_{\ddot{O}} \rightarrow (Al'_{Si}V_{\ddot{O}}Al'_{Si}) \quad (3.12)$$

Moreover, the occurrence of a second phase as α-$Al_2O_3$ or β-quartz at the grain boundaries will change the oxygen ion transportation path, increasing the resistance. In fact, α-$Al_2O_3$ was identified in $Al_2O_3$-rich mullite sample, and the precipitation of α-$Al_2O_3$ probably increases even more for sample processed at higher temperatures, which explained the different conductivity for samples with the same composition, but prepared at different temperatures (Figs.12a,b).

Ko et al. assumed a similar individual oxide ion conduction of mullite and zirconia through the $V_O^{\cdot\cdot}$, and considered that the electrochemical performance could be modified by their blend. Therefore, the incorporation of different $ZrO_2$ amounts as second phase into a suitable mullite matrix has great potential as solid electrolyte at high temperatures (Fig. 14). Even that, the composite ionic conduction must be strongly dependent on the intrinsic nature and the volume fractions of constituent phases [37]. It was observed that the conductivities of the zirconia-mullite composites increased with zirconia content, and the composites activation energies are well labelled by the determined for grain conductivity of mullite and zirconia (Fig. 14) [37].

The ionic conduction of the mullite-zirconia composites for the different volume ratio is given by the mixing equation [38]:

$$\sigma_c{}^n = (1 - V)\sigma_M{}^n + V\,\sigma_Z{}^n \quad (3.13)$$

where $V$ is the $ZrO_2$ volume fraction, $\sigma_c$, $\sigma_M$ and $\sigma_Z$ are the conductivity of the composite, mullite and zirconia, respectively and $n$ is a constant $-1 \leq n \leq 1$ ($n = 1$ if both phases are aligned with the direction of the ionic current and $n = -1$ if both phases are perpendicularly). In the intermediate cases, $n \rightarrow 0$ and so the equation becomes (Lichtenecker's rule) [38]:

$$\log \sigma_c = (1 - V)\log \sigma_M + \mathrm{V}\log \sigma_Z \quad (3.14)$$

In fact, the conductivities of composites prepared by hot pressing at 1600 ºC were well-fitted by Lichtenecker's rule [38].

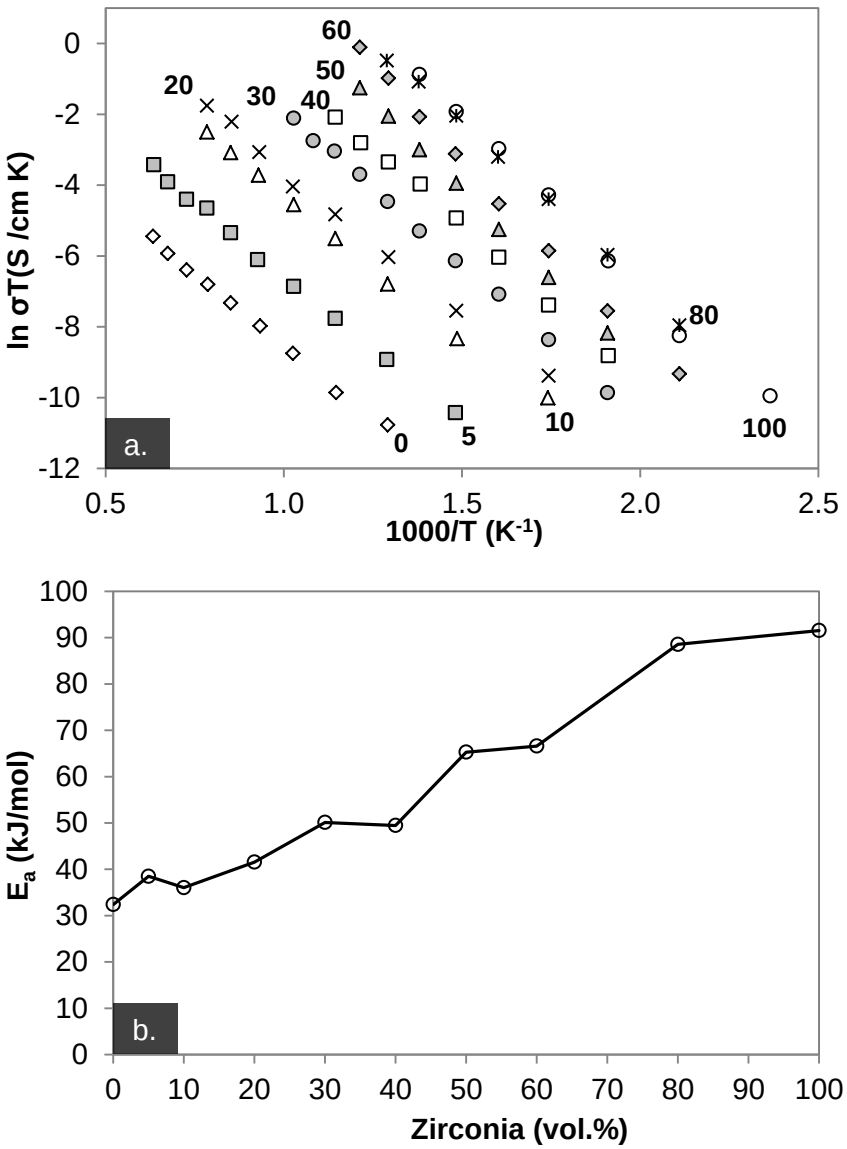


***Figure 14: (a)*** *Arrhenius plots of conductivities determined in the high-frequency region (related to grains). The numeric inscriptions corresponds to the zirconia volume fraction.* ***(b)*** *Activation energy versus zirconia content curve of mullite/zirconia composites in the high-frequency regions, adapted from [37].*

**References**

[1] I.A. Aksay, D.M. Dabbs, M. Sarikaya, Mullite for structural, electronic, and optical applications, Journal of the American Ceramic Society, 74 (1991) 2343-2358.

[2] H. Schneider, K. Okada, J.A. Pask, Mullite and mullite ceramics, John Wiley & Sons, Chichester, 1994.

[3] H. Schneider, S. Komarneni, Mullite, WILEY-VCH Verlag GmbH & Co. KGaA, Weinheim, 2005.

[4] W. Guse, D. Mateika, Growth of mullite single-crystals ($2Al_2O_3.SiO_2$) by Czochralski method, Journal of Crystal Growth, 22 (1974) 237-240.
[5] H. Schneider, J. Schreuer, B. Hildmann, Structure and properties of mullite - A review, Journal of the European Ceramic Society, 28 (2008) 329-344.
[6] A. Sayir, S.C. Farmer, Directionally solidified mullite fibers, R.A. Lowden, M.K. Ferber, J.R. Hellmann, K.K. Chawla, S.G. DiPietro (Eds.) Ceramic Matrix Composites Advanced High-Temperature Structural Materials, 1995, 11-20.
[7] R.G. Carvalho, A.J.S. Fernandes, F.J. Oliveira, E. Alves, N. Franco, C. Louro, R.F. Silva, F.M. Costa, Single and polycrystalline mullite fibres grown by laser floating zone technique, Journal of the European Ceramic Society, 30 (2010) 3311-3318.
[8] J.R. Kelly, I. Denry, Stabilized zirconia as a structural ceramic: an overview, Dental Materials, 24 (2008) 289-298.
[9] R.C. Garvie, R.H. Hannink, R.T. Pascoe, Ceramic steel, Nature, 258 (1975) 703-704.
[10] H.S. Maiti, E.C. Subbarao, K.V.G. Gokhale, Kinetics and burst phenomenon in $ZrO_2$ transformation, Journal of the American Ceramic Society, 55 (1972) 317-322.
[11] A.H. Heuer, N. Claussen, W.M. Kriven, M. Ruhle, Stability of tetragonal $ZrO_2$ particles in ceramic matrices, Journal of the American Ceramic Society, 65 (1982) 642-650.
[12] M.H. Bocanegra-Bernal, S.D. De la Torre, Phase transitions in zirconium dioxide and related materials for high performance engineering ceramics, Journal of Materials Science, 37 (2002) 4947-4971.
[13] P.F. Becher, Microstructural design of toughened ceramics, Journal of the American Ceramic Society, 74 (1991) 255-269.
[14] F.F. Lange, Transformation toughening 3. Experimental-observations in the $ZrO_2$-$Y_2O_3$ system, Journal of Materials Science, 17 (1982) 240-246.
[15] J. Wang, R. Stevens, Zirconia-toughened alumina (ZTA) ceramics, Journal of Materials Science, 24 (1989) 3421-3440.
[16] P.F. Becher, T.N. Tiegs, Toughening behavior involving multiple mechanisms - whisker reinforcement and zirconia toughening, Journal of the American Ceramic Society, 70 (1987) 651-654.
[17] A.G. Evans, R.M. Cannon, Toughening of brittle solids by martensitic transformations, Acta Metallurgica, 34 (1986) 761-800.
[18] R.H.J. Hannink, P.M. Kelly, B.C. Muddle, Transformation toughening in zirconia-containing ceramics, Journal of the American Ceramic Society, 83 (2000) 461-487.

[19] P.F. Becher, M.V. Swain, M.K. Ferber, Relation of transformation temperature to the fracture toughness of transformation-toughened ceramics, Journal of Materials Science, 22 (1987) 76-84.
[20] N. Claussen, J. Jahn, Mechanical-properties of sintered, *in situ*-reacted mullite-zirconia composites, Journal of the American Ceramic Society, 63 (1980) 228-229.
[21] S. Prochazaka, J.S. Wallace, N. Claussen, Microstructure of sintered mullite-zirconia composites, Journal of the American Ceramic Society, 66 (1983) C125-C127.
[22] P. Boch, J.P. Giry, Preparation and properties of reaction-sintered mullite-$ZrO_2$ ceramics, Materials Science and Engineering, 71 (1985) 39-48.
[23] R. Ruh, K.S. Mazdiyasni, M.G. Mendiratta, Mechanical and microstructural characterization of mullite and mullite-SiC-whisker and $ZrO_2$-toughened-mullite-SiC-whisker composites, Journal of the American Ceramic Society, 71 (1988) 503-512.
[24] J. Gong, W. Si, Z. Guan, Weibull modulus of fracture strength of toughened ceramics subjected to small-scale contacts, Journal of Materials Science, 36 (2001) 2391-2396.
[25] K. Rundgren, P. Elfving, H. Tabata, S. Kanzaki, R. Pompe, Microstructures and mechanical-properties of mullite-zirconia composites made from inorganic sols and salts, Ceramic Transactions Mullite and Mullite Composites, The American Ceramic Society, Ohio, 1990.
[26] I. Rommerskirchen, F. Chávez, D. Janke, Ionic conduction behaviour of mullite ($3Al_2O_3$:$2SiO_2$) at 1400 to 1600 °C, Solid State Ionics, 74 (1994) 179-187.
[27] G.-Y. Meng, R.A. Huggins, A new chemical method for preparation of both pure and doped mullite, Materials Research Bulletin, 18 (1983) 581-588.
[28] G.-Y. Meng, R.A. Huggins, The oxygen ion conductivity of mullite prepared using a wet chemical process, Solid State Ionics, 11 (1984) 271-278.
[29] I.A. Aksay, J.A. Pask, Stable and metastable equilibria in system $SiO_2$-$Al_2O_3$, Journal of the American Ceramic Society, 58 (1975) 507-512.
[30] A. Nagatani, R. Inoue, H. Suito, Determination of electronic conductivity limits of mullite and $ZrO_2$-9 mol% MgO solid electrolytes, Journal of Applied Electrochemistry, 22 (1992) 859-864.
[31] J.F. Shackelford, R.H. Doremus, Ceramic and glass materials structure, properties and processing, Springer, New York, 2008.
[32] K. Yamana, M. Miyamoto, K. Doi, T. Arahori, J. Nowotny, Impact of grain boundaries on properties of mullite as a solid electrolyte, N. Janusz (Ed.) Materials Science Monographs, Elsevier, 1995, 571-591.

[33] W.A. Fischer, D. Janke, Electrolytic deoxidation of liquid-metals at 1600 ºC, Scripta Metallurgica, 6 (1972) 923-928.
[34] H. Suito, R. Inoue, A. Nagatani, Mullite as an electrochemical probe for the determination of low oxygen activity in liquid-iron, Steel Research, 63 (1992) 419-425.
[35] J.A. Kilner, C.D. Waters, The effects of dopant cation oxygen vacancy complexes on the anion transport-properties of nonstoichiometric fluorite oxides, Solid State Ionics, 6 (1982) 253-259.
[36] J.A. Kilner, R.J. Brook, A study of oxygen ion conductivity in doped nonstoichiometric oxides, Solid State Ionics, 6 (1982) 237-252.
[37] H.-D. Ko, C.C. Lin, K.C. Chin, Effect of zirconia content on electrical conductivities of mullite/zirconia composites measured by impedance spectroscopy, Journal of Materials Research, 23 (2008) 2125-2132.
[38] D.S. McLachlan, M. Blaszkiewicz, R.E. Newnham, Electrical-resistivity of composites, Journal of the American Ceramic Society, 73 (1990) 2187-2203.

## III.2. Directionally solidified eutectic and off-eutectic mullite-zirconia fibres

R.G. Carvalho[a], M.S. Pires[a], A.J.S. Fernandes[a], R.F. Silva[b], F.M. Costa[a]

[a]I3N, Department of Physics, University of Aveiro, 3810-193 Aveiro, Portugal

[b]CICECO, Department of Materials and Ceramic Engineering, University of Aveiro, 3810-193 Aveiro, Portugal

Journal of the European Ceramic Society, 33 (2013) 953-963

**DOI:** http://dx.doi.org/10.1016/j.jeurceramsoc.2012.09.032

### Abstract

Eutectic and off-eutectic mullite-zirconia fibres were grown by LFZ (laser floating zone) directional solidification. The microstructure of the mullite-zirconia eutectic fibres varies from planar coupled eutectic (1 mm/h pulling rate) through mullite columnar growth with coarse zirconia inclusions (10 mm/h pulling rate) to faceted mullite eutectic dendrites, which enclose a dispersion of fine zirconia fibrils (100-500 mm/h pulling rates). Near-equilibrium conditions determine the crystallization of monoclinic zirconia and the absence of any amorphous phase, whereas for higher speeds the tetragonal structure is retained and a residual liquid is kept after the eutectic solidification. Similar structural and morphological characteristics are displayed by the mullite-rich off-eutectic composition added to the development of prismatic crystals of mullite primary phase. In opposition, heavy constitutional undercooling takes place in the case of the zirconia-rich off-eutectic fibres, where equiaxed zirconia dendrites soon form as a primary phase, leaving a non-equilibrium mixture of alumina and sillimanite as interdendritic constituent.

***Keywords:*** Laser floating zone (LFZ), directional solidified eutectics, mullite, zirconia.

### III.2.1. Introduction

Eutectic materials combine the characteristics of each phase in order to improve performance and properties. New, highly homogenous and very fine microstructures based on eutectic constituents, having strongly bonded phases, high density of interphase area as well as short interphase distances, are thus promising solutions for technical ceramics. Another way to enhance materials properties is by controlling their texture. Therefore, by combining both aspects, directional solidified eutectic (DSE) ceramics are very attractive materials. DSEs are free from transverse grain boundaries which limit the rupture strength, and, if microcracks develop, their size is limited by the small spacing between phases [1]. Much work have been done in DSEs of different oxide-oxide systems such as: $Al_2O_3$-YAG, $Al_2O_3$-$ZrO_2$, $Al_2O_3$-YAG-YSZ, $Al_2O_3$-$Gd_2O_3$, $ZrO_2$-CaO, NiO-$ZrO_2$, NiO-$ZrO_2$($Y_2O_3$) [1-3]. Particularly, they have a great interest for thermo-mechanical applications due to their intrinsic thermodynamic stability and improved mechanical properties [2, 4,5].

Among many directional solidification processes, the laser floating zone (LFZ) is frequently used to produce textured eutectic materials. The use of a laser as heating source promotes very large thermal gradients at the solid/liquid interface and so high pulling rates can be used during the growth process. Another advantage of the technique is the absence of crucibles or dies thus avoiding chemical contamination. This method is also very convenient to grow single crystals from melting at high temperatures [2,6,7].

Special relevance has been given to the $Al_2O_3$-$ZrO_2$($Y_2O_3$) system processed by the LFZ method [8-12]. The influence of growth parameters and yttria amount to stabilize zirconia on the final microstructure, and consequently on the mechanical properties is thoroughly investigated [8-12]. Pastor et al. obtained a notable value for the flexural strength (1.6 GPa) at room temperature for an homogeneous dispersion of $ZrO_2$ lamellae in a $Al_2O_3$ matrix [11]. However, a reduction in mechanical strength takes place at high temperature to approximately 800 MPa at 1673 K [8].

In this context, mullite appears as an alternative component with the advantage of presenting a lower mechanical degradation with temperature comparing to alumina and zirconia [13]. Mullite-zirconia belongs to the $Al_2O_3$-$SiO_2$-$ZrO_2$ system and is one of most promising ceramic composite for advanced refractory, structural and electrical applications [13-15]. In order to increase the fracture toughness partially-stabilised zirconia was incorporated in the mullite matrix, also promoting densification and reducing the glassy phase content [16]. Mullite-zirconia composites have been synthesized by different routes, such as chemical reaction, sol-gel technique, spark plasma sintering, tape casting, template

grain growth (TGG), thermal plasma reaction, laser surface treatment and slow-cooling floating zone (SCFZ) [13].

The novelty of the present study is the development of mullite-zirconia DSE structures grown by the LFZ method seeking grain alignment together with a refinement of their size, namely at high pulling rates, both characteristics contributing to better mechanical behaviour. Also, comparing to similar DSE ceramics already grown by the LFZ technique, like those of the $Al_2O_3$-$ZrO_2$ and $Al_2O_3$-$ZrO_2$-$Y_2O_3$ systems [12], the mullite-zirconia composition can present less problems of crack formation upon cooling due to the higher fracture toughness of the mullite matrix. Eutectic and off-eutectic compositions are compared along with the influence of the growth parameters on the final microstructure and phase development.

### III.2.2. Experimental

Mullite-zirconia ceramic fibres were obtained by the laser floating zone (LFZ) method from precursor rods prepared from commercial powders of zirconia ($ZrO_2$, TZ-8Y yttria stabilized tetragonal zirconia, Tosho, co.), alumina ($Al_2O_3$, Merck anhydrous γ-alumina) and silica ($SiO_2$, Sigma). Three different compositions regarding the starting $ZrO_2$-$Al_2O_3$-$SiO_2$ amounts were studied in the mullite-zirconia binary system (Table 1): the eutectic $C_1$ and the two off-eutectic $C_2$ (zirconia rich) and $C_3$ (mullite rich), marked in Figs. 1a,b [17]. Powders were mixed by ball-milling during 1h 30m. Polyvinyl alcohol (PVA 0.1 g/ml) was further added in order to bind the grains for subsequent cold extrusion of the cylindrical precursor rods (~1.5 mm in diameter) for LFZ. After extrusion, these cylindrical rods were air dried 48 hours.

***Table 1:*** *Nominal $ZrO_2$-$Al_2O_3$-$SiO_2$ compositions of the studied fibres: $C_1$ - eutectic composition, $C_2$ - zirconia rich off-eutectic composition and $C_3$ - mullite rich off-eutectic composition.*

| | $ZrO_2$ (wt.%) | $SiO_2$ (wt.%) | $Al_2O_3$ (wt.%) |
|---|---|---|---|
| $C_1$ | 30 | 20 | 50 |
| $C_2$ | 67 | 10 | 23 |
| $C_3$ | 16 | 24 | 60 |

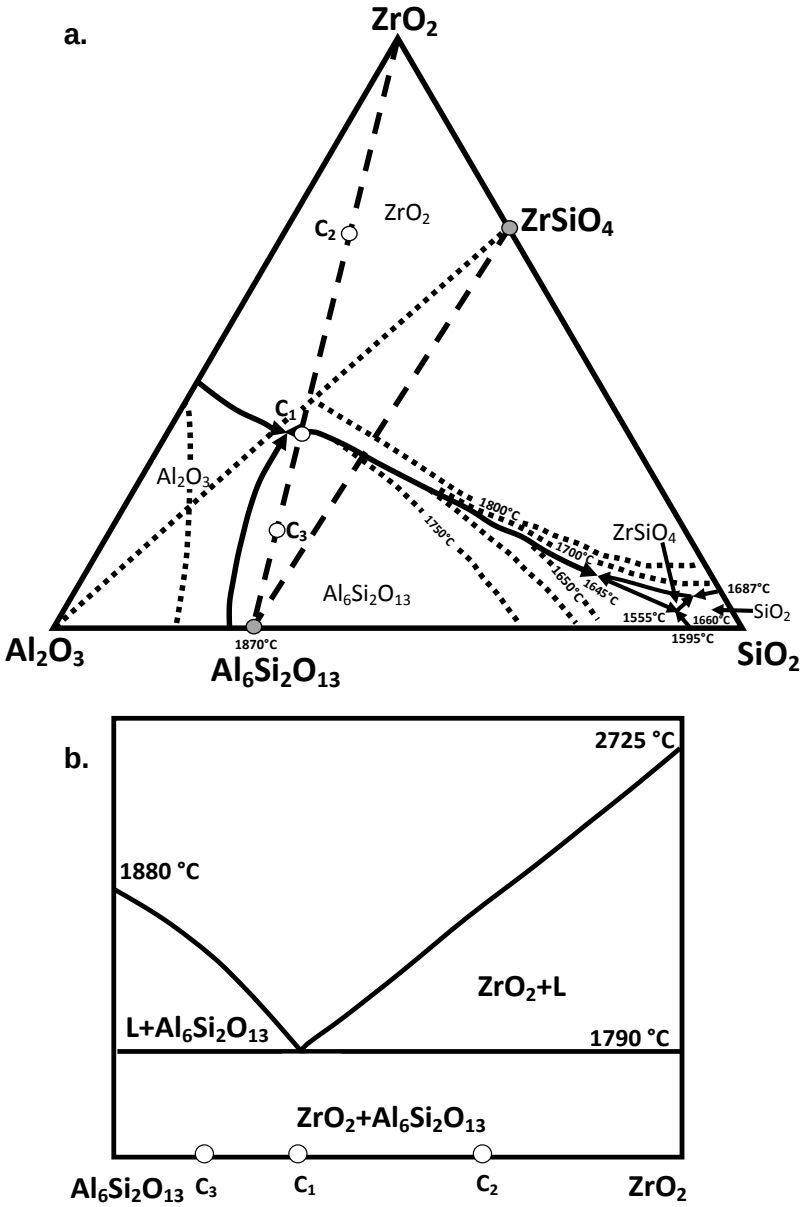


***Figure 1: (a)*** *Ternary phase diagram (in wt.%) of the $Al_2O_3$-$SiO_2$-$ZrO_2$ system and* ***(b)*** *mullite-zirconia binary phase diagram, adapted from ref. [17]. The compositions investigated are pointed out: $C_1$ - eutectic composition, $C_2$ - zirconia rich off-eutectic composition and $C_3$ - mullite rich off-eutectic composition.*

Directional solidified eutectic (DSE) fibres were then obtained by the LFZ method using a 200 W $CO_2$ laser (Spectron, SLC). An illustration from this technique is depicted in Fig. 2a. Fibres like that in Figure 2b were grown in atmospheric conditions between 1 and 500 mm/h of growth rate. All fibres were pulled downwards in order to avoid the incorporation of bubbles and voids in the final material.

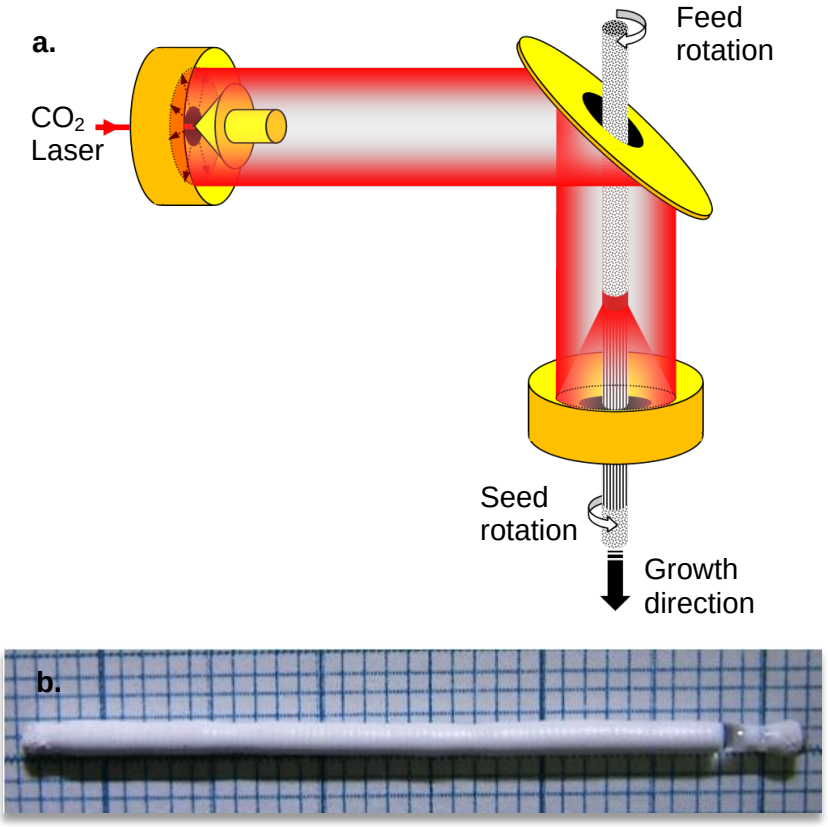


***Figure 2: (a)*** *Illustration of the laser floating zone apparatus.* ***(b)*** *Mullite-zirconia fibre with the eutectic composition, grown at 10 mm/h.*

Structural information was obtained from powdered fibres by X-ray diffraction (XRD) carried out in a Rigaku Geigerflex diffractometer (Cu-$K_\alpha$ radiation, λ = 1.54056 Å, step width 0.02º) from 5 to 80º and with a scan rate of 3º/min. Microstructural features were studied in polished surfaces, at longitudinal and transversal cross sections. The studies were performed in a Hitachi S4100 scanning electron microscope (SEM), helped by chemical elemental mapping by energy dispersive X-ray spectroscopy (EDS). Raman spectroscopy was done in the same cross sections in a Horiba Jobin Yvon HR800 system (532 nm).

### III.2.3. Results

#### III.2.3.1. Eutectic composition ($C_1$)

Significant changes in the microstructure of the mullite-zirconia fibres take place as a function of the pulling rate. At the slowest condition, 1 mm/h, a coupled eutectic morphology comprising mullite (dark grey phase) and zirconia (white phase) is obtained (Figs. 3a,b). This eutectic presents a coarse interpenetrating distribution of mullite and zirconia

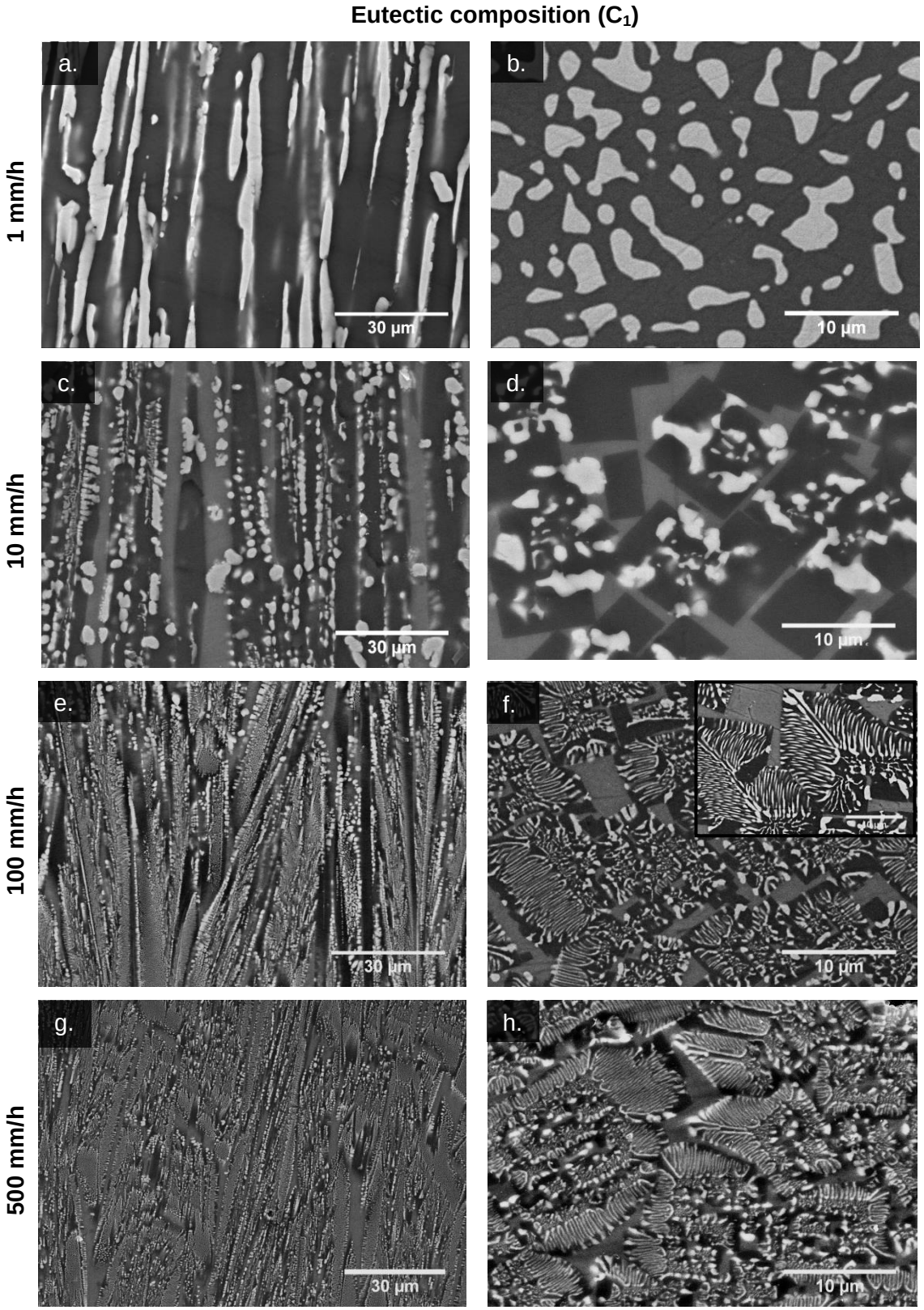


***Figure 3:*** *SEM micrographs of the longitudinal* ***(a**, **c, e** and **g)** and transversal **(b**, **d**, f and **h)** cross-sections of fibres with the eutectic composition ($C_1$) grown in the 1 - 500 mm/h range. The inset in (**f**) shows the zirconia fibrils of the eutectic dendrites perpendicular oriented to the mullite facets.*

phases aligned along the fibre axis (Fig. 3a). The zirconia phase appears as inclusions in a continuous mullite matrix (Fig. 3b). At 10 mm/h, a columnar morphology of polyhedral mullite crystals (~56 vol.%) develops with zirconia inclusions (~21 vol.%) (Figs. 3c,d). These crystals are embedded in a light grey phase of Al-Y-Si oxide (~23 vol.%). The transversal cross-sections disclose the prismatic habit of such crystals (Fig. 3d) that grow preferentially along the fibre axis (Fig. 3c). By increasing the pulling rate to 100 mm/h, a dendritic eutectic microstructure develops (Figs. 3e-h). The faceted mullite crystals, oriented along the growth direction, enclose a fine dispersion of zirconia fibrils, forming eutectic dendrites. Inside these mullite crystals, the zirconia fibrils grow perpendicularly to the mullite facets (Fig. 3f). A detail of this feature shows that primary zirconia fibrils tend to grow along the diagonal planes of the prisms, from which secondary arms develop at 45º (inset of Fig. 3f). The intercolumnar phase amount (mainly Al-Si-Y) increases in comparison to that observed in the 10 mm/h grown fibre. Mullite-zirconia fibres grown at the highest speed, 500 mm/h, present a similar microstructure (Figs. 3g,h) to the 100 mm/h ones, although finer and with an even higher content of intercolumnar phase.

The EDS cross-section map image taken from a 100 mm/h fibre (Fig. 4a,b) presents a picture of the elemental distribution.

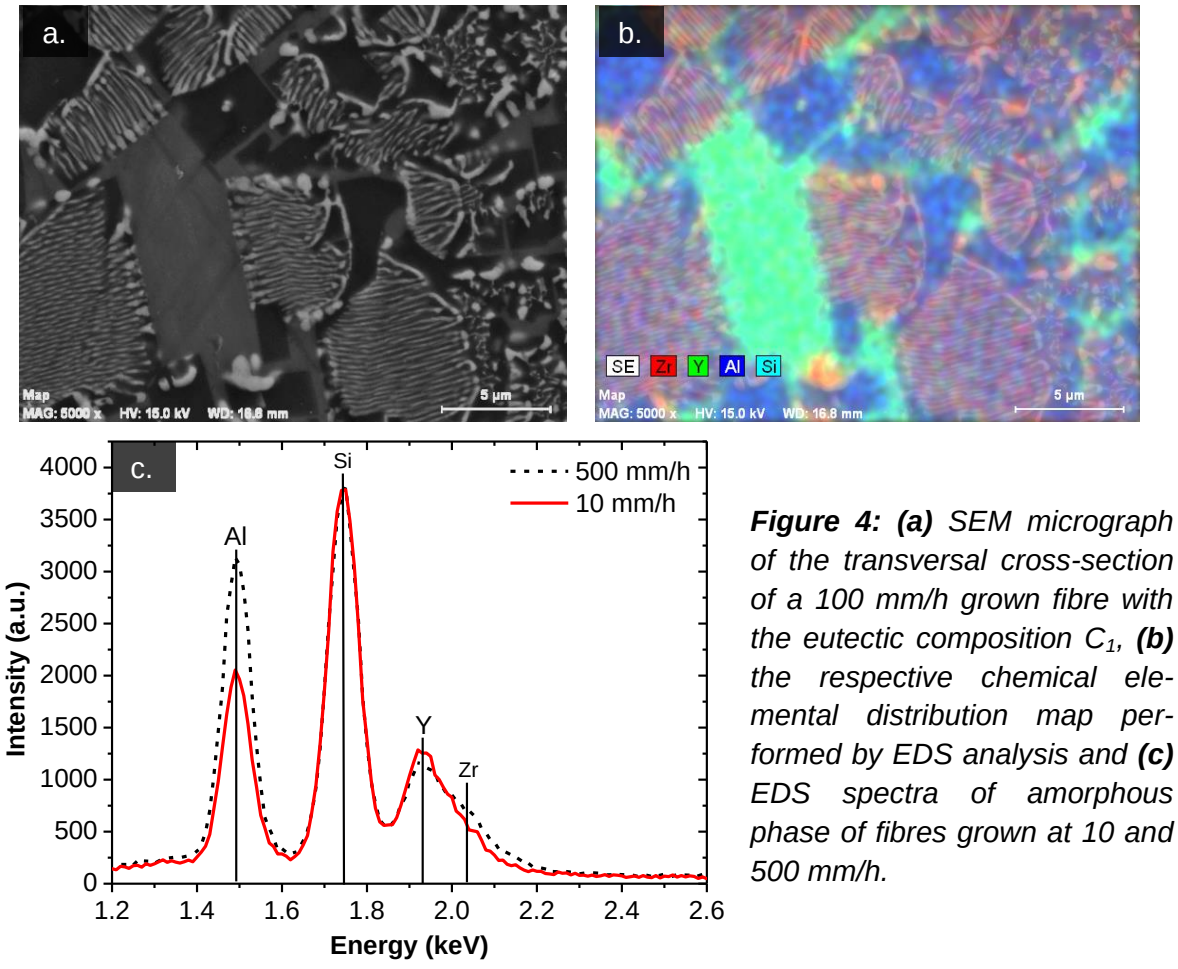


***Figure 4:*** ***(a)*** *SEM micrograph of the transversal cross-section of a 100 mm/h grown fibre with the eutectic composition* $C_1$, ***(b)*** *the respective chemical elemental distribution map performed by EDS analysis and* ***(c)*** *EDS spectra of amorphous phase of fibres grown at 10 and 500 mm/h.*

The composition of the intercolumnar phase was estimated as: Al=40 at.%; Si=24 at.%; Zr=3 at.%; Y=33 at.%, being the yttrium percentage function of the pulling rate, with slight increases for the lowest pulling rate (Fig. 4c). The XRD patterns of the different fibres only present diffraction peaks corresponding to mullite, monoclinic and tetragonal zirconia phases (Fig. 5), so the intercolumnar phase is amorphous, which is corroborated by the presence of a broad band in the XRD spectra.

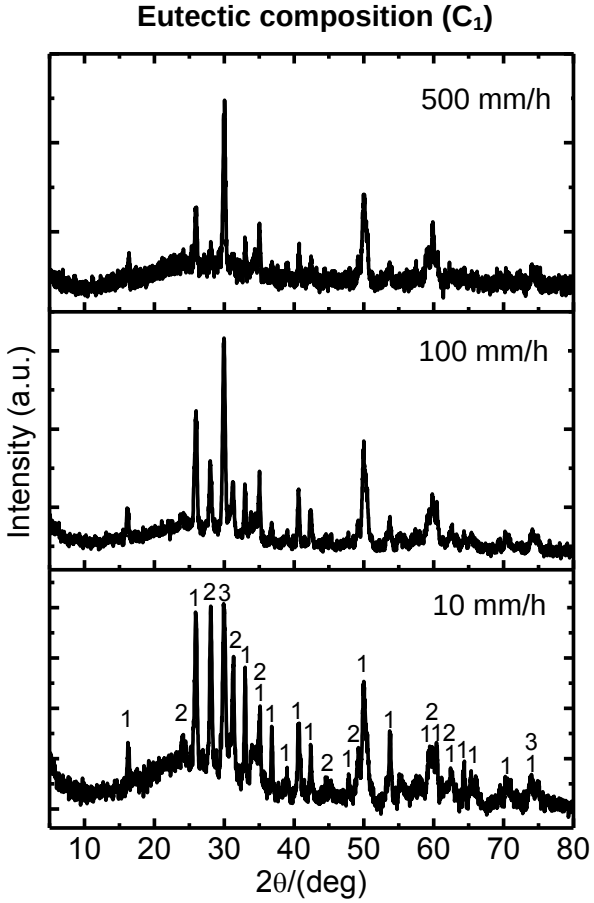


***Figure 5:*** *XRD data from fibres with eutectic composition $C_1$ from 10 to 500 mm/h. The diffraction pattern corresponds to* ***(1)*** *mullite JCPDS: 01-089-2645,* ***(2)*** *monoclinic zirconia JCPDS: 00-007-0343 and* ***(3)*** *tetragonal zirconia JCPDS: 01-072-2743.*

Figure 6 shows Raman spectra taken from transverse surfaces of fibres grown in the 1-500 mm/h range. The selected wavelength for the Raman analysis (532 nm) allows sub-surface interaction, since the electronic absorption is rather low [18]. The spectra taken from the fibres were fitted with lorentzian curves (LabSpec) and the bands were assigned by comparison with literature data [19-24] in Table 2. Zirconia produces a much stronger Raman signal than mullite, overlapping it when both phases are present. Consequently, for the eutectic composition, all identified Raman bands were assigned to monoclinic and

tetragonal zirconia metastable phases [25,26]. The Raman-active modes of zirconia are defined as $A_{1g}+2B_{1g}+3E_g$ for the tetragonal phase and $9A_g+9B_g$ for the monoclinic one [39,40].

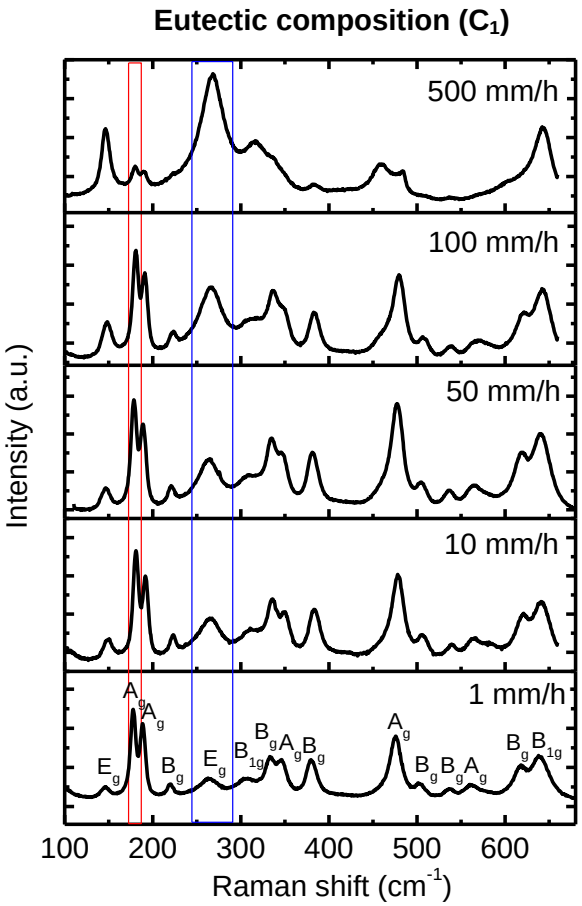


***Figure 6:*** *Raman data from transversal cross section of mullite-zirconia fibres, with eutectic composition $C_1$ grown with pulling rates in the range 1 to 500 mm/h. Raman-active modes $A_g$ and $B_g$ are from monoclinic zirconia, while $E_g$ and $B_{1g}$ correspond to tetragonal zirconia, according to Table 2.*

***Table 2:*** *Comparison between experimental peaks of the three compositions ($C_1$, $C_2$, $C_3$) and those reported in literature for mullite and zirconia phases. Raman-active modes for mullite, monoclinic and tetragonal zirconia are shown [19-24].*

| Fibres grown by LFZ | | | Mullite | Zirconia | |
|---|---|---|---|---|---|
| $C_1$ | $C_2$ | $C_3$ | | Monoclinic | Tetragonal |
| 146 | 149 | 148 | | | 149 ($E_g$-Zr and O along XY) |
| 179 | | 180 | | 179 ($A_g$ Zr-Zr) | |
| 191 | | 191 | | 190 ($A_g$ Zr-Zr) | |
| 223 | | 223 | | 222 ($B_g$ Zr-Zr) | |
| 266 | 262 | 267 | | | 269 ($E_g$-Zr and O along XY) |
| 314 | | 309 | 310-315 ($A_g$) | 305 ($A_g$ Zr-O) | |
| | 320 | | | | 319 ($B_{1g}$-Zr and O along Z) |
| 335 | | 336 | | 336 (Zr-Zr) | |
| 346 | | 349 | | 350 (Zr-O) | |
| 382 | | 383 | | 381 ($B_g$ O-O) | |
| 457 | 464 | 460 | | | 461 ($E_g$-Zr and O along XY) |
| 483 | | 482 | 460-482 ($A_g$) | 476 ($A_g$ O-O) | |
| 507 | | 510 | | 500 ($B_g$ O-O) | |
| 539 | | 541 | | 534 ($B_g$ O-O) | |
| 569 | | 564 | 578 ($A_g$) | 556 ($A_g$ O-O) | |
| 621 | 604 | 621 | 610-620 ($A_g$) | 615 ($B_g$ O-O) | 602 ($A_{1g}$-O along Z) |
| 642 | 642 | 643 | | 637 ($A_g$ O-O) | 648 ($B_{1g}$-Zr and O along Z) |

A particular phenomenon that is associated to DSE growth is banding, that follow the solidification front shape being dependent on the pulling rate [10]. The banding phenomenon is depicted in Figure 7. Bands correspond to distinct regions of the same constituent but alternating coarser and finer morphologies, with a sharp transition between them [9, 27]. The bands are identified in longitudinal cross-sections, spaced between 30 to 120 µm, this value being proportional to the pulling rate. The banding phenomenon in fibres is due to local perturbations in the growth parameters, e.g. energy laser absorption, temperature, velocity, and convection [1,9,27]. Such perturbations may induce segregation or phase coarsening, in this case of bigger sized zirconia inclusions inside the mullite crystals [9,27].

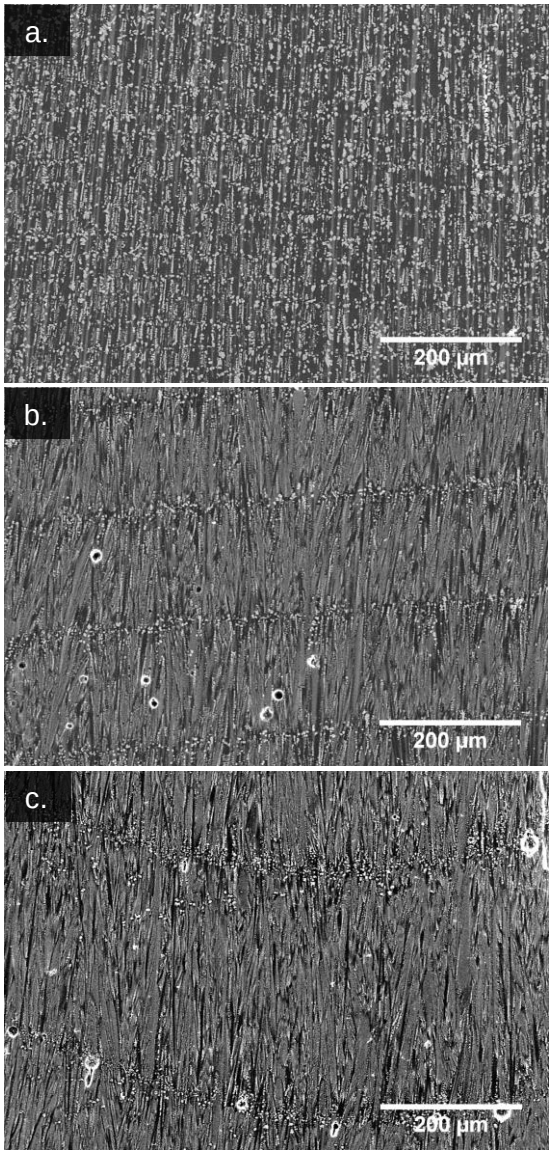


***Figure 7:*** *SEM micrographs illustrating the increase of the bands distance with the growth rate:* ***(a)*** *10 mm/h,* ***(b)*** *50 mm/h and* ***(c)*** *100 mm/h.*

### III.2.3.2. Off-eutectic zirconia rich composition ($C_2$)

All fibres grown with zirconia rich off-eutectic composition $C_2$ present a non-directional morphology, an uncommon result in directional solidification processes, as disclosed in Figure 8. In these micrographs, the longitudinal microstructure view (Fig. 8a) is undistinguishable from that in cross section (Fig. 8b).This phenomenon takes place for all pulling rates. Fibres are mainly composed by zirconia phase (white phase) around 55 vol.% irregularly distributed with an arborescent shape (in the equiaxed dendrites), surrounded by two different phases, sillimanite (dark grey) and alumina (light grey).

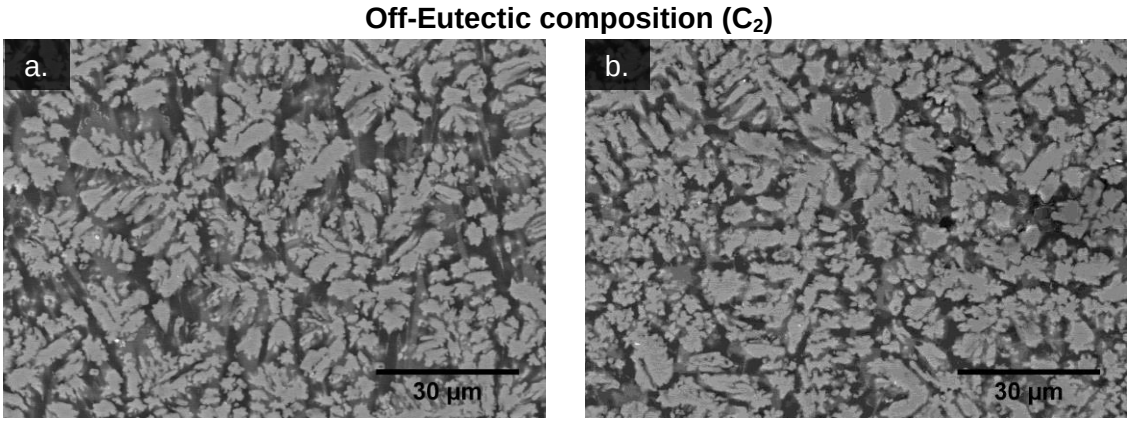


***Figure 8:*** *SEM micrographs of the longitudinal* ***(a)*** *and transversal* ***(b)*** *cross-sections of a fibre with the off-eutectic composition ($C_2$) grown at 500 mm/h.*

X-ray diffraction data in Figure 9 confirm the presence of tetragonal zirconia and alumina, mainly in the slowest grown fibres, at 10 mm/h, while sillimanite essentially appears at 500 mm/h. The Raman spectra taken from the $C_2$ fibres are shown in Figure 10. For this composition, regardless the pulling rate, only the tetragonal structure of zirconia is detected. Additionally, a small contribution from the $A_{1g}$ mode of alumina (418 $cm^{-1}$) is arrowed, in concomitance with the XRD data for the fibre grown at 10 mm/h grown (Fig. 9).

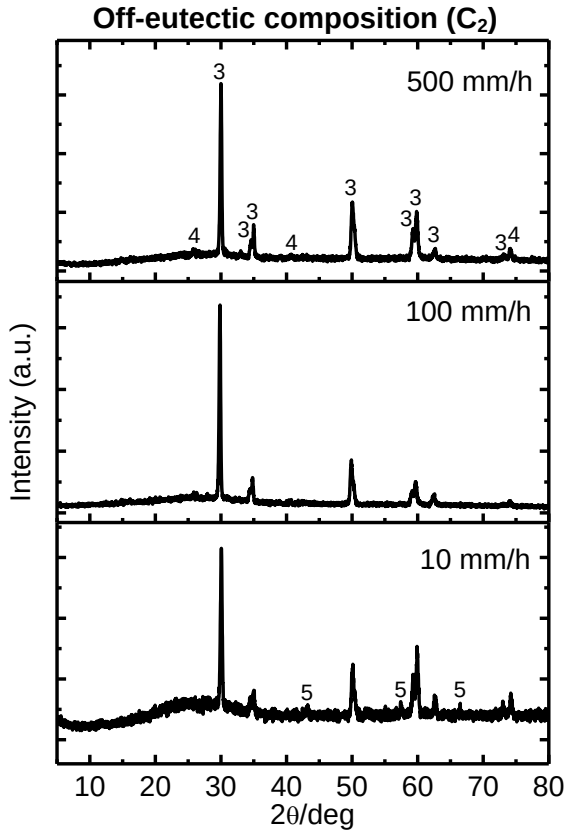


***Figure 9:*** *XRD data from fibres with off-eutectic composition ($C_2$) grown from 10 to 500 mm/h. The diffraction pattern corresponds to (3) tetragonal zirconia phase JCPDS:01-082-1241, (4) sillimanite JCPDS:01-074-0274 and (5) alumina JCPDS:01-076-0144.*

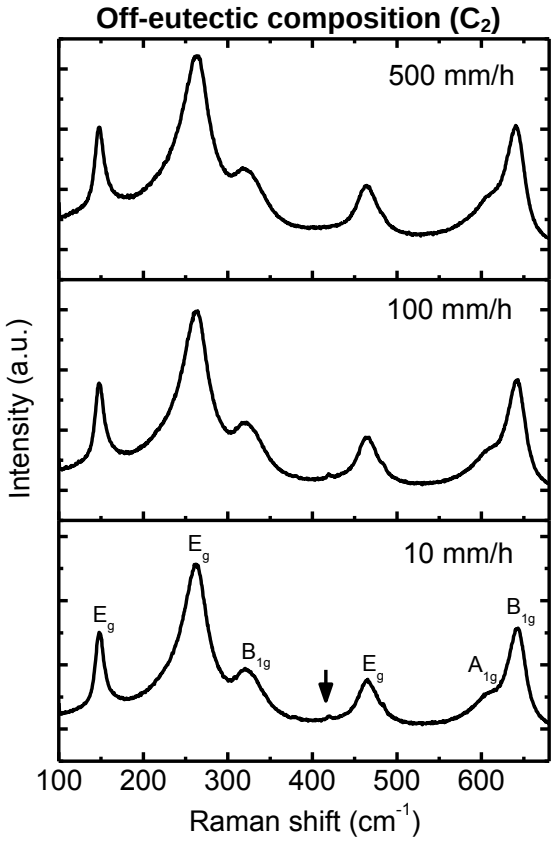


***Figure 10:*** *Raman spectra from transversal cross sections of mullite-zirconia fibres with off-eutectic composition ($C_2$), from 10 to 500 mm/h. The Raman-active modes $E_g$, $A_{1g}$ and $B_{1g}$ correspond to tetragonal zirconia, according to Table 2. The arrowed small feature corresponds to an alumina contribution at 418 $cm^{-1}$.*

### III.2.3.3. Off-eutectic mullite rich composition ($C_3$)

The microstructure of the fibres grown with mullite rich off-eutectic composition $C_3$ is characterized by the development of axial-oriented mullite prismatic crystals. At a pulling rate of 10 mm/h, the mullite crystals (~68 vol.%) are surrounded by a coarse eutectic mullite-zirconia phase (~19 vol.% of zirconia) (Figs.11a,b), which differs from composition $C_1$, where the zirconia globules appear inside the mullite crystals (Figs. 3c,d). The intercrystalline region is filled by the amorphous phase (~13 vol.%, light grey phase) (Figs. 11a,b).

For fibres grown at 100 mm/h, the eutectic microconstituent becomes a complete shell around the mullite crystals with the major difference of being much finer (Figs. 11c,d). In this case the fibrils zirconia phase tends to grow perpendicularly to the mullite facets. For the highest pulling rate (500 mm/h), the zirconia phase is even finer and more dispersed within the eutectic, which fills all the intercrystalline region (Figs.11e, f). Figure 12 shows the XRD powder spectra of $C_3$ fibres that confirm the presence of mullite, monoclinic zirconia, tetragonal zirconia and some amorphous phase.

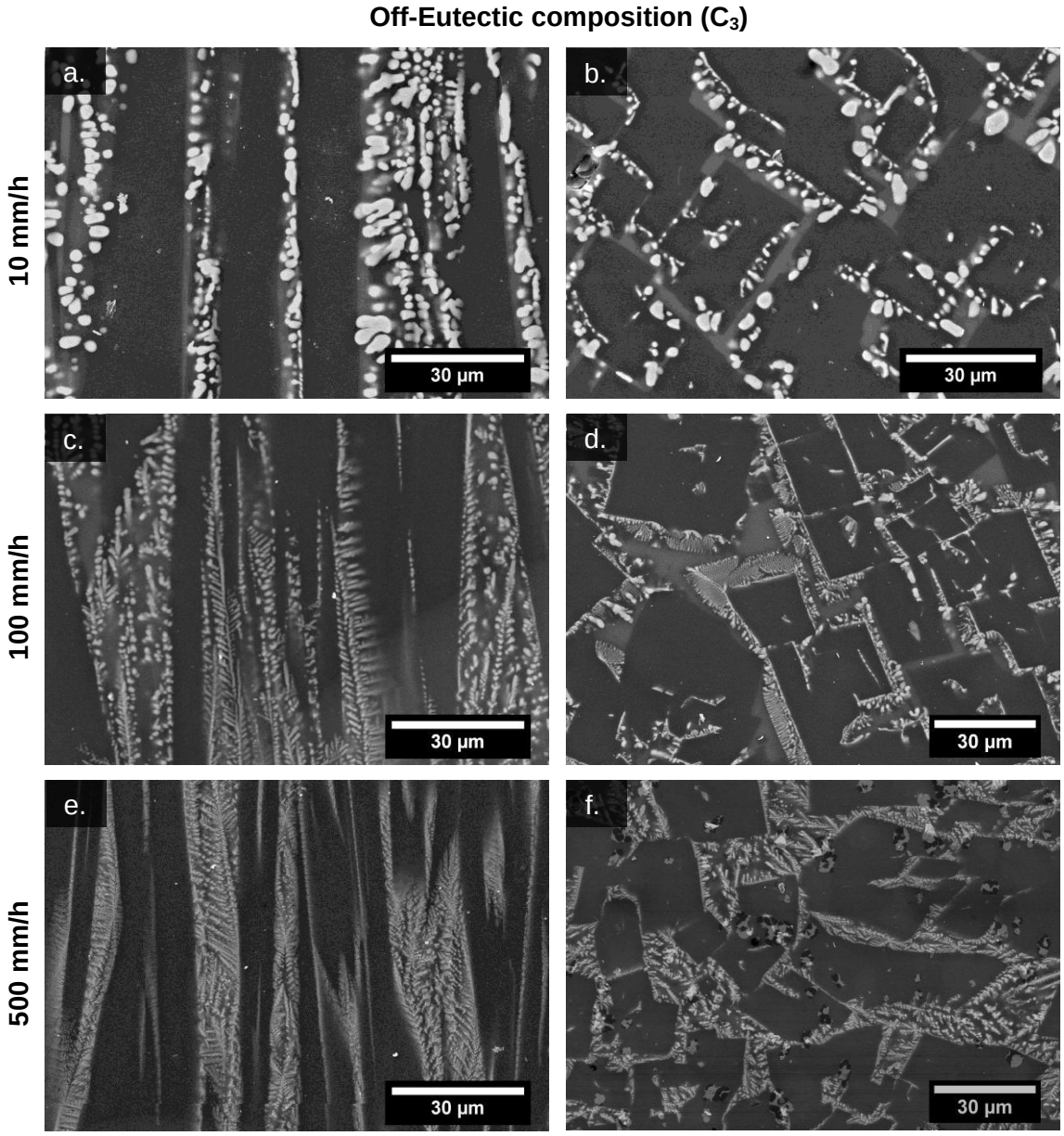


***Figure 11:*** *SEM micrographs of the longitudinal* ***(a****,* ***c*** *and* ***e)*** *and transversal* ***(b****,* ***d*** *and* ***f)*** *cross-sections of fibres with the off-eutectic composition ($C_3$) grown with pulling rates in the range 10 - 500 mm/h.*

The Raman data on the $C_3$ fibres are shown in Figure 13, the two zirconia phases dominating the spectra. As observed for the $C_1$ composition, the same trend is verified for the evolution of the tetragonal/monoclinic phase amount, the monoclinic phase being replaced by the tetragonal one as the pulling rate increases.

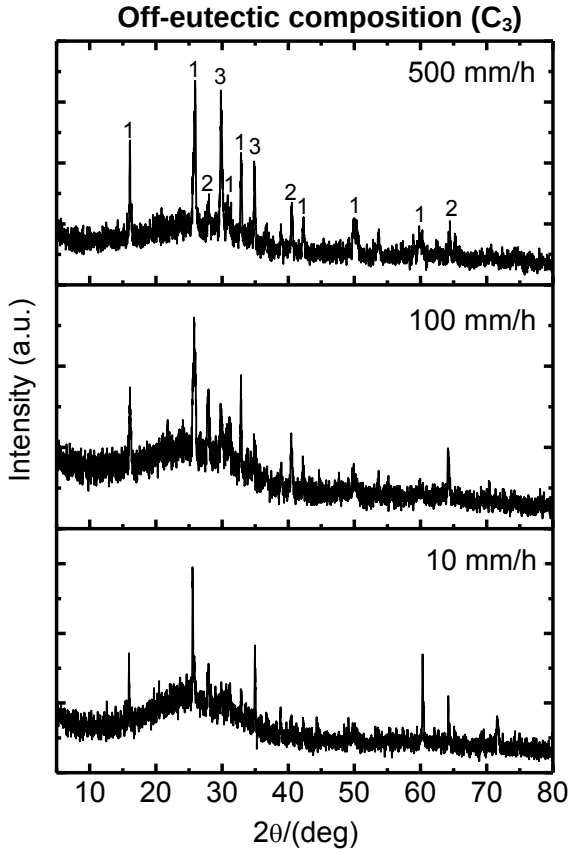


***Figure 12:*** *XRD data from fibres with off-eutectic composition ($C_3$) grown at 10 to 500 mm/h. The diffraction pattern corresponds to (1) mullite JCPDS: 00-015-0776, (2) monoclinic zirconia JCPDS: 01-070-8739 and (3) tetragonal zirconia JCPDS: 01-075-9646.*

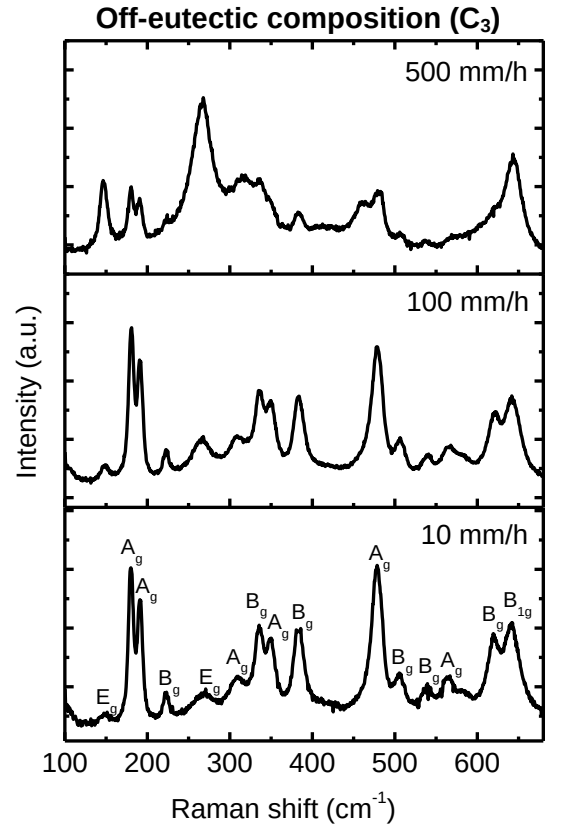


***Figure 13:*** *Raman spectra from transversal cross sections of mullite-zirconia fibres with eutectic composition ($C_3$), grown with pulling rates in the range 10 - 500 mm/h. Raman-active modes $A_g$ and $B_g$ are from monoclinic zirconia, while $E_g$ and $B_{1g}$ are from tetragonal zirconia, according to Table 2.*

### III.2.4. Discussion

Homogeneity and morphology have special relevance in the mullite-zirconia eutectic fibres processed by LFZ since their properties strongly depend on these factors. An important feature is the size and shape of eutectic colonies or columns and their crystallographic orientation [2,28]. The occurrence of coupled or dendritic eutectics depends on the growth rate assuming a constant solidification thermal gradient. Theoretically, the coupled growth occurs in equilibrium conditions and promotes regular structures where two eutectic phases crystallize simultaneously [2,28]. Coupled eutectic solidification, which occurs bellow a critical growth rate [2], happens in the present system at 1 mm/h (Figs. 3a,b) for composition $C_1$, the eutectic composition of the mullite-zirconia binary system that solidifies at 1790ºC (Fig. 1b).

At intermediate pulling rates of 10 mm/h (Figs. 3c,d), disruption of the planar solidification front leads to columnar growth, still exhibiting an irregular distribution of coarse zirconia inclusions in the mullite phase. However, at this pulling rate, the crystallization course does not finish at the eutectic invariant of the mullite-zirconia binary system (Fig. 1b), progressing with an Al-Y-Si rich residual liquid that solidifies as an amorphous phase between the crystals. As a consequence of faster cooling, the amount of residual liquid increases with the pulling rate. So, in order to have a complete redistribution of all chemical elements, and to avoid amorphous phases, slow growth is helpful (<10 mm/h).

For higher speeds (100-500 mm/h), competitive growth of dendrites surpasses coupled eutectics solidification [2] and faceted eutectic dendrites develop (Figs. 3e-h). The formation of facets by the phase with high melting entropy led to irregular eutectic structures in ceramic systems like $Al_2O_3$-$Y_2O_3$, where alumina and yttrium aluminium garnet are examples of phases which have a tendency to facet. Like in the present mullite-zirconia system, this results in very restricted conditions for coupled growth in DSEs [2,28].

The pulling rate as also a net effect on the relative amount of tetragonal zirconia with respect to monoclinic structure. The evolution of the most prominent peaks of each phase (highlighted by coloured lines in Fig. 6) changes contrariwise with the pulling rate. This way, Raman spectroscopy confirmed the trend dependency of the tetragonal/monoclinic amount ratio (T/M) with the growth rate observed in XRD (Fig. 5). The good agreement between the two techniques is put in evidence in the plot of Figure 14, where T/M increases monotonically with the pulling rate. In this plot, the XRD zirconia peak intensities at 29.9º (tetragonal) and 31.4º (monoclinic) were considered, whereas for Raman spectroscopy, the integrated areas of the bands at 178 $cm^{-1}$ (monoclinic) and 264 $cm^{-1}$ (tetragonal) were used. The simultaneous presence of monoclinic and non-transformable

tetragonal structures corresponds to a well-known region of the zirconia-yttria system [29]. The monoclinic phase is favoured in slow cooling (low pulling rates) that approaches equilibrium conditions. Kinetically, at high pulling rates, yttrium diffusion from the zirconia phase to the outer residual liquid is hindered, so tetragonal zirconia is stabilized [30]. Moreover, the amorphous shell around the tetragonal zirconia grains helps on this stabilizing role [30].

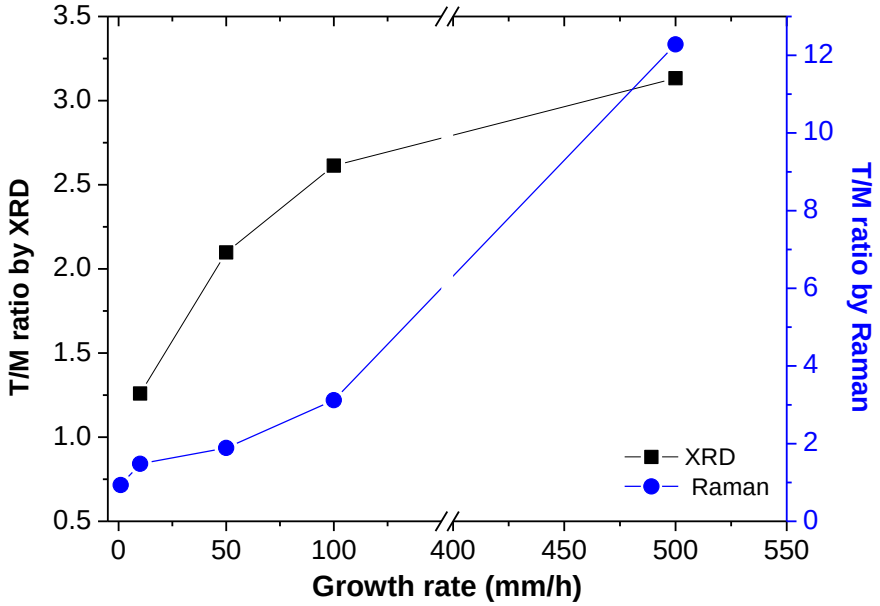


***Figure 14:*** *Tetragonal/monoclinic (T/M) ratio dependence on pulling rate, measured by XRD and Raman spectroscopy in the C1 composition. In XRD, zirconia peak intensities at 29.9º (tetragonal) and 31.4º (monoclinic) were considered. In Raman spectroscopy, the integrated areas of the bands at 178 $cm^{-1}$ (monoclinic) and 264 $cm^{-1}$ (tetragonal) were used.*

The above described tetragonal/monoclinic phase ratio dependency with pulling rate was clearly verified for the compositions $C_1$ and $C_3$, while for $C_2$ (the richest in zirconia) only the tetragonal zirconia phase was detected. In fact, compositional moving from the binary eutectic ($C_1$) towards the zirconia-rich ($C_2$) or mullite-rich ($C_3$) fields leads to strong modifications in the fibres microstructure (Figs. 3, 8 and 11). This is particularly pronounced for the zirconia-rich off-eutectic $C_2$. This composition situates in the primary crystallization region of zirconia (Fig. 1a) so that zirconia develops as primary phase. Additionally, since the used zirconia precursor was the yttrium pre-stabilized form, only tetragonal zirconia develops in this composition due to its high yttrium concentration. The remaining $Al_2O_3$-$SiO_2$ liquid after primary crystallization solidifies as a mixture of alumina and silimanite interdendritic phases. The absence of mullite shows that $C_2$ solidification is far from equilibrium justifying the crystallization of the metastable sillimanite ($Al_2O_3.SiO_2$).

As this silicate is alumina-poor with respect to mullite, it is compensated by alumina formation, as detected by both XRD and Raman (Figs. 9, 10) in the 10 mm/h grown fibre.

The final morphology of the off-eutectic compositions is determined by the constitutional undercooling criterion [1]:

$$G/R = -m(C_E - C_0)/D \quad (1)$$

where $m$ is the slope of the *liquidus*, $C_E$ the eutectic composition, $C_0$ the nominal composition and $D$ the diffusion coefficient of the solute in the melt. This equation can take the form [1]:

$$G/R = k\,\Delta T \quad (2)$$

where $k$ is a constant and $\Delta T$ is the solidification range of $C_o$.

When the left side of equation (2) decreases or the right side increases, the following morphological sequence takes place: planar $\rightarrow$ cells (columns) $\rightarrow$ dendrites $\rightarrow$ equiaxed grains [1]. Fibres from off-eutectic zirconia rich composition ($C_2$) are mainly composed by equiaxed zirconia grains which do not show any preferential orientation and are randomly distributed. This happens when constitutional undercooling strongly prevails and the solid nucleates in the melt ahead of the solid/liquid interface. Here, primary dendrites of zirconia began to develop and later branching in all directions, resulting in equiaxed dendrites. For a given G/R, the solidification range $\Delta T$ is thus the determinant parameter of the constitutional undercooling condition. For the off-eutectic $C_2$ composition, the very high value $\Delta T$~500ºC (Fig. 1b) explains the development of equiaxed dendrites of zirconia.

Contrarily to $C_2$, the much smaller $\Delta T$~50ºC (Fig. 1b) for the off-eutectic $C_3$ composition determines the growth of axial-oriented grains in the form of prismatic crystals of mullite, the primary phase of $C_3$. This is characteristic of a competitive growth, where the primary phase is heavily constitutionally undercooled thus growing faster than the eutectic one [31]. The microstructure of the off-eutectic mullite rich composition ($C_3$) also comprises the two-phase mullite-zirconia eutectic as an interdendritic constituent, according to the phase diagrams (Figs. 1a,b). Like for $C_1$ composition, the morphology of the eutectic constituent in $C_3$ is much coarser at low pulling rates (Figs. 11a,b) than for the higher speeds (Figs. 11c-f) that have shorter diffusion paths.

### III.2.5. Conclusions

Fibres of the mullite-zirconia binary system composites were grown by the LFZ method from 1 to 500 mm/h of pulling rate. Fibres with the eutectic composition show a net dependence of microstructure on the pulling rate. A coupled eutectic morphology devel-

ops at the lowest speed, 1 mm/h, due to planar solidification conditions that lead to a regular structure of the two eutectic components mullite and zirconia.

When the pulling rate was increased above 10 mm/h, disruption of the planar solidification front leads to columnar growth and well-aligned mullite crystals with coarse zirconia inclusions inside. A Al-Y-Si residual liquid solidifies as an amorphous phase between the crystals. At even higher speeds (100-500 mm/h), the crystals that develop along the fibre axis take the form of faceted eutectic dendrites.

Fibres with the mullite-rich off-eutectic composition follow a similar microstructural evolution for the eutectic constituent, i.e. coarse and fine morphology at low and high speeds, respectively. The difference is the crystallization of prismatic primary mullite crystals. A very distinct behaviour is found for the zirconia-rich off-eutectic composition where randomly distributed equiaxed zirconia dendrites crystallize within a matrix of alumina and sillimanite phases.

A good agreement between XRD analysis and Raman spectroscopy was found on the tetragonal/monoclinic zirconia amount ratio dependence with the pulling rate. It was observed that the increase of growth rate was proportional to the inverse of monoclinic phase amount.

## Acknowledgments

Ricardo Carvalho thanks to Fundação para a Ciência e a Tecnologia (FCT) for the financial funding SFRH/BD/64891/2009 and PEst-C/CTM/LA0025/2011.

## References

[1] R.L. Ashbrook, Directionally solidified ceramic eutectic, Journal of the American Ceramic Society, 60 (1977) 428-435.

[2] J. Llorca, V.M. Orera, Directionally solidified eutectic ceramic oxides, Progress in Materials Science, 51 (2006) 711-809.

[3] A. Revcolevschi, G. Dhalenne, Engineering oxide-oxide and metal-oxide microstructures in directionally solidified eutectics, Advanced Materials, 5 (1993) 657-662.

[4] R.M. White, J.M. Kunkle, A.V. Polotai, E.C. Dickey, Microstructure and hardness scaling in laser-processed $B_4C$-$TiB_2$ eutectic ceramics, Journal of the European Ceramic Society, 31 (2011) 1227-1232.

[5] L.B. Garrido, E.F. Aglietti, L. Martorello, M.A. Camerucci, A.L. Cavalieri, Hardness and fracture toughness of mullite-zirconia composites obtained by slip casting, Materials Science and Engineering: A, 419 (2006) 290-296.
[6] R.G. Carvalho, A.J.S. Fernandes, F.J. Oliveira, E. Alves, N. Franco, C. Louro, R.F. Silva, F.M. Costa, Single and polycrystalline mullite fibres grown by laser floating zone technique, Journal of the European Ceramic Society, 30 (2010) 3311-3318.
[7] R.I. Merino, J.I. Peña, Á. Larrea, G.F.d.l. Fuente, V.M. Orera, Melt grown composite ceramics obtained by directional solidification: structural and functional applications, Recent Research Developments in Materials Science, 4 (2003) 1-24.
[8] J.Y. Pastor, P. Poza, J. Llorca, J.I. Peña, R.I. Merino, V.M. Orera, Mechanical properties of directionally solidified $Al_2O_3$-$ZrO_2$($Y_2O_3$) eutectics, Materials Science and Engineering A, 308 (2001) 241-249.
[9] J. Llorca, J.Y. Pastor, P. Poza, J.I. Pena, I. de Francisco, A. Larrea, V.M. Orera, Influence of the $Y_2O_3$ content and temperature on the mechanical properties of melt-grown $Al_2O_3$-$ZrO_2$ eutectics, Journal of the American Ceramic Society, 87 (2004) 633-639.
[10] I. de Francisco, R.I. Merino, V.M. Orera, A. Larrea, J.I. Peña, Growth of $Al_2O_3$/$ZrO_2$($Y_2O_3$) eutectic rods by the laser floating zone technique: effect of the rotation, Journal of the European Ceramic Society, 25 (2005) 1341-1350.
[11] J.Y. Pastor, J. Llorca, P. Poza, I. de Francisco, R.I. Merino, J.I. Peña, Mechanical properties of melt-grown $Al_2O_3$-$ZrO_2$($Y_2O_3$) eutectics with different microstructure, Journal of the European Ceramic Society, 25 (2005) 1215-1223.
[12] D. Sola, F.J. Ester, P.B. Oliete, J.I. Peña, Study of the stability of the molten zone and the stresses induced during the growth of $Al_2O_3$-$Y_3Al_5O_{12}$ eutectic composite by the laser floating zone technique, Journal of the European Ceramic Society, 31 (2011) 1211-1218.
[13] H. Schneider, S. Komarneni, Mullite, WILEY-VCH Verlag GmbH & Co. KGaA, Weinheim, 2005.
[14] C. Zanelli, M. Dondi, M. Raimondo, G. Guarini, Phase composition of alumina-mullite-zirconia refractory materials, Journal of the European Ceramic Society, 30 (2010) 29-35.
[15] W.Y. Wang, A.H. Wang, C.S. Xie, W.L. Song, D.W. Zeng, Microstructural features of an $Al_2O_3$-$ZrO_2$-$SiO_2$ refractory material treated with $CO_2$ laser melting, Materials Letters, 58 (2004) 2848-2851.
[16] B. Mitra, N. Biswas, P. Aggarwal, Zirconia-mullite ceramics by reaction-sintering, Bulletin of Materials Science, 12 (1989) 457-460.
[17] J.S. Moya, J.F. Bartolomé, P. Pena, Diagramas de equilibrio cuaternarios ZrO2-$Al_2O_3$-$SiO_2$-(CaO, MgO, $TiO_2$). Una poderosa herramienta para el desarrollo de nuevos

materiales por sinterización reactiva, Boletín de la Sociedad Española de Cerámica y Vidrio, 50 (2011) 291-300.

[18] C. Li, M.J. Li, UV Raman spectroscopic study on the phase transformation of $ZrO_2$, $Y_2O_3$-$ZrO_2$ and $SO_4^{2-}$/$ZrO_2$, Journal of Raman Spectroscopy, 33 (2002) 301-308.

[19] C.H. Ruscher, Phonon spectra of 2:1 mullite in infrared and Raman experiments, Physics and Chemistry of Minerals, 23 (1996) 50-55.

[20] P. Bouvier, G. Lucazeau, Raman spectra and vibrational analysis of nanometric tetragonal zirconia under high pressure, Journal of Physics and Chemistry of Solids, 61 (2000) 569-578.

[21] M. Maczka, E.T.G. Lutz, H.J. Verbeek, K. Oskam, A. Meijerink, J. Hanuza, M. Stuivinga, Spectroscopic studies of dynamically compacted monoclinic $ZrO_2$, Journal of Physics and Chemistry of Solids, 60 (1999) 1909-1914.

[22] L. Kumari, W. Li, D. Wang, Monoclinic zirconium oxide nanostructures synthesized by a hydrothermal route, Nanotechnology, 19 (2008) 195602.

[23] X.P. Tan, S.Q. Liang, G.W. Zhang, Y. Zhang, L.Y. Chai, Structural evolution of $ZrO_2$-mullite nanocomposites from the Si-Al-Zr-O amorphous bulk, Phase Transitions, 84 (2011) 157-166.

[24] X.L. Tang, X.H. Zheng, Raman scattering and t-phase lattice vibration of 3% (mole fraction) $Y_2O_3$-$ZrO_2$, Journal of Materials Science & Technology, 20 (2004) 485-489.

[25] N.R. Harlan, R.I. Merino, J.I. Peña, A. Larrea, V.M. Orera, Phase Distribution and Residual Stresses in Melt-Grown $Al_2O_3$-$ZrO_2$($Y_2O_3$) Eutectics, Journal of the American Ceramic Society, 85 (2002) 2025-2032..

[26] J.A. Pardo, R.I. Merino, V.M. Orera, J.I. Pena, C. Gonzalez, J.Y. Pastor, J. Llorca, Piezospectroscopic study of residual stresses in $Al_2O_3$-$ZrO_2$ directionally solidified eutectics, Journal of the American Ceramic Society, 83 (2000) 2745-2752.

[27] M. Gremaud, M. Carrard, W. Kurz, Banding phenomena in Al-Fe alloys subjected to laser surface-treatment, Acta Metallurgica et Materialia, 39 (1991) 1431-1443.

[28] V.S. Stubican, R.C. Bradt, Eutectic Solidification in Ceramic Systems, Annual Review of Materials Science, 11 (1981) 267-297.

[29] J.R. Brandon, R. Taylor, phase-stability of zirconia-based thermal barrier coatings 1. zirconia yttria alloys, Surface & Coatings Technology, 46 (1991) 75-90.

[30] S. Yugeswaran, V. Selvarajan, P. Dhanasekaran, L. Lusvarghi, Transferred arc plasma processing of mullite-zirconia composite from natural bauxite and zircon sand, Vacuum, 83 (2009) 353-359.

[31] W. Kurz, D.J. Fisher, Fundamentals of solidification, Trans. tech. Publications Ltd, Switzerland, 1992.

## III.3. Ionic conductivity of directionally solidified zirconia-mullite eutectics

Ricardo G. Carvalho[a], Andrei V. Kovalevsky[b], Michael W. Lufaso[c], Rui F. Silva[b], Florinda M. Costa[a], Filipe M. Figueiredo[b]

[a]I3N, Department of Physics, University of Aveiro, 3810-193 Aveiro, Portugal

[b]CICECO, Department of Materials and Ceramic Engineering, University of Aveiro, 3810-193 Aveiro, Portugal

[c]Department of Chemistry, University of North Florida, 1 UNF Drive, Jacksonville, FL 32224, USA

Solid State Ionics, 256 (2014) 45-51

**DOI:** http://dx.doi.org/10.1016/j.ssi.2013.12.033

### Abstract

The properties of directionally solidified eutectic (DSE) zirconia-mullite composites are presented. These materials combine two oxide ion conductors in eutectic microstructures stable over broad temperature (570-1415 °C) and oxygen partial pressure ($10^{-20}$ to $10^{5}$ Pa) ranges, which are pertinent for their application as high temperature (>1200 °C) solid electrolytes, e.g. in nernstian sensors. X-ray diffraction and scanning electron microscopy / energy dispersive spectroscopy results reveal a composite structure comprising eutectic crystals of mullite and zirconia, and an intergranular amorphous phase rich in Al-Y-Si-O. The amorphous phase is crystallised upon annealing at 1400 °C, and the resulting composites have a composition close to the nominal eutectic consisting of 79 vol.% mullite and 21 vol.% zirconia. The electrical conductivity of these materials is rationalized in terms of percolation, fraction and the properties of each phase, attaining values in excess of 0.01 S/cm at 1370 °C and displaying Arrhenius behaviour with activation energy of 70 kJ/mol. The broad electrolytic domain of these solid electrolytes is demonstrated by conductivity measurements carried out in $O_2$, air, Ar and 10%$H_2$+90%$N_2$ atmospheres from 600 °C to 1370 °C.

***Keywords:*** Zirconia, mullite, eutectics, directional solidification, ionic conductivity.

### III.3.1. Introduction

Directionally solidified eutectic (DSE) oxide composites are characterized by very particular microstructures displaying textured and homogeneous fine mixtures of the components. These microstructures can be tailored as rod-like, lamellar or fibrous by a relatively simple control of the processing conditions [1-5]. These features are attractive to the design of electroceramics with low percolation threshold volumes [2-4]. Most of the investigations have been carried out in oxide DSE composite fibres grown by the laser floating zone (LFZ) method [1], with the composites of alumina and an ionic conductor such as yttria-stabilized zirconia being a good example where higher bending strength is expected when compared to pure zirconia [6-8].

Yttria-stabilized zirconia (YSZ, $(Zr,Y)O_2$) is an excellent oxide ion conductor with high thermo-mechanical and chemical stability. YSZ is by far the most studied and used solid electrolyte for high temperature electrochemical applications, from promising technologies such as solid oxide fuel cells and electrolysers, to well-established mass-produced oxygen sensors [9-10]. The ionic conductivity of zirconia is (besides a minor contribution from intrinsic anti-Frenkel defects) mainly due to the extrinsic oxide vacancies ($V_O^{\cdot\cdot}$) formed to balance the partial substitution of $Zr^{4+}$ cations with lower valence $Y^{3+}$ according to the equilibrium expressed in Kröger-Vink notation by $Y_2O_3 \xrightarrow{ZrO_2} 2Y'_{Zr} + 3O_O^x + V_O^{\cdot\cdot}$ [9].

Mullite is an aluminosilicate with excellent chemical and thermo-mechanical stability that is widely employed in structural applications [11,12], having also been suggested as a possible substitute for zirconia electrolytes in potentiometric sensors able to operate in reducing conditions at very high temperatures (1400-1600 °C) [13-14]. The oxide conductivity of mullite is due to the oxide vacancies created by the substitution of $Si^{4+}$ for $Al^{3+}$ ($Al_2O_3 \xrightarrow{SiO_2} 2Al'_{Si} + V_O^{\cdot\cdot} + 3O_O^x$). However, the concentration of free vacancies is low and so is the conductivity, e.g. 3.2 x$10^{-5}$ S/cm at 800 °C for $3Al_2O_3$-$2SiO_2$ [16,17]. As desired for a solid electrolyte, the electronic conductivity is negligible, with ionic transference numbers higher than 0.99 at oxygen partial pressures ($P_{O_2}$) higher than $10^{-5}$ Pa, at 1400 °C, or 1 Pa at 1600 °C [13].

Zirconia-mullite composites are potentially interesting high temperature solid electrolytes because they combine the high ionic conductivity and broad electrolytic domain of zirconia with the good creep resistance, excellent chemical stability and strength of mullite at high-temperature [18]. Moreover, zirconia may improve the fracture toughness. Such composites were indeed proposed as oxygen sensors to work under the thermally and chemically harsh environment of steel making [18-19]. As expected, the ionic conductivity

increases with increasing zirconia fraction, with major changes near the percolation limit ($2.0x10^{-5}$ S/cm and $1.4x10^{-4}$ S/cm for 20 vol.% and 30 vol.% zirconia, respectively, at 700 °C) [16,18].

It was previously shown by some of the authors that zirconia-mullite DSE composites obtained by LFZ may display various microstructures (planar coupled eutectic, faceted mullite crystals enclosing a dispersion of fine zirconia fibrils or mullite columnar growth with coarse zirconia inclusions), depending on the pulling rate [20]. In the present work, the study of the $ZrO_2$-$SiO_2$-$Al_2O_3$ eutectic composition is refined in order to explore the potential of zirconia-mullite DSEs with low zirconia content (21 vol.%) as a dual-phase solid oxide electrolyte for application at temperatures higher than 1300 °C.

### III.3.2. Experimental

Feed and seed rods were prepared from commercial powders with a composition of 50 wt.% $\gamma$-$Al_2O_3$ (Merck, anhydrous, >99.9%), 20 wt.% $SiO_2$ (Sigma, 99%) and 30 wt.% 8 mol.% $Y_2O_3$–stabilized $ZrO_2$ (Tosoh Co., 99.9% with approximately 2% $HfO_2$). The powders were mixed during 90 minutes at 500 rpm in a planetary ball-mill (Retsch, PM100). Green rods were then processed by extrusion with the help of a polyvinyl alcohol (PVA 0.1 g/ml) binder. A LFZ apparatus described elsewhere [20] was used to grow fibres in air using pulling rates of 10, 100 and 500 mm/h. Typical fibres are ~1.5 mm in diameter and ~30 mm in length. Selected fibres were subjected to a post-synthesis annealing for 10 hours at 1400 °C in air.

The structural analysis of powdered fibres was carried out by X-ray diffraction (XRD, X'Pert MPD Philips, Cu-$K_\alpha$ radiation) with a step width of 0.01° and a scan rate of 3°/min. Variable temperature X-ray diffraction patterns (HTXRD) were collected between 300 °C and 1000 °C in the same apparatus, using a step width of 0.02°. The system is equipped with a Anton-Parr GmbH HTK16 chamber, containing a Pt filament and a Pt-Pt/Rh(10%) thermocouple. Rietveld analysis of the XRD patterns collected at each temperature was performed with Fullprof [21] and refining the scale factor, background, lattice parameters, sample displacement, and peak profile parameters.

The microstructural characterization was carried out in a scanning electron microscope (SEM Hitachi S4100) linked to an energy dispersive X-ray spectroscopy (EDS) system. The fractional area occupied by each phase was estimated based on SEM images, using Image J 1.45s [22], and assumed as equivalent to the volume fraction of each phase. At least 10 images for each sample were analyzed in order to obtain an average value and the associated dispersion.

The electrical conductivity was measured by impedance spectroscopy along the growth direction of samples with ~4.5 mm in length, which were cut from the original fibres. Platinum electrodes were applied at the tips and thermally treated at 1000 °C for 1 h to provide good electrical contacts. The impedance spectra were acquired with a Hewlett Packard 4984a LCR meter in the frequency range 20-$10^6$ Hz and using a test signal amplitude of 1 V. The measurements were carried out during cooling under flows (50 mL/min) of air, argon, oxygen or a mixture of 90%$N_2$+10%$H_2$ ($P_{O_2}$ monitored *in situ* using a YSZ nernstian sensor) and as a function of temperature in the range 570 °C - 1415 °C. Two experimental set-ups were used, one covering the high temperature range from ~900 °C up to ~1400 °C where only air, argon and oxygen atmospheres could be used (hydrogen is avoided for security reasons), and another specified for a low temperature range (up to 1000 °C) which is compatible with hydrogen containing gas mixtures, offering in addition the possibility to humidify the gases. The sample holders have the same design in set-ups.

### III.3.3. Results and discussion

#### III.3.3.1. Microstructural characterization and phase analysis

The room temperature XRD pattern of the fibre pulled at 100 mm/h (Fig. 1, thick line) shows the presence of three phases: orthorhombic mullite (M, space group Pbam [23]), and tetragonal ($Z^t$, space group $P4_2/nmc$ [24]) and monoclinic ($Z^m$, space group P21/c [25]) zirconias.

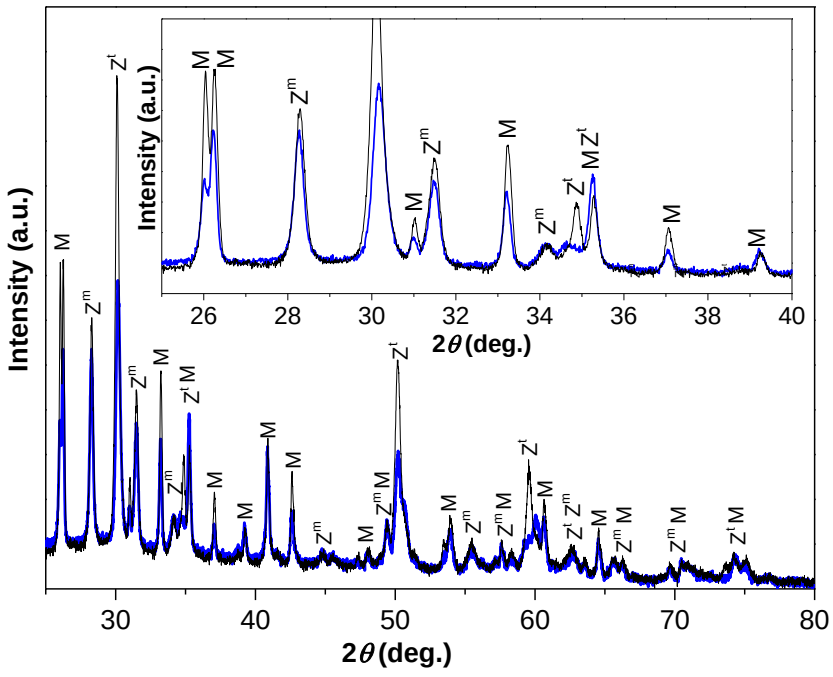


***Figure 1:*** *Powder XRD patterns of a zirconia-mullite eutectic fibre obtained at 100 mm/h (thick blue line) and of the same fibre annealed at 1400 °C in air for 10h (thin black line). M is mullite (JCPDS card n° 01-074-4146), $Z^m$ is monoclinic zirconia (JCPDS card n° 00-007-0343) and $Z^t$ is tetragonal zirconia (JCPDS card n° 04-016-2094).*

The HTXRD data in Figure 2 show the expected decrease of the intensity of the mullite reflections upon heating, due to the temperature factor. They also clearly depict the progressive transformation of $Z^m$ into $Z^t$ with increasing temperature, suggesting that the $YO_{1.5}$ content in $ZrO_2$ is lower than ~6 mol.%, and thus that the existing $Z^t$ lies on the category of the transformable tetragonal zirconia [26,27]. One may thus obtain an estimate of the yttria content as a function of temperature by the XRD intensity ratio between the $Z^m$ $(\bar{1}11)$ and $Z^t$ $(101)$ reflections.

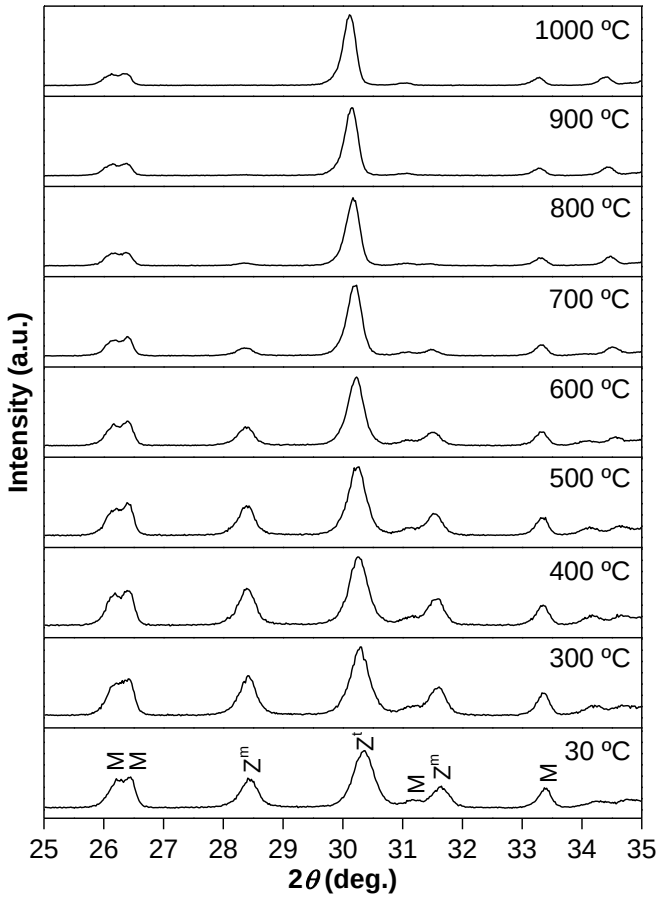


***Figure 2:*** *Powder HTXRD patterns of a fresh zirconia-mullite eutectic fibre grown at 100 mm/h.*

The HTXRD patterns did not support refinement of the fractional coordinates and thermal parameters for each independent atom of the three phases, but these restrictions are expected to have a minimal influence on the estimated weight fractions. The full list of the refined lattice parameters, unit cell volume, Rietveld R factors and fit statistics are provided as supplementary information. The results are depicted in Figure 3, with the inset showing the crystalline weight fractions of both $Z^t$ and $Z^m$. Between 400 and 800 °C the $Z^m \rightarrow Z^t$ transformation rate has an approximately linear temperature dependence, and thus one may express the temperature at which the free energies of the tetragonal and the

monoclinic phases are equal as $T_0^{t-m} = 1114 - 159.44x$, where *x* is the molar fraction of $YO_{1.5}$ [28]. Using this relation and assuming $T_0^{t-m}$ = 562°C at the inflection point of the polynomial fit in Figure 3, the estimated concentration of $YO_{1.5}$ in $ZrO_2$ is 3.5 mol.%. This value is much lower than that in the initial precursor (16 mol.% $YO_{1.5}$).

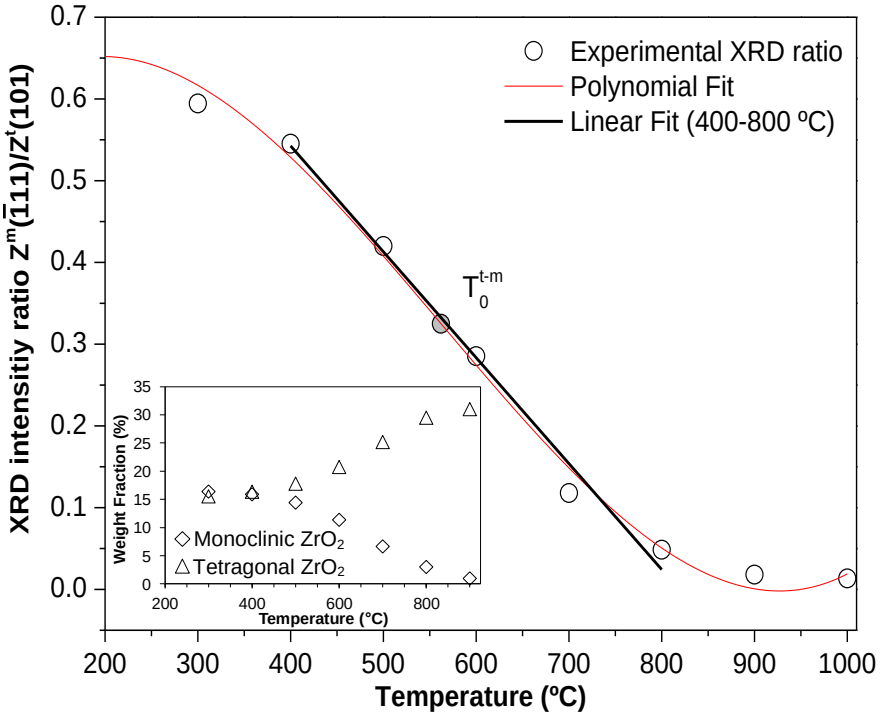


***Figure 3:*** *XRD intensity ratio between the $Z^m$ ($\bar{1}11$) and $Z^t$ (101) reflections plotted as a function of temperature. The transition temperature ($T_0^{t-m}$ ~ 562 °C) is depicted on the polynomial fit. The inset shows the weight fractions of both phases estimated by Rietveld refinement.*

The most likely explanation for such difference is the segregation of yttria to a glassy Si-Y-Al intergranular phase, as shown by SEM/EDS (Figs. 4 and 5). This phase appears with light grey contrast surrounding the eutectic colonies in the SEM images (Figs. 4 a,b,c), whereas the eutectic constituent grows aligned with the fibre axis comprising a mullite (dark grey) matrix enclosing fibrils of zirconia (white). The amount of amorphous phase increases substantially when increasing the pulling rate from 100 mm/h to 500 mm/h (Figs. 4a and 4b). After annealing the fibre at 1400 °C, small crystallites begin to nucleate inside the amorphous phase (Fig. 4d). Such precipitates have a faceted habit, as shown in Figure 5a.

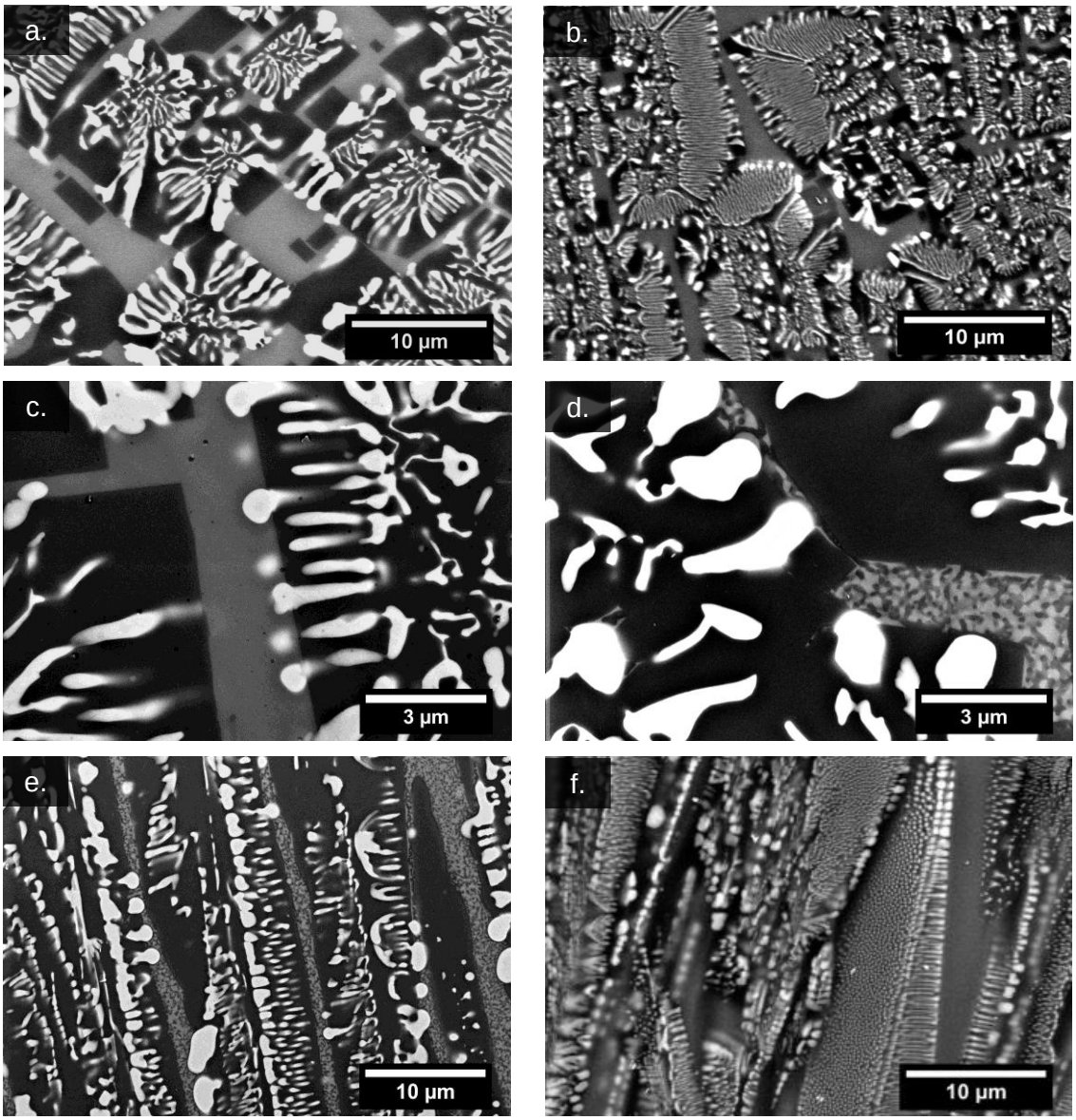


***Figure 4:*** *SEM micrographs obtained at the transversal cross-sections of fresh fibres grown at* ***(a)*** *100 and* ***(b)*** *500 mm/h.* ***(c)*** *and* ***(d)*** *compare the 100 mm/h fibres before and after annealing at 1400 °C in air for 10 h, respectively.* ***(e)*** *and* ***(f)*** *show the longitudinal cross-section of the fibre grown at 100 mm/h and annealed at 1400 °C/ 10 h and of the fresh fibre obtained at 500 mm/h, respectively. Mullite appears dark, zirconia is white and the glassy phase shows up in light grey contrast.*

The semi-quantitative EDS analysis of the mullite crystals (Region 1 in Fig. 5a) yields a Al:Si atomic ratio close to 4:1 (Fig. 5b), confirming the $2Al_2O_3$:$SiO_2$ stoichiometry. Such composition is typical of mullite crystals obtained from a melt [11] The EDS spectrum of Region 2 is similar to the one of Region 1, although suggesting higher amount of Si, whereas Y is highly concentrated in the precipitates of Region 3, also containing Zr (Fig. 5b). The EDS maps in Figs. 5c and 5d provide evidence for the described elemental dis-

tribution in the different regions, namely the Y (and possibly also Zr) in the precipitated crystallites, and the Si enrichment in the intergranular phase.

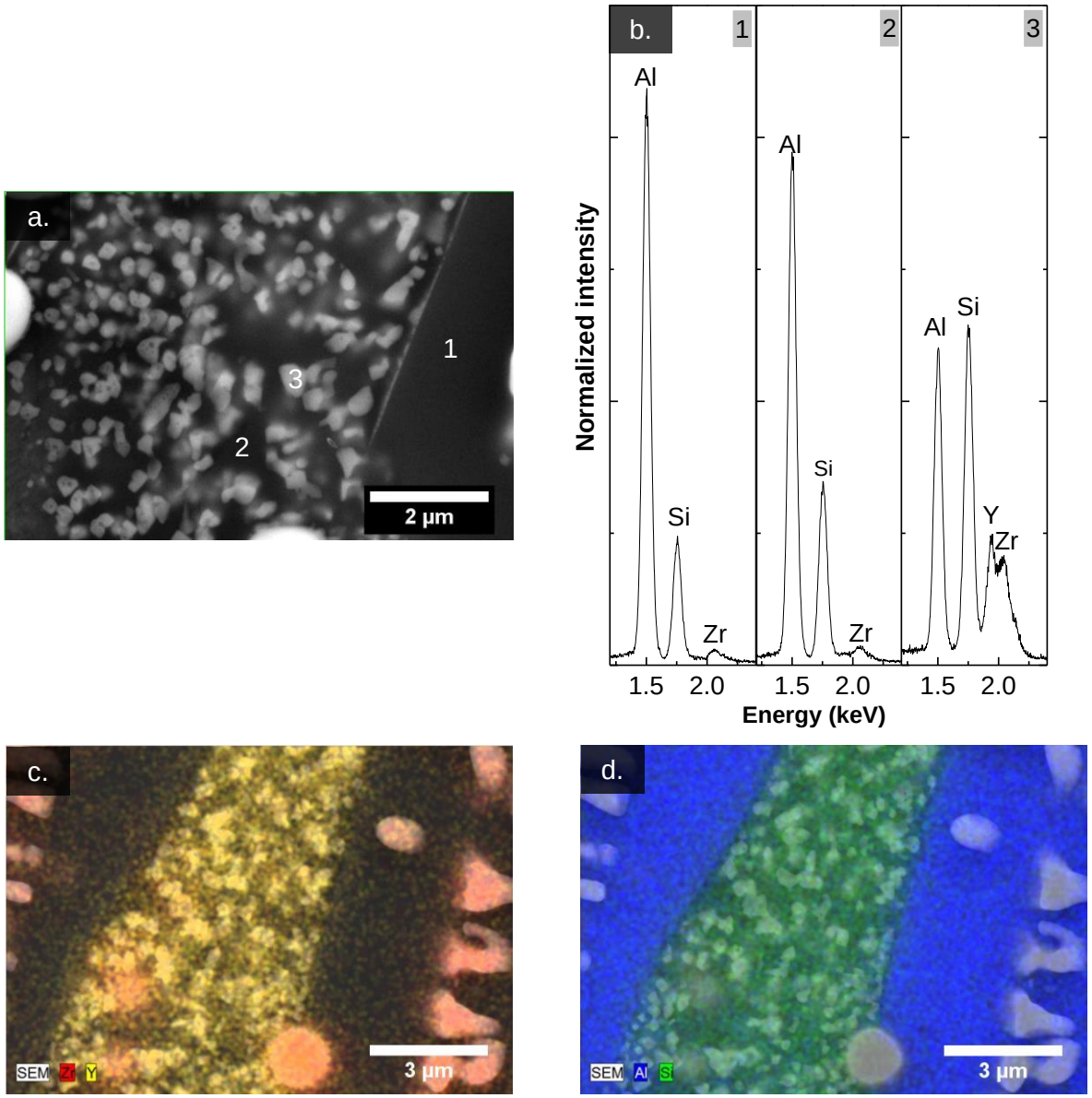


***Figure 5: (a)*** *SEM micrograph acquired on the longitudinal cross-section of the 100 mm/h fibre after electrical measurements up to 1415 °C. The three labelled regions correspond to: 1 - mullite crystal, 2 - intergranular region, and 3 - crystalline precipitates in the intergranular region.* ***(b)*** *EDS spectra corresponding to the regions 1, 2 and 3 labelled in (a).* ***(c, d)*** *Elemental EDS maps for Zr/Y and Al/Si binaries, respectively.*

The differences in the relative intensity of the reflections observed in the XRD patterns of the as grown (thick blue line in Fig. 1) and annealed fibres (thin black line) confirm that irreversible structural changes have indeed occurred upon annealing, namely the transformation of monoclinic zirconia into the tetragonal or cubic polymorph (both phases are difficult to distinguish without filtering out the Cu-$k_{\alpha 2}$ radiation) and the increase of the frac-

tion of mullite suggested by the higher relative intensity of the mullite reflections. The stabilization of tetragonal/cubic zirconia at room temperature is probably due to the enrichment in yttrium released from the glassy phase during annealing, which is paired to the crystallisation of mullite. Indeed, changes in the relative intensity of the (120) and (210) mullite reflections (the doublet at ~26 °), and a slight shift towards higher angles, apparent when comparing both patterns in Figure 1 can be due to a decrease of the global Al:Si ratio in mullite [29]. This is expected since, as determined by EDS, the Al:Si atomic ratio is lower in the amorphous phase than in the mullite grains, and thus the mullite crystallised form the glassy phase should be richer in Si. These changes are confirmed by the quantification of the phase composition obtained by the analysis of the SEM micrographs (Table 1). These values are affected by non-quantified errors due to the lack of contrast of the images, but the observed differences are well above these errors and are fundamental for the subsequent discussion of the electrical properties (note that the dispersion values given in Table 1 are statistical).

Firstly, note the higher fraction of the metastable amorphous phase for the faster growth rate, as expected for a kinetically limited crystallization. Likewise, kinetic reasons may hinder the $Z^t \rightarrow Z^m$ phase transition, leading to a higher content of tetragonal zirconia [20]. The EDS mapping results suggest the presence of yttrium in the amorphous phase, thus corroborating the decrease of the yttrium concentration in zirconia for low growth rates [20]. Annealing the samples at high temperature for long periods of time, increases the fraction of mullite, with the final composition approaching the nominal equilibrium composition (Table 1). This is accompanied by the decrease of the amount of amorphous phase, the formation of small Y-rich precipitates, and the Y-diffusion into the zirconia lattice, all contributing to the observed stabilization of the tetragonal phase (Fig. 1). Noteworthy is that the fraction of zirconia remains nearly unchanged for all composites.

### III.3.3.2. Impedance spectroscopy

Figure 6 shows typical impedance spectra obtained at temperatures below 750 °C for the zirconia-mullite eutectic fibres. All spectra consist of one single, slightly depressed semicircle with a capacitance of 10 to 15 pF that is observed up to temperatures as high as 900 °C. For higher temperatures, this semicircle tends to disappear and a new phenomenon (already suggested by the low frequency tail in the high temperature spectra), becomes dominant. These spectra deviate from those typically observed in polycrystalline ceramic ionic conductors such as YSZ, usually depicting the two semicircles of the bulk

and grain boundary resistances [30], for two main reasons. Firstly, the particular geometry of the fibres (very low cross-sectional area - 0.017 $cm^2$ - and relatively large length - 0.3 to 0.4 cm) originates (for a dielectric constant of 30 typical of ionic conductors) a bulk capacitance of approximately 0.15 pF. This value is about 2 orders of magnitude lower than the measured capacitance, which obviously cannot be ascribed to ionic relaxation in the bulk of either of the composite phases. The most likely reason for this high value is the stray capacitance of the coaxial cables and platinum wires (measured separately with a dummy cell), which is connected in series with the sample and hence dominates the overall capacitive response of the system. However, the ohmic drop due to the experimental set-up is less than 1Ω, and hence the amplitude of the semicircle can be safely used to estimate the fibre resistance (R), and thus the conductivity by $\sigma=L(RS)^{-1}$, where L and S are the length and the cross sectional area of the fibres.

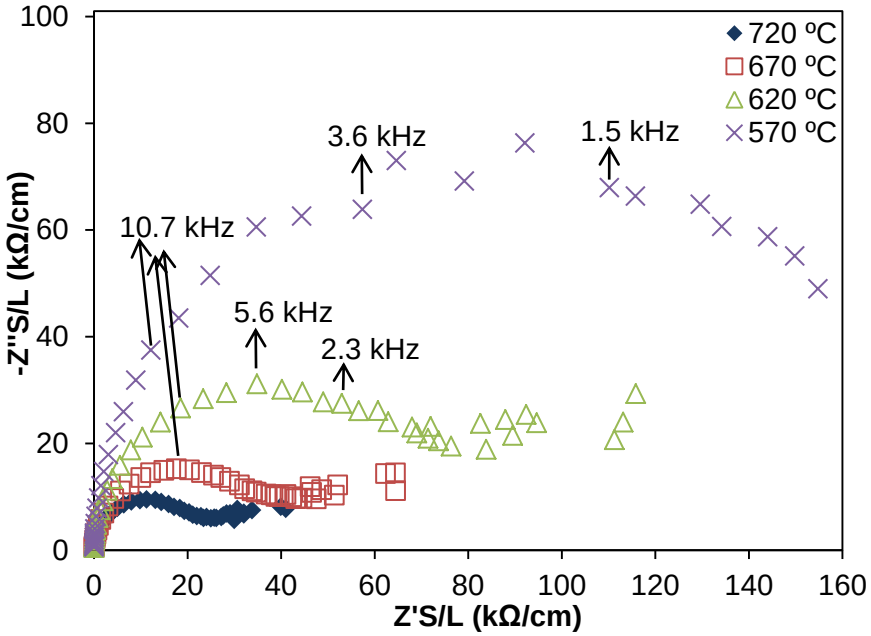


***Figure 6:*** *Nyquist plots obtained for a fresh fibre grown at 100 mm/h.*

Figure 7 shows the conductivity data measured in air for the DSE zirconia-mullite fibres produced by LFZ, including for comparison relevant literature data on the individual components and for a hot-pressed zirconia-mullite composite (20 vol.% $ZrO_2$). The values obtained for our fibres are all within the limits defined by mullite and yttria-substituted zirconia. One expects that the amount of amorphous phase, which is believed to be highly resistive, may have a pronounced effect on the conductivity. In fact, very low conductivity values (of the order of $6x10^{-9}$ S/cm at 600 °C) were reported by Gödickemeier et al. for

glasses with compositions in the systems $Y_2O_3$-$Al_2O_3$-$SiO_2$ and $Y_2O_3$-$Al_2O_3$-$SiO_2$-$ZrO_2$, similar to the intergranular glassy phase in the now reported LFZ fibres [31].

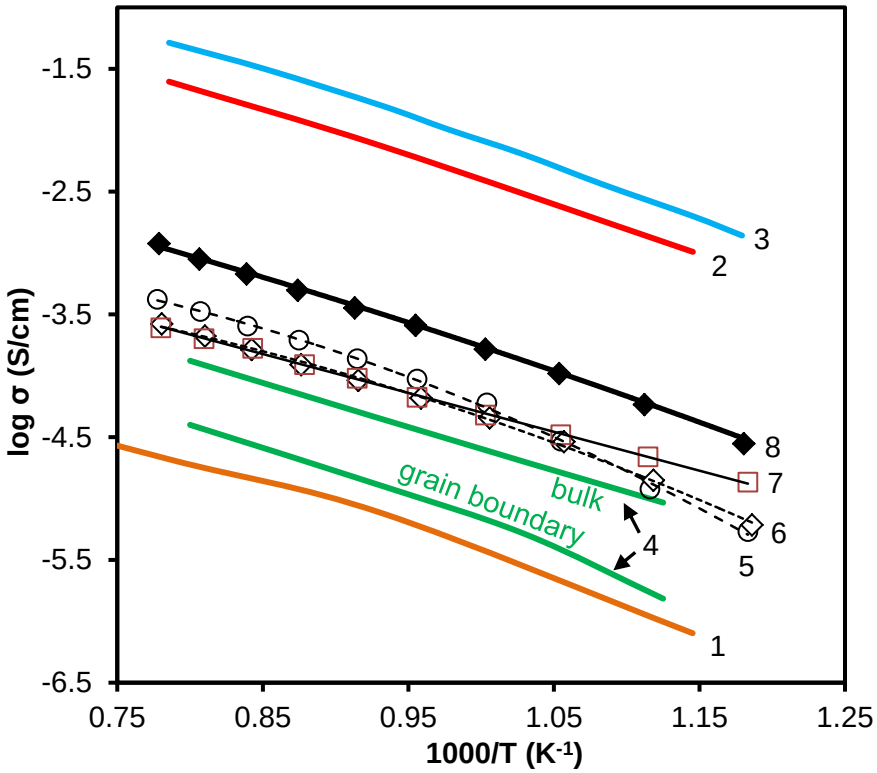


***Figure 7:*** *Arrhenius plots for the total conductivity in air of various samples (except for the noticed exception of **4**), including literature data: **1** - 3.75$Al_2O_3$-2$SiO_2$ mullite [17], **2** - tetragonal zirconia single-crystal (4 mol.% $YO_{1.5}$) [33], **3** - tetragonal zirconia polycrystal (6 mol.% $YO_{1.5}$) [34], **4** – bulk and grain boundary conductivity of hot-pressed zirconia-mullite composite with 20 vol.% $ZrO_2$ [18]. LFZ fibres grown at: **5** - 10 mm/h, **6** - 100 mm/h, **7** - 500 mm/h, and **8** - 100 mm/h after annealing at 1400 °C. Lines are guides for the eye.*

The set of data presented in Figure 7 can be qualitatively understood considering the above mentioned compositional and microstructural (essentially percolation) differences of the three fibres grown at distinct growth rate, and the known transport properties of zirconia and mullite. For the 10 mm/h fibre, the data clearly deviate from the Arrhenius behaviour. A similar curved tendency is observed for the fibre grown at 100 mm/h, but this is clearly less pronounced than in the previous case. Following the trend for a decreasing curvature with increasing pulling rate, the fibre grown at 500 mm/h displays an almost linear trend. Due to the different activation energies, the ionic conductivity in the low temperature regime is slightly higher for the fibre grown at 500 mm/h, while, at higher temperatures, the slowest grown fibre is the most conductive.

Considering the fibre composition presented in Table 1, it is reasonable to assume that mullite (~55 vol.% of the fibre) plays an important role in the conductivity of the fibres

grown at 10 and 100 mm/h. This is indeed suggested by the curvature in the data, closely matching the behaviour of pure mullite [17]. The bending in the Arrhenius of mullite was ascribed to the significant reduction of the concentration of free oxide vacancies at the lower temperatures, due to the formation of defect associates with the dopant cations. These defect clusters dissociate at high temperature leading to a decrease of the activation energy, which is mainly determined by the migration enthalpy of the oxide vacancies [17,32].

The 500 mm/h fibre has only ~19 vol.% of mullite and about 60 vol.% of the highly resistive glassy phase (Table 1). In this case, even considering that $ZrO_2$ corresponds to about 20 vol.% (Table 1), a higher $ZrO_2$ conductivity was registered, due to the higher fraction of tetragonal phase resulting from the increased Y content explained by kinetic reasons [20]. Moreover, the highest pulling rate also leads to a much finer eutectic microstructure, potentially reducing the critical volume of zirconia required to ensure percolation (Fig. 4f), whereas it has the opposite effect on the mullite crystals growing perpendicularly to the zirconia (see Fig. 4b and detailed analysis in ref. [20]). In these conditions, the percolation through the zirconia is expected to prevail over that of mullite, due to the higher connectivity between $ZrO_2$ fibrils and their high coarseness at the eutectic crystals borders [20]. Consequently, the Arrhenius plot for the 500 mm/h fibre (line 7 in Fig. 7) displays the linear trend expected for $ZrO_2$ with low yttrium contents (≤ 6 mol.% $YO_{1.5}$ [33,34]). Conversely, in the 10 mm/h fibre the percolation is favoured along the mullite well-aligned with fibre axis [20], which is also present in a much higher volume fraction. This explains the enhanced performance above ~670 °C when compared with the 500 mm/h fibre, where the oxide transport remains mainly sustained by the zirconia phase.

***Table 1:*** *Fibre composition estimated from image analysis. Note that the lack of contrast in some images may affect these measurements. The nominal composition is also given.*

| Growth rate (mm/h) | Mullite (vol.%) | Zirconia (vol.%) | Amorphous (vol.%) |
|---|---|---|---|
| 10 | 56±4 | 21±3 | 23±4 |
| 100 | 53±4 | 18±2 | 29±4 |
| 500 | 19±3 | 21±4 | 60±5 |
| 100 (Annealed), Fig 7 | 63±3 | 20±3 | 17±5 |
| 100 (Annealed), Fig 8 | 65±3 | 21±3 | 14±4 |
| Nominal composition | 79 | 21 | - |

The conductivity of the as-grown fibres is considerably higher than for zirconia-mullite composites with the same volume fraction of zirconia obtained by a more conventional hot-pressing route [18]. The literature bulk and grain boundary data are plotted to illustrate the highly negative impact of the grain boundaries on the total conductivity of conventional polycrystalline composites. The low grain boundary density is, paradoxically, one of the key advantages of DSE materials. The second key microstructural feature of DSE materials is the preferential alignment of the phases along the fibre axis, favouring percolation and hence conductivity. This advantageous morphological feature of the DSE materials prevails over the larger fraction of monoclinic zirconia and the presence of glassy intergranular phase, both detrimental for conductivity. In fact, the significant conductivity enhancement observed after annealing the fibre grown at 100 mm/h at 1400 °C for 10 h, is due to the minimization of the impact of these non-favourable characteristics. The annealed sample has about 12% less glassy phase and a clearly higher fraction of $Z^t$ for a similar overall quantity of zirconia (Table 1). In the annealed fibre (grown at 100 mm/h), however, the stabilization of the tetragonal zirconia phase is achieved by an increased amount of yttrium, which would also increase the conductivity. As a consequence, the relative contribution of mullite to the conductivity of the composite is decreased and the curvature in the Arrhenius is strongly reduced (although still apparent). Despite the presence of a considerable amount of glassy phase (~17%), the conductivity of the annealed fibre grown at 100 mm/h is 6 to 7 times higher than the bulk conductivity of hot-pressed composites with similar amount of zirconia. This confirms the potential of the LFZ method to develop optimized microstructures.

Figure 8 (data series number 1) shows the conductivity of a freshly prepared 100 mm/h fibre that was annealed *in situ* at 1400 °C overnight before the measurements. This fibre was measured over a broad temperature (570 °C - 1415 °C) and $P_{O_2}$ ($10^{-20}$ Pa - $10^5$ Pa) ranges, as required by the envisaged application. It is interesting to notice that the conductivity of this fibre is significantly higher than the conductivity of the 100 mm/h fibre annealed *ex-situ* at 1400 °C (identified with number 2), previously shown in Figure 7. The considerably higher conductivity of the new fibre from Figure 8 can be understood in view of the coarser, longer and parallel zirconia grains observed in this fibre (Fig. 9b) in comparison to the fibre from Figure 7 (Fig. 9a). It should be noticed that the phase composition of both fibres should be very similar, according to the quantification based on the digital analysis of SEM micrographs (Table 1), which also suggests the microstructure as the key factor to explain the differences of conductivity between the two samples.

In fact, given the relatively low volume fraction of the amorphous phase and its very high resistivity, one may on first approximation describe the multiphase, complex DSE materials as a bi-phasic mixture of zirconia and mullite. The conductivity of such composite mixture ($\sigma_{composite}$) can be expressed by a simple logarithmic mixture rule as a function of the conductivity of mullite and zirconia ($\sigma_Z^n$ and $\sigma_M^n$, respectively) and the volume fraction of zirconia ($\varphi$) according to

$$\sigma_{composite} = \varphi\sigma_Z^n + (1-\varphi)\sigma_M^n, \quad (1)$$

where $n$ is an exponent closely related to the distribution of both phases. This exponent is 1 for the simplest case of a model composite consisting of parallel slabs (or rods) of the 2 phases aligned with the current flow.

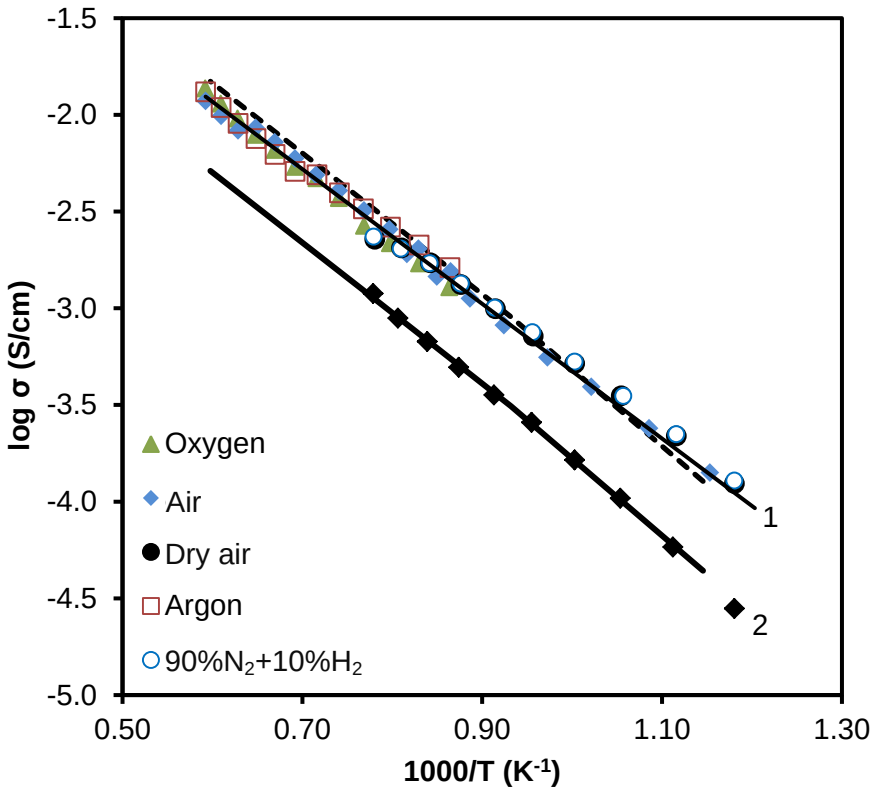


***Figure 8:*** *Arrhenius plots showing a mix of conductivity measurements carried out on **1** a 100 mm/h fibre under different atmospheres, from reducing (90%$N_2$+10%$H_2$ mixture, $P_{O_2}$ <$10^{-20}$ Pa; Argon, $10^{-7}$ Pa<$P_{O_2}$<$10^{-4}$ Pa) to oxidizing conditions (Air, $P_{O_2}\approx 2.1\times10^4$ Pa; oxygen, $P_{O_2}\approx10^5$ Pa). The fibre was first measured in the range 1400-900 °C, after an annealing overnight in situ at 1415 °C. The thin solid line is the fit to the Arrhenius equation of the data collected in air, and the thick dashed line is the prediction based on a simple mixture rule ($n$=0.5 details in the text). The data series **2** for the 100 mm/h fibre previously annealed at 1400 °C (series **8** in Fig. 7), and the corresponding fit to the mixture rule ($n$=0.75), are included for comparison.*

This would be the optimum situation where all the highly conductive zirconia grains are percolated and parallel to the fibre longitudinal axis along which the conductivity was measured. Lower $n$ values obviously represent a deviation from this model behaviour. If we assume $\varphi \approx 0.2$ from the image analysis and literature values for $\sigma_Z^n$ (4 mol.% $YO_{1.5}$ substituted $ZrO_2$ [33]) and $\sigma_M^n$ [17], the data series **2** (the fibre from Fig. 7) can be fitted with $n$=0.5, which is indicative of a significant deviation of the model description. This is an indication that a significant fraction of the zirconia phase is fragmented and perpendicular to the fibre axis, in agreement with Figure 9a. In the ideal situation of a totally aligned and percolating zirconia network corresponding to $n$=1, the conductivity would be about 5 times higher. The same model yields $n$=0.75 when fitting the new fibre data series **1** in Figure 8, which is much closer to the ideal parallel model than the fibre of the data series **2**. This qualitative result is in very good agreement with the simple qualitative observation of the micrographs in Figure 9 and quantifies the potential improvement of the conductivity attainable by manipulation of the microstructure.

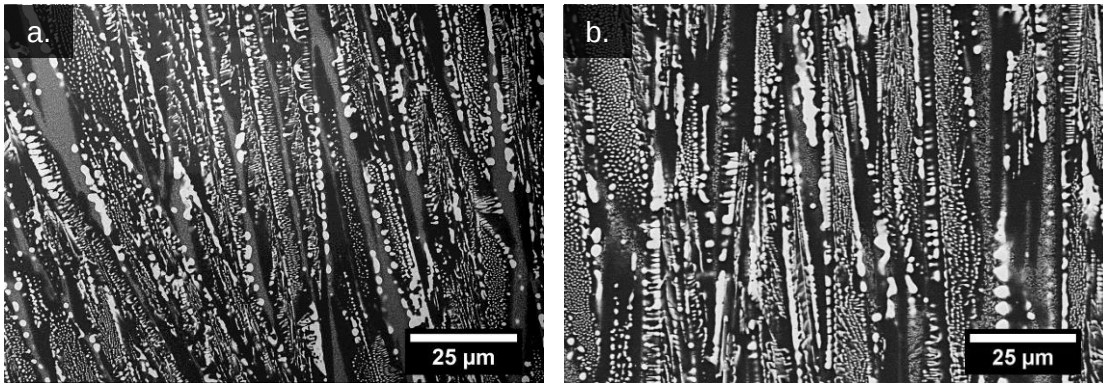


***Figure 9:*** *Comparison of the microstructures of the longitudinal sections of the two 100 mm/h fibres annealed at 1400 °C shown in* ***(a)*** *Fig. 7 and* ***(b)*** *Fig. 8.*

The remainder analysis of conductivity at high temperature and under variable atmosphere is based on the data shown in Figure 8 obtained with the best fibre (data series **1**). The Arrhenius behaviour is observed in all conditions with an activation energy close to 70 kJ/mol, which is in excellent agreement with values found for tetragonal zirconia (66 kJ/mol [35]) and mullite (72 kJ/mol [17]) in similar conditions. The conductivity value attained at 1370 °C is in excess of ~0.01 S/cm, nearly 2 orders of magnitude higher than pure $3.75Al_2O_3$-$2SiO_2$ mullite [17]), but more than 1 order of magnitude lower than yttria-substituted zirconia [33,34]. Moreover, the conductivity remains independent of the oxygen partial pressure over the entire temperature range, confirming the expected (in view

of the properties of the individual components) broad electrolytic domain of the composites.

### III.3.4. Conclusions

Directional solidified eutectic (DSE) zirconia-mullite composites were grown by the laser floating zone (LFZ) technique using variable pulling rates (10, 100 and 500mm/h). The eutectic crystals, comprising mullite, and monoclinic and tetragonal zirconia, are immersed in a highly resistive Al-Y-Si-O amorphous phase. The phase composition and percolation depend on the growth rate, and determine the ionic conductivity of the composite. At temperatures below ~700 °C, the fibres pulled at 500 mm/h show better oxide-ion conduction owing to the fine zirconia distribution favouring the reduction of the percolation threshold. The fraction of mullite is the highest for the lower pulling rates, and Arrhenius plot displays the curvature typical of pure mullite.

Conductivity values in excess of 0.01 S/cm were attained at 1350 °C for a fibre with just 20 vol.% zirconia, showing Arrhenius behaviour (70 kJ/mol) and no dependence of $P_{O_2}$ within the studied temperature range, further demonstrating the broad electrolytic domain of these solid electrolytes. From the view point of electrical and electrochemical properties, these results demonstrate the potential of directional solidification by LFZ for the preparation of zirconia-mullite composites with favourable microstructure and high ionic conductivity at very high temperature (>1300 °C), in comparison with other methods. These properties suggest the application of these materials as solid oxide electrolytes, namely as oxygen sensors in thermally and chemically aggressive environments such as steel or glass melts. Other properties such as the chemical stability should be assessed, and the likely enhancement of the thermo-mechanical properties of these composites in comparison with pure YSZ should be confirmed.

### Acknowledgements

Work funded by FCT (Portugal) through projects CICECO PEst-C/CTM/LA0011/2013 and I3N PEst-C/CTM/LA0011/2011. Ricardo G. Carvalho also acknowledges FCT for a PhD grant (SFRH/BD/64891/2009).

## References


[1] J. Llorca, V.M. Orera, Directionally solidified eutectic ceramic oxides, Progress in Materials Science, 51 (2006) 711-809.

[2] A. Revcolevschi, G. Dhalenne, Engineering oxide-oxide and metal-oxide microstructures in directionally solidified eutectics, Advanced Materials, 5 (1993) 657-662.

[3] R. Čička, V. Trnovcová, M. Starostin, Phase composition, microstructure and electrical properties of alumina-zirconia eutectic composites, Ionics, 8 (2002) 314-320.

[4] V. Trnovcová, M. Starostin, V. Labas, R. Cicka, Microstructure and physical properties of directionally solidified alumina-zirconia eutectic composites, Ionics, 4 (1998) 275-284.

[5] R.L. Ashbrook, Directionally solidified ceramic eutectic, Journal of the American Ceramic Society, 60 (1977) 428-435.

[6] V.M. Orera, R.I. Merino, J.A. Pardo, A. Larrea, J.I. Peña, C. González, P. Poza, J.Y. Pastor, J. Llorca, Microstructure and physical properties of some oxide eutectic composites processed by directional solidification, Acta Materialia, 48 (2000) 4683-4689.

[7] R.I. Merino, I. de Francisco, J.I. Peña, Ionic conductivity in directionally solidified $Al_2O_3$-$ZrO_2$(3 mol.% $Y_2O_3$) near eutectic composites, Solid State Ionics, 178 (2007) 239-247.

[8] R.I. Merino, J.I. Peña, V.M. Orera, G.F. de la Fuente, Conductivity anisotropy in directionally solidified $CaZrO_3$-CaSZ and MgO-MgSZ eutectics, Solid State Ionics, 100 (1997) 313-318.

[9] F.M.L. Figueiredo, F.M.B. Marques, Electrolytes for solid oxide fuel cells, Wiley Interdisciplinary Reviews: Energy and Environment, 2 (2013) 52-72.

[10] N. Claussen, M. Ruhle, A.H. Heuer, Science and technology of zirconia II, American Ceramic Society Ohio, 1984.

[11] H. Schneider, S. Komarneni, Mullite, WILEY-VCH Verlag GmbH & Co. KGaA, Weinheim, 2005.

[12] R.G. Carvalho, A.J.S. Fernandes, F.J. Oliveira, E. Alves, N. Franco, C. Louro, R.F. Silva, F.M. Costa, Single and polycrystalline mullite fibres grown by laser floating zone technique, Journal of the European Ceramic Society, 30 (2010) 3311-3318.

[13] Rommerskirchen, F. Chávez, D. Janke, Ionic conduction behaviour of mullite ($3Al_2O_3$-$2SiO_2$) at 1400 to 1600 °C, Solid State Ionics, 74 (1994) 179-187.

[14] K. Yamana, M. Miyamoto, K. Doi, T. Arahori, J. Nowotny, Impact of grain boundaries on properties of mullite as a solid electrolyte, N. Janusz (Ed.) Materials Science Monographs, Elsevier (1995) 571-591.

[15] C. Kawai, T. Arahori, K. Yamana, M. Miyamoto, K. Nakagawa, H. Suito, A. Inoue, Sensor for measuring oxygen/metal concentration in fused metal, Sumitomo metal Ind. Ltd., 1992.
[16] H.-D. Ko, C.-C. Lin, Oxygen Diffusivities and Surface Exchange Coefficients in Porous Mullite/Zirconia Composites Measured by the Conductivity Relaxation Method, Journal of the American Ceramic Society, 93 (2010) 176-183.
[17] G.-Y. Meng, R.A. Huggins, The oxygen ion conductivity of mullite prepared using a wet chemical process, Solid State Ionics, 11 (1984) 271-278.
[18] H.-D. Ko, C.C. Lin, K.C. Chin, Effect of zirconia content on electrical conductivities of mullite/zirconia composites measured by impedance spectroscopy, Journal of Materials Research, 23 (2008) 2125-2132.
[19] K. Yamana, S. Nakamura, J. Nowotny, Z.M. Zhang, F. Terasaki, Electrical-resistance and related properties of mullite zirconia composites, Journal of the Ceramic Society of Japan, 103 (1995) 184-188.
[20] R.G. Carvalho, M.S. Pires, A.J.S. Fernandes, R.F. Silva, F.M. Costa, Directionally solidified eutectic and off-eutectic mullite-zirconia fibres, Journal of the European Ceramic Society, 33 (2013) 953-963.
[21] J. Rodriguez-Carvajal, Fullprof: A program for Rietveld refinement and pattern matching analysis, 1990.
[22] W.S. Rasband, ImageJ, in, Bethesda, MD: National Institutes of Health, 1997-2012.
[23] G. Brunauer, H. Boysen, F. Frey, T. Hansen, W. Kriven, High temperature crystal structure of a 3:2 mullite from neutron diffraction data, Zeitschrift Fur Kristallographie, 216 (2001) 284-290.
[24] R.J. Hill, L.M.D. Cranswick, International union of crystallography commission on powder diffraction Rietveld refinement round robin II. Analysis of monoclinic $ZrO_2$, Journal of Applied Crystallography, 27 (1994) 802-844.
[25] U. Martin, H. Boysen, F. Frey, Neutron powder investigation of tetragonal and cubic stabilized zirconia, TZP and CSZ, at temperatures up to 1400 K, Acta Crystallographica Section B-Structural Science, 49 (1993) 403-413.
[26] C. Viazzi, J.-P. Bonino, F. Ansart, A. Barnabe, Structural study of metastable tetragonal YSZ powders produced via a sol-gel route, Journal of Alloys and Compounds, 452 (2008) 377-383.
[27] J. Chevalier, L. Gremillard, A.V. Virkar, D.R. Clarke, The tetragonal-monoclinic transformation in zirconia: lessons learned and future trends, Journal of the American Ceramic Society, 92 (2009) 1901-1920.

[28] M. Yashima, M. Kakihana, M. Yoshimura, Metastable-stable phase diagrams in the zirconia-containing systems utilized in solid-oxide fuel cell application, Solid State Ionics, 86-88, Part 2 (1996) 1131-1149.
[29] R.X. Fisher, H. Schneider, M. Schmücker, Crystal structure of Al-rich mullite, American Mineralogist 79 (1994) 983-990.
[30] C.M. Fernandes, A. Castela, F.M. Figueiredo, J.R. Frade, Microstructure-property relations in composite yttria-substituted zirconia solid electrolytes, Solid State Ionics, 193 (2011) 52-59.
[31] M. Godickemeier, B. Michel, A. Orliukas, P. Bohac, K. Sasaki, L. Gauckler, H. Heinrich, P. Schwander, G. Kostorz, H. Hofmann, O. Frei, Effect of intergranular glass-films on the electrical-conductivity of 3Y-TZP, Journal of Materials Research, 9 (1994) 1228-1240.
[32] Y. Arachi, H. Sakai, O. Yamamoto, Y. Takeda, N. Imanishai, Electrical conductivity of the $ZrO_2$-$Ln_2O_3$ (Ln=lanthanides) system, Solid State Ionics, 121 (1999) 133-139.
[33] S. Ikeda, O. Sakurai, K. Uematsu, N. Mizutani, M. Kato, Electrical conductivity of yttria-stabilized zirconia single crystals, Journal of Materials Science, 20 (1985) 4593-4600.
[34] M.A. Lourenco, G.G. Cunto, F.M. Figueiredo, J.R. Frade, Materials Chemistry and Physics 126 (2011) 262-271.
[35] L.A. McClaine, C.P. Coppel, Electrical conductivity studies of tetragonal zirconia, Journal of the Electrochemical Society, 113 (1966) 80-85.

## III.4. Mechanical behaviour of zirconia-mullite directionally solidified eutectics

R.G. Carvalho[a], F.J. Oliveira[b], R.F. Silva[b], F.M. Costa[a]

[a]I3N, Department of Physics, University of Aveiro, 3810-193 Aveiro, Portugal

[b]CICECO, Department of Materials and Ceramic Engineering, University of Aveiro, 3810-193 Aveiro, Portugal

Submitted for publication: Materials & Design

**Abstract**

Laser floating zone technique (LFZ) is used to grow directionally solidified eutectic (DSE) zirconia-mullite composite fibres (30:70 in wt.%). A notable increase in hardness is observed from 11.3 to 21.2 GPa as the pulling rate increases from 10 to 500 mm/h, due to the ultra-fine eutectics developed at very high growth rates. The indentation fracture toughness reaches a maximum value of 3.5 MPa.m$^{1/2}$ for the fibre pulled at 100 mm/h, almost three times the value of 1.2 MPa.m$^{1/2}$ determined for LFZ single-crystal mullite. The eutectic dendrites that develop along the growth direction are immersed in a glassy phase whose brittleness is counteracted by the beneficial ultra-fine morphology, giving a bending strength maximum of 534 MPa. Yet, the soft nature of the glassy matrix prevails at the high temperature testing (1400 ºC), causing a decrease to about one-half of the RT value in the fibres with less glassy phase content.

***Keywords:*** Directional solidification, fibres, mechanical properties, mullite, zirconia.

### III.4.1. Introduction

Directionally solidified eutectic (DSE) ceramics are exciting materials given their singular microstructural characteristics, namely the prevalence of very fine eutectic constituents with strongly bonded phases [1-5]. The absence of grain boundaries and the small spacing between phases in DSEs confines microcrack propagation, resulting in superior rupture strength. A DSE zirconia-mullite ceramic was recently grown using the laser floating zone (LFZ) technique [6]. Mullite is a well-known aluminosilicate with excellent chemical and thermo-mechanical stability that can advantageously replace alumina in structural applications [7-10]. However, the main drawback of mullite-based materials is the low fracture toughness (~2 MPa.$m^{1/2}$) at room temperature (RT), which significantly limits their mechanical strength (~200 MPa) [7,10-11]. Thus, addition of yttria partially stabilized $ZrO_2$ has been suggested owing to their transformation toughening effect in reducing the brittleness of ceramic materials [5,12-14]. The $ZrO_2$ martensitic transformation implies a change from the tetragonal to the monoclinic phase and it has been observed not only in $ZrO_2$ but also in ceramic-matrix composites where $ZrO_2$ is a second phase [12-15].

Zirconia-mullite ceramic composites have been used in power generation engines, glass melting, in steel industry, among other applications [8,10]. Recently, great attention is being given as heat-resistant materials for combustors, nozzles and thermal insulation [10,16] and also in high temperature oxygen sensors in steel casting processes [17-19]. Indeed, the technology involved in steel metallurgy raises the demand for $ZrO_2$-mullite composites with an improve performance in different chemical environments and at high pressures and temperatures.

Claussen et al. used the reaction sintering process to obtain $ZrO_2$-mullite composite materials with a fracture toughness value of 5-6 MPa.$m^{1/2}$, twice that of monolithic mullite [20]. Boch et al. reported mullite and 5 and 15 vol.% $ZrO_2$-mullite ceramics synthesized by tape casting and sintering [21]. The RT bending strength of tape-cast mullite was 250 MPa and the fracture toughness 2.6 MPa.$m^{1/2}$, but $ZrO_2$ inclusions increased both the bending strength (265 MPa in 5 vol.%-$ZrO_2$; 328 MPa in 15 vol.%-$ZrO_2$) and the fracture toughness (2.8 MPa.$m^{1/2}$ and 3.5 MPa.$m^{1/2}$, respectively in 5 and 15 vol.%-$ZrO_2$ composites) [21].

Leriche prepared $ZrO_2$-mullite composites with and without additives to stabilize zirconia, by different routes [22]. The composites synthesized by sintering of sol-gel powders (20 vol.% $ZrO_2$) were completely dense and homogeneous. The absence of intergranular glassy phase is responsible for an interesting high temperature bending strength (300 MPa at 1400ºC). Likewise, Rundgren et al. investigated a 20 vol.% $ZrO_2$-mullite composite

(with 3 mol.% $Y_2O_3$ stabilized-$ZrO_2$) obtained by the same technique [23]. The presence of tetragonal $ZrO_2$ particles in the intergranular phase was believed to increase the mechanical strength by stress-induced transformation, from ~400 to ~560 MPa at RT. The relatively high fracture toughness of 4.1 MPa.$m^{1/2}$ was also explained by the amount of transformable tetragonal zirconia and microcrack arresting at the transformed monoclinic zirconia particles [23].

Industrially, $ZrO_2$-mullite materials are prepared using the melt-growth method (electric arc furnace) taking a mixture of zircon and alumina or a mixture of zirconia, silica and alumina [24]. Typically the composite microstructure has large $ZrO_2$ grains (of about 100 μm), which precipitate as a primary phase during cooling, and then the smaller $ZrO_2$-eutectic constituent crystals (~10 μm). In these composites, a glassy phase fills the gap between the precipitated eutectic colonies [24], which has been pointed out as the main reason for rapidly decreasing of bending strength with temperature [8].

In a previous work, we have shown that the $ZrO_2$-mullite DSE composites obtained by LFZ may display various microstructures (planar coupled eutectic, faceted mullite crystals enclosing a dispersion of fine zirconia fibrils, or mullite columnar growth with coarse zirconia inclusions), depending on the pulling rate [6]. We now intend to investigate the influence of phase amount and morphology on the mechanical behaviour of such fibres, taking advantage of microstructural design, the mullite stability and the yttria-stabilized zirconia toughening mechanism.

### III.4.2. Experimental

The precursor powders for the laser floating zone (LFZ) process were mixed considering a previously optimized pseudo-eutectic composition: 30 wt.% zirconia – 70 wt.% mullite [25]. This composition corresponds to molar fractions of 0.4597 of Al2O3 (Merck anhydrous γ-$Al_2O_3$), 0.3120 of $SiO_2$ (Sigma, $SiO_2$) and 0.2282 of $ZrO_2$ (Tosoh TZ-8Y, 16 mol.% $YO_{1.5}$-$ZrO_2$). Mixing was carried out in a planetary ball-mill (Fritsch, Pulverisette 7 premium line) during 90 minutes at 500 rpm. An organic binder (polyvinyl alcohol, 0.1 g/ml) was added to shape the seed and feed cylindrical rods by cold-extrusion. The LFZ system and the growth conditions of the $ZrO_2$-mullite fibres were described elsewhere [6]. Fibres with final dimensions of about ~1.3 mm in diameter and ~20 mm in length were grown at pulling rates at 10, 50, 100 and 500 mm/h.

The bending strength ($\sigma$) of the fibres was measured at RT and at 1400 ºC in a universal mechanical testing machine (Zwick, model BT1-FR020TNA50) equipped with a high temperature furnace and a 1 KN load cell. Measurements were performed using an alu-

mina three point bending cell with a span distance of 9 mm and rods of 2 mm in diameter. The high temperature tests were carried out in air with a heating rate of 10 ºC/min, under a constant pre-load of 5 MPa, up to 1400 ºC, where a dwell time of 15 min ensured the thermal stabilization before applying the load under a displacement rate of 0.5 mm/min. The bending strength was determined from the equation:

$$\sigma = \frac{8FL}{\pi D^3} \quad (1)$$

where $F$ is the rupture load, $L$ is the holder span, $D$ is the diameter of the fibres.

The Vickers hardness ($H_V$) and the indentation fracture toughness ($K_{IC}$) were measured on polished longitudinal cross-sections of the fibres, using a Shimadzu M apparatus, under 9.8 N of load ($P$) during 15 s. Ten indentations were performed for each pulling rate condition. The hardness was quantified taking the average lengths of the indentation diagonals ($d$) using the equation:

$$H_V = 1.8544 \frac{P}{d^2} \quad (2)$$

The indentation fracture toughness ($K_{IC}$) was determined from Anstis' equation (3) [26], where $c$ is the length of cracks emerging from indentation corners, $E$ the composite Young's modulus;

$$K_{IC} = 0.016 \left(\frac{E}{H_V}\right)^{1/2} \left(\frac{P}{c^{3/2}}\right) \quad (3)$$

$E$ was estimated by the mixing rule $E = fE_{ZrO_2} + (100 - f)E_{mullite}$, where $f$ corresponds to the zirconia weight fraction. In this case, $f$ was assumed equal to 0.35, while the mullite and zirconia Young's moduli were considered as 225 GPa and 205 GPa, respectively [8, 27].

Microstructural characterization was carried out on the polished longitudinal and transversal cross-sections by scanning electron microscopy (SEM, Hitachi SU-70) equipped with energy dispersive X-ray microanalysis (EDS, Bruker Quantax 400).

### III.4.3. Results and discussion

#### III.4.3.1. Microstructural development

The microstructure of $ZrO_2$-mullite DSE fibres is strongly tailored by the growth rate, changing from columnar morphology at low pulling rates, to dendritic eutectic morphology at high pulling rates, as reported with detail in a previous work [6]. These morphologies are illustrated in Figure 1 taking representative SEM micrographs of transversal and longi-

tudinal cross-sections of fibres grown at 10 and 500 mm/h. The developed phases are numerically labelled in Figure 1a as: (1) mullite, (2) Al-Si-Y glassy phase and (3) zirconia.

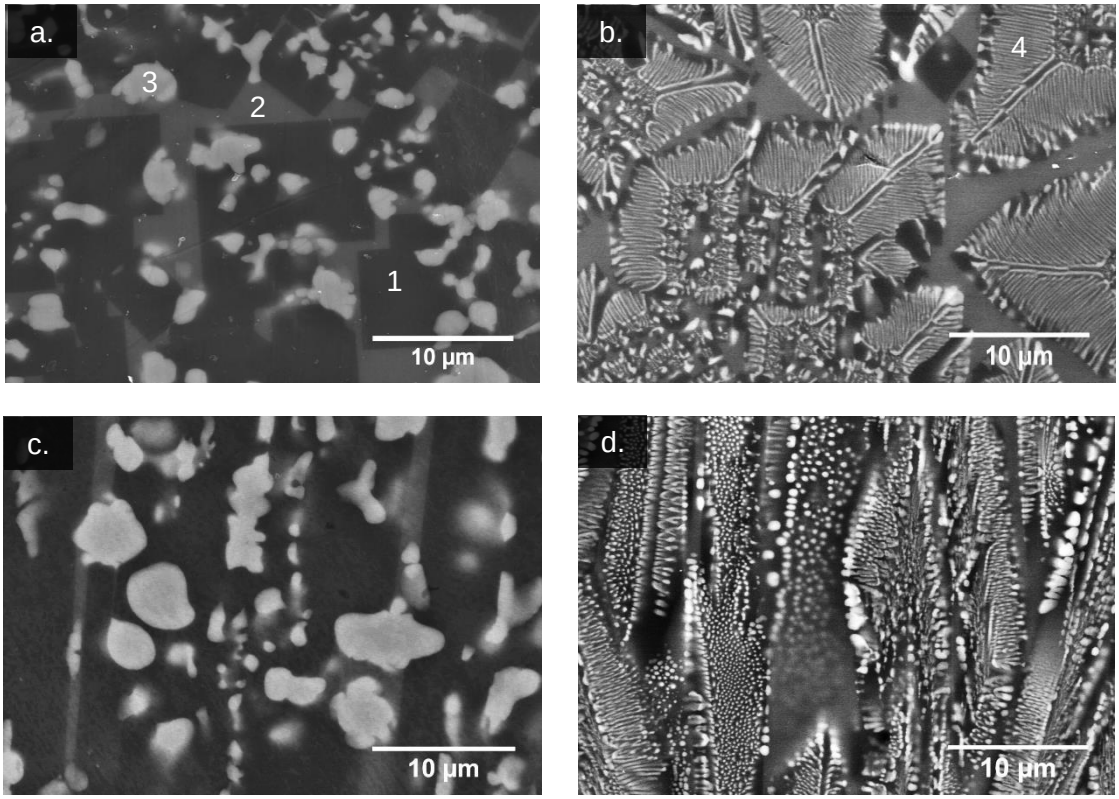


***Figure 1:*** *SEM micrographs obtained along the transversal cross-section of zirconia-mullite DSE fibres grown at 10 mm/h* ***(a)*** *and 500 mm/h* ***(b)****; the corresponding longitudinal cross-sections microstructures are depicted in* ***(c)*** *and* ***(d)****, respectively. The numeric labels correspond to: (1) mullite, (2) glassy phase, (3) globular $ZrO_2$ inclusions and (4) $ZrO_2$ fibrils.*

The shape and dispersion of the zirconia phase in the eutectic domains are a function of the growth rate. At the lowest pulling rate, globular zirconia inclusions (0.6 to 3.5 µm in diameter) develop inside polyhedral mullite crystals (Figs. 1a). At higher pulling rates, zirconia appears as self-organized fibrils (~0.1µm in diameter and 1 to 5 µm in length) in the eutectic constituent, as identified by number (4) in Figure 1b. However, minor globular zirconia grains (0.1 to 0.3 µm in diameter) are still observed at high pulling rates (Fig. 1b). Therefore, the eutectic domains can be described as coarse eutectic, at 10 mm/h, and fine dendritic eutectic for higher pulling rates. The increase of the growth rate under constant thermal gradients increases the constitutional undercooling phenomenon and promotes dendritic eutectic growth [6]. The longitudinal section of the 10mm/h grown fibre (Fig. 1c) corroborates the aligned columnar morphology, which results from preferential growth along the fibre axis, immersed in a Al-Si-Y glassy phase matrix. Dendrites of fine

$ZrO_2$-mullite eutectic develop along the growth direction at higher pulling rates but with a significant amount of interdendritic glassy phase (Figs. 1b,d).

### III.4.3.2. Mechanical properties

#### III.4.3.2.1. Hardness and fracture toughness

The hardness and indentation fracture toughness values of the $ZrO_2$-mullite DSE fibres are plotted in Figure 2. The hardness linearly increases with the growth rate, reaching an outstanding value of about 21.2 GPa for the fibres pulled at 500 mm/h. The slight increase from 11.3 GPa to 12.2 GPa in the 10-100 mm/h range is the opposite of that early found for LFZ-grown pure mullite fibres, which experiment a slight decrease in microhardness (1N of indentation load) from 15.6 GPa to 14.2 GPa in the same range of pulling rates [9]. However, in that case, the single-crystal nature of the fibre grown at 10 mm/h explains the higher hardness result, contrasting to the polycrystalline nature of the fibre grown at 100 mm/h, in which the glassy interdentritic phase is much softer [9]. The addition of zirconia to mullite switches this trend due to the predominance of tetragonal zirconia phase above 50 mm/h with respect to the monoclinic polymorph, as determined in a previous work [19]. Tetragonal structure of yttria-stabilized zirconia is reported as a phase harder than monoclinic zirconia [28,29].

The net increase in hardness observed for the highest pulling rate of 500 mm/h is explained in the light of microstructural characteristics. The improvement of microhardness is consistently observed for the fastest pulled DSE fibres of other compositions and it is related to the very small colony size. Indeed, the decrease of the microstructural domains size for high growth rates induces a interfacial strengthening mechanism by dislocation arresting [1,4]. The ultra-fine eutectic morphology of DSE fibres pulled at 500 mm/h (Figs. 1b,d) contrasts with the coarse morphology of fibres pulled at low rates (Figs. 1a,c) and so is the huge difference in hardness. This feature overcomes the drawback effect of a higher content of interdendritic glassy phase, a softer phase that increases with pulling rate, as above referred. The hardness of similar $YO_{1.5}$-$SiO_2$-$Al_2O_3$ glasses was found to vary from 6.36 to 8.29 GPa and it is greatly controlled by the $YO_{1.5}$ content [30]. Even though the $ZrO_2$ precursor contains 16 mol.% $YO_{1.5}$, DSE fibres are synthesized from a melt and during solidification yttrium is partly incorporated into the glassy phase, as identified by EDS analysis [6]. An amount of 3.5 mol.% $YO_{1.5}$ in $ZrO_2$ was estimated for the 100 mm/h grown fibre [19]. The $YO_{1.5}$ content in tetragonal zirconia is determinant for the hardness of zir-

conia ceramics, varying from ~7 GPa (pure-$ZrO_2$), ~9 GPa (2 mol.% $YO_{1.5}$-$ZrO_2$), ~13 GPa (4 mol.% $YO_{1.5}$-$ZrO_2$) to ~15 GPa (6 mol.% $YO_{1.5}$-$ZrO_2$) [28].

Figure 2 also shows the indentation fracture toughness values of the $ZrO_2$-mullite DSE fibres. Contrary to hardness, the fracture toughness reveals a non-monotonic behaviour in the range of 10-100 mm/h of pulling rate, varying between 2.5 and 3.5 MPa. The $YO_{1.5}$ stabilized-$ZrO_2$ addition leads to an effective increase of fracture toughness over the value 1.2 MPa.$m^{1/2}$ determined for single-crystal mullite synthesized by the same directional solidification method [9]. Asaumi et al. reported a similar fracture toughness increase from 1.6 up to 3.5 MPa.$m^{1/2}$ with $ZrO_2$ incorporation in a $ZrO_2$-mullite composite made by partial zirconia infiltration [31].

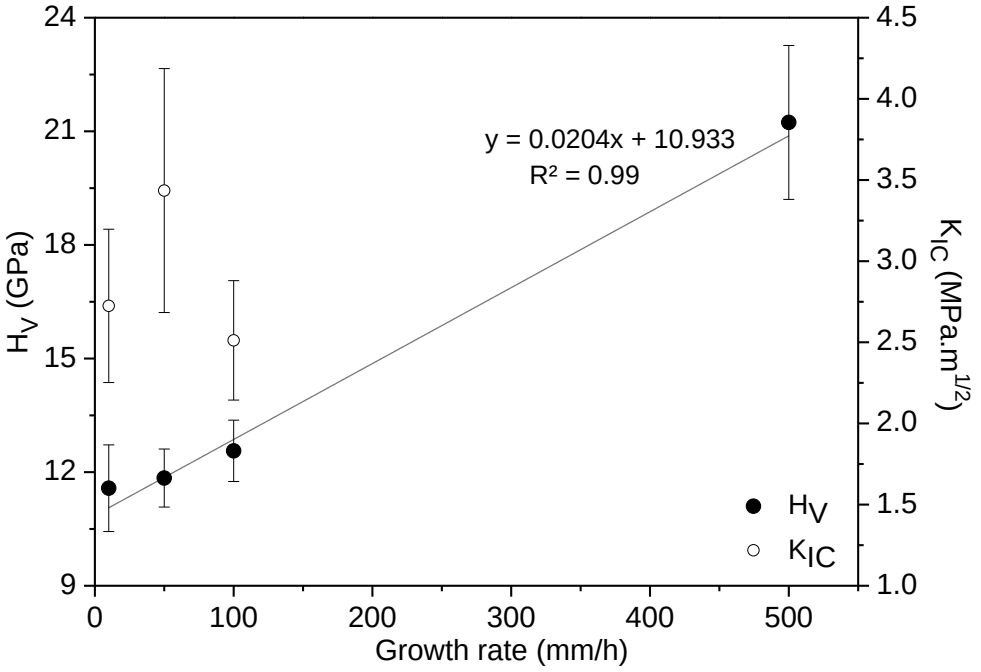


***Figure 2:*** *Vickers hardness ($H_V$) and indentation fracture toughness ($K_{Ic}$) of zirconia-mullite DSE fibres as a function of the growth rate.*

The $K_{IC}$ value for the fibre pulled at 500 mm/h was not possible to estimate by the indentation method as the cracks emanating from the indentation mark were extensive, as shown in Figure 3a. This denotes a net drop in fracture toughness compared to the other fibres where the length of the cracks is much smaller, Figure 3b and in the closer view at the inset. Another characteristic of the crack pattern in the 500 mm/h pulled fibre is the crack deflection towards the fibre axis following the preferential alignment of the eutectic dendrites (Fig. 3a).

The fracture toughness values of the present 20 vol.% $ZrO_2$-mullite DSE fibres are in line with previously published data for $ZrO_2$-mullite composites prepared by conventional

sintering: (i) 3-4 MPa.m$^{1/2}$ for 25 vol.% $ZrO_2$-fused mullite [22]; (ii) 2.8 and 2.4 MPa.m$^{1/2}$ for 10 and 17 vol.% $ZrO_2$-$Al_2O_3$-$SiO_2$ [22] and (iii) 2.9 and 3.0 MPa.m$^{1/2}$ for 10 and 20 vol.% $ZrO_2$-premullite, respectively [22]; (iv) 2.8-3.5 MPa.m$^{1/2}$ for tape-cast 5-15 vol.% $ZrO_2$-mullite composites [21]; and (v) 3.5-4.0 MPa.m$^{1/2}$ for extruded and then hot-pressed 10 vol.% $ZrO_2$-mullite composites [32,33]. Furthermore, for composites prepared in two steps by reactive sintering of $ZrSiO_4$ and $Al_2O_3$, the fracture toughness attained after the first step was 3.5-5.0 MPa.m$^{1/2}$, and 4.3 MPa.m$^{1/2}$ after the second step [22]. The fracture toughness of composites having $YO_{1.5}$ stabilized-$ZrO_2$, prepared by sintering of sol-gel derived powders was 3.0 MPa.m$^{1/2}$ for 19 vol.% $ZrO_2$-mullite, increasing to 4.0 MPa.m$^{1/2}$ for 19 vol.% $ZrO_2$ (6 mol.% $YO_{1.5}$)-mullite [22].

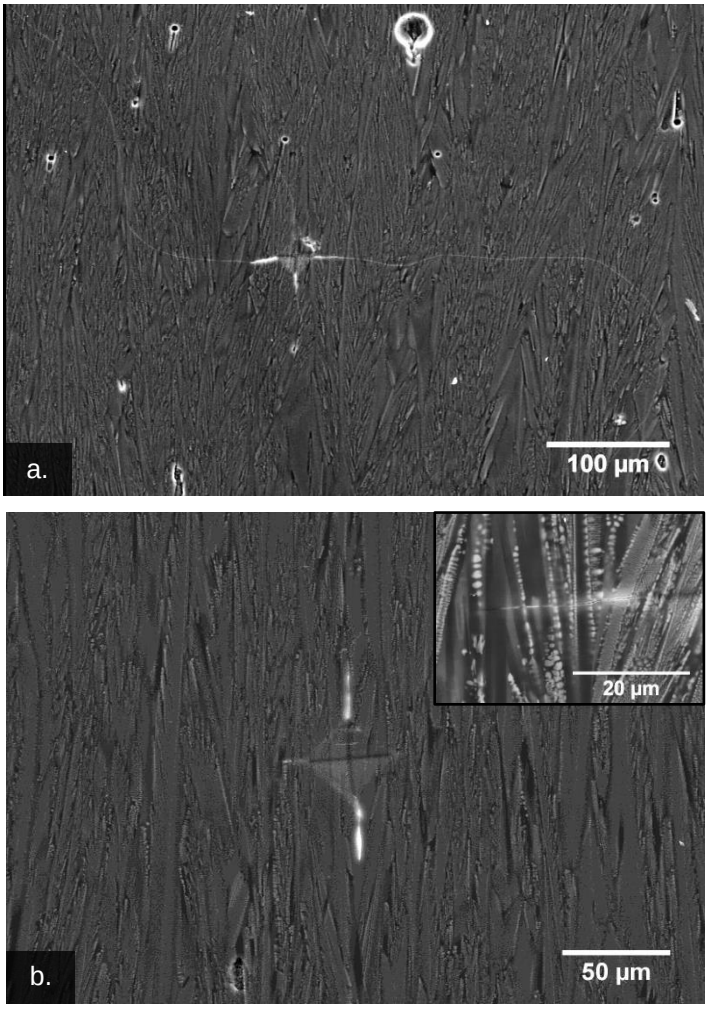


***Figure 3:*** *SEM micrographs showing the Vickers indentations and the distinct crack propagation pattern along longitudinal cross-sections of zirconia-mullite DSE fibres grown at 500 mm/h* ***(a)*** *and 100 mm/h* ***(b)****. The inset in (b) corresponds to a magnified view of crack arresting at dendrites.*

Later, Rundgren et al. corroborated this result and explained it based on the larger amount of transformable tetragonal $ZrO_2$ phase (55-70%) and the microcrack nucleation

at the transformed monoclinic $ZrO_2$ [23]. Moreover, it was observed that the decrease of the $ZrO_2$ grain size retained the spontaneous transformation during cooling, and this suggests that no toughening by microcracking occurs. Such lead to the decrease of $K_{IC}$ in composites with almost fully tetragonal zirconia (97%) to 3.4 MPa.$m^{1/2}$ [23].

The transformation toughening mechanisms induced by the yttria-stabilized $ZrO_2$ addition to mullite are: (i) stress-induced volume change during the martensitic tetragonal-monoclinic transformation of zirconia, (ii) microcracking caused by thermal expansion mismatch of zirconia and mullite, (iii) grain-boundary strengthening due to the metastable $ZrO_2$ incorporation into mullite, (iv) surface compression induced by occurrence of monoclinic zirconia [8,10]. Crack-deflection toughening can also take place at zirconia/mullite interfaces [8]. High resolution transmission electron microscopy performed in $ZrO_2$-mullite directionally solidified eutectic (DSE) samples revealed microcracking phenomena associated with twinning of the thermally transformed (i.e., during cooling) monoclinic zirconia phase [34,35].

Figure 4 is a SEM view of the 10 mm/h $ZrO_2$-mullite fibre that illustrates the predominant toughening mechanisms, namely crack arresting at zirconia phase, joining two neighbour $ZrO_2$ grains through the mullite matrix, probably caused by stress-induced volume change (1); microcraking branching in the mullite crystals (2); crack deflection around the $ZrO_2$ phase (3); and crack deflection at the interface between mullite and the intergranular glassy phase (4).

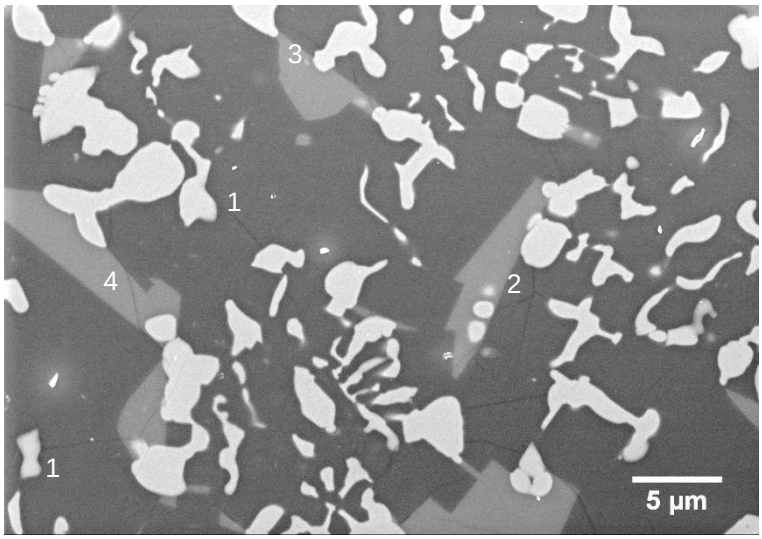


***Figure 4:*** *SEM micrograph of cracking pattern on a transversal cross-section of 10 mm/h zirconia-mullite DSE fibres. The numerically labelled points correspond to different crack-types: (1) stress-induced, (2) microcraking, (3) crack deflection around the $ZrO_2$ phase, (4) crack deflection at the interface between mullite and the intergranular glassy phase.*

The brittle behaviour of the fibre pulled at 500 mm/h is the outcome of the very small $ZrO_2$ particle size that makes thermodynamically unfavourable the martensitic transformation, due to surface phenomena associated with microcracking and/or monoclinic zirconia twinning [34-36]. Also, the very small particle size is adverse to crack deflection toughening. Both effects add to the detrimental higher content of intergranular glassy phase, as above referred.

### III.4.3.2.2. Bending strength

The effect of growth rate on the DSE bending strength is depicted in Figure 5. The average and standard errors of RT bending strength correspond to at least five tests for each growth rate. The lowest RT bending strength value was obtained for the 100 mm/h fibres, while the fibres grown at 500 mm/h present the best mechanical performance. The strength improvement up to 534 MPa for the present DSE fibres grown at the fastest rate of 500 mm/h can be ascribed to the minor size of the eutectic constituents (Figs. 1b,d). Indeed, the DSE fibres strength is proportional to the eutectic domain sizes, being ruled by the microstructural features, phase nature/distribution but also by defect density (voids, cavities, etc.) [4,37].

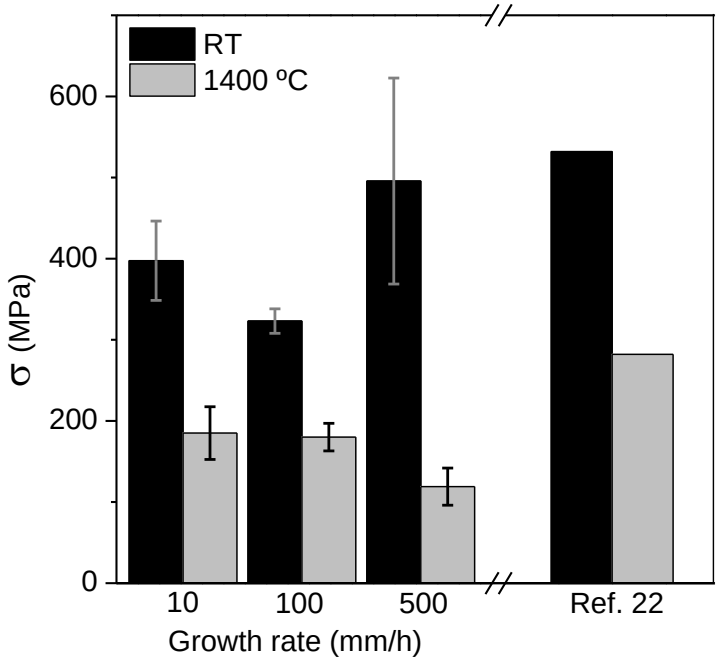


***Figure 5:*** *Bending strength of zirconia-mullite DSE fibres as a function of the growth rate (10 to 500 mm/h) and temperature (RT and 1400 ºC). For sake of comparison, data was added for 20 vol.% $ZrO_2$-mullite composites tested at the same temperatures in ref. [22].*

Even though the fracture toughness is much lower than for the other fibres, the very fine microstructure limits the defect size, and so catastrophic failure requires higher applied stresses. This result indicates that the fibres obtained with the fastest growth may have accentuated anisotropic facture toughness, as Figure 3b already indicated.

The bending strength of the DSE fibres at RT reported in the present work are comparable to results previously published in the literature for $ZrO_2$-mullite composites. In fact, the bending strength for 10, 20 vol.% $ZrO_2$-mullite composites produced by conventional sintering from pre-mullite reached 250 MPa and 290 MPa, respectively [22]. Moreover, composites processed from fused mullite (10 vol.% $ZrO_2$) or fused mixtures of $Al_2O_3$-$SiO_2$ with 10 to 17 vol.% $ZrO_2$, decrease their strength values to 200-250 MPa and 200-210 MPa, respectively [23]. The two step reactive sintering route led to different results, firstly 450 MPa and then a decrease to 270 MPa [22]. Notice too, the distinct results attained with stabilized-$ZrO_2$ by sintering of sol-gel powders by Leriche that reported only a slight increase from 240 to 250 MPa, when adding $ZrO_2$ and/or stabilized-$ZrO_2$ (considering the same 19 vol.% amount) [22]. However, Rundgren et al. disclosed a different behaviour, the addition of non-stabilized $ZrO_2$ (20 vol.%) resulted in a slight increase of the RT bending strength, of about 25% with respect to pure mullite (~350 MPa). A much significant strength increase up to 632 MPa was achieved using $ZrO_2$ (3 mol.% $Y_2O_3$), due to higher volume fraction of tetragonal $ZrO_2$, explained by the stress-induced tetragonal to monoclinic transformation in the stress field of propagating cracks [23].

The bending strength of the 500 mm/h pulled fibre considerably drops at 1400 ºC (Fig. 5), as the soft nature of the glassy-matrix prevails. The decrease in viscosity of the glassy grain-boundary phase plays an important role in the high temperature mechanical properties [38-40]. Indeed, the strength of zirconia-mullite composites is retained up to 1200 ºC, but above this temperature the yttrium rich glassy grain-boundary phase is reported to lead to a drastic strength drop [10,23]. For comparison, the bending strength values at RT and 1400ºC determined for a zirconia-mullite composite sintered from sol-gel powders [22] are given in Figure 5, showing enhanced behaviour at 1400 ºC due to the absence of intergranular phase.

The variability of bending strength results for the DSE materials was characterized by the Weibull modulus (Fig. 6). The common high microstructural homogeneity of other DSE materials may lead to a high Weibull modulus (13-15) but the presence of shrinkage cavities or banding result in a significant reduction of this parameter (down to 3-6) [4]. The banding effect in the present $ZrO_2$-mullite DSE fibres was already disclosed in an early work [6]. Banding phenomena are very common on melt-grown materials and are the out-

come of growth perturbations. Indeed, they correspond to sharp transitions between finer and coarser microstructures, the latter regions being known as bands. The highest RT bending strength attained by $ZrO_2$-mullite DSE fibres (at 500 mm/h) is followed by a large data scattering resulting in a very low Weibull modulus (m=3). However, this is not due to banding phenomena because the lowest band density in zirconia-mullite DSE fibres is attained exactly for such high pulling rates [6]. So, this behaviour should be attributed to the presence of a very high amount of glassy phase and its intrinsic brittle nature. Similarly, in DSE alumina-zirconia fibres, the Weibull modulus decreased from 9 to 3 with increasing growth rates, due to the thicker amorphous phase dispersion [41]. The highest value obtained in the present work for fibres grown at low pulling rate (m=9) is lower than the Weibull modulus disclosed for lamellar DSE alumina-zirconia (m=12.9), but it is considerably higher than those estimated for cellular/colony structures (between 3 to 4) [41].

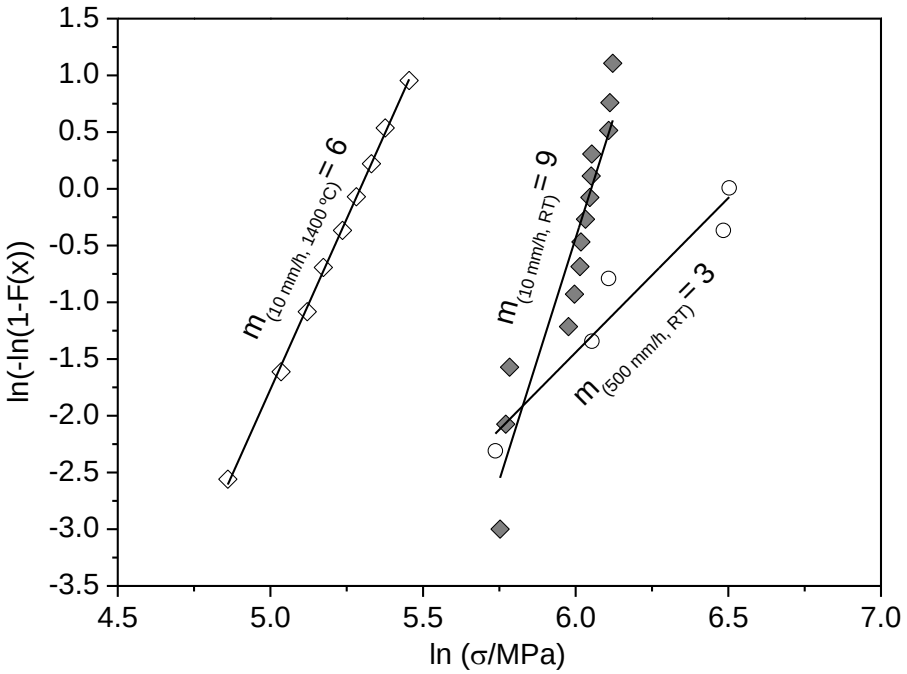


***Figure 6:*** *Weibull probability plot of the bending strength (σ) at RT and 1400 ºC of zirconia-mullite DSE fibres pulled at different rates (10 and 500 mm/h).*

The temperature influence on the Weibull modulus is also plotted in Figure 6. Only the 10 mm/h fibres were considered in order to reduce the glassy phase induce heterogeneous behaviour with the temperature rise. The Weibull modulus only decreased from 9 to 6, disclosing the retention of the microstructure homogeneity at high temperatures, albeit the decrease in mechanical strength. The drop in bending strength is probably due to crack propagation mode both in mullite and zirconia components, changing from intergranular, at low temperatures, to intragranular, at higher ones [8,42]. Moreover, the DSE fibre

strength at high temperatures can be suppressed by interface degradation [43]. The zirconia present in the $ZrO_2$-mullite DSE is almost fully tetragonal, above 1000 ºC [19]. Considering that above this temperature mullite has a higher bending strength than tetragonal $ZrO_2$, it is expected that mullite rules the strength of the 10 mm/h pulled DSE fibres [44].

### III.4.4. Conclusions

Zirconia-mullite fibres synthesized by laser floating zone (LFZ) directional solidification method reveal a change in microstructure from coarse columnar morphology at low pulling rates (10 mm/h), to ultra-fine eutectic morphology at high pulling rates (500 mm/h). Eutectic dendrites develop along the growth direction but with a significant amount of interdendritic glassy phase for the fibres pulled at 500 mm/h. In these fibres, the composite nature of eutectic constituent with tetragonal zirconia fibrils (~0.1μm in diameter and 1 to 5 μm in length) gives rise to an outstanding hardness value to about 21.2 GPa.

The indentation fracture toughness varies between 2.5 and 3.5 MPa.$m^{1/2}$ in the range of 10-100 mm/h of pulling rate, higher than the value of 1.2 MPa.$m^{1/2}$ determined for single-crystal mullite synthesized by the same directional solidification method. This is the outcome of toughening mechanisms ascribed to the addition of $YO_{1.5}$ stabilized-$ZrO_2$ to the mullite matrix. However, in the fibres pulled at 500 mm/h, the $ZrO_2$ fibrils are very small which may turn thermodynamically unfavourable the martensitic transformation and diminish crack deflection toughening. This added to a higher content of intergranular glassy phase, results in an overall decrease of the fracture toughness of the fibres.

The fibres grown at 500 mm/h have the highest RT bending strength (534 MPa). The very fine eutectic microstructure hinders the occurrence of critical defects and so catastrophic failure requires higher applied stresses despite the lower indentation fracture toughness of these fibres. However, the bending strength of these fibres considerably drops at 1400 ºC due to the decrease in viscosity of the glassy phase. The highest Weibull modulus at room temperature (m=9) was attained for the 10 mm/h pulled fibres that only exhibit a residual amount of glassy phase, decreasing to m=6 for bending tests at 1400 ºC, reflecting the preservation of the microstructure homogeneity.

### Acknowledgments

Work funded by FCT (Portugal) through projects CICECO PEst-C/CTM/LA0011/2013 and I3N PEst-C/CTM/LA0011/2011. Ricardo G. Carvalho also acknowledges FCT for a PhD grant (SFRH/BD/64891/2009).

## References


[1] R.L. Ashbrook, Directionally solidified ceramic eutectic, Journal of the American Ceramic Society, 60 (1977) 428-435.

[2] A. Sayir, S.C. Farmer, The effect of the microstructure on mechanical properties of directionally solidified $Al_2O_3/ZrO_2(Y_2O_3)$ eutectic, Acta Materialia, 48 (2000) 4691-4697.

[3] S. Ochiai, T. Ueda, K. Sato, M. Hojo, Y. Waku, N. Nakagawa, S. Sakata, A. Mitani, T. Takahashi, Deformation and fracture behavior of an $Al_2O_3$/YAG composite from room temperature to 2023 K, Composites Science and Technology, 61 (2001) 2117-2128.

[4] J. Llorca, V.M. Orera, Directionally solidified eutectic ceramic oxides, Progress in Materials Science, 51 (2006) 711-809.

[5] H. Su, J. Zhang, L. Liu, H. Fu, Microstructure and mechanical properties of a directionally solidified $Al_2O_3/Y_3Al_5O_{12}/ZrO_2$ hypoeutectic *in situ* composite, Composites Science and Technology, 69 (2009) 2657-2667.

[6] R.G. Carvalho, M.S. Pires, A.J.S. Fernandes, R.F. Silva, F.M. Costa, Directionally solidified eutectic and off-eutectic mullite-zirconia fibres, Journal of the European Ceramic Society, 33 (2013) 953-963.

[7] I.A. Aksay, D.M. Dabbs, M. Sarikaya, Mullite for Structural, Electronic, and Optical Applications, Journal of the American Ceramic Society, 74 (1991) 2343-2358.

[8] H. Schneider, S. Komarneni, Mullite, WILEY-VCH Verlag GmbH & Co. KGaA, Weinheim, 2005.

[9] R.G. Carvalho, A.J.S. Fernandes, F.J. Oliveira, E. Alves, N. Franco, C. Louro, R.F. Silva, F.M. Costa, Single and polycrystalline mullite fibres grown by laser floating zone technique, Journal of the European Ceramic Society, 30 (2010) 3311-3318.

[10] H. Schneider, K. Okada, J.A. Pask, Mullite and Mullite Ceramics, John Wiley & Sons, Chichester, 1994.

[11] P. Boch, T. Chartier, J.P. Giry, Zirconia-Toughened Mullite/The role of zircon dissociation, Ceramic Transactions Mullite and Mullite Composites, The American Ceramic Society, Ohio,1990.

[12] R.C. Garvie, R.H. Hannink, R.T. Pascoe, Ceramic steel, Nature, 258 (1975) 703-704.

[13] R.M. McMeeking, A.G. Evans, Mechanics of transformation-toughening in brittle materials, Journal of the American Ceramic Society, 65 (1982) 242-246.

[14] A.G. Evans, R.M. Cannon, Toughening of brittle solids by martensitic transformations, Acta Metallurgica, 34 (1986) 761-800.

[15] R.H.J. Hannink, P.M. Kelly, B.C. Muddle, Transformation toughening in zirconia-containing ceramics, Journal of the American Ceramic Society, 83 (2000) 461-487.

[16] S.T. Mileiko, Single crystalline oxide fibres for heat-resistant composites, Composites Science and Technology, 65 (2005) 2500-2513.
[17] K. Yamana, S. Nakamura, J. Nowotny, Z.M. Zhang, F. Terasaki, Electrical-resistance and related properties of mullite zirconia composites, Journal of the Ceramic Society of Japan, 103 (1995) 184-188.
[18] H.-D. Ko, C.C. Lin, K.C. Chin, Effect of zirconia content on electrical conductivities of mullite/zirconia composites measured by impedance spectroscopy, Journal of Materials Research, 23 (2008) 2125-2132.
[19] R.G. Carvalho, A.V. Kovalevsky, M.W. Lufaso, R.F. Silva, F.M. Costa, F.M. Figueiredo, Ionic conductivity of directionally solidified zirconia-mullite eutectics, Solid State Ionics, accepted for publication.
[20] N. Claussen, J. Jahn, Mechanical-properties of sintered, *in situ*-reacted mullite-zirconia composites, Journal of the American Ceramic Society, 63 (1980) 228-229.
[21] P. Boch, T. Chartier, Tape casting and properties of mullite and zirconia mullite ceramics, Journal of the American Ceramic Society, 74 (1991) 2448-2452.
[22] A. Leriche, Mechanical-properties and microstructures of mullite-zirconia composites, Ceramic Transactions Mullite and Mullite Composites, The American Ceramic Society, Ohio,1990.
[23] K. Rundgren, P. Elfving, H. Tabata, S. Kanzaki, R. Pompe, Microstructures and mechanical-properties of mullite-zirconia composites made from inorganic sols and salts, Ceramic Transactions Mullite and Mullite Composites, The American Ceramic Society, Ohio,1990.
[24] M. Takenami, K. Akamine, D. Masako, A. Geichiro, T. Masako, A. Keiichiro, Zirconia/mullite refractory raw material used for plate brick, comprises zirconia crystals and mullite as main components, and eutectic zirconia crystals having crystal grain diameter of below specified quantity, Kurosaki Harima Corp., 2012.
[25] J.S. Moya, J.F. Bartolomé, P. Pena, Diagramas de equilibrio cuaternarios $ZrO_2$-$Al_2O_3$-$SiO_2$-(CaO, MgO, $TiO_2$). Una poderosa herramienta para el desarrollo de nuevos materiales por sinterización reactiva, Boletín de la Sociedad Española de Cerámica y Vidrio, 50 (2011) 291-300.
[26] G.R. Anstis, P. Chantikul, B.R. Lawn, D.B. Marshall, A critical-evaluation of indentation techniques for measuring fracture-toughness 1. Direct crack measurements, Journal of the American Ceramic Society, 64 (1981) 533-538.
[27] D.J. Green, An introduction to the mechanical properties of ceramics, Cambridge University Press, Cambridge, 1998.

[28] T. Sakuma, Y. I. Yoshizawa, H. Suto, The microstructure and mechanical properties of yttria-stabilized zirconia prepared by arc-melting, Journal of Materials Science, 20 (1985) 2399-2407.
[29] I.J. McColm, Ceramic Hardness, Springer Science-Business Media, New York, 1990.
[30] M.J. Hyatt, D.E. Day, Glass properties in the yttria-alumina-silica system, Journal of the American Ceramic Society, 70 (1987) C283-C287.
[31] J. Asaumi, H. Yoshida, N. Miyata, H. Kamiaka, C. Yamagishi, Surface modification of mullite by partial infiltration of zirconia, Journal of the Ceramic Society of Japan, 98 (1990) 49-55.
[32] N. Claussen, G. Petzow, Whisker-reinforced oxide ceramics, Journal de Physique, 47 (1986) 693-702.
[33] N. Claussen, Strengthening strategies for $ZrO_2$-toughened ceramics at high-temperatures, Materials Science and Engineering, 71 (1985) 23-38.
[34] M.R. Notis, V.P. Dravid, C.E. Lyman, AEM and HRTEM studies of the eutectic system zirconia-mullite, Ceramic Transactions Mullite and Mullite Composites, The American Ceramic Society, Ohio,1990.
[35] V.P. Dravid, M.R. Notis, C.E. Lyman, Twinning and microcracking associated with monoclinic zirconia in the eutectic system zirconia-mullite, Journal of the American Ceramic Society, 71 (1988) C219-C221.
[36] F.F. Lange, Transformation toughening 3. Experimental observations in the $ZrO_2$-$Y_2O_3$ system, Journal of Materials Science, 17 (1982) 240-246.
[37] S.C. Farmer, A. Sayir, Tensile strength and microstructure of $Al_2O_3$-$ZrO_2$ hypo-eutectic fibers, Engineering Fracture Mechanics, 69 (2002) 1015-1024.
[38] S. Kanzaki, H. Tabata, T. Kumazawa, Sintering and mechanical-properties of mullite derived via spray pyrolysis, Ceramic Transactions Mullite and Mullite Composites, The American Ceramic Society, Ohio, 1990.
[39] T. Kumazawa, S. Ohta, S. Kanzaki, H. Tabata, Influence of powder characteristics on microstructure and mechanical properties of mullite ceramics, Ceramic Transactions Mullite and Mullite Composites, The American Ceramic Society, Ohio, 1990.
[40] P. Descamps, S. Sakaguchi, M. Poorteman, F. Cambier, High-temperature characterization of reaction-sintered mullite zirconia composites, Journal of the American Ceramic Society, 74 (1991) 2476-2481.
[41] J.Y. Pastor, J. Llorca, P. Poza, I. de Francisco, R.I. Merino, J.I. Peña, Mechanical properties of melt-grown $Al_2O_3$-$ZrO_2$($Y_2O_3$) eutectics with different microstructure, Journal of the European Ceramic Society, 25 (2005) 1215-1223.

[42] K. Kobayashi, H. Kuwajima, T. Masaki, Phase change and mechanical properties of $ZrO_2$-$Y_2O_3$ solid electrolyte after ageing, Solid State Ionics, 3-4 (1981) 489-493.
[43] S.V. Nair, K. Jakus, High temperature mechanical behaviour of ceramic composites, Butterworth-Heinemann, Newton, 1995.
[44] Z. Zhang, Y. Huang, L. Zheng, Z. Jiang, Preparation and mechanical properties of SiC whisker and nanosized mullite particulate reinforced TZP composites, Journal of the American Ceramic Society, 79 (1996) 2779-2782.

# Chapter IV

## Conclusions and Future work

*This chapter tries to summarize the main conclusions of this thesis (IV.1.) and prospects future work under the frame of the subjects here developed (IV.2.).*

## IV.1. Conclusions

Along this project, zirconia-based directionally solidified eutectic (DSE) fibres with high microstructural stability envisaging electrochemical and/or mechanical applications were developed and characterized. The employment of the laser floating zone (LFZ) method equipped with a 200 W $CO_2$ laser was fundamental, due to the high melting point of zirconia (~2680 ºC) and the other eutectic constituent phases. Moreover, the accurate control of the fibre growth rate had an important influence in the development of morphologies and compositions of the eutectics.

The zirconia-barium zirconate eutectic was the first chosen system aiming the development of a mixed ionic conductor combining protonic and oxide-ionic conduction. The $ZrO_2$-$BaZrO_3$ fibres prepared according with the eutectic composition are in good agreement with the $ZrO_2$-BaO binary phase diagram reported by Paschoal et al. In a first approach, the rod precursors were prepared with $Y_2O_3$ stabilized-zirconia (4.4 mol.% $YO_{1.5}$). The fibres pulled from 20 to 100 mm/h reveal two crystalline phases: tetragonal zirconia and barium zirconate. However, the yttrium remains at the fluorite structure of zirconia as shown by Raman spectroscopy and validated by the EDS analysis. Fibres combine two alternating eutectic microstructures: bands having a coarser zirconia microstructure and the inter-band region changing from lamellar to colony type microstructure, with the increasing of the growth rate. In fact, it was observed that the $ZrO_2$-rich bands strongly manage the total ionic conductivity.

Considering these results, an yttria-richer composition (18.2 mol.% $YO_{1.5}$) was studied and the growth rate was simultaneously increased up to 300 mm/h in order to decrease the band density. The increase of growth rate lead to the development of $ZrO_2$-dendrites enclosed in barium zirconate thin layers leading to a fine-interpenetrated microstructure combining 50 vol.% of each eutectic constituent phase. Structural characterization by Raman spectroscopy confirmed the presence of yttrium in both zirconia and barium zirconate phases. Such result was corroborated by elemental chemical EDS maps.

The single semicircle at the Nyquist plots confirms the absence of grain-boundaries between grains of the same phase, which is ensured by the finer-interpenetrating microstructure and the barium zirconate developed around the zirconia dendrites. Moreover, the reduction of the semi-circle amplitude in wet atmospheres and temperatures below 500 ºC denotes a protonic conductivity resulting from the yttrium-doping of the $BaZrO_3$ phase. The measurements under different conditions (dry/wet and reduction/oxidizing) allow to define domains where different charge carriers transportation prevail. In this sense, pro-

tonic conduction is dominant for low temperatures and under wet/reducing environments (the activation energies vary from 35 to 48 kJ/mol, between 320 and 500 ºC), while above 500 ºC in dry/oxidizing atmospheres the oxide-ion conduction through highly-doped zirconia and/or hole conduction along yttrium-doped $BaZrO_3$ prevails (reaching values of $E_a$~90 kJ/mol). Therefore, the mixed ionic conduction behaviour was achieved by the designed DSE materials working in different atmospheres and temperatures ranges.

A second system consisting of eutectic and off-eutectic zirconia-mullite fibres was also produced by LFZ directional solidification. Off-eutectic fibres (mullite-rich and zirconia-rich compositions) were grown from 10 to 100 mm/h, while the zirconia-mullite DSE fibres were prepared in a broad range of pulling rates, from 1 to 500 mm/h. Microstructural characterization reveals that the growth rate has no influence on the nature and morphology of the phases in both the two off-eutectic fibres. On the other hand, the zirconia-mullite DSE fibres show a clear different trend. These fibres comprise three crystalline phases: mullite and two of the polymorphic phases of zirconia, namely monoclinic and tetragonal. It was found that the amounts of each phase are strongly dependent on the fibres growth rate. In detail, the tetragonal/monoclinic phase amount ratio is a function of the growth rate, increasing with it. Furthermore, the microstructure of zirconia-mullite DSE fibres varies from coupled to colony microstructure, when the growth rate increases. Such microstructural changes are accompanied by the development of a high amount of Al-Si-Y glassy phase, where the eutectic crystals are immersed.

Likewise in the zirconia-barium zirconate DSE fibres, the banding pattern observed in the zirconia-mullite DSE fibres exchange the finer microstructure with the coarser one, with the band interspacing increasing for higher growth rates. The HTXRD analysis revealed that the monoclinic zirconia fraction almost fully transforms into the tetragonal phase as the temperatures increases up to ~1000 ºC. Moreover, such characterization allow to infer about the yttrium content (3.5 mol.% $YO_{1.5}$) into zirconia.

The zirconia-mullite DSE fibres combine two oxide-ion conductors in a stable eutectic microstructure over a broad electrolytic domain. Ionic conduction is managed by the growth rate, since this parameter rules the phase composition and percolation. It is of extremely importance the reduction of the highly-resistive glassy phase which was accomplished by annealing at 1400 ºC, leading to substantial improvement of the conductivity. In detail, values above 0.01 S/cm at 1370 ºC are attained in the zirconia-mullite DSE fibres, with just 20 vol.% zirconia.

The mechanical behaviour of the zirconia-mullite fibres was also found to be tailored by the fibre microstructure, which is a consequence of the growth rate. In fact, the bending strength increases with the growth rate up to maximum of 534 MPa at 500 mm/h, due to ultra-fine eutectic microstructure which prevails over the brittle nature of the phases. However, for high temperature testing (1400 ºC) the soft nature of the glassy phase becomes dominant. A remarkable hardness (21.2 GPa) is achieved in the fastest as-grown DSE fibres (500 mm/h), which is triggered by the development of self-organized arrangement of fibrils of tetragonal zirconia in a very fine eutectic morphology.

## IV.2. Future work

The future research lines here mentioned are divided in two main topics, due to the distinct potential of the DSE materials covered in this thesis. The first concerns with the investigation developed in the yttrium-doped zirconia-barium zirconate DSE fibres, while the second one is devoted to the zirconia-mullite DSE materials.

**i.** Yttrium-doped zirconia-barium zirconate DSE

It would be imperative to quantify the yttrium amount in the barium zirconate and in the zirconia. Such quantification could be obtained by transmission electron microscopy (TEM) or by particle-induced X-ray emission (PIXE) on the longitudinal fibres cross-section. Yttria-rich compositions could be evaluated in order to increase the yttrium incorporation into the barium zirconate, and so to improve the proton conductivity. Furthermore, other dopant ions like $Yb^{3+}$ or $Sc^{3+}$ could be investigated, in order to enhance the dopant incorporation into the barium zirconate. The fibres growth under different atmospheres has a huge interest due to the barium carbonate evaporation (alternatively BaO-rich compositions can be considered) and the thermal instabilities in the molten region promoted by physical displacement minimized. The growth conditions could be even more explored in order to achieve more homogenous and well-aligned eutectic microstructures. The banding structure in the zirconia-barium zirconate DSE ceramics desires more attention, due to the proved influence of this feature in the electrical behaviour. Therefore, understanding of their formation might be useful for the improvement of the electrical properties. Notice that, most of the investigation realized in this topic is focused in metallic alloys, so it will be interesting to understand how it works in ceramic materials.

**ii.** Zirconia-mullite DSE

It would be essential to reduce the glassy phase amount, since this revealed a damaging influence in the electrical and mechanical properties of the zirconia-mullite DSE fibres. In this sense, two different approaches could be prospected: starting from $Al_2O_3$-richer compositions or subject the as-grown DSE fibres to thermal treatments, like those reported in the second paper of chapter III, but now for even longer periods and/or temperatures. Moreover, it would be interesting to analyse the influence of faster growth rates (e.g. 1000 mm/h) in the mechanical strength and the effect of rotation in the final microstructure. The investigation of the thermal properties of the zirconia-mullite DSE fibres is also attractive, considering the high thermal-shock resistance, low thermal conductivity and the low thermal expansion coefficient of these composites. Indeed, these have been

prospected (in a series of patents) as thermal barrier coatings of the future Si-based ceramics ($Si_3N_4$ and SiC) components to be used in high temperature gas turbines.

Considering that both systems showed banding profiles, it would be important to control the temperature in the molten zone. Thus could be managed using a pyrometer with resolution enough to measure quickly even slight temperature fluctuations in such a small molten zone.

## Appendix

Kroger-Vink notation for point defects in crystals.

| Type of defect | Symbol | Remarks |
|---|---|---|
| Vacant M site | $V_M''$ | Divalent ion are chosen as example with MX as compound formula |
| Vacant X site | $V_X^{\cdot\cdot}$ | $M^{2+}$, $X^{2-}$, cation and anion |
| Ion o lattice site | $M_M^x$, $X_X^x$ | $x$ uncharged |
| L on M site | $L_M'$ | $L^+$ dopant ion |
| N on M site | $N_M^{\cdot}$ | $N^{3+}$ dopant ion |
| Free electron | $e'$ | |
| Free hole | $h^{\cdot}$ | |
| Interstitial M ion | $M_i^{\cdot\cdot}$ | $\cdot$ effective positive charge |
| Interstitial X ion | $X_i'$ | ' effective negative charge |